

ABSTRACT

Title of dissertation: EXPERIMENTAL CHARACTERIZATION
 OF TURBULENT
 SUPERFLUID HELIUM

Matthew S. Paoletti, Doctor of Philosophy, 2010

Dissertation directed by: Professor Daniel Lathrop
 Department of Physics

Fundamental processes in turbulent superfluid ^4He are experimentally characterized by refining a visualization technique recently introduced by Bewley *et al.*. A mixture of hydrogen and helium gas is injected into the bulk fluid, which produces a distribution of micron-sized hydrogen tracer particles that are visualized and individually tracked allowing for local velocity measurements. Tracer trajectories are complex since some become trapped on the quantized vortices while others flow with the normal fluid.

This technique is first applied to study the dynamics of a thermal counterflow. The resulting observations constitute the first direct confirmation of two-fluid motions in He II and provide a quantitative test of the expression for the dependence of the normal fluid velocity, \mathbf{v}_n , on the applied heat flux, q , derived by L. D. Landau in 1941.

Nearly 20,000 individual reconnection events are identified for the first time and used to characterize the dynamics by the minimum separation distance, $\delta(t)$,

between two reconnecting vortices. Dimensional arguments predict that this separation behaves asymptotically as $\delta(t) \approx A(\kappa|t - t_0|)^{1/2}$, where $\kappa = h/m$ is the quantum of circulation. The major finding of the experiments is strong support for this asymptotic form with κ as the dominant controlling quantity. Nevertheless there are significant event-to-event fluctuations that are equally well fit by two modified expressions: (a) an arbitrary power-law expression $\delta(t) = B|t - t_0|^\alpha$ and (b) a correction-factor expression $\delta(t) = A(\kappa|t - t_0|)^{1/2}(1 + c|t - t_0|)$. In light of various physical interpretations we regard the correction-factor expression (b), which attributes the observed deviations from the predicted asymptotic form to fluctuations in the local environment and boundary conditions, as best describing the experimental data. The observed dynamics appear statistically time-reversible, suggesting that an effective equilibrium has been established in quantum turbulence on the time scales investigated.

The hydrogen tracers allow for the first measurements of the local velocity statistics of a turbulent quantum fluid. The distributions of velocity in the decaying turbulence are strongly non-Gaussian with $1/v^3$ power-law tails in contrast to the near-Gaussian statistics of homogenous and isotropic turbulence of classical fluids. The dynamics of many vortex reconnection events are examined and simple scaling arguments show that they yield the observed power-law tails.

EXPERIMENTAL CHARACTERIZATION
OF TURBULENT
SUPERFLUID HELIUM

by

Matthew S. Paoletti

Dissertation submitted to the Faculty of the Graduate School of the
University of Maryland, College Park in partial fulfillment
of the requirements for the degree of
Doctor of Philosophy
2010

Advisory Committee:
Professor Daniel Lathrop, Chair/Advisor
Professor Michael E. Fisher
Professor James Drake
Professor Victor Galitski
Professor William McDonough

© Copyright by
Matthew S. Paoletti
2010

Dedication

To my grandfather, Lt. Col. James G. Steger,
who has been my lifelong role model and was the
first to show me the great joy of studying physics.

Acknowledgments

I would like to express my profound gratitude to everyone who has influenced me over the many years and made this research possible. Without their efforts and belief in me, I would not be the person that I am today.

First, I would like to thank my grandfather, James G. Steger. I have aspired to emulate many of my grandfather's admirable characteristics throughout my life, not least of which is the pursuit of knowledge and a passionate curiosity of the universe. Whether it was simple tricks with paper clips or homemade electromagnetic cranes, my grandfather has shown me the wonderful joy and beauty of physics throughout my entire life. I am deeply honored that he took the time to motivate me and inspire me to use my God-given talents.

I would also like to thank my parents, Michael and Mary, for their consummate support. It has been truly wonderful to have parents that have always believed in me and guided me in all of my pursuits. I want to extend a most loving thanks to my wife, Rachel. She has provided me with a solid foundation to stand upon for over seven years. I cannot express my gratitude for all of the joy that she has brought me and the times when she believed in me even though I found it difficult to do so myself.

I am grateful for the number of insightful discussions that I have had over the years with Carlo Barengi, Russell Donnelly, James Drake, Nigel Goldenfeld, Christopher Lobb, Yuri Sergeev, Ladik Skrbek, Marc Swisdak, Makoto Tsubota, Steven van Sciver, and Joe Vinen. These conversations have been educational for

me, especially given my lack of knowledge in these areas before I began my thesis work.

My fellow graduate students both in my early years of classes as well as those in the lab have truly enhanced my graduate school experience. It is without question that I have learned much from all of them. I would also like to acknowledge the technical supervision of Don Martin and Jay Pyle. Their efforts and guidance were an essential component to all of the experimental apparatus that I designed and built over the years.

Lastly, none of this work would have been possible without those that directly contributed. I would like to acknowledge Gregory Bewley for previous collaboration as well as Katepalli Sreenivasan for his advisory role throughout the years. I am also deeply indebted to Michael Fisher, who has served as an “academic grandfather” in many ways. The conversations that we had were the most stimulating of my graduate career. I am also quite grateful for all of the time and effort that he put forth towards the publications that we co-authored. I will always cherish the drafts that he gave back to me covered in more of his own red, blue and green ink than the original black text that I provided to him. Lastly, none of this work would have been possible without the support and contributions of my advisor, Daniel Lathrop. I have learned a great deal from him that I will take with me throughout all of my future endeavors.

Table of Contents

List of Tables	viii
List of Figures	ix
List of Abbreviations	xiii
1 Introduction	1
1.1 Turbulence	3
1.2 Turbulence in Quantum Fluids	5
1.3 Comparing Classical Fluid and Quantum Fluid Turbulence	7
1.3.1 Energy Cascades	8
1.3.2 Large-Scale Motions	9
1.3.3 Small-Scale Motions	14
1.3.4 Heat Transport	15
1.4 State of Quantum Turbulence Research	18
1.4.1 Experimental Challenges	18
1.4.2 Theoretical and Computational Challenges	22
2 Theoretical Background	26
2.1 Discovery of Superfluidity	26
2.2 Two-Fluid Model	34
2.3 Quantized Vortices and Dynamics	43
2.3.1 An example: Ferromagnetism	43
2.3.2 Superfluid Order Parameter and Quantized Vortices	46
2.3.3 Quantized Vortex Dynamics	49
2.4 Thermal Counterflows	53
2.5 Reconnection	57
3 Apparatus and Experimental Techniques	61
3.1 Apparatus	61
3.1.1 Oxford Cryostat	65
3.1.2 Heater Design and Counterflow Channel	67
3.1.3 Injection Technique	70
3.2 Temperature Measurement and Control	73
3.2.1 Temperature Measurement	75
3.2.2 Temperature Control	79
3.3 Visualization	83
3.3.1 Optics	84
3.3.2 Cameras	86
3.4 Particle-Image Velocimetry vs. Particle-Tracking	88
3.4.1 Particle Image Velocimetry	88
3.4.2 Particle Tracking	90

4	Tracer Particles in Superfluid ^4He	94
4.1	Particle-trapping Mechanism	95
4.2	Particle-trapping Dependencies	96
4.3	Effects of Particle Concentration	101
5	Thermal Counterflows	104
5.1	Previous Work	104
5.2	Particle Trajectories	106
5.3	Effects of Temperature and Vortex-line Density	107
5.4	Measured Normal Fluid and Vortex Tangle Velocities	110
5.5	Discussion	112
6	Reconnection	114
6.1	Pulsed-Counterflow Experiments	114
6.2	Visualizing and Identifying Reconnection Events	116
6.3	Arbitrary Power-Law Model	120
6.4	Correction-factor Expression	127
6.5	Effects of Temperature	133
6.6	Model Comparison	134
6.7	Time-Reversibility	137
6.8	Anisotropy	141
6.9	Implications for Classical Turbulence	144
6.10	Conclusion	145
7	Quantum Turbulence	147
7.1	Similarities with Classical Turbulence	147
7.2	Pulsed Counterflow Experiments	149
7.3	Time-Varying Velocity Distributions	149
7.4	Predictable Power-Law Tails	151
7.5	Velocity Statistics	153
7.6	Analogies with MHD	155
7.7	Conclusions	157
8	Conclusions and Future Work	159
8.1	Summary	159
8.2	Ring Collapse - Dynamics and Effects on Velocity Statistics	162
8.3	Narrow Channel Counterflows	163
8.3.1	Extended Range of Heat Fluxes	165
8.3.2	Poiseuille Flow	167
8.3.3	Turbulent Normal Fluid	168
8.4	Rotating Superfluids	170
8.4.1	Lattice Formation	171
8.4.2	Tkachenko Waves and Rotating Counterflows	173
8.4.3	Taylor-Couette Flow	174
8.5	Injection Improvements	174

8.5.1	Pre-cooled Mixtures	174
8.5.2	Injection Below Transition	176
8.6	Computational Studies	177
A	Codes	179
A.1	Matlab Codes	179
A.2	C codes for data analysis	184
B	Raw Data and Parameters	195
B.1	Counterflow Experiments	195
B.2	Thermistor Calibration	201
B.3	Mutual Friction Coefficients	202
B.4	Pulsed Counterflow Parameters	203
	Bibliography	205

List of Tables

3.1	Parameters of the SR830 lock-in amplifier used to measure the resistance of the temperature probe	77
3.2	Comparison between the specifications of the two cameras used in the experiments	87
6.1	Summary of the amplitude A and correction factor c values for distinct ranges of temperature	134
B.1	Experimental parameters for the counterflow experiments presented in Chapter 5	195
B.2	Measured normal fluid velocities compared to the theoretically computed velocities as plotted in Fig. 5.5(a)	197
B.3	Measured vortex line velocities compared to the theoretically computed superfluid velocities as plotted in Fig. 5.5(b)	199
B.4	Thermistor calibration values	201
B.5	Values of the mutual friction parameters	202
B.6	Experimental parameters for the pulsed counterflow experiments presented in Chapters 6 and 7	203

List of Figures

1.1	Example images of the von Kármán vortex street and wing-tip vortices	10
1.2	Schematic of a triangular array of quantized vortices	12
1.3	Experimental visualizations of vortex lattices in superfluid ^4He , Bose-Einstein condensates and superconductors	13
1.4	Experimental visualization of the flow and temperature profile of Rayleigh-Bénard convection	16
2.1	Plot of the heat capacity C_S for ^4He	28
2.2	Phase diagram for ^4He near the λ -transition	29
2.3	Images of vigorously boiling He I and quiescent He II	30
2.4	Images of the thermo-mechanical “fountain effect”	33
2.5	Plot of the normal fluid fraction and superfluid fraction as a function of temperature	39
2.6	Schematic representation of the paramagnetic to ferromagnetic transition	45
2.7	Schematic of a multiply-connected space	47
2.8	Nonlocal and local contributions to vortex filament calculations pioneered by Schwarz	51
2.9	Schematic representation of the vectors \mathbf{s}' , \mathbf{s}'' and $\mathbf{s}' \times \mathbf{s}''$ for a vortex filament	52
2.10	Common experimental counterflow channel configuration	54
2.11	Schematic of reconnecting linear topological defects	58
2.12	Feynman’s initial proposition for the reconnection of quantized vortices	59
3.1	Schematic diagram of the experimental components	62
3.2	Photograph of the Oxford Instruments Optistat-SXM cryostat	64
3.3	Mechanical drawing of the Oxford Instruments Optistat-SXM cryostat	66

3.4	Drawings of the spiral heater and counterflow channel	68
3.5	Diagram of the heater power measurement	69
3.6	Photograph of a “mist” of particles immediately after injection	71
3.7	Schematic diagram of the injection tube inside of the test section of the cryostat	74
3.8	Calibration curve for the thermistor used for temperature measurements	76
3.9	Schematic diagram of the resistance measurement of the temperature probe	78
3.10	An example temperature trace showing typical oscillations about the set point	82
3.11	Schematic diagram of the visualization technique	85
3.12	Two examples of the cross-correlation plane used in PIV measure- ments of our counterflow data	90
3.13	An example batch of commands used to particle track a movie using IDL	92
3.14	Example trajectories obtained by the particle-tracking algorithm . . .	92
4.1	Statistics of pairwise particle separation velocities v_δ	99
4.2	Effects of varying hydrogen volume fraction	103
5.1	Thermal counterflow experiments parameter space diagram	105
5.2	Thermal counterflow particle trajectories	106
5.3	Thermal counterflow vertical velocity distributions	108
5.4	Horizontal velocity and trajectory angle statistics for example coun- terflow experiments	109
5.5	Observed normal fluid and superfluid counterflow velocities	111
6.1	Vortex line length density and heat flux as a function of time for the pulsed counterflow experiments	115

6.2	Parameter space diagram summarizing the pulsed counterflows used to generate quantum turbulence	117
6.3	Images of quantized vortex reconnection	118
6.4	Example variation of χ^2 for given values of the scaling exponent α . .	121
6.5	Example reconnection trajectories well fit by the arbitrary power-law expression	122
6.6	Normalized frequency distributions of the scaling exponent α	123
6.7	Plots of the average fitted amplitude \bar{B} as correlated with the scaling exponent α	125
6.8	Variation of χ^2 with the time origin t_0	128
6.9	Four example reconnection trajectories well fit by the correct-factor expression	129
6.10	Normalized frequency distributions of the amplitude A for the correction-factor expression	130
6.11	Normalized frequency distributions of the correction factor c	132
6.12	Normalized frequency distributions of the amplitude A and correction factor c for distinct ranges of temperature	135
6.13	Normalized frequency distributions of χ^2 for both the arbitrary power-law expression and the correction-factor expression	136
6.14	Three pairs of particles showing both reverse and forward events . . .	139
6.15	Scatter plots of the correction-factor expression fit parameters separately determined pre- and post-reconnection	140
6.16	Scatter plots of the reconnection displacement vectors	142
6.17	Normalized frequency distributions of the differences of the displacement vectors for reconnecting vortices	143
7.1	Time-varying pulsed counterflow velocity distributions	150
7.2	Local velocity statistics for decaying counterflow turbulence compared to those typical of classical turbulence	154

7.3	Local energy statistics of decaying counterflow turbulence compared to those of electrons accelerated by magnetic reconnection in the diffusion region of the earth's magnetotail	156
8.1	Drawings of the square heater designed and built for use in narrower counterflow channel experiments	164
8.2	Glass cell built to serve as a narrower counterflow channel	166
8.3	Images from preliminary experiments of uniformly rotating He II . . .	172
A.1	Givetemplo.c code used to convert the voltage measurements of the thermistor into temperature for $T < 4.5$ K	180
A.2	Givetemphi.c code used to convert the voltage measurements of the thermistor into temperature for $T > 4.5$ K	182
A.3	Pairsubcritexp.c code used to fit the correction-factor expression to the reconnection events	186
A.4	Pairedeltavecsreal.c code used to perform the arbitrary power-law fits to the reconnection events	191

List of Abbreviations

α	scaling exponent
η	Kolmogorov length-scale
γ	surface tension
Γ	circulation
δ	minimum separation distance between reconnecting vortices
$\bar{\epsilon}$	mean energy dissipation rate per unit mass
κ	quantum of circulation; 9.97×10^{-4} cm/s ² for ⁴ He
μ	dynamic fluid viscosity
ξ_1	dimensionless, temperature-dependent Vinen equation coefficient
ξ_2	dimensionless, temperature-dependent Vinen equation coefficient
ρ	density
ρ_n	normal fluid density
ρ_s	superfluid density
ϕ	azimuthal angle
ψ	order parameter field
$\boldsymbol{\omega}$	vorticity vector
ω	frequency
$\boldsymbol{\Omega}$	angular velocity vector
a	particle radius
a_0	vortex cutoff parameter
c_K	Kolmogorov constant
C_S	heat capacity
h	Planck's constant
\hbar	$h/2\pi$
He I	classical fluid state of ⁴ He
He II	superfluid state of ⁴ He
k	wavenumber
l	typical intervortex spacing
L	vortex line length density
LIA	localized-induction approximation
m	mass
\mathbf{M}	magnetization vector
pdf	probability distribution function
PIV	particle image velocimetry
psi	pounds per square inch
P	pressure
\mathbf{q}	heat flux
Q	heater power
Ra	Rayleigh number

s	cylindrical radius
S	specific entropy
t	time
T	temperature
T_λ	superfluid transition temperature for ^4He , 2.17 K
T_c	Curie temperature
u_1	speed of first sound
u_2	speed of second sound
\mathbf{v}_n	normal fluid velocity
\mathbf{v}_s	superfluid velocity
v_x	horizontal velocity component
v_z	vertical velocity component

Chapter 1

Introduction

Significant problems regarding turbulent processes in superfluid ^4He (He II) remain unresolved. In particular, the local dynamics of turbulent He II have barely been explored experimentally. This issue is exacerbated by the inability to visualize the motions of He II in a manner very common to the study of classical fluid turbulence. As such, the aim of this thesis is to undertake experimental studies of turbulence in He II using a recently developed technique to directly visualize the flow [1][†]. The technique uses micron-sized solid hydrogen particles, which have been shown to trace the motions of the normal fluid or be trapped by quantized vortices [2], and enables one to characterize the dynamics of both the normal fluid and superfluid components. We seek to fill in gaps in the body of work pertaining to He II by using this modern technique in simple, standard experimental settings. Specifically, we obtain the first direct observations of: the two-fluid motions of He II, tens of thousands of individual reconnection events between quantized vortices, and the statistics of the local velocity field in quantum turbulence.

The initial discovery of the ability to observe the two-fluid motions in He II was made by my predecessor Gregory Bewley and is detailed in his thesis [1]. All of the experimental apparatus used for the work presented here has been designed

[†]The bibliography can be found at the end of the thesis.

and constructed by the author under the technical supervision of Don Martin. The entire apparatus used in Gregory Bewley's thesis has been heavily modified or completely replaced and the author also introduced several original components. The experiments and particle-tracking presented in this thesis have all been conducted solely by the author. Analysis of the data is conducted by the author under the supervision of Daniel Lathrop with additional support for theoretical models provided by Michael E. Fisher. Katepalli Sreenivasan has played an advisory role as well and commented on the published manuscripts pertinent to the work detailed here [3–6].

We present a more extensive discussion of the relevant theoretical background in Chapter 2. Details of the experimental apparatus and visualization technique are described in Chapter 3. The mechanism by which particles may be trapped on quantized vortices in He II is discussed in Chapter 4. Since particles interact with both the normal fluid and the quantized vortices, we also discuss the relevant factors that determine whether particles will trap on vortices or only follow the normal fluid and present novel experiments showing the transition between the two regimes. The visualization technique allows us to directly observe the two-fluid nature of He II for the first time in the thermal counterflow experiments presented in Chapter 5. We present the first observations of quantized vortex reconnection in He II and two separate models that characterize the dynamics in Chapter 6. The local dynamics of quantum turbulence and its distinctions with classical turbulence are described in Chapter 7. We conclude in Chapter 8 and discuss potential future directions of inquiry. Appendix A includes codes that are used in to analyze the data and Appendix B contains tables of pertinent raw data.

1.1 Turbulence

Turbulent processes are ubiquitous on Earth and throughout the observable universe. Turbulence provides crucial mechanisms necessary to sustain life on Earth by, for example, transporting spores of plants across land, nutrients, heat and salinity in the oceans and various gases in the atmosphere. Turbulent motions of molten iron in Earth's core produce the magnetic field used for navigation as well as providing a barrier to potentially harmful charged particles emitted by the sun. To the layperson, more familiar experiences with turbulence might be found on disturbing airplane flights, the aesthetic patterns and motions of clouds or the ebb and flow of a rushing river. In addition to these naturally-occurring phenomena, turbulence plays a vital role in the design and operation of many industrial processes. In chemical mixers, turbulence is used as a tool to increase efficiency whereas it is suppressed in pipe flows to reduce pumping costs.

Despite the abundant examples of turbulence, there is no consensus definition of the term. Here, we will define turbulence as a field that is spatially-complex, aperiodic in time, and involves processes spanning several orders of magnitude in spatial extent and temporal frequency. Therefore, turbulence by this definition is not restricted to fluid motions alone. The human heart, for example, undergoes filament turbulence immediately before fibrillation [7], magnetohydrodynamic turbulence dominates the behavior of many astrophysical bodies [8–10] and electromagnetic waves in laboratory plasmas may also be turbulent [11].

The important interplay between large and small scales in turbulent fields has

made the study of such systems particularly difficult owing to the need to resolve several orders of magnitude in spatial and temporal extent. For the experimentalist this requires large experiments that are also capable of observing very fast fluctuations on microscopic to mesoscopic scales. For theoreticians the equations of motion are always nonlinear and extremely difficult to work with because individual terms in the equations couple large- and small-scale motions. Furthermore, owing to the vast span of scales involved in the problem, terms in the equations of motion cannot simply be neglected because the contribution from each may vary greatly over the relevant scales. As such, numerical simulations of experimental and naturally-occurring systems require extremely large simulation domains that are also capable of resolving the small scales dominated by dissipation.

The pioneering work of Kolmogorov [12, 13] remains the cornerstone of the statistical theory of turbulence in classical fluids. Kolmogorov made two key assumptions: (1) local isotropy and homogeneity prevail, and (2) there exists an inertial range in which turbulent energy is transferred from large to small scales independent of viscosity and generation mechanisms. Dimensional arguments then yield the spectral density

$$E(k) = c_K \bar{\epsilon}^{2/3} k^{-5/3}, \quad (1.1)$$

where $\bar{\epsilon}$ is the average energy dissipation rate per unit mass and c_K is the universal Kolmogorov constant. While experiments have found the effects of intermittency to be important for high-order moments, the correction to the spectral form is quite small. Kolmogorov also hypothesized that for sufficiently intense turbulence the

statistics of small-scale motions are universally and uniquely determined by the mean energy dissipation rate $\bar{\epsilon}$ and the kinematic viscosity of the fluid ν . Dimensional arguments stemming from this hypothesis yield a single length scale

$$\eta = \left(\frac{\nu^3}{\bar{\epsilon}} \right)^{1/4}, \quad (1.2)$$

which is referred to as the Kolmogorov length. On scales comparable to η viscosity homogenizes the flow and dissipation converts mechanical energy into heat.

To summarize the importance and difficulty of studying turbulence we will appeal to two famous quotes on the subject: the first is given by Richard Feynman who stated

“Turbulence is the most important unsolved problem of classical physics.”

The second is from Horace Lamb who is quoted as saying

“I am an old man now, and when I die and go to heaven there are two matters on which I hope for enlightenment. One is quantum electrodynamics, and the other is the turbulent motion of fluids. And about the former I am rather optimistic.”

In this thesis we endeavor to further the understanding of this extremely broad field of study by directly visualizing fundamental, turbulent processes in a quantum fluid.

1.2 Turbulence in Quantum Fluids

Quantum fluids, put simply, are fluids that are constrained by quantum-mechanical effects. Such fluids are typically described as two interpenetrating fluids:

a viscous normal fluid akin to water and an inviscid superfluid exhibiting long-range quantum order. Each component has a distinct velocity field $\{\mathbf{v}_n, \mathbf{v}_s\}$ and temperature-dependent density $\{\rho_n, \rho_s\}$ for the normal and superfluid components, respectively. There is no conventional viscous dissipation in the superfluid component; rather the flow of a superfluid is similar to the resistance free motion of electrons in a superconductor.

Turbulence can arise in either or both of the fluid components. Turbulence in the normal fluid appears to be indistinguishable from turbulence in classical fluids such as water. Turbulence in the superfluid component, though, is dominated by quantum-mechanical constraints. Specifically, vorticity is constrained to the atomically-thin cores of vortex filaments. Quantum mechanics requires the circulation around each vortex filament to be quantized and given by an integer multiple of $\kappa = h/m$, where h is Planck's constant and m is the mass of a fluid atom. Turbulence then in the superfluid component exhibits a complex, interacting tangle of quantized vortices as initially imagined by Feynman [14].

The relevant length scales of a quantum turbulent state have a lower threshold given by the diameter of a quantized vortex core ($\sim 10^{-8}$ cm) and an upper bound of the system size or at least many times the typical intervortex spacing (~ 1 cm). The slowest time-scales are typically produced by long-range vortex-vortex interactions, which are on the order of 1 s, while the fastest are wave motions along the quantized vortices with periods less than 10^{-9} s [15]. These waves are transverse, circularly polarized displacements that are restored by vortex tension produced by the kinetic energy per unit length of a quantized vortex. Such “Kelvin waves” along a rectilinear

vortex have an approximate dispersion relation given by [15]

$$\omega = \frac{\kappa k^2}{4\pi} \left[\ln \left(\frac{1}{ka_0} \right) + c \right], \quad (1.3)$$

where a_0 is a vortex cutoff parameter and $c \approx 1$. Evidently, a quantized vortex tangle involves the interaction of a wide breadth of spatial and temporal scales, as required for the system to be called turbulent.

Additional complications arise from interactions between the normal and superfluid components mediated by the quantized vortices. Since the two fluids couple, turbulence in one is capable of triggering turbulence in the other. A consensus on the coupled equations of motion for the two fluid components still evades theoreticians, although several propositions have been made. One approach is to describe the normal fluid with the Navier-Stokes equation [16], which is the standard equation of motion used for Newtonian fluids, and the Gross-Pitaevskii equation for the superfluid component [17, 18], which involves a complex field and is applicable for superfluids at $T = 0$ K. To each equation coupling terms are added to describe the mutual friction between the two fluids, as initially observed and described phenomenologically by Vinen [19–21].

1.3 Comparing Classical Fluid and Quantum Fluid Turbulence

Despite the fundamental differences between classical fluids and quantum fluids, there have been notable studies since 1992 demonstrating similarities between quantum and classical turbulence [18, 22–30]. Experiments by Maurer and Tabeling on turbulence generated in ^4He by two counter-rotating disks observed Kolmogorov

energy spectra typical of classical fluids that were indistinguishable above and below the superfluid transition [26]. The Kolmogorov energy spectrum was also seen by Kobayashi and Tsubota in numerical simulations of the Gross-Pitaevskii equation with small-scale dissipation added to the otherwise energy-conserving dynamics [18]. The classical decay of vorticity [23] has been observed in towed grid [23, 27], thermal counterflow [29], and impulsive spin down [30] experiments using superfluid ^4He .

1.3.1 Energy Cascades

Turbulence in both systems is often described as an energy cascade mediated by nonlinear interactions from large scales to small scales where dissipation prevails [12, 13]. In classical fluids this takes the form of a “Richardson cascade” [31] whereby energy is injected at small wavenumbers k , which spawn larger wavenumber structures through inertia until k grows sufficiently large that the energy is lost to viscous heating. However, one should not picture large vortices or eddies spawning smaller ones, since this has never been observed. Rather the correct picture is that large eddies (small k) interact with one another producing small-scale structures (large k) with high strain and shear that dissipate energy.

The cascade process is quite different for quantum fluids since all of the vortex cores are atomically-thin and there are no viscous losses [32]. The conventional picture for the quantum turbulent cascade is as follows: (*i*) bundles of nearly-parallel quantized vortices form through interactions with the normal fluid that tend to align them. These bundles produce large-scale motions similar to small wavenumber

(large spatial extent) eddies in classical fluids. *(ii)* Energy is transmitted to larger k via reconnections between individual vortices, which is described in Section 2.5. *(iii)* Reconnection events trigger polychromatic helical, Kelvin waves on the vortex lines. *(iv)* The Kelvin waves interact nonlinearly producing even larger wavenumbers until they lose energy to phonon emission, which radiates energy to the boundaries [15]. It is important to note that aspects of the quantum turbulent cascade remain controversial and this is an active area of research and debate.

1.3.2 Large-Scale Motions

Large-scale motions in classical fluid turbulence typically refer to eddies and other coherent structures that are much larger than length-scales where molecular diffusion converts mechanical energy into heat. These large-scale motions contain much of the kinetic energy of the system, which then cascades to smaller scales through a nearly inviscid, inertial mechanism [12, 13] described in the previous subsection. In addition to their dynamical relevance, large-scale motions in classical fluids can produce amazingly aesthetic phenomena that are commonplace in everyday life such as patterns in rising steam from a tea kettle or smoke from a fire, vortical structures in sink drains and mixing gradients between hot coffee and cool creamer. One example of such phenomena, known as the von Kármán vortex street, is shown to occur in experimental and natural environments in Fig. 1.1. It is quite remarkable that images taken from a controlled, table-top experiment share such resemblance to clouds in Earth's extremely complicated atmosphere.

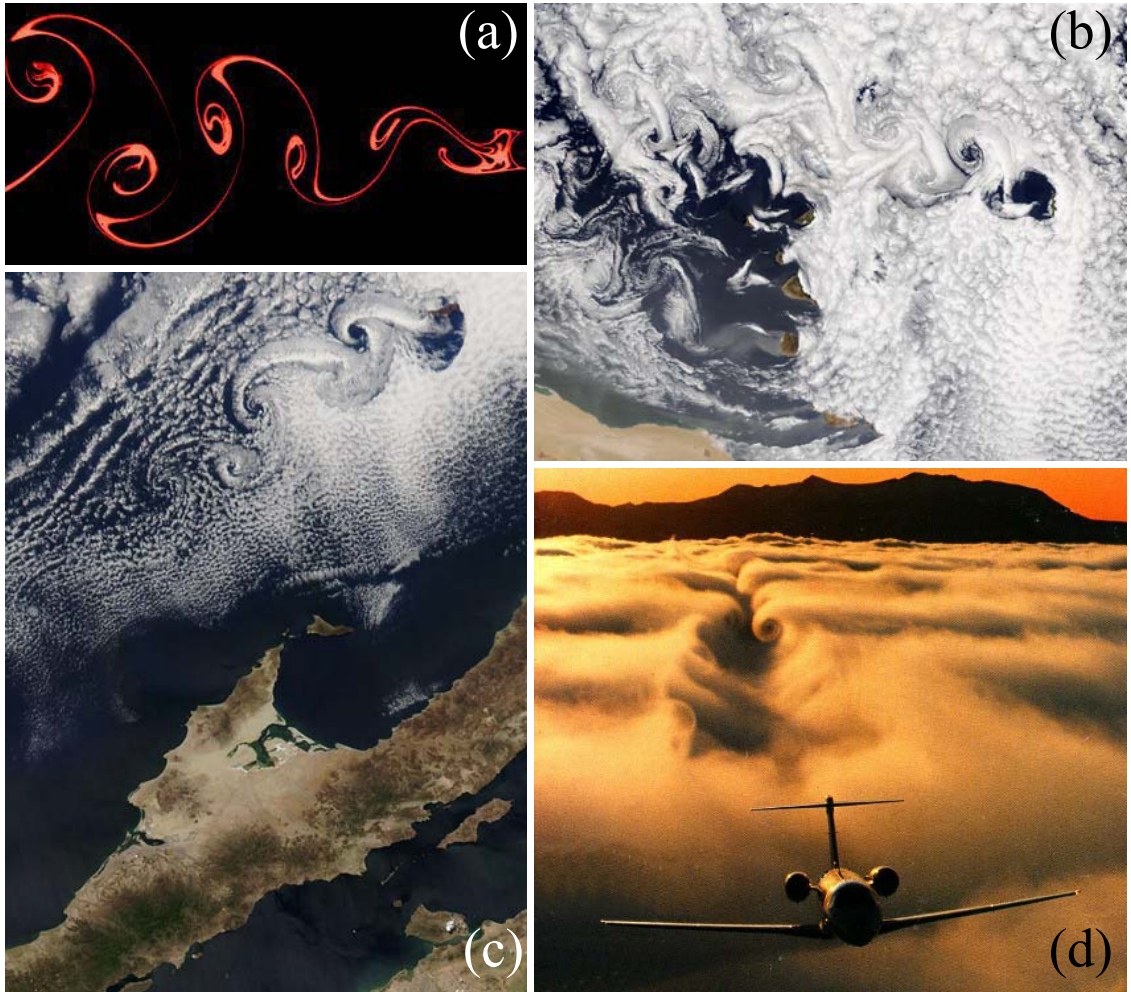


Figure 1.1: Example images of the von Kármán vortex street and wing-tip vortices. (a) Experimental image of the flow of water from right to left past a cylindrical obstacle shown as the black semicircle on the right edge of the image. This image was taken from <http://wikipedia.org>. (b-c) Satellite images of clouds showing strikingly similar behavior to the controlled experimental conditions in panel (a). The images in (b) and (c) were taken from <http://wikipedia.org> and <http://alg.umbc.edu>, respectively. (d) Vortex formation behind a Cessna airplane taken from <http://www.diam.unige.it>. These vortices are known as wing-tip vortices.

The nature of large-scale motions in quantum fluids would appear to bear no analogy to classic fluids since vorticity in the superfluid component does not diffuse and is incapable of forming such coherent structures. However, it is possible for groups of quantized vortices to mimic large-scale circulations common in classical fluids. As a simple example, we will consider the case of a fluid contained in an infinitely-long, cylindrical vessel that rotates at a constant angular velocity about its vertical axis such that $\boldsymbol{\Omega} = \Omega \hat{z}$. If the fluid inside the vessel is classical then it will eventually reach a state of solid-body rotation where every fluid element rotates about the z -axis at a frequency Ω . This flow yields a simple velocity field $\mathbf{v} = \Omega s \hat{\phi}$, where s is the cylindrical radius and ϕ the azimuthal coordinate, with vorticity equal to $\boldsymbol{\omega} = \nabla \times \mathbf{v} = 2\Omega \hat{z}$. Since vorticity in a quantum fluid is quantized, it is clear that many quantized vortices aligned parallel to the z -axis are required to produce a similar coarse-grained velocity field to the classical case. The flow around each quantized vortex, though, is given by $\mathbf{v} = \hat{\phi} \kappa / (2\pi s)$; this is at odds with the velocity field for solid-body rotation, which grows linearly with s rather than decaying. These complications can be overcome if the quantized vortices are arranged in a regular lattice, with a triangular lattice producing the lowest energy state, as depicted schematically in Fig. 1.2. Feynman first calculated this triangular arrangement as the lowest energy approximation to solid-body rotation. This lattice structure has been observed experimentally in superfluid ^4He [33], and analogously in superconductors [34] and Bose-Einstein condensates [35] as shown in Fig. 1.3.

It is therefore possible both in principle and in practice for quantized vortices to closely approximate the large-scale flows of classical fluids. This approximation

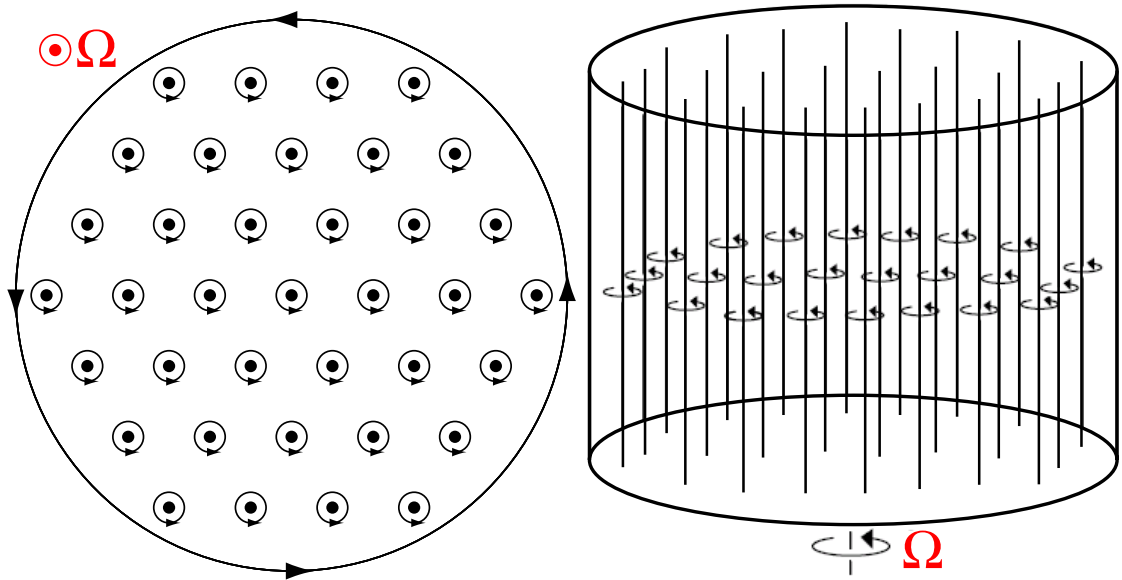


Figure 1.2: Schematic diagram of a superfluid in a cylinder uniformly rotating with $\boldsymbol{\Omega} = \Omega \hat{z}$ (a) as viewed from above and (b) as viewed from the side. The quantized vortices (black dots or lines) align with the axis of rotation and form a triangular lattice as first calculated by Feynman [14]. The resulting course-grained flow closely approximates the analogous situation in a classical fluid even though quantum mechanics imposes stringent constraints on vorticity.

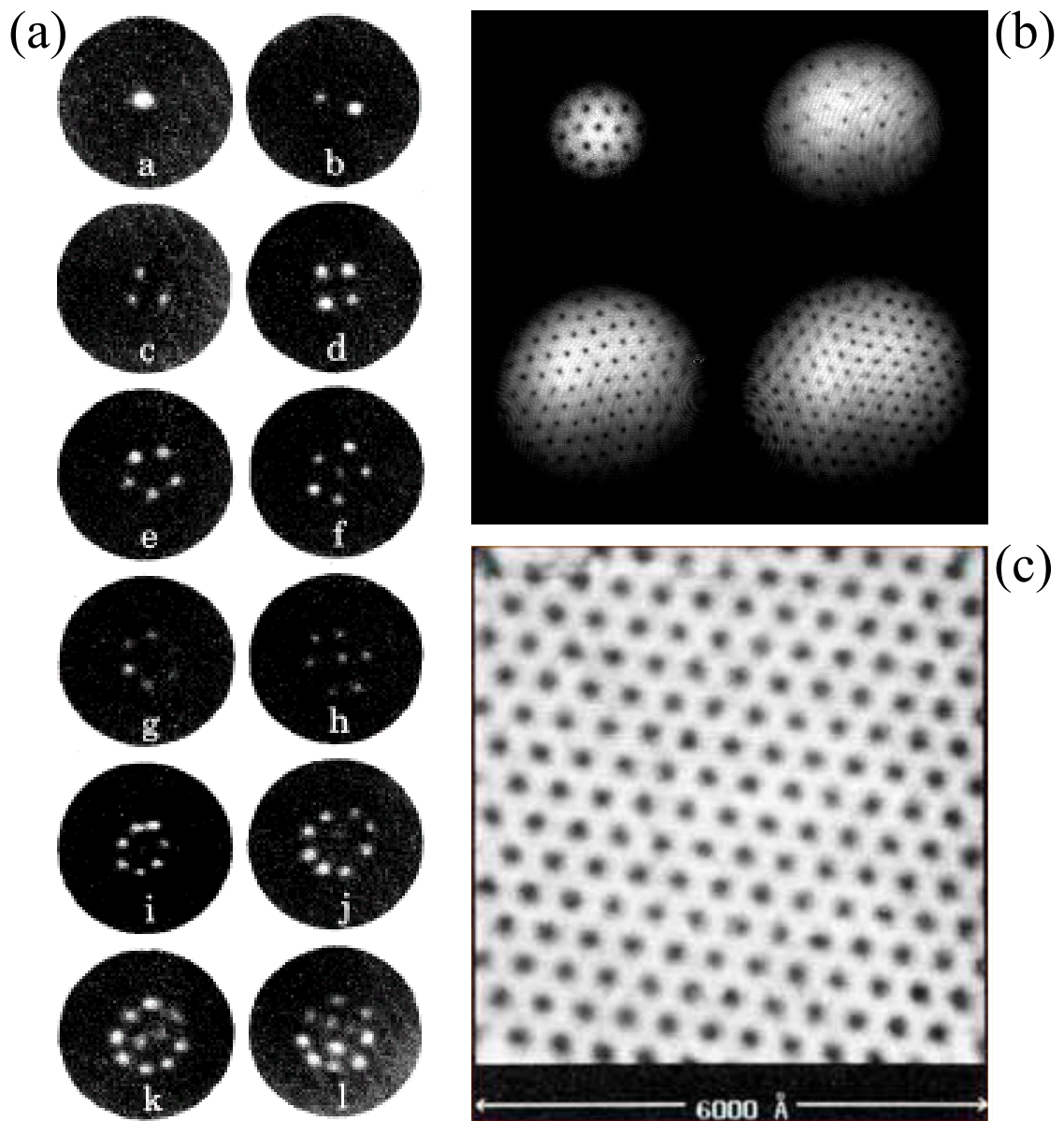


Figure 1.3: Experimental visualizations of vortex lattices in (a) superfluid ^4He (Yarmchuk *et al.* [33]), (b) Bose-Einstein condensates (Abo-Shaeer *et al.* [35]) and (c) superconductors (Hess *et al.* [34]). The locations of the vortex cores are shown in white in (a) and black in (b) and (c). The progression of twelve images a–l in (a) shows the increase in the number of vortices as the rotation rate of the system is increased.

is only applicable, though, *on length-scales much larger than the typical spacing between quantized vortices*. In all of the quantum turbulence studies mentioned above ([18, 22–30]) that observed similarities to classical turbulence, the flow scales observed were considerably larger than typical intervortex spacings. These results may be attributed to the fact that on such scales the pairwise interactions of quantized vortices are insignificant while the normal and superfluid components become “locked” as a result of mutual friction, which is discussed in Section 2.3.

1.3.3 Small-Scale Motions

Small-scale motions in classical turbulence are drastically different from those in quantum fluids. In classical fluids, small-scale motions take place over length-scales comparable with the Kolmogorov length η defined in (1.2) [12, 13], below which viscosity smooths the flow. Even though local quantities undergo intermittent bursts and are nonuniform in both space and time, viscosity diffuses momentum and homogenizes mean quantities on dissipative length-scales.

We consider small-scales in quantum fluids as bounded above by the typical spacing between quantized vortices, which we will define as l . As mentioned in the previous subsection, on scales much greater than l it is assumed that the interactions between quantized vortices are negligible. Vorticity in the superfluid component cannot diffuse, rendering it incapable of homogenizing even on atomic length-scales. For scales below l , vorticity in a quantum fluid undergoes extreme fluctuations since it is topologically constrained to dynamic, line-like filaments, thereby bearing

no resemblance to a classical fluid observed on scales comparable to η . The local interactions between quantized vortices, such as reconnection and ring collapse, can produce very large velocities bounded only by the speed of sound of the fluid. Consequently, it is generally accepted that the small-scale dynamics of quantum turbulence and classical turbulence are quite different.

1.3.4 Heat Transport

Heat applied to the bottom of a classical fluid system may be transported by two different means depending upon the Rayleigh number Ra , which compares the driving forces from the imposed heating to diffusive effects. For small values of Ra , heat is carried entirely by thermal conduction through a stationary fluid. Above a critical value of Ra , buoyancy forces grow sufficiently large that Rayleigh-Bénard convection ensues as depicted in Fig. 1.4 [36]. First, warm, positively-buoyant fluid at the heated bottom flows along one side of the system towards the top where it then begins to cool. Then, cooler, negatively-buoyant fluid displaces the rising, warm fluid by sinking down along the opposite side of the system where it then begins to heat and expand. These processes form a cycle with warm fluid always rising in some region of the system and cool fluid always sinking to conserve mass in another. The resulting flow greatly enhances the transport of heat through the system as compared to thermal conduction alone. Convection is an essential component to turbulence in the molten iron core of Earth, oceans and planetary atmospheres as well as stars.

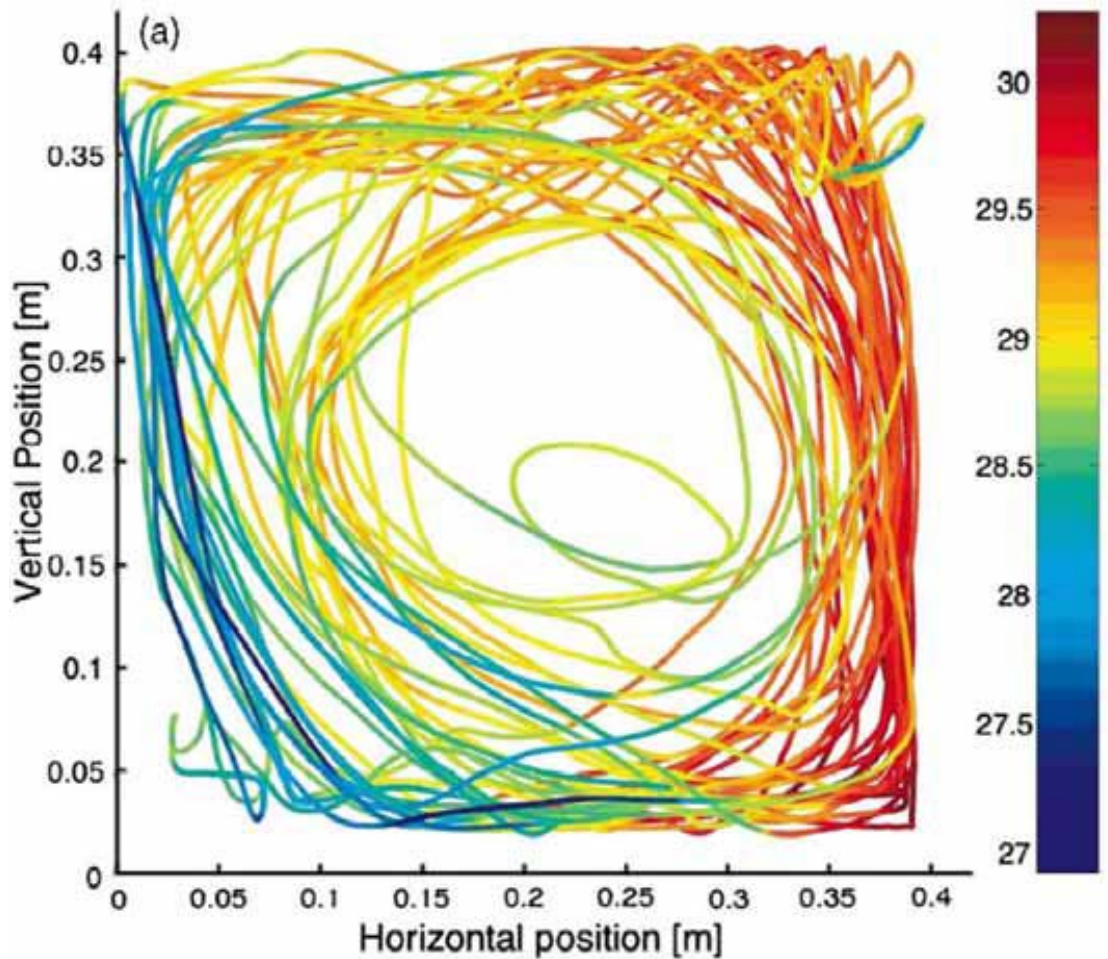


Figure 1.4: Example trajectory of a temperature-sensitive tracer particle from a Rayleigh-Bénard convection experiment that is heated from below and cooled from above. The axes give the position of the tracer particle and color denotes the temperature in $^{\circ}\text{C}$. The large-scale circulation is evidenced by the warm fluid rising along the right-side of the apparatus (red lines) and the sinking, cooler fluid (blue lines) along the left edge of the system (from Gasteuil *et al.* [36]).

The two-fluid nature of quantum fluids results in a very different heat transfer mechanism [37, 38]. The superfluid component resides in the ground state of the system and therefore cannot carry entropy or convey heat. All of the heat must be transferred through the system by motions of the normal fluid. If a superfluid is heated at the bottom of a closed channel in analogy to the classical fluid case described above, then the normal fluid will flow away from the heat source, while the superfluid component will flow towards the heat source to conserve mass. Since the two fluids are interpenetrating, there is no need for the normal fluid to rise along one side of the system and the superfluid to sink along the other as shown for the classical fluid case in Fig. 1.4; rather, on average the normal fluid flows upward *everywhere* in the system and the superfluid flows towards the heat source *everywhere* to conserve mass. This flow state is often referred to as a thermal counterflow and in Chapter 5 we present the first direct observation of these two-fluid motions. It is important to note that thermal counterflows are not driven by buoyancy, in contrast to Rayleigh-Bénard convection. Any arbitrary heat flux $\mathbf{q} = q\hat{q}$ will produce a normal fluid velocity aligned with \hat{q} and a superfluid velocity anti-aligned.

Thermal counterflows transport heat ballistically, which is much more efficient than even the enhanced convective transport of heat by Rayleigh-Bénard convection. Indeed, experiments attempting to measure the thermal conductivity of a superfluid require long, thin capillary tubes in order to even produce a measurable temperature gradient on the order of 1 mK/m. Experimentally determined values of the thermal conductivity of superfluid ^4He are 10^7 times greater than its classical

counterpart above the superfluid transition temperature and 800 times greater than copper at room temperature [39]. This unique means of heat transfer in superfluids has found applications in environments requiring advanced cooling abilities such as superconducting magnets used to accelerate particles in research colliders.

1.4 State of Quantum Turbulence Research

In this section, we seek to summarize some of the recent achievements and shortcomings of quantum turbulence research. The breadth of research requires us to only highlight a select few areas of endeavor. Here, we will focus only on superfluid ^4He , since it is the main topic of this thesis. For a more extensive discussion we suggest the review article by Vinen and Niemela [40].

1.4.1 Experimental Challenges

Performing turbulence experiments in He II presents all of the challenges of classical turbulence with several additional complications. The boiling point of classical liquid helium (He I) at 1 atm is 4.2 K, and at saturated vapor pressure He II exists only at temperatures below 2.18 K. These low temperatures coupled with the low heat of vaporization of liquid helium (100 times smaller than liquid nitrogen) require experiments to be conducted in vacuum insulated cryostats. Wall-shear stress sensors and hot-wire probes, commonly used in classical fluids, measure the amount of heat required to maintain the sensor at a constant temperature. Since the thermal conductivity of He II is 800 times larger than solid copper, very large

heat fluxes that would drive spurious counterflows in the system would be required to detect a signal.

Probes that measure dynamic pressure fluctuations are also commonly used in classical fluid experiments. The size of the probe is designed to be no larger than the length-scales of interest and ideally are smaller than the Kolmogorov length-scale η . As discussed in Section 1.1, turbulent flows are composed of fluid motions on length-scales spanning several orders of magnitude. Fixing the typical fluid velocities in the system, the turbulent intensity in an experiment can be increased toward naturally-occurring levels of interest by either: *(i)* increasing the largest scale of the fluid motions by increasing the system size or *(ii)* by decreasing the smallest scales of the flow by using a lower viscosity fluid. Liquid helium has the lowest kinematic viscosity of any fluid thereby yielding very small dissipative length-scales. The Kolmogorov length-scale for experiments conducted in He I [41] are typically on the order of only 10 μm . Turbulence in He II produces even smaller length-scales in the normal fluid and dynamics in the superfluid component can occur on atomic length scales. Pressure probes sufficiently small to detect even the small-scale motions of the normal fluid are presently unavailable. Even if probes were available the exact role of pressure in quantum turbulence is still unknown, so interpretations of such measurements would be less concrete than similar measurements in classical fluids.

The most common and important method of studying classical turbulence stems from directly visualizing the flow. Whether it be tracer particles or dyes, adding impurities into classical fluids that scatter light allow the observer to see the motions of the fluid, such as in Fig. 1.1. Even though all impurities will undergo

trajectories different than the fluid elements of interest, deviations between tracer particles and fluid elements can be minimized through judicious choice of the particle properties. Specifically, neutrally-buoyant, spherical particles with diameters comparable to or smaller than η are generally accepted as viable tracers [42]. The density of liquid helium is an order of magnitude smaller than that of water. As such, all tracer particles designed for studying turbulent flows in water produce undesirable systematic effects when used in liquid helium. Furthermore, the relevant length-scales of the flow require tracer particles that are on the order of $1 \mu\text{m}$ or smaller. Lastly, particles tend to aggregate owing to van der Waals forces; even if the particles are initially small enough to serve as tracers, over time their mean size will increase until they cease to be useful. This problem in water is countered by coating the particles with surfactants. This approach fails in both He I and He II, since “helio-philic” and “helio-phobic” surfactants have not been discovered. Instead, we use micron-sized solid hydrogen tracers that have been shown to serve as viable tracers for normal fluid motions [42] or may be used to mark the position of quantized vortex cores [2] in He II. Therefore, for the first time, we are able to visualize the dynamics of both the normal fluid and superfluid components in He II.

The technical challenges of implementing tracer particles in He II are further compounded by the two-fluid nature of superfluids. Particles in He II are influenced by both the normal fluid and the superfluid components. Specifically, it is possible for the tracers to follow motions of the normal fluid as they would in water or they can be trapped on the cores of quantized vortices [43] as we discuss in detail in Chapter 3. Thus, visualizing the motions of particles in He II alone is insufficient;

detailed models must accompany experimental data to determine the information that may be gleaned from particle trajectories. Several models and numerical studies [44–48] describing the dynamics of tracer particles in He II have recently been published, but quantitative experimental tests are lacking. We present detailed experimental observations and our interpretations of tracer particle motion in He II in Chapters 4 and 5.

In spite of these challenges, many techniques have been developed to experimentally probe turbulence in He II. The most common measurement is of the spatially-averaged vortex line length density L [23, 27, 29, 30, 49] first introduced by Vinen in 1957 [19–21], which is simply the total quantized vortex line length per unit volume. Therefore, L has the units of inverse area (length/volume) and κL , which has units of inverse time, is often regarded as the quantum analogue to classical fluid vorticity. Measurements of the attenuation of second sound or electrical current, coupled with theoretical interpretations, are used to determine L in experimental settings. The vortex line length density L is often used as a measure of the turbulent intensity in the superfluid component. As external forcing, whether by mechanical means such as impellers and towed grids or by driving a thermal counterflow, increases the steady-state value of L also increases. The clear counterexample to this interpretation, though, is the case of uniform rotation since the equilibrium state has $L > 0$ and typically quite large.

A great deal of progress has been made in the study of turbulent He II through experiments and theories that focus on the properties of the vortex line length density. Even though a great deal can be gleaned by measuring L , it is exceedingly

difficult to gain insight into the small-scale dynamics, the individual interactions between quantized vortices and the dynamics of normal fluid. In short, L does not yield the type of information that can be extracted by directly visualizing the flow as is so often done in classical fluids. This serves as a major motivation for our direct visualization studies that permit us to examine the local dynamics of both the normal fluid and superfluid components in He II. We have the ability to see quantized vortices interacting, the two-fluid nature of the flow, the motion of vortex rings, and coupling between the normal fluid and superfluid components for the first time. Our experiments provide tests for many long-standing hypotheses while also initiating future directions of inquiry.

1.4.2 Theoretical and Computational Challenges

Performing numerical simulations of any turbulent system is a great challenge owing to the extent of spatial and temporal scales of relevance, as discussed in Section 1.1. The two-fluid nature of He II requires simulations to take into account the complex motions of the normal fluid component, as in any simulation of a classic fluid, while also incorporating the dynamics of the superfluid component and coupling between the two fluids. Unlike classical fluid turbulence, there is no consensus on well-tested equations of motion for He II, resulting in many simulations of distinct equations.

Since the study of turbulence in He II provides challenges in addition to those present for studying classical fluid turbulence, many numerical simulations are re-

stricted to turbulence in the superfluid component alone. These studies initiated by Schwarz in 1978 [50] and extended by Tsubota, Nemirovskii and others [51, 52] prescribe a fixed normal fluid velocity field or ignore it entirely and then simulate the dynamics of a turbulent superfluid velocity field. More specifically, numerical simulations typically begin with an initial distribution of quantized vortices within the simulation domain and a fixed normal fluid velocity field that affects the quantized vortices. These studies are referred to as line-vortex simulations since the problem is reduced to following only the dynamics of the quantized vortices, which are treated as one-dimensional.

Although this is a great reduction in complexity, several important difficulties remain. The first is that the resulting superfluid velocity field from a given spatial distribution of quantized vortices is given by a Biot-Savart type integral in analogy to the magnetic field derived from a distribution of electrical current, which has non-local effects. Fully computing these integrals greatly increases the computational cost of the simulation. Many numericists prefer to assume the localized-induction approximation (LIA) [51–54], which neglects all nonlocal contributions to the velocity field and greatly reduces the computational workload. This assumption allows for simulations that contain a greater density of quantized vortices at the cost of a restricted range of validity. Indeed, this approach has recently been questioned in studies by Tsubota and his collaborators [55, 56] that compute the full Biot-Savart integral.

The second shortcoming of vortex-line simulations stems from quantized vortex reconnection [14]. Reconnection occurs when two quantized vortices are driven

by their mutual velocity field to cross at a point, exchange tails, which results in a different velocity field that drives them apart as discussed in detail in Subsection 2.5 below. In the naive implementation of vortex-line simulations, reconnections cannot occur naturally. To compensate for this defect, numerical schemes implement special algorithms to induce reconnection. One method is to always reconnect any two vortices that are separated by less than a prescribed distance [53–56], while another only reconnects vortices that appear to cross [52]. These distinct methods of reconnecting vortices introduce systematic effects that are not yet clearly understood. Furthermore, reconnection has a different impact on the turbulent state depending upon whether or not the simulation assumes the LIA as recently discussed by Adachi *et al.* [55].

A few numerical studies have separately investigated reconnection in He II. de Waele and Aarts numerically simulated the dynamics of two vortex lines immediately *before* a reconnection event [57] using line-vortex methods. However, the resulting dynamics after the event were not computed. A study of the complete reconnection process was performed by Koplik and Levine [58] using the Gross-Pitaevskii equation, which is thought to properly describe the dynamics of quantized vortices at $T = 0$ K. In both of these studies, though, the entire simulation was composed of only the two reconnecting vortices. Simulations of turbulent He II, on the other hand, have employed many densely-packed quantized vortices as well as the normal fluid, which is quite different than simulations of individual reconnection events. The specific effects of a more turbulent environment on reconnection events have yet to be studied. By contrast the observations we detail below, have characterized

the dynamics of approximately 20,000 reconnection events in turbulent He II. One may hope that these experimental observations will aid in a deeper understanding of the vortex reconnection process that can be implemented in future numerical simulations of turbulent He II.

Chapter 2

Theoretical Background

This chapter seeks to provide the theoretical background that is necessary to understand the experimental results presented in the forthcoming chapters. It begins with a description of the discovery of superfluidity in He II for both its historical significance and so that we may introduce some of the amazing properties of He II. We then discuss the two-fluid model attributed to Tisza [37] and Landau [38]. The quantum mechanical constraint on fluid circulation, which gives rise to quantized vortices, is discussed in section 2.3. In addition to introducing quantized vortices, we also discuss their dynamics and interaction with the normal fluid. A more detailed discussion of thermal counterflows follows and we end this chapter with details regarding reconnection, which occurs in a wide variety of systems including He II.

2.1 Discovery of Superfluidity

The more naturally-abundant isotope of helium, ^4He , was first liquified by Heike Kamerlingh Onnes at the University of Leiden in the Netherlands in 1908. This was a great achievement since ^4He at atmospheric pressure must be cooled to 4.2 K before it will condense into a liquid state. By that time it was quite commonplace to liquefy gases and study their properties. In fact, helium was the last gas to be liquefied since it has the lowest boiling point of any element, and perhaps

even more remarkably, elevated pressures (> 25 atm) are required to solidify helium even at absolute zero.

As scientists continued characterizing various properties of liquid helium, as had been done for many other liquids, they began to notice anomalies in quantities such as the density and specific heat near $T = 2.2$ K. In the late 1920s, Keesom *et al.* [60] had observed a sharp peak in the specific heat near $T = 2.2$ K that resembled the shape of the Greek letter λ (see Fig. 2.1), hence the name “lambda-transition,” which occurs at a temperature denoted T_λ . For temperatures $T > T_\lambda$, Keesom called the liquid “helium I” (He I) and for $T < T_\lambda$ he referred to the fluid as “helium II” (He II) as shown in the phase diagram in Fig. 2.2. In 1930 Keesom also discovered that He II could flow through very tiny pores that blocked He I [61]. McLennan, Smith and Wilhelm in 1932 observed vigorous boiling of ^4He as $T \rightarrow T_\lambda$ by using a transparent glass cryostat, but the more startling phenomenon they observed was that the boiling completely ceased for all temperatures below T_λ . An example of this striking disparity in behavior is shown in Fig. 2.3. Soon afterward this behavior was attributed to an exceptionally large thermal conductivity of He II as measured by Keesom *et al.* [39, 62] and Allen *et al.* [63].

At the time, researchers believed the anomalously large thermal conductivity must be caused by convection or turbulence in the fluid. Thus, they set out to measure the viscosity of liquid helium, particularly its temperature dependence near T_λ . Wilhelm *et al.* were the first to observe a dramatic decrease in the viscosity of liquid helium below T_λ by measuring the damping of an oscillating cylinder immersed in the fluid [65]. However, the breakthrough came in successive articles in 1938 in the

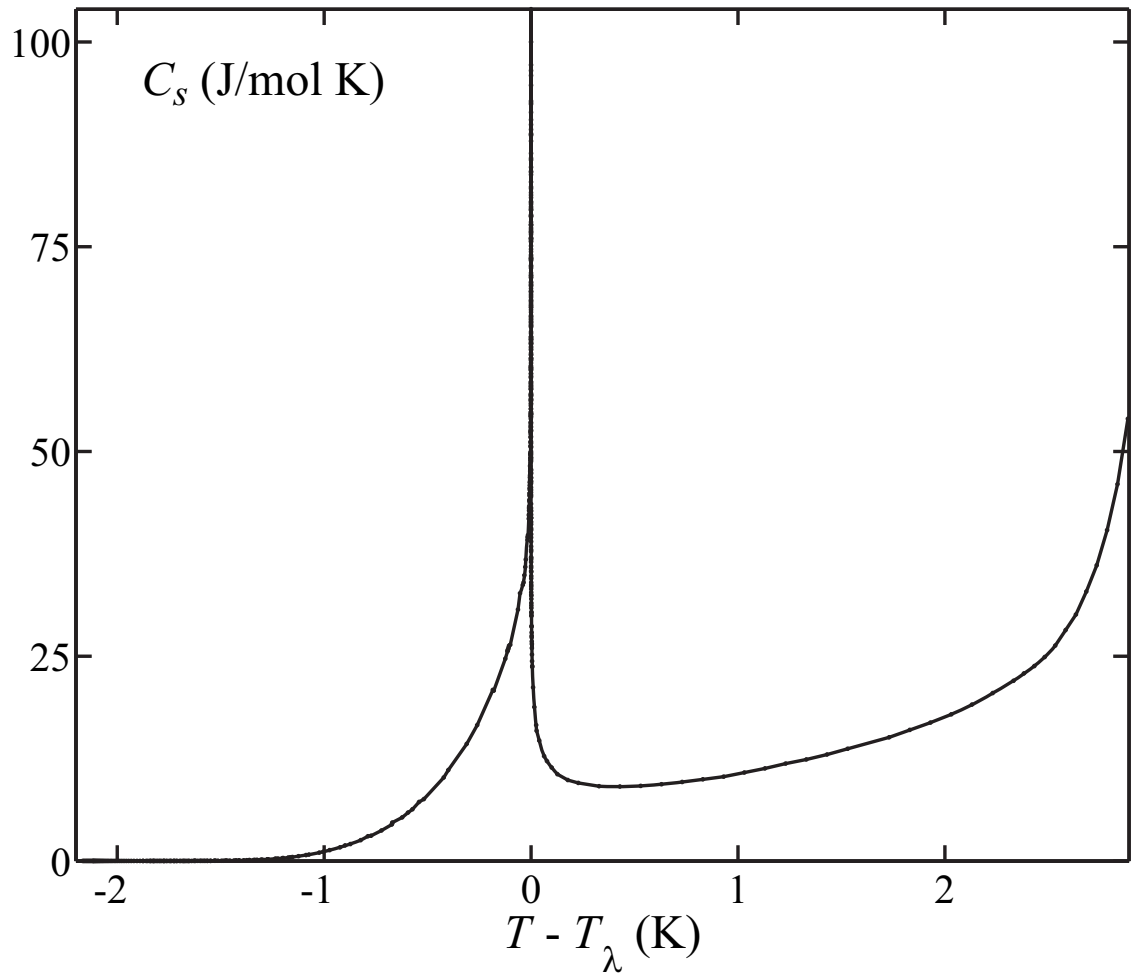


Figure 2.1: Plot of the accepted values of the heat capacity C_S as a function of temperature T measured from the transition temperature T_λ [59]. The specific heat anomaly is evidenced at $T - T_\lambda = 0$.

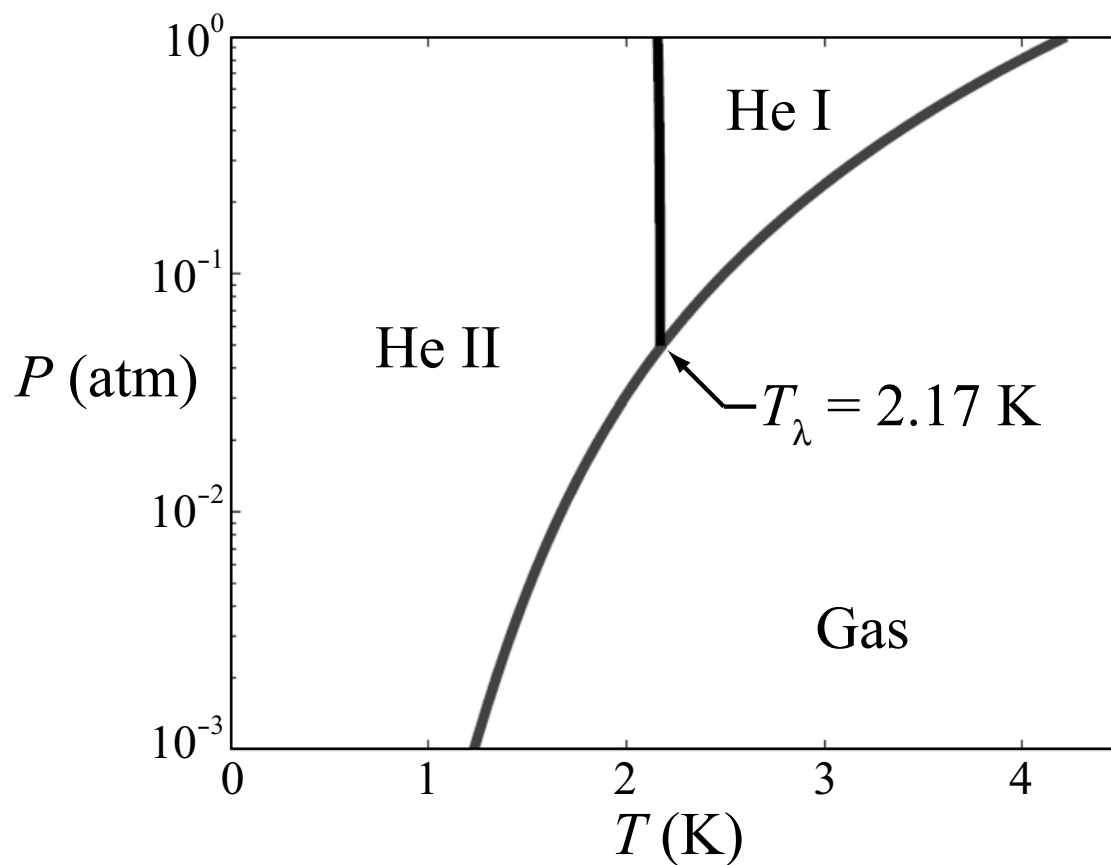


Figure 2.2: Phase diagram for ${}^4\text{He}$ near the λ -transition [64]. The intersection of the liquid-gas coexistence curve and the He I – He II curve is defined as the λ -point, which occurs at $T_\lambda = 2.17$ K.

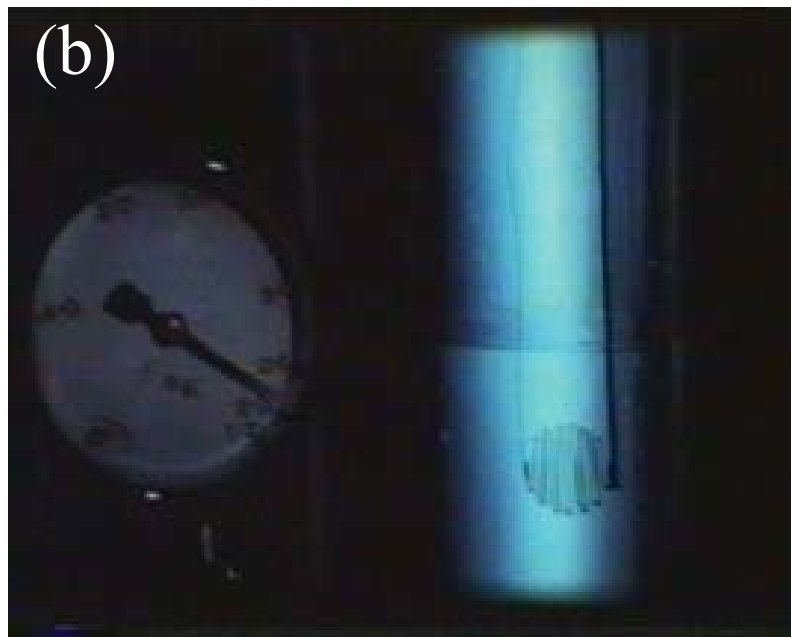
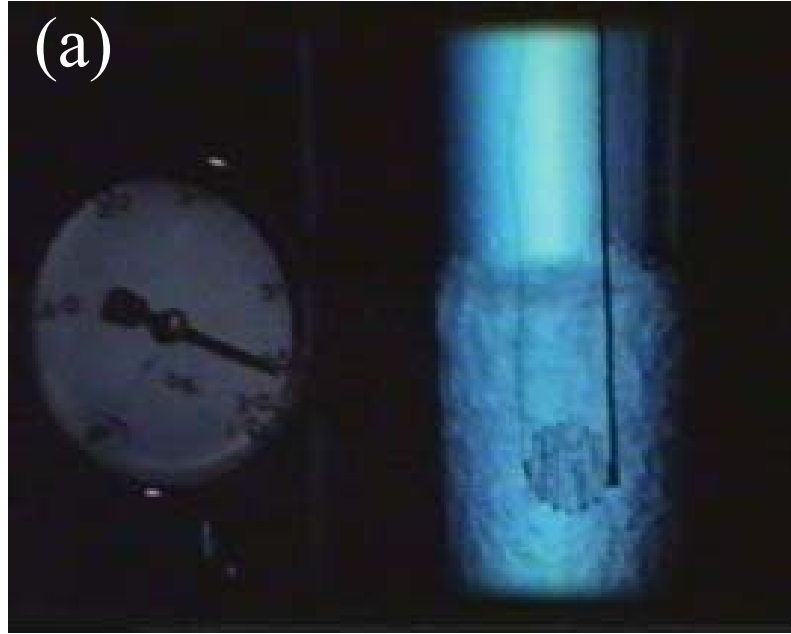


Figure 2.3: Two images from a film by J. F. Allen and J. Armitage of heated ${}^4\text{He}$ for two distinct temperatures. (a) He I at $T = 2.4\text{ K}$ and (b) He II just below the λ -transition temperature T_λ . The thermal conductivity of He I is very poor, which produces the vigorous boiling evidenced by the bubbles in (a). He II, though, has a much higher thermal conductivity, which homogenizes the temperature causing the boiling to cease.

journal *Nature*. The measurements by Wilhelm *et al.* were questioned since it was not clear if the flow around the oscillating cylinder was laminar or turbulent. In an attempt to obtain laminar flow, which would make measurements of the viscosity more reliable and accurate, two experimental groups observed the flow of He II through very thin, long capillary tubes. In the first, Kapitza estimated that the upper bound for the viscosity of He II was $\sim 10^{-9}$ P, which is 10^7 times smaller than the viscosity of water and 10^4 times smaller than any viscosity measured to that point in history [66]. He remarked:

“The present limit is perhaps sufficient to suggest, by analogy with superconductors, that the helium below the λ -point enters a special state which might be called a ‘superfluid.’”

On the very next page of the journal, Allen and Misener obtained a consistent upper bound of 4×10^{-9} P for the viscosity of He II by performing similar measurements [67]. The authors commented:

“The observed type of flow, however, in which the velocity becomes almost independent of pressure, most certainly cannot be treated as laminar or even as ordinary turbulent flow. Consequently any known formula cannot, from our data, give a value of the ‘viscosity’ which would have much meaning. It may be possible that the liquid helium II slips over the surface of the tube. In this case any flow method would be incapable of showing the ‘viscous drag’ of the liquid.

. . . It seems, therefore, that undamped turbulent motion cannot

account for an appreciable part of the high thermal conductivity which has been observed for helium II.”

These two main conclusions of these experiments: (*i*) the flow of He II may bear analogy with superconductivity owing to the immeasurably small viscosity and (*ii*) the efficient transport of heat through He II could not be explained by turbulent convection common to all other fluids, truly sparked a great deal of interest in He II. Only one month after these amazing discoveries, Allen and Jones also reported in *Nature* yet another extremely peculiar effect present only in He II [68]. The experimentalists were preparing a modified apparatus to extend studies of the viscosity of He II when the following observation was made:

“Observations were being made on the flow of liquid helium II through a tube packed with fine emery powder (Fig. 2). The top of the tube was allowed to project several centimetres above the level of the liquid helium bath, and an electric pocket torch was flashed on the lower part of the tube containing the powder. A steady stream of liquid helium was observed to flow out of the top of the tube as long as the powder was irradiated.”

The original figure from the paper by Allen and Jones is shown in Fig. 2.4 along with a clearer portrayal of the phenomenon. The original photograph was taken using a 60 W light bulb for illumination, which also provided the radiant thermal energy absorbed by the powder that drove the “helium pump.” Allen and Jones reported observing jets as high as 16 cm above the tip of the capillary tube. The rapid pace

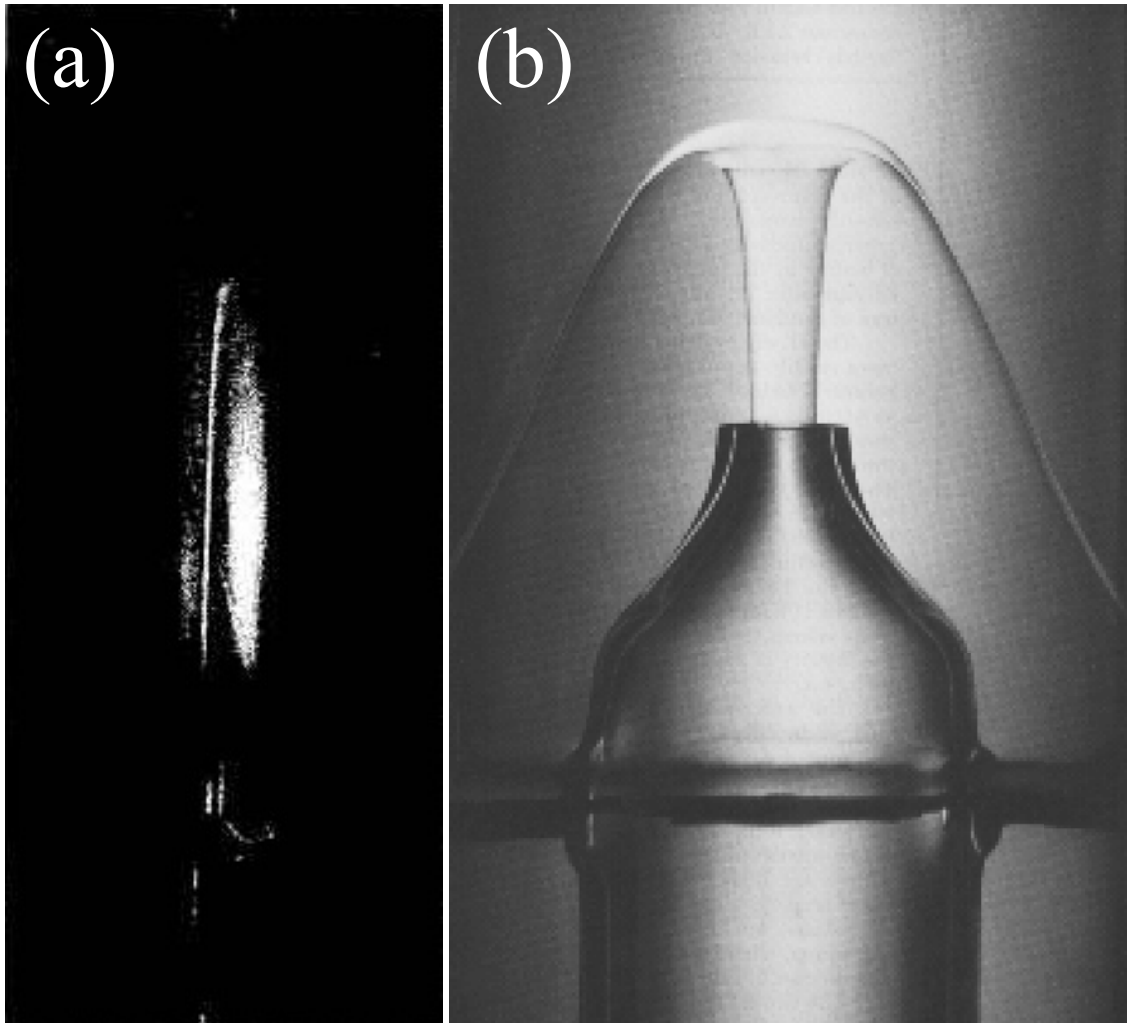


Figure 2.4: Images of the thermo-mechanical “fountain effect.” The image on the left is from the initial observation reported by Allen and Jones in 1938 [68]. The image on the right is taken from nature.com. Both images show a jet of He II exiting from the top of a tube that resides above the free surface of the liquid. The flow is driven thermally by the absorption of heat at the bottom of the tube. This phenomenon was later explained by the two-fluid model of Tisza [37] and Landau [38].

of experimental discoveries in He II was soon followed by theoretical breakthroughs discussed in the next section.

2.2 Two-Fluid Model

Only months after the analogy between the low viscosity flow of He II and the resistance-free motion of electrons in superconductors was put forth by Kapitza [66], London stated that the λ -transition in ^4He was analogous to Bose-Einstein condensation in dilute gases [69]. London calculated a transition temperature for an *ideal* Bose gas of $T = 3.09$ K. This is higher than the observed value of T_λ , but it is expected that the interactions of the helium atoms that make it nonideal will result in a lower transition temperature. Even though the relationship between Bose-Einstein condensation and superfluidity is quite subtle and still debated, this initial idea by London led to future theoretical achievements.

Tisza was afforded the opportunity to read London's paper before it was published and followed it up with one of his own a month afterward. Tisza began with London's hypothesis [37]:

“F. London has recently proposed a new conception of helium II, according to which this liquid can be regarded as a degenerate Bose-Einstein gas, that is, as a system in which one fraction of the substance – say, n atoms per cm^3 – is distributed over the excited states in a way determined by the temperature, while the rest — $n_0 - n$ atoms per cm^3 — is ‘condensed’ in the lowest energy level. If T_0 denotes the temperature

of degeneracy, the ratio n/n_0 is given by $n/n_0 = (T/T_0)^s$ for $T < T_0$.”

Thus, Tisza was putting forth the idea that He II could be considered as partially composed of atoms in an excited state and condensed atoms that would behave coherently.[†] He used this idea to make arguments for the rapid decrease in the viscosity of He II with temperature by stating:

“A preliminary estimation shows that the atoms belonging to the lowest energy state do not take part in the dissipation of momentum. Thus, the viscosity of the system is entirely due to the atoms in excited states.”

Since the fraction of atoms belonging to the ground energy state (condensed atoms) grows as the temperature is decreased and they do not contribute to dissipation, the viscosity must also decrease with temperature. Tisza explained the remarkably high flow velocities observed in thin capillary tubes by proposing that the condensed atoms will behave like a “superfluid” that can flow with essentially zero viscosity while the excited atoms would be blocked or would at best diffuse like a solution under an osmotic pressure gradient. This concept explained the different experimental values of viscosity measured in open geometries (an oscillating cylinder immersed in a bath of He II), where the excited atoms could easily flow, as compared to confined geometries (thin capillary tubes), where the flow of excited atoms is greatly

[†]The author would like to stress that the division of He II into “normal” atoms residing in excited states and “superfluid” atoms condensed into the ground state is only a *model* that provides a convenient description of many of the observed phenomena. The two-fluid model does not constitute a microscopic theory of He II.

restricted. In accord with the idea that the fraction of condensed atoms changes with temperature Tisza made the following prediction:

“Thus, the total flow represents a rather complex combination of both these effects. It will largely depend on the ratio $(n_0 - n)/n$ and, therefore, on T , in agreement with experiment. According to this interpretation, a temperature gradient should arise during the flow of helium II through a thin capillary.”

The experimentalists had not reported the observation of a temperature gradient along the capillary tube. However, Tisza made this testable prediction, which later would prove to be true. He used this very argument to explain the otherwise inexplicable “fountain effect” that had been observed only months before by Allen and Jones discussed above [68] in the following manner:

“If one maintains a temperature difference between the ends of a capillary, a gradient of density of excited atoms, n , and, thus, of pressure is produced. In consequence, (a) the excited atoms will diffuse towards the colder end, and (b) the super-fluid fraction of the liquid moves in the opposite direction. In the case of a wide tube, these currents must be equal and no resulting flow will be observed. If, however, the capillary is sufficiently narrow, the rate of the process (a) becomes reduced and the temperature gradient causes a surplus convection current opposite to heat flow.”

These few sentences were the first to conceive of a thermal counterflow as mentioned

in Subsection 1.3.4 and discussed in greater detail in Section 2.4. Thermal counterflows have no classical analogue and they form an invaluable cornerstone of past He II research as well as an active area of study today (the entirety of Chapter 5 of this thesis is dedicated to our contributions to thermal counterflow research).

Landau followed up the pioneering work of Tisza with a much more detailed microscopic picture of the two-fluid nature of He II [38]. Landau did not find the degenerate Bose gas description of He II adequate and instead developed his own theory that extends the qualitative two fluid ideas of Tisza. Landau sought a hydrodynamic description of He II that characterized states of the fluid rather than only considering individual atoms. The first very important idea put forth in his theory was that arbitrary values of vorticity were not possible in a quantum liquid. He posited that there must be an energy gap Δ between the case of potential flow (zero vorticity) and vortex motions in the fluid. Landau discussed elementary excitations as being composed of two branches: phonons, which are the standard longitudinal sound waves in the fluid, and rotons which are elementary excitations of the vortex spectrum. At $T = 0$, Landau stated that the flow of He II would not dissipate energy so long as the velocity was below two minima. Since there is an energy gap Δ to produce any vortex motions, rotons can only be excited for velocities $v > (2\Delta/\mu)^{1/2}$, where μ is the effective mass of a roton. Similarly, phonons could only be produced for $v > c$, where c is the speed of sound in the fluid.

At temperatures above absolute zero, excitations must be present. Landau considered the case of a rotating vessel of He II and envisioned that only part of the liquid would be dragged along by the walls while the other part would remain

stationary. This, he then regarded, could be considered as He II being composed of a mixture of two liquids — one a zero viscosity “superfluid” and the other a “normal” fluid. Landau stated that these two fluids could pass through one another without any exchange of momentum. This concept is almost true — Vinen discovered a “mutual friction” between the two fluids in 1957 [19–21], which is briefly discussed in the next section. It is important to note, as Landau himself pointed out, that one should not imagine that some helium atoms are normal and others are superfluid; it is not possible to separate the normal fluid and superfluid components of a quantum fluid. This is simply used as a convenient tool to describe the various phenomena.

Landau then outlined the standard two-fluid concepts that are still used today. The density of the fluid ρ is given by $\rho = \rho_n + \rho_s$, where ρ_n is the normal fluid density and ρ_s is the superfluid density, which both depend upon temperature. At $T = 0$, the excitations must completely vanish resulting in $\rho_n/\rho = 0$. For $T > 0$, $0 < \rho_n/\rho \leq 1$ with the fraction of normal fluid equal to unity only above T_λ (see Fig. 2.5). Furthermore, everywhere in the fluid there are two velocities — \mathbf{v}_s and \mathbf{v}_n , which correspond to the superfluid and normal fluid components, respectively.

The superfluid component resides in the ground state of the system, which has zero entropy, and therefore it cannot carry heat. Landau concluded from this fact that any motion of the superfluid component alone must be thermodynamically reversible. Furthermore, if He II flows through a restricted geometry, such as a thin capillary tube, only the superfluid component is able to slide along the boundaries without friction. As Tisza also predicted, the helium that flows out of the restricted geometry should be at a lower temperature than the initial vessel of He II. Landau

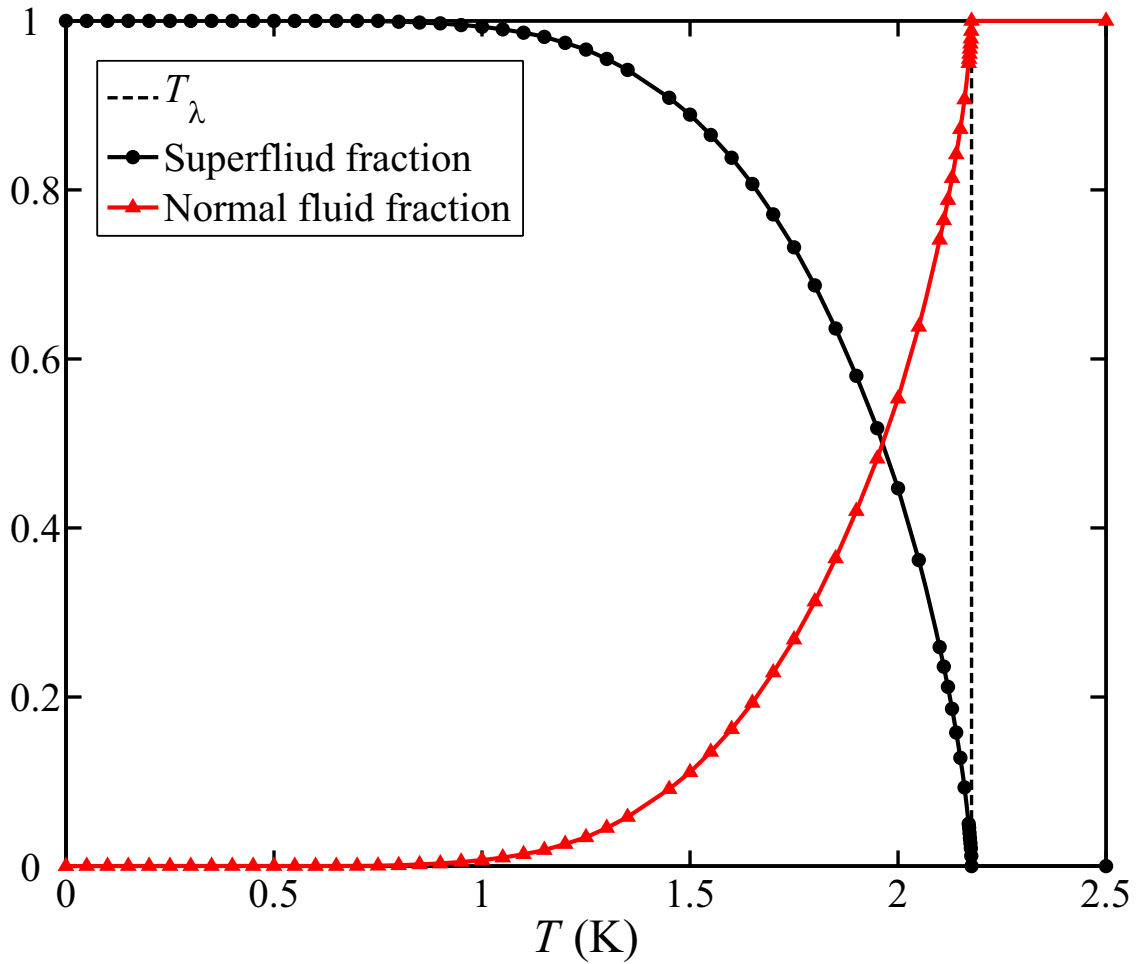


Figure 2.5: Plot of the normal fluid fraction (red curve) and superfluid fraction (black curve) [59]. Above the transition temperature T_λ , only normal fluid is present. As the temperature is decreased through T_λ the fraction of normal fluid monotonically decreases until only superfluid is present at $T = 0$ K.

put Tisza's initial comments regarding the flow of heat into his precise two-fluid context: any thermal gradient in the fluid will drive two currents — the normal fluid will carry the heat away from the hot to the cold end and an antiparallel current of superfluid will flow towards the heat source to conserve mass. Landau pointed out that this would be a very efficient mechanism for transporting heat, as had been observed in the aforementioned experiments [39, 62, 63].

Landau concluded this seminal work with the first macroscopic, hydrodynamic equations of motion for a superfluid. Again taking $\rho = \rho_n + \rho_s$ we have the flux of mass given by,

$$\mathbf{j} = \rho_s \mathbf{v}_s + \rho_n \mathbf{v}_n. \quad (2.1)$$

The continuity equation,

$$\frac{\partial \rho}{\partial t} + \nabla \cdot \mathbf{j} = 0, \quad (2.2)$$

expresses the conservation of mass. The law of conservation of momentum yields

$$\frac{\partial j_i}{\partial t} + \frac{\partial \Pi_{ik}}{\partial x_k} = 0, \quad (2.3)$$

where $\Pi_{ik} = P\delta_{ik} + \rho_n v_{ni} v_{nk} + \rho_s v_{si} v_{sk}$ is the momentum flux density tensor, which is a generalization of $\Pi_{ik} = P\delta_{ik} + \rho v_i v_k$ appropriate for classical fluids where P is the pressure. In this presentation Landau neglected the role of dissipative processes, so the flow is thermodynamically reversible. Thus, the conservation of entropy is given by

$$\frac{\partial(\rho S)}{\partial t} + \nabla \cdot (\rho S \mathbf{v}_n) = 0, \quad (2.4)$$

where S is the specific entropy (entropy per unit mass). We note that only \mathbf{v}_n enters into this conservation law since entropy and heat are only carried by the normal fluid,

so the flux of entropy per unit volume is given by $\rho S \mathbf{v}_n$. Lastly, Landau assumed that the viscous-free flow of the superfluid must be potential flow ($\nabla \times \mathbf{v}_s = 0$) for all times. This implies that the derivative of \mathbf{v}_s can be described as the gradient of a scalar thus

$$\frac{\partial \mathbf{v}_s}{\partial t} = -\nabla \left\{ \phi + \frac{v_s^2}{2} - \frac{\rho_n}{\rho} (\mathbf{v}_n - \mathbf{v}_s)^2 \right\}, \quad (2.5)$$

where ϕ is the thermodynamic potential per unit mass. The precise form of the scalar chosen stems from the law of conservation of energy and Galilean invariance; a more detailed derivation of this scalar and all of the equations in this section are presented in Chapter XVI of Ref. [70].

The boundary conditions of these two-fluid equations can differ from those of a classical fluid. Since the normal fluid is viscous, the velocity component parallel to any solid boundary v_n^{\parallel} must vanish at that boundary, as in a classical fluid. The superfluid, though, is free to slip along solid boundaries owing to the lack of viscosity. The perpendicular component of the mass flux \mathbf{j} must also be zero at any solid boundary. However, this does not imply that $v_n^{\perp} = 0$ or $v_s^{\perp} = 0$, since the flow involves two independent velocity fields. Indeed, the heat transfer between He II and a solid surface is executed by the boundary either emitting or absorbing excitation quanta (normal fluid). The corresponding boundary condition requires that only the heat flux perpendicular to a surface be continuous. If there is no heat transfer between the boundary and the fluid then we recover the usual impenetrable boundary conditions for any fluid, namely the perpendicular components of both \mathbf{v}_n and \mathbf{v}_s vanish at the surface.

The above two-fluid equations admit two sound velocities. The first wave equation, describing what is now referred to as first sound, is given by

$$\frac{\partial^2 P}{\partial t^2} = u_1^2 \nabla^2 P, \quad (2.6)$$

where $u_1 = (\partial P / \partial \rho)^{1/2}$ is the speed of first sound. This equation describes the propagation of longitudinal sound waves with both fluid components moving in concert, which is analogous to any classical fluid. The other wave equation describing second sound is given by

$$\frac{\partial^2 T}{\partial t^2} = u_2^2 \nabla^2 T, \quad (2.7)$$

where $u_2 = (TS^2 \rho_s / C_S \rho_n)^{1/2}$ and C_S is the heat capacity. The second-sound velocity vanishes at T_λ since $\rho_s \rightarrow 0$. These disturbances are waves of temperature, which are not present in classical fluids. Second-sound waves have velocities $\mathbf{v}_n = -\rho_s \mathbf{v}_s / \rho_n$ and therefore the two fluid components oscillate with a π phase difference. Furthermore, the net mass flux $\mathbf{j} = \rho_s \mathbf{v}_s + \rho_n \mathbf{v}_n = 0$, so the center of mass of any fluid element remains stationary. In summary, first-sound waves are coherent oscillations of both fluid components with $\mathbf{v}_n = \mathbf{v}_s$ and $\mathbf{j} \neq 0$ and second-sound waves, unique to quantum fluids, are temperature (entropy) oscillations with \mathbf{v}_n and \mathbf{v}_s π out of phase and $\mathbf{j} = 0$.

2.3 Quantized Vortices and Dynamics

2.3.1 An example: Ferromagnetism

To aid in the introduction of quantized vortices in He II we will appeal to the more familiar example of ferromagnetism. Many materials, such as iron, cobalt, and nickel, undergo a spontaneous symmetry breaking, continuous phase transition at their respective Curie Temperature (T_c). Above T_c , these materials behave as paramagnets by weakly amplifying any external magnetic field but failing to remain permanently magnetized in the absence of one. Below T_c , these materials become ferromagnetic and obtain a permanent magnetic moment. Clearly describing such systems only by their typical thermodynamic variables, such as temperature and pressure, is insufficient to clarify the distinction between the states above and below T_c . As such, additional variables, referred to as order parameters, are introduced to describe the system. Order parameters are typically normalized to take on values between zero and unity with zero corresponding to complete disorder (typical for temperatures greater than the corresponding transition temperature) and unity where the order in the system has reached its saturated value.

In the example of ferromagnetism, the corresponding order parameter is the magnetization \mathbf{M} , which is a three-dimensional vector of the magnetic field produced by the system of interest. Ferromagnetic materials are composed of atoms or molecules that have magnetic moments produced primarily by electron spin. Above T_c , the system has enough thermal energy to randomize the individual magnetic moments as shown schematically in Fig. 2.6(a). Computing the vector sum of the

individual, randomly-oriented magnetic moments yields zero net magnetization in physical samples owing to the vast number (within a few orders of magnitude of Avogadro's number $\sim 10^{23}$) of individual magnetic moments. Therefore, the system is completely disordered as described by the zero value of the order parameter.

Below the ferromagnetic transition temperature T_c , random regions of common magnetization form, separated by domain walls that preserve some of the disorder in the system (Fig. 2.6(b)). The magnetic domains are composed of aligned magnetic moments that are not necessarily aligned with the net magnetization vector. However, since the magnetic moments are no longer completely random their vector sum yields a nonzero net magnetization that describes the underlying order of the system. The energetic cost of misaligned magnetic moments increases as the temperature decreases. Thus, in simple magnetic materials the net magnetization monotonically increases with decreasing temperature until it saturates.

For the system to become more ordered, areas of disparate values in the order parameter must coalesce and form larger areas of common local magnetization, as shown in the transition from part (b) to part (c) in Fig. 2.6. To achieve this end, the domain walls that preserve disorder in the system must be removed. These defects in many systems do not diffuse and therefore are able to frustrate the ability of the system to become more ordered.

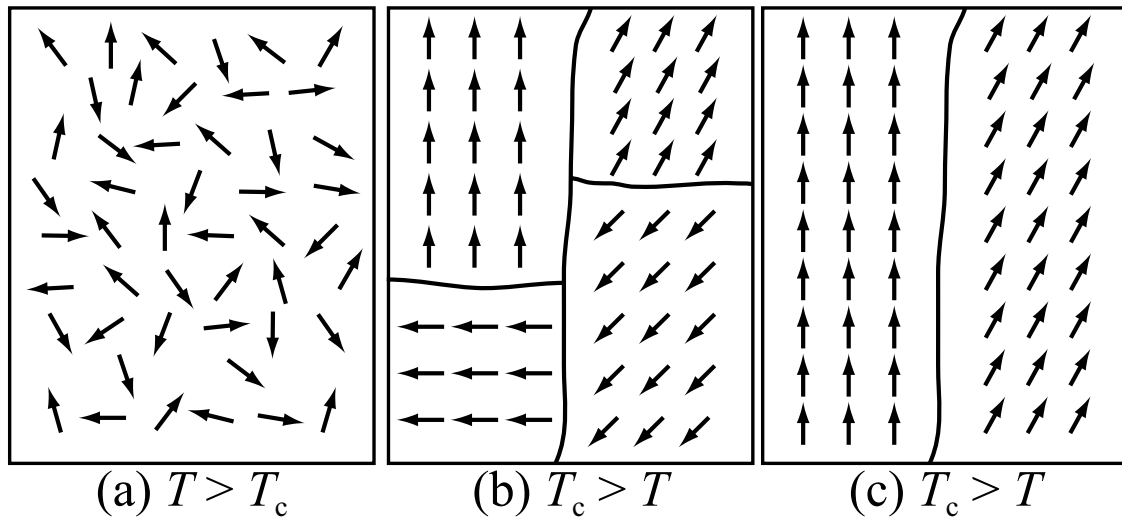


Figure 2.6: Schematic representation of the paramagnetic to ferromagnetic transition. The local orientation and amplitude of individual magnetic moments are shown as arrows. (a) Above the transition temperature T_c the magnetic moments are randomly oriented. (b) Below T_c , magnetic domains of aligned magnetic moments form and are separated by domain walls (black lines). (c) States with fewer domain walls and more order may be produced by changing initial and boundary conditions as well as other parameters such as applying an external magnetic field.

2.3.2 Superfluid Order Parameter and Quantized Vortices

The transition from He I to He II is also a symmetry-breaking, continuous phase transition. Again, the system may be described by an order parameter. In the context of the two-fluid model, only the superfluid component is described by the order parameter, which takes the form of a complex field analogous to a wave function

$$\psi = f e^{i\phi}, \quad (2.8)$$

for real values of f and ϕ . The superfluid density is given by

$$\rho_s = m\psi^*\psi = mf^2, \quad (2.9)$$

where m is the mass of a ${}^4\text{He}$ atom. In analogy with the increase in net magnetization as $T \rightarrow 0$ K in ferromagnets, the order in He II also increases as exemplified by the increase in the superfluid fraction ρ_s/ρ for decreasing temperature (black curve in Fig. 2.5). The superfluid fraction is zero at T_λ (complete disorder) and unity at $T = 0$ K (complete order).

The typical quantum-mechanical mass current \mathbf{j}_s takes the form

$$\mathbf{j}_s = \frac{\hbar}{2i} (\psi^* \nabla \psi - \psi \nabla \psi^*) = \hbar f^2 \nabla \phi. \quad (2.10)$$

Recognizing that a mass current is given by the product of a density and a velocity we can combine these two equations to obtain the superfluid velocity $\mathbf{v}_s = \mathbf{j}_s/\rho_s$. This yields

$$\mathbf{v}_s = (\hbar f^2 \nabla \phi)/(mf^2) = (\hbar/m) \nabla \phi. \quad (2.11)$$

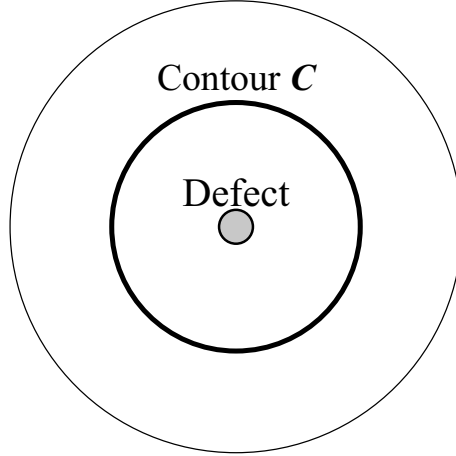


Figure 2.7: Schematic of a multiply-connected space with a topological defect at the center. The contour C shown by the thick, black line cannot contract to a point because of the presence of the defect at the center of the space.

If we assume that ψ represents the ordered part of the atomic wavefunctions, any gradients in the phase of the order parameter ϕ will produce a flow in the superfluid component. As discussed above, Landau stated that the flow of the superfluid component is potential flow ($\nabla \times \mathbf{v}_s = 0$). This is true in any simply connected region of the fluid since $\nabla \times \nabla \phi = 0$ for any scalar ϕ . A simply connected space is defined as a region where every path between any two points can be continuously transformed, without leaving the space, into every other path preserving the endpoints. Less formally, if every contour in a space can be contracted to a point without leaving the space then it is simply connected. Thus the Euclidean plane \mathbb{R}^2 is simply connected, but if a hole is placed at the origin, for example, it ceases to be simply connected. Spaces with such “holes” are called multiply connected, as shown schematically in Fig. 2.7.

Multiply connected regions of He II are formed by topological defects that are analogues of the domain walls present in ferromagnets. In He II the defects are line-like objects (diameters on the order of 0.1 nm) that must either end on boundaries or form closed loops. Topological defects generally separate areas with different values of the order parameter. In He II topological defects produce gradients in the phase ϕ . Thus, the value of ϕ varies along any contour that encloses such a defect. Continuity of the order parameter ψ defined in Eq. (2.8) requires that the change in phase along a closed contour C be a multiple of 2π . Therefore, we have the following quantization condition

$$\oint_C \nabla\phi \cdot d\ell = 2\pi n, \quad (2.12)$$

for nonzero integers n . The standard definition for circulation around a classical vortex with velocity field \mathbf{v} is

$$\Gamma = \oint_C \mathbf{v} \cdot d\ell, \quad (2.13)$$

for any contour C containing the vortex. Recognizing that we can replace $\nabla\phi$ in Eq. (2.12) with $m\mathbf{v}_s/\hbar$ using Eq. (2.11), we can define the circulation around a topological defect in He II thus

$$\Gamma = \oint_C \mathbf{v}_s \cdot d\ell = 2\pi\hbar n/m. \quad (2.14)$$

Identifying that $2\pi\hbar = h$, where h is Planck's constant, and defining the quantum of circulation $\kappa \equiv h/m \simeq 9.97 \times 10^{-4} \text{ cm}^2/\text{s}$, we arrive at

$$\Gamma = \oint_C \mathbf{v}_s \cdot d\ell = n\kappa. \quad (2.15)$$

Therefore, the circulation around a topological defect in He II is quantized in units of κ . If we consider a contour C that is a circle of cylindrical radius s around a

straight defect and that the gradient in the phase ϕ is constant (producing a constant $\mathbf{v}_s = v_s \hat{\phi}$) then we have

$$\oint_C \mathbf{v}_s \cdot d\ell = 2\pi s \mathbf{v}_s = n\kappa. \quad (2.16)$$

$$\mathbf{v}_s = \frac{n\kappa}{2\pi s}, \quad (2.17)$$

This velocity field is analogous to the flow field around a classical, singular vortex with circulation $n\kappa$. However, the circulation of vortices in He II is quantized, which is why these line-like defects are referred to as quantized vortices. Multiply-quantized vortices ($n \neq 1$) are energetically unfavorable and are expected to break up into multiple singly-quantized ($n = 1$) vortices. For this reason, it is often assumed that a vortex state in He II is composed of identical, singly-quantized vortices.

2.3.3 Quantized Vortex Dynamics

Landau's initial formulation of the two-fluid model stated that the superfluid and normal fluid components pass through one another without interacting. The mutual interactions between the two fluids were restricted to those required to satisfy the conservation laws outlined in Section 2.2. Since quantized vortices are topologically constrained and do not diffuse, they are locked to the superfluid, meaning that they move with the local superfluid velocity. Determining the dynamics of the quantized vortices, then, amounts to computing the velocity field induced by the vortices themselves and the "background" superfluid velocity \mathbf{v}_s produced by other means such as heat fluxes.

Following the pioneering work of Schwarz [50, 53, 54], we will consider a single

quantized vortex in an infinite fluid with a position parameterized by the curve $\mathbf{s} = \mathbf{s}(\xi, t)$. The velocity produced at a position \mathbf{r} by the vortex filament \mathbf{v}_ω is given by a Biot-Savart expression of the form

$$\mathbf{v}_\omega = \frac{\kappa}{4\pi} \int_{\mathcal{L}} \frac{(\mathbf{s}_1 - \mathbf{r}) \times d\mathbf{s}_1}{|\mathbf{s}_1 - \mathbf{r}|^3}, \quad (2.18)$$

where the integral is taken along the filament and \mathbf{s}_1 is a point on the vortex. This integral diverges as \mathbf{r} approaches a point on the vortex filament. To control this divergence, theories typically divide the velocity of the vortex filament itself, say $\dot{\mathbf{s}}$, at the point \mathbf{s} into two components [53]

$$\mathbf{v}_\omega(\mathbf{s}) = \dot{\mathbf{s}} = \frac{\kappa}{4\pi} \mathbf{s}' \times \mathbf{s}'' \ln \left(\frac{2(l_+ l_-)^{1/2}}{e^{1/4} a_0} \right) + \frac{\kappa}{4\pi} \int_{\tilde{\mathcal{L}}} \frac{(\mathbf{s}_1 - \mathbf{r}) \times d\mathbf{s}_1}{|\mathbf{s}_1 - \mathbf{r}|^3}, \quad (2.19)$$

where primes denote differentiation with respect to the arc length ξ , a_0 is a cutoff parameter corresponding to the radius of the vortex filament, l_+ and l_- are the lengths of the two adjacent line elements connected to the point \mathbf{s} , and $\tilde{\mathcal{L}}$ represents integration along the vortex line outside the region specified by l_+ and l_- as shown schematically in Fig. 2.8. A schematic representation of the vectors \mathbf{s}' , \mathbf{s}'' and $\mathbf{s}' \times \mathbf{s}''$ is given in Fig. 2.9.

Computing the full Biot-Savart integral is computationally expensive. Many researchers choose to assume the localized-induction approximation (LIA) [51–54] which ignores the nonlocal, second term in Eq. (2.23); the validity of this approximation, though, has recently been questioned [55, 56]. The commonly used equation invoking the LIA is

$$\dot{\mathbf{s}} = \beta \mathbf{s}' \times \mathbf{s}''. \quad (2.20)$$

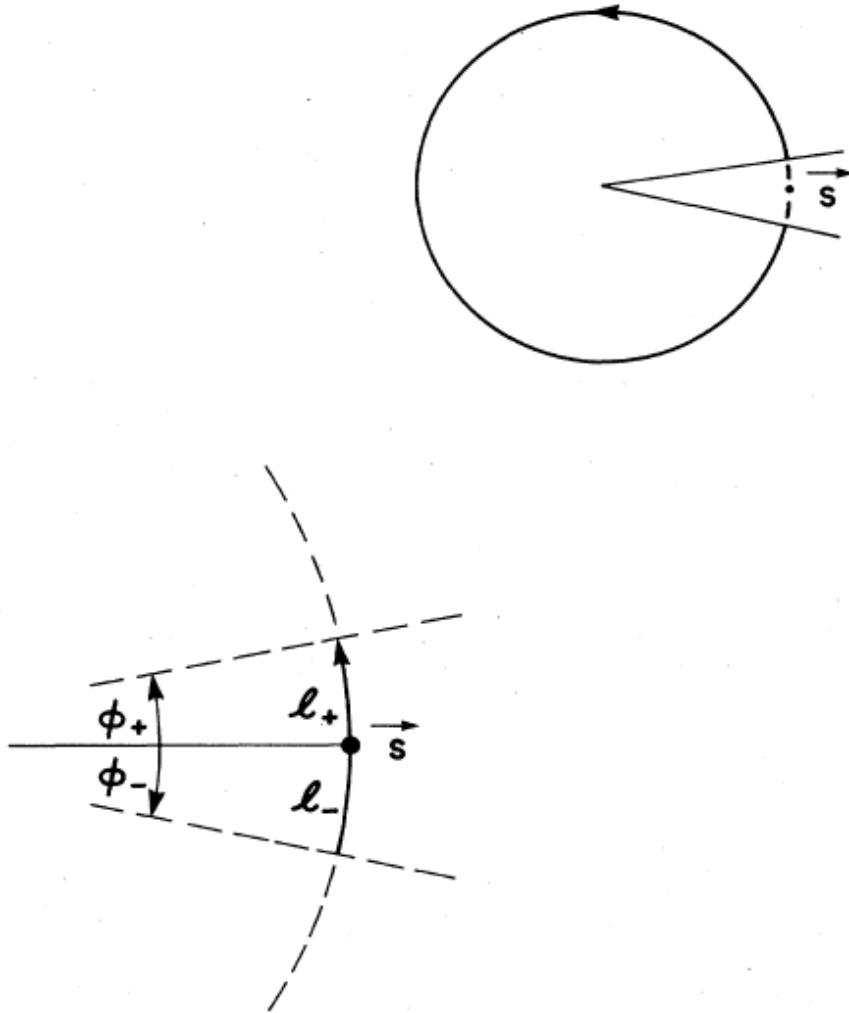


FIG. 2. Nonlocal (top) and local (bottom) contributors to the motion of the point s . The division is purely formal, and neither part can exist by itself.

Figure 2.8: Original figure taken from Schwarz's [53] pioneering implementation of vortex-filament methods that define the nonlocal and local contributions from a vortex filament. The nonlocal term in Eq. (2.19) is determined by computing the modified line integral $\tilde{\mathcal{L}}$ along the vortex filament outside the small wedge centered on the point s as shown in the top figure. The definitions of l_+ and l_- used to compute the local contribution in Eq. (2.19) are shown in the bottom figure.

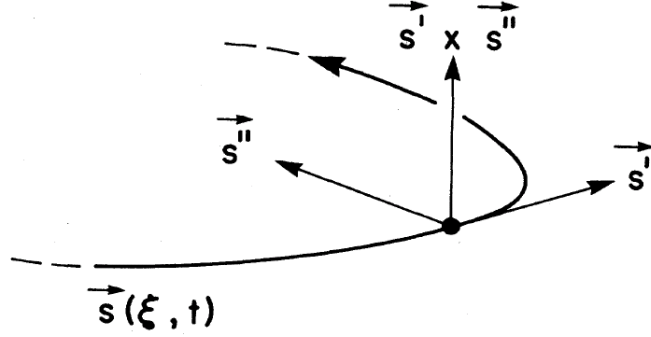


FIG. 3. Triad of vectors characterizing the instantaneous local configuration of the curve $\mathbf{s}(\xi, t)$.

Figure 2.9: Schematic representation of the vectors \mathbf{s}' , \mathbf{s}'' and $\mathbf{s}' \times \mathbf{s}''$ for a vortex filament defined by the curve $\mathbf{s} = \mathbf{s}(\xi, t)$ taken from [53].

The coefficient β is defined as

$$\beta = \frac{\kappa}{4\pi} \ln \left(\frac{c\langle R \rangle}{a_0} \right), \quad (2.21)$$

with c a constant of order unity and the quantity $(l_+ l_-)^{1/2}$ replaced by the characteristic radius of curvature $\langle R \rangle$ of the vortex lines.

Assuming that there is a background flow of the superfluid \mathbf{v}_s produced by a thermal counterflow (see next section) or by some other means, then the motion of the vortex filament is given by

$$\dot{\mathbf{s}}_0 = \mathbf{v}_s + \frac{\kappa}{4\pi} \mathbf{s}' \times \mathbf{s}'' \ln \left(\frac{2(l_+ l_-)^{1/2}}{e^{1/4} a_0} \right) + \frac{\kappa}{4\pi} \int_{\tilde{\mathcal{L}}} \frac{(\mathbf{s}_1 - \mathbf{r}) \times d\mathbf{s}_1}{|\mathbf{s}_1 - \mathbf{r}|^3}. \quad (2.22)$$

Equation 2.22 would approximately describe the dynamics of quantized vortices in the absence of any exchange of momentum between the superfluid and normal fluid components. However, in 1957 Vinen [19–21] discovered that momentum is exchanged between \mathbf{v}_s and \mathbf{v}_n through a “mutual friction” that acts on the vortices.

The common phenomenological description yields the following velocity for a point

\mathbf{s} on a vortex filament [53]

$$\dot{\mathbf{s}} = \dot{\mathbf{s}}_0 + \alpha \mathbf{s}' \times (\mathbf{v}_n - \dot{\mathbf{s}}_0) - \alpha' \mathbf{s}' \times [\mathbf{s}' \times (\mathbf{v}_n - \dot{\mathbf{s}}_0)], \quad (2.23)$$

where α and α' are temperature-dependent coefficients tabulated in Section B.3. The most common implementation of Eq. (2.23) is in numerical simulations of counterflow turbulence where values of \mathbf{v}_n and \mathbf{v}_s are prescribed and the steady-state dynamics of the quantized vortices are characterized.

2.4 Thermal Counterflows

The most commonly studied form of turbulence in He II is counterflow turbulence. The typical experimental setting consists of a channel immersed in He II that is closed on one end. A heat flux \mathbf{q} is applied, typically by passing electrical current through a resistive coil of wire, to the closed end of the channel driving a flow in both the normal fluid and superfluid components, as shown schematically in Fig. 2.10. The heat escapes the channel and eventually is removed by some cooling mechanism such as evaporative cooling at the free surface of the liquid.

The resulting flows of both the normal fluid and superfluid components are not driven by buoyancy as in a classical fluid. Indeed, applying a heat flux orthogonal to the local gravity vector or in the absence of gravity will still drive a flow. The flow is driven by a gradient in entropy. As discussed in Section 2.2, only the normal fluid component is capable of transporting heat. The amount of entropy carried per unit volume is the product of the fluid density ρ and the specific entropy S , which is the entropy per unit mass. To convert the entropy per unit volume into heat per

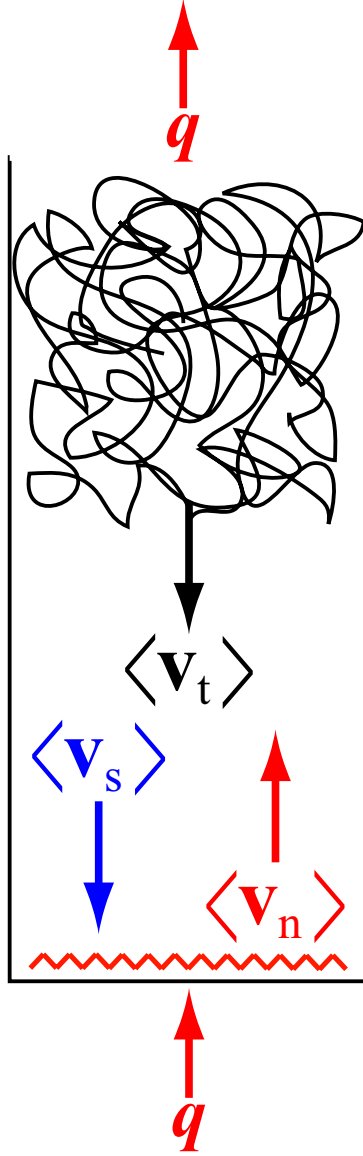


Figure 2.10: Schematic representation of an experimental counterflow channel and the resulting fluid velocities. The channel is immersed in a bath of He II and closed at one end (the bottom in this case). A known heat flux \mathbf{q} is applied to the closed end of the channel by passing an electrical current through a resistive element. The normal fluid carries the heat away from the source by moving in the direction of the heat flux with an average velocity $\langle \mathbf{v}_n \rangle$ given by Eq. (2.25). To conserve mass, the superfluid moves towards the heat source with an average velocity $\langle \mathbf{v}_s \rangle$ defined in Eq. (2.26). The counterflow motions drive a vortex tangle that on average moves downward with the superfluid component but with a different velocity $\langle \mathbf{v}_t \rangle$. The injected heat passes through the channel and is eventually removed by some cooling mechanism, such as evaporative cooling at the free surface of the liquid.

unit volume, one must multiply by the temperature T . The heat flux through the fluid is given by the product of the entropy per unit volume ρsT and the normal fluid velocity \mathbf{v}_n . Thus, equating this with the driving heat flux \mathbf{q} we can compute the normal fluid velocity \mathbf{v}_n as first given by Landau [70]

$$\mathbf{q} = \rho sT \mathbf{v}_n \quad (2.24)$$

$$\mathbf{v}_n = \frac{\mathbf{q}}{\rho sT}. \quad (2.25)$$

Applying the conservation of mass given by $\rho_n \mathbf{v}_n + \rho_s \mathbf{v}_s = 0$, the resulting superfluid velocity is

$$\mathbf{v}_s = -\frac{\rho_n}{\rho_s} \mathbf{v}_n, \quad (2.26)$$

which opposes the motion of the normal fluid. The counterflow velocities \mathbf{v}_n and \mathbf{v}_s depend strongly on the temperature. For temperatures near T_λ , the superfluid density is very small, which requires very large superfluid velocities to conserve mass. Conversely, for temperatures below ~ 1 K, the density of normal fluid is very small and therefore the specific entropy S is correspondingly small yielding very large values of \mathbf{v}_n necessary to conserve heat.

The opposing motions of \mathbf{v}_n and \mathbf{v}_s also drive the formation of a vortex tangle, which moves with a mean velocity \mathbf{v}_t as shown in Fig. 2.10. The mutual friction forces between the quantized vortices and the normal fluid discussed briefly in the previous section, can exchange momentum between the quantized vortices and the normal fluid. Depending upon the local flow velocities and the orientation of the quantized vortex, \mathbf{v}_n may act to either extend the vortex line or shrink it.

Vinen developed a theory to characterize the total amount of vorticity present

in the superfluid component by considering the average vortex line length per unit volume L [19–21]. Higher values of L imply that there are more quantized vortices present within the system. In the case of a thermal counterflow where the vortices and normal fluid motions oppose one another, mutual friction tends to increase L . However, the increase in L is accompanied by an increase in dissipation in the superfluid component via mutual friction and the process of reconnection between the vortices, as discussed in the next section. Assuming homogeneity and isotropy of the vortex tangle, Vinen was able to phenomenologically describe the evolution of the vortex line length density in a thermal counterflow. The following kinetic equation is now termed the Vinen equation, namely,

$$\frac{\partial L}{\partial t} = \xi_1 |\mathbf{v}_{\text{ns}}| L^{3/2} - \xi_2 \kappa L^2, \quad (2.27)$$

where $\xi_1, \xi_2 > 0$ are dimensionless, temperature-dependent coefficients while $\mathbf{v}_{\text{ns}} = \langle \mathbf{v}_{\text{n}} \rangle - \langle \mathbf{v}_{\text{s}} \rangle$, where the brackets imply spatial averages. The first term on the right-hand side is always nonnegative and acts to increase L by means of counterflowing motions, which are defined by nonzero values of \mathbf{v}_{ns} . The second term is always nonpositive and acts to reduce the vortex line length through dissipative processes, namely mutual friction and quantized vortex reconnections. A statistical steady-state, given by $\partial L / \partial t = 0$, is reached when the two terms on the right-hand side are equal, which yields a saturated vortex line length density

$$L_{\text{sat}} = \left(\frac{\xi_1}{\xi_2 \kappa} |\mathbf{v}_{\text{ns}}| \right)^2. \quad (2.28)$$

2.5 Reconnection

Relaxation toward equilibrium requires dissipative processes but can be inhibited by topological defects that cannot diffuse. Linear topological defects, analogous to quantized vortices in He II, occur in a variety of systems such as liquid crystals [71] and superconductors [72]. Dissipation normally accompanies the reconnection of two defect lines that cross, change topology by exchanging ends and separate (as illustrated in Fig. 2.11). Prime examples [73] of dissipation by reconnection occur in astrophysical plasmas (such as solar flares [74, 75] and magnetic substorms [76, 77]) and sawtooth crashes in fusion devices [78], where magnetic energy is dissipated by the acceleration of nearby particles [10, 79–82]. Reconnection has also been studied in liquid crystals [71], superconductors [72, 83, 84], cosmic strings [85], viscous [86–88] and Euler [89] vortices and Bose-Einstein condensates [90].

Quantized vortex reconnection in He II has been previously studied numerically and analytically by employing vortex-line methods [50, 53, 54, 57, 91, 92] and by integrating the Gross-Pitaevskii equation [58, 93] given by

$$i\hbar\frac{\partial\psi}{\partial t} = \left(-\frac{\hbar^2}{2m}\nabla^2 + V(\mathbf{r}) + g|\psi|^2 \right) \psi, \quad (2.29)$$

where ψ is the order parameter field, $V(\mathbf{r})$ is an external potential and g a coupling constant. The reconnection process in He II was first proposed as a necessary dissipative mechanism by Feynman in 1955 [14]. Schwarz [53, 54] forced reconnection upon any two vortices that were separated by less than some threshold distance in his vortex-line simulations of counterflow turbulence. He invoked reconnection, even though it had not yet been proven to occur in He II, in order to attain an otherwise

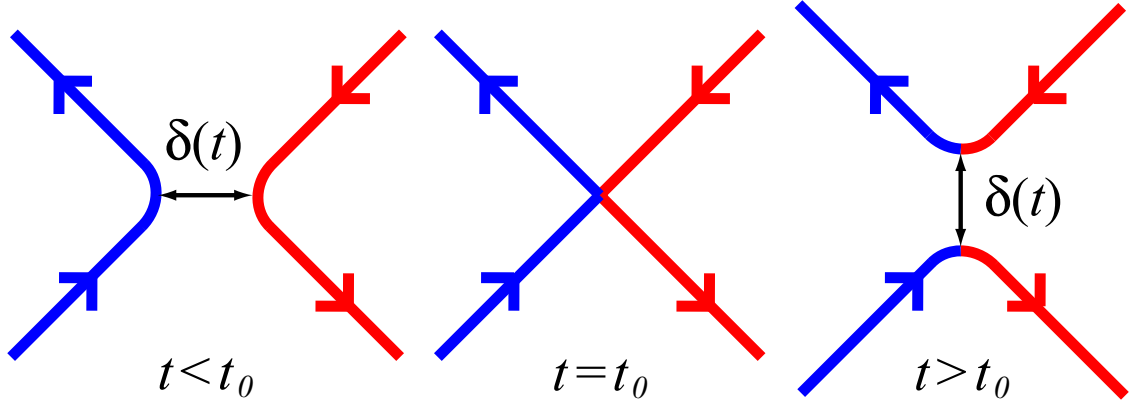


Figure 2.11: Schematic of the evolution of reconnecting antiparallel directed linear topological defects; in the case of vortices the arrows indicate the sense of the vorticity. The minimum separation between the defects is $\delta(t)$ with $\delta(t_0) = 0$. Although not evident here, reconnection need not be planar and, indeed, has been predicted to be intrinsically three-dimensional [53, 57].

elusive statistical steady-state for the vortex line density L in his pioneering simulations. Koplik and Levine [58] were the first to show that two quantized vortices will reconnect using the Gross-Pitaevskii equation, even though there is no diffusion, which was thought to play an essential role in reconnection. To characterize the evolution of reconnecting vortices, some of these theoretical studies examined the minimum separation distance $\delta(t)$ between the vortices as shown in Fig. 2.11. Assuming that the only relevant parameter in reconnection dynamics is the quantum of circulation κ , dimensional analysis yields the relation

$$\delta(t) = A (\kappa |t - t_0|)^{1/2}, \quad (2.30)$$

where t_0 is the moment of reconnection and A is a dimensionless factor of the order unity. One may optimistically expect this scaling to be valid for length scales

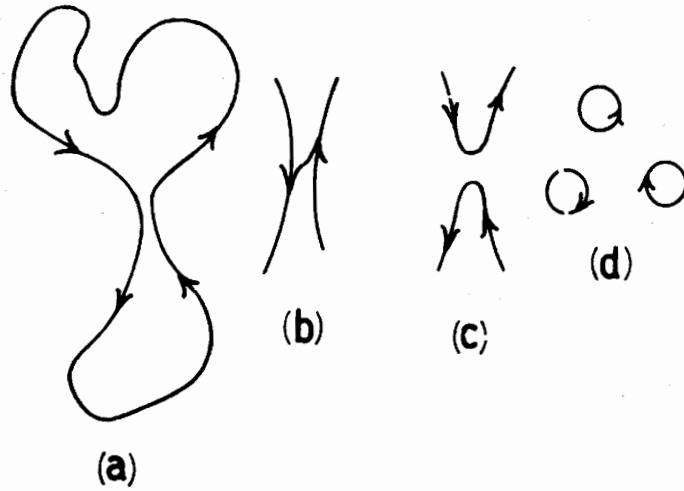


Fig. 10. A vortex ring (a) can break up into smaller rings if the transition between states (b) and (c) is allowed when the separation of vortex lines becomes of atomic dimensions. The eventual small rings (d) may be identical to rotons.

Figure 2.12: Feynman's initial proposition for the reconnection of quantized vortices taken from [14].

between the vortex core size (~ 0.1 nm) and the typical intervortex spacing, which ranges from ~ 0.1 to 1 mm in our experiments. Basically, however, Eq. (2.30) should represent an asymptotic expression, subject at least to corrections for longer times. Indeed, slight deviations were observed in prior simulations implementing line-vortex models [53, 57]. The Gross-Pitaevskii equation is Hamiltonian and time-reversal invariant, but particular solutions may well break this symmetry.

Reconnection is considered to be an essential mechanism for removing vortex line length and dissipation in He II, particularly as $T \rightarrow 0$ K. One means of removing vortex line length via reconnection is shown in Fig. 2.12, which is taken from Ref. [14] where Feynman first proposed the process of reconnection in He II. Feynman argued

that if reconnection could occur, then larger quantized vortex loops could form smaller ones and so on until the loops became sufficiently small to decay from friction with the normal fluid or interactions with the boundaries. Another mechanism stems from the anomalously large velocities associated with reconnection for times near t_0 . For temperatures $T > 1$ K, reconnecting vortices with large, atypical velocities will lose more of their energy to the normal fluid via mutual friction. For temperatures $T < 1$ K, where the normal fluid density is essentially negligible, the dissipative mechanism is less clear and actively debated. Reconnection is also thought to produce Kelvin waves on the vortex lines, which as described above in Section 1.2, are helical disturbances that propagate down the vortices. Since the waves are underdamped, they persist and interact nonlinearly. The nonlinear coupling between waves will produce higher frequency oscillations until they become high enough to emit phonons into the surrounding fluid that are eventually absorbed by the boundary [15, 32]. It is important to stress that dissipation in He II for temperatures near absolute zero remains a controversial and active area of research.

Chapter 3

Apparatus and Experimental Techniques

In this chapter we discuss details of the experimental apparatus and methods used to obtain the results presented in the forthcoming chapters. In addition to the newly implemented apparatus and techniques contributed by the author, all of the components used in prior experiments have been heavily modified or completely replaced. To begin we give a brief overview of the optical cryostat used in these studies, which is the central component to all of this work. We then give an overview of the injection technique developed in our laboratory that is used to produce viable tracer particles in He II used for flow visualization. The details of the heater design and operation as well as the channel used for the counterflow studies presented in Chapter 5 are also discussed. We follow this with an overview of the temperature measurements and control mechanisms. We end the chapter with a discussion of the visualization and particle-tracking methods used to acquire and analyze the trajectories of tracer particles.

3.1 Apparatus

A schematic diagram of the important components of the experiments is shown in Fig. 3.1. The central component is the cryostat, which serves as the vessel for the liquid helium. The details of the cryostat are given in Subsection 3.1.1 followed

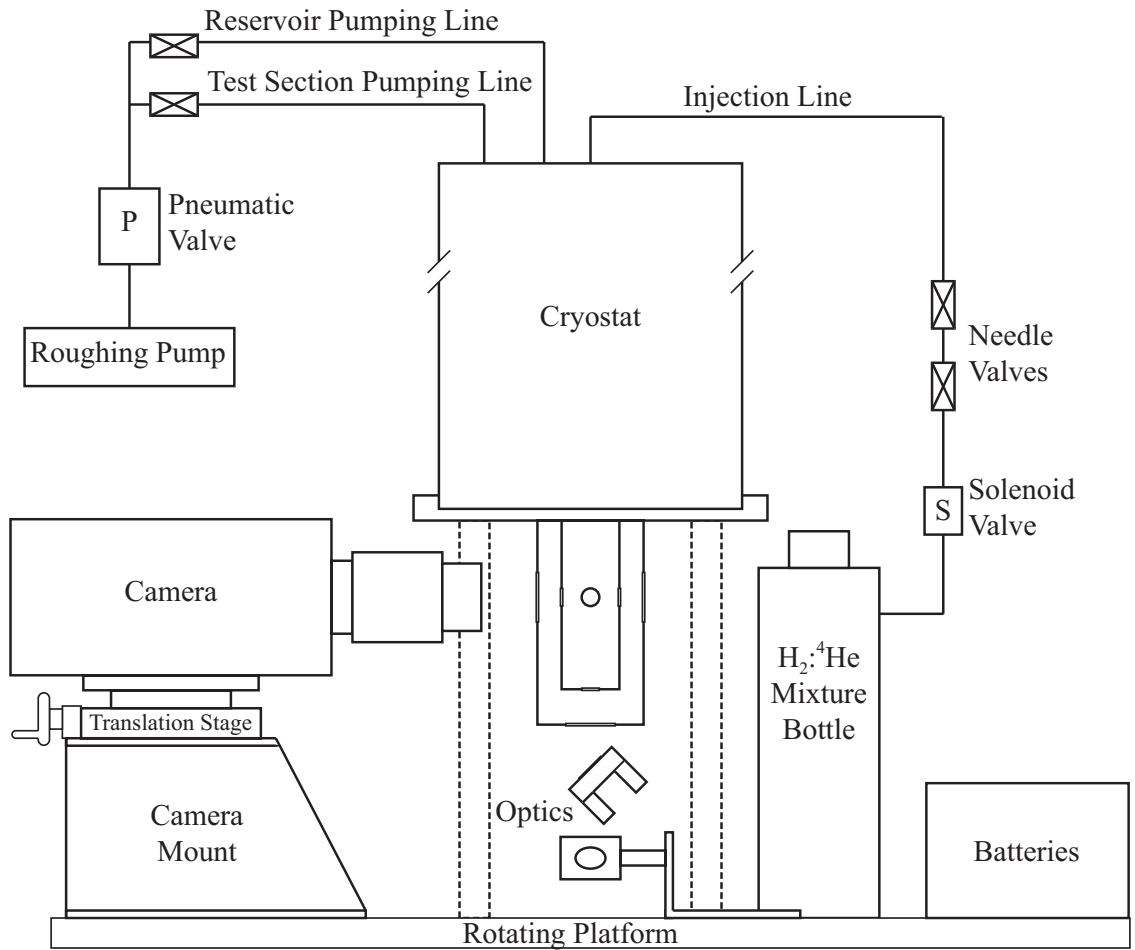


Figure 3.1: Schematic diagram of the essential components of the experimental apparatus. The cryostat serves as the liquid helium vessel. The injection technique is composed of the mixture bottle, a series of valves and the injection line that ends 1 cm above the cryostat windows. The temperature control system is composed of internal and external electronics not shown in this figure as well as the pumping lines, pneumatic valve and the roughing pump. The camera, optics and laser (not shown) comprise the visualization technique. All of the apparatus is placed on a rotating table that is attached to an air bearing, which allows the entire system to rotate.

by a discussion of the apparatus placed within the cryostat used for driving thermal counterflows in Subsection 3.1.2. External to the cryostat are several instruments for measurements as well as components used for producing and visualizing the tracer particles. The injection technique used to produce the hydrogen tracer particles is composed of the mixture bottle, a series of valves and the injection line, which are further detailed in Subsection 3.1.3. The details of the temperature measurement and control system, shown by the pumping lines, pneumatic valve and roughing pump are discussed in Section 3.2. Lastly, the optics and camera implemented for visualizing the tracer particles as well as the particle-tracking method used for analysis are discussed in Sections 3.3 and 3.4.

All of the apparatus is attached to a platform designed and built by the author. The purpose of the newly-designed platform is to allow the entire apparatus to rotate so that the dynamics of He II in the rotating frame may also be studied. Preliminary rotating experiments have been conducted, but the details of which will not be discussed here. The platform is designed to attach to the air bearing used in previous experiments. These other experiments using water had caused the air bearing to seize from rust, which prevented it from being able to rotate. This was corrected by carefully repolishing every part without modifying any of the significant dimensions of the air bearing.



Figure 3.2: Photograph of the Oxford Instruments Optistat-SXM cryostat used in the experiments presented here.

3.1.1 Oxford Cryostat

The liquid ^4He used in this experiments is contained within an Oxford Instruments Optistat-SXM cryostat, pictured in Fig. 3.2. The cryostat is primarily composed of a 4 L helium reservoir, a variable temperature test section and a vacuum space that provides thermal insulation to the surrounding environment as shown in Fig. 3.3. The test section is designed for use at temperatures between 1.6 K and 300 K. Cooling is provided by allowing liquid helium to flow from the reservoir into the test section through a thin tube with the flow rate modulated by a needle valve. A heat exchanger is embedded in the wall of the test section immediately above the windows, which is fitted with a thermometer and tunable heater to control the temperature within the test section. Temperatures below the atmospheric boiling point of liquid helium (4.2 K) are achievable by pumping on the liquid as described in Section 3.2.2.

The cylindrical test section has a diameter of 49 mm and is 645.5 mm long. Optical access is provided by four windows 78 mm above the bottom of the test section each 90° apart. An additional window is located at the center of the bottom of the test section, which affords us the ability to view the dynamics along the axis of rotation when the system spins. The liquid levels in both the reservoir and the test section are measured with independent level meters.

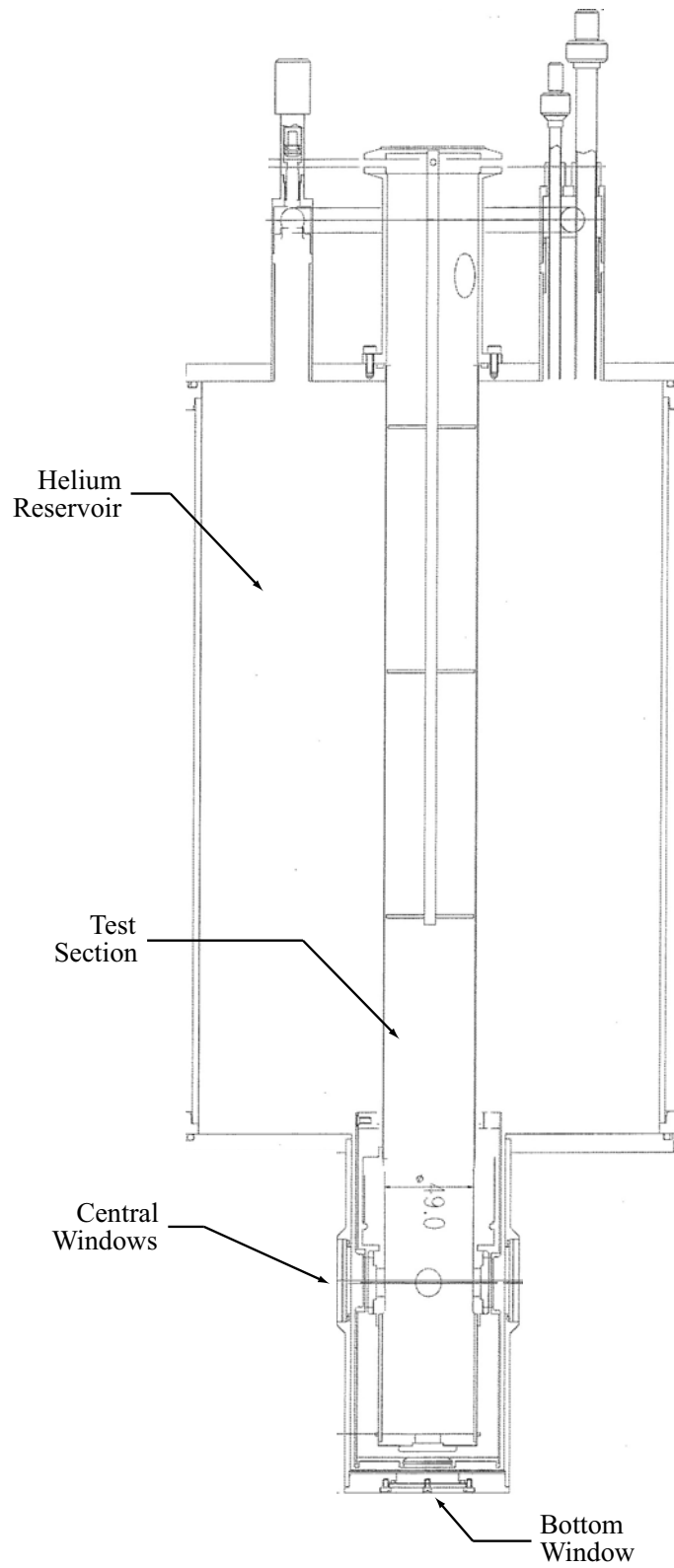


Figure 3.3: Mechanical drawing of the Oxford Instruments Optistat-SXM cryostat used in the experiments presented here.

3.1.2 Heater Design and Counterflow Channel

Two separate heaters and channels have been designed and constructed for thermal counterflow studies. Only one of the counterflow channels has been used for the studies presented here, and will therefore be the focus. Details of the smaller counterflow channel are discussed in Subsection 8.3.1.

Quantitative comparisons between experimental and theoretical studies of thermal counterflow turbulence require precise knowledge of the heat flux \mathbf{q} that drives the system. We have constructed the counterflow channel shown in Fig. 3.4. The heater is formed by a spiral pattern of nichrome wire bonded to G10 fiberglass using stycast. The heater is placed at the bottom of the channel 7.5 cm below the observation volume. The nichrome wire is chosen because it maintains its electrical resistivity at liquid helium temperatures, thereby allowing Ohmic dissipation to serve as the source of heat. The G10 substrate is electrically insulating and also machinable. This allowed us to machine spiral grooves in the G10 that would form the heater pattern. A thin layer of stycast covers the entire heater surface to prevent the wire from detaching itself from the G10 substrate. Stycast is one of the few substances that provide a very strong bond as well as excellent thermal conductivity at liquid helium temperatures. The spiral heater pattern minimizes nonuniformities in the local heat flux; the largest deviation of only a few percent occurs at the center of the spiral. Copper wires with a much lower resistivity than the nichrome, particularly at liquid helium temperatures, are soldered to the two ends of the spiral heater and passed through the top of the test section using a vacuum-sealed electri-

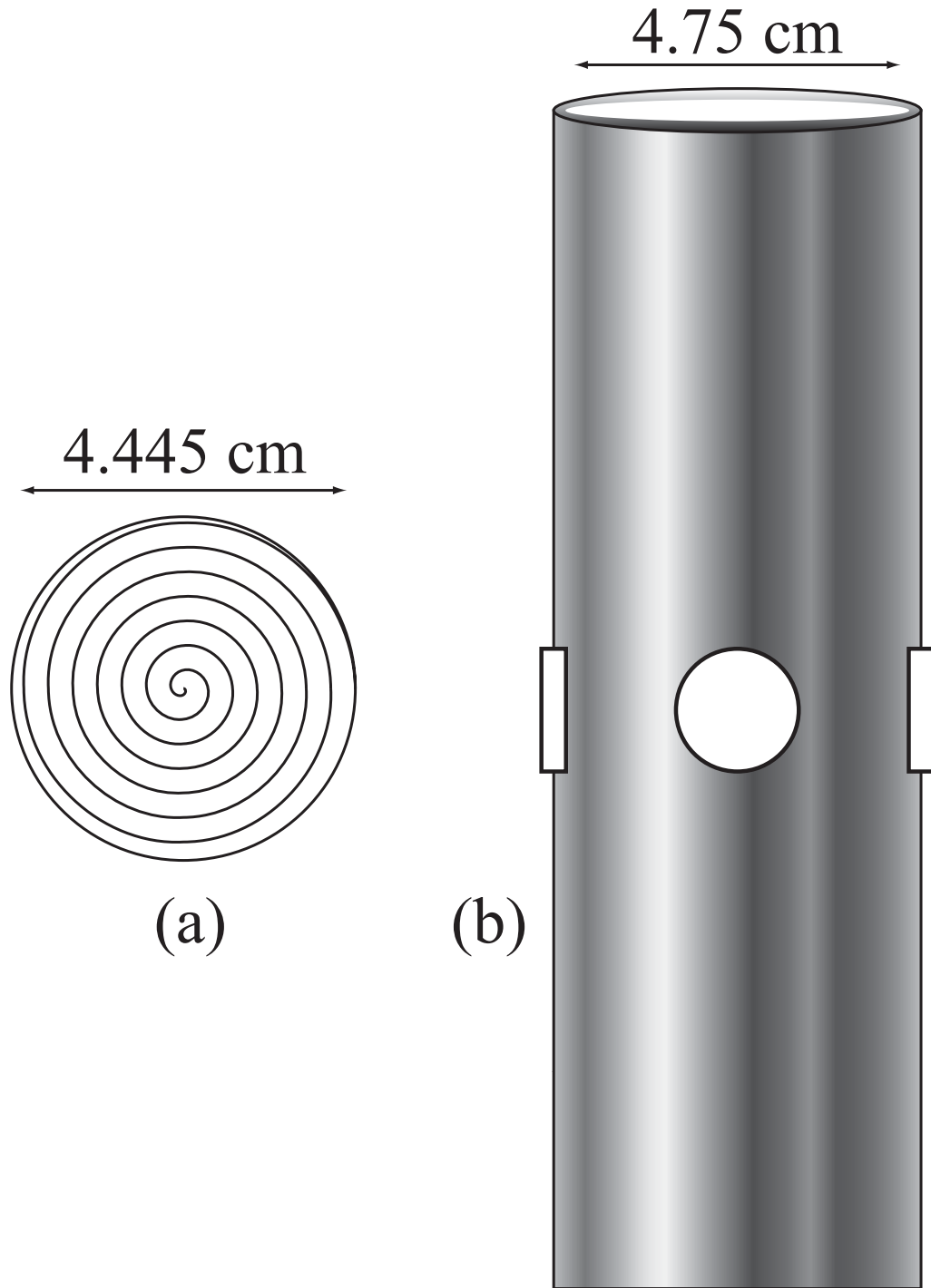


Figure 3.4: Scaled drawings of the (a) spiral heater and (b) counterflow channel. The spiral heater is concentrically placed in the bottom of the counterflow channel. The channel is open to the surrounding He II at the top. Laser light passes through the channel through two slits at the mid-height and 90° scattered light is observed through a hole in the channel. The channel (4.75 cm diameter) essentially occupies the entire cross-section of the test section (4.9 cm diameter).

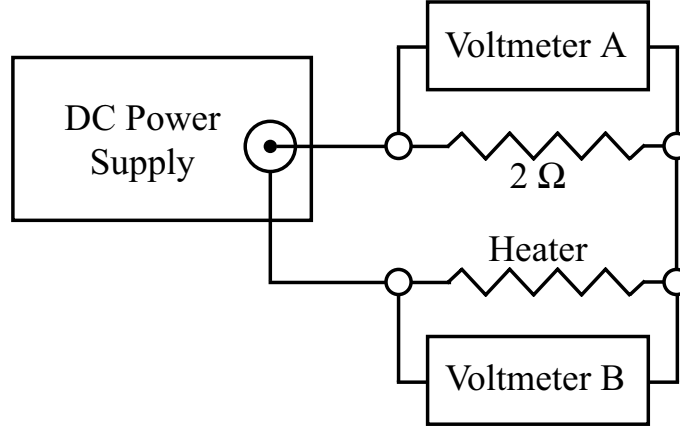


Figure 3.5: Diagram of the heater power measurement necessary to compute the heat flux. A DC power supply provides the source of current that flows through a constant $2\ \Omega$ resistor and the heater. Independent voltmeters determine the voltage drop across each resistor, which is then used to compute the electric power dissipated by the heater.

cal fitting. Since the resistivity of the copper wires is much lower than the nichrome, effectively all of the Ohmic dissipation occurs in the nichrome wires, which allows for accurate measurements of the heat flux in the counterflow channel.

The measurement of the electrical power of the heater is shown diagrammatically in Fig. 3.5. A DC power supply is used to drive a current through the heater. In series with the heater is a $2\ \Omega$ shunt that is used to measure the electrical current. The resistance of the shunt is steady and known. Therefore, by measuring the voltage drop across the shunt V_A using Voltmeter A the current is given by $I = V_A/2$. A separate voltmeter measures the voltage drop across the heater itself V_B . The total power dissipated by the heater is $P = IV_B = V_AV_B/2$. The magnitude of the heat flux \mathbf{q} is the power dissipated divided by the area $A = 15.52\ \text{cm}^2$,

$$q = \frac{P}{A} = \frac{V_AV_B}{31.04}\ \text{W/cm}^2. \quad (3.1)$$

For each experimental run the output of the DC power supply is set and the values of V_A and V_B are measured and recorded.

3.1.3 Injection Technique

Hydrogen tracer particles are produced *in situ* by directly injecting a room temperature mixture of hydrogen and helium gas into the bulk of the liquid helium in the test section. As the mixture passes down the injector tube inside the test section it cools from room temperature to liquid helium temperatures causing the hydrogen to solidify and the helium to liquefy. The result is a polydisperse distribution of solid hydrogen tracers that are approximately $1\ \mu\text{m}$ in diameter, as evidenced in Gregory Bewley's thesis [1], with an initial volume fraction of 10^{-6} – 10^{-5} . The solid hydrogen has a higher index of refraction than the surrounding liquid. This difference in refractive index allows the particles to be imaged since light will be scattered from the solid-liquid interface, as shown in Fig. 3.6. This technique was developed by Gregory Bewley [1]. The apparatus used in these previous studies was manually controlled and we have replaced the entire system to allow for computer control.

The mean of the initial particle size distribution is controlled by the relative fraction of hydrogen and helium present in the room temperature mixture. Using pure hydrogen gas produces unusable, macroscopic chunks of hydrogen while particles hundreds of nanometers in size may be produced by using a fraction of a percent of hydrogen. For all of the experiments presented here the mixture contained 2%

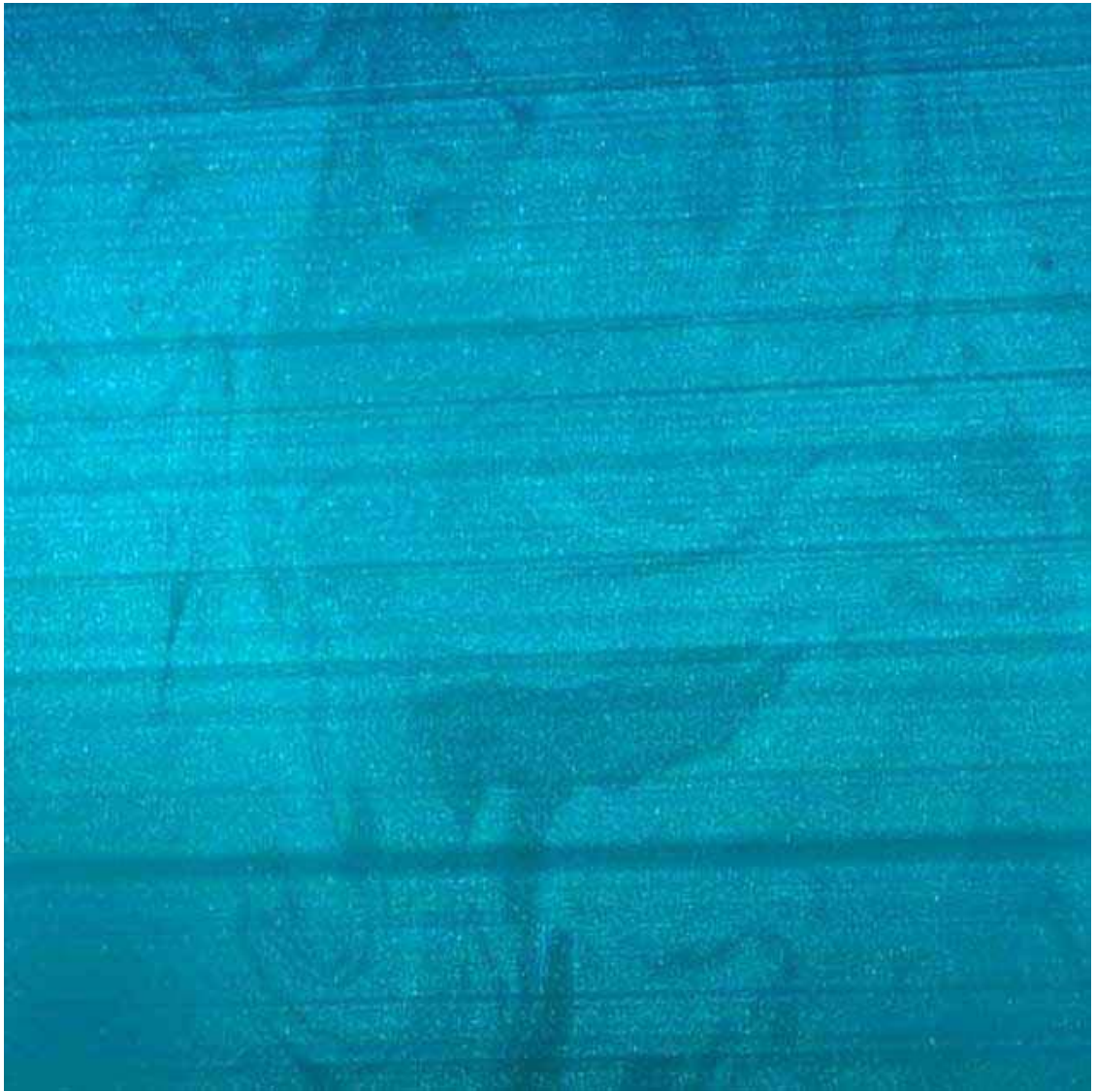


Figure 3.6: A $1\text{ cm} \times 1\text{ cm}$ photograph of a “mist” of hydrogen tracer particles in He I immediately after injection. Since this photograph is taken within only a few seconds after the injection, mixing gradients are still evident. Horizontal stripes are produced by bubbles of boiling helium at the windows that distort the laser sheet. The boiling ceases for all temperatures below T_λ .

H₂ and 98% ⁴He, which we found produced the optimal mean particle size for our purposes. It is important to note that owing to van der Waal's interactions the hydrogen particles irreversibly aggregate over time, shifting the mean particle size to larger values. Since the solid hydrogen is slightly buoyant ($\rho_{H_2} = 0.088 \text{ g/cm}^3$) as compared to the fluid density of ($\sim 0.145 \text{ g/cm}^3$), large particles will float to the free surface of the liquid. It is possible to match the particle density to the density of the liquid by introducing deuterium into the room temperature mixture as well. However, large, neutrally-buoyant particles would not be appropriate for studying the flow and they would not float to the free surface. As such, we prefer to accept the density mismatch so that it is possible to easily remove large, disruptive particles from the field of view.

The valves that are used to allow the ⁴He–H₂ mixture to enter the cryostat are shown in Fig. 3.1. The two needle valves are manually adjusted before any injection to toggle the flow rate through the injection tube, which is a 0.125 inch copper tube outside of the cryostat coupled to a thin-walled 0.25 inch stainless steel tube inside the cryostat that ends immediately above the windows used for visualization (Fig. 3.7). For all of the experiments discussed here, the first needle valve is opened only two “clicks” while the second is left fully open. The pressure on the vessel containing the mixture is always set to 20 psi. The solenoid valve that allows the gas to enter the injection line is computer controlled. Using a digital output on a computer-controlled National Instruments data acquisition control board (DAQ), the solenoid valve is opened by applying 5 V to a control circuit. The solenoid valve can be opened for times as short as tens of milliseconds or left open indefinitely.

Typical injections using the various experimental parameters given above last for 0.5–3 seconds.

It is important to note that this injection technique only produces satisfactory results when the liquid helium is in the He I state. Injections that take place in the He II state produce much larger particles that cannot be used as fluid tracers. Thus, the standard protocol is to inject at a temperature slightly above T_λ , slowly cool the system ($\sim 400 \mu\text{K/s}$) to the set temperature then acquire the desired data. The slow cooling process minimizes particle aggregation and fluid disturbances, but in doing so a portion of the hydrogen leaves the observation volume resulting in typical hydrogen volume fractions of $\sim 10^{-7}$.

3.2 Temperature Measurement and Control

Accurately measuring the temperature and also having the ability to control it are essential to these experiments since many properties of He II change with temperature. In order to compare experimental measurements with any theory or computations of He II the temperature must be precisely known. Prior to the work presented here, temperature control was performed by manually opening and closing a valve and the temperature was sporadically recorded by hand. In an effort to improve upon these methods, we interface temperature measurements and control with a computer. This allows for better knowledge of the temperature, more precise control and the ability to synchronize the temperature measurements with other attributes of the experiment.

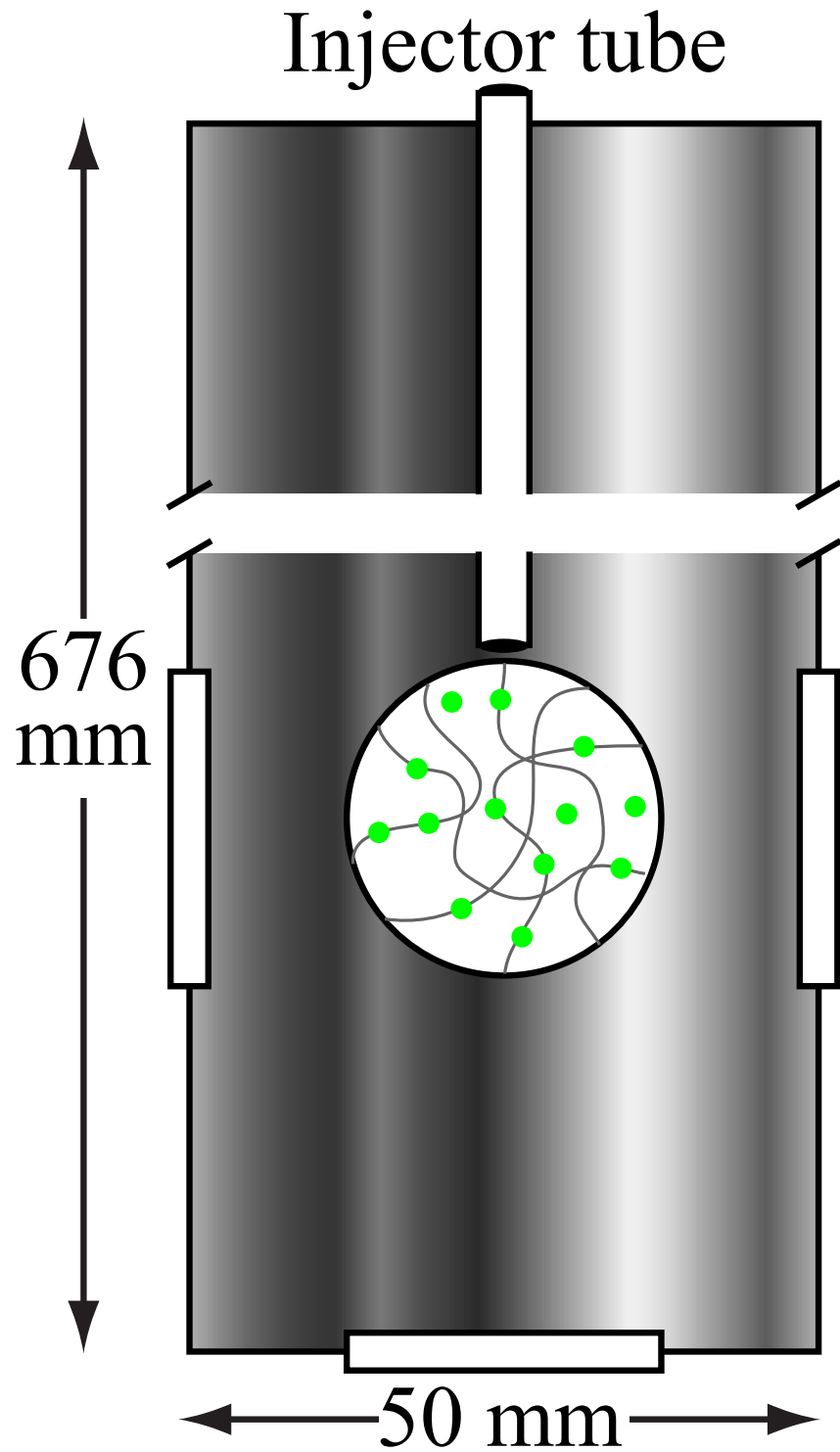


Figure 3.7: Schematic diagram of the injection tube inside of the test section of the cryostat. The tube is made of stainless steel with an outer diameter of 0.25 inches and inner diameter of 0.22 inches. The tube ends in the bulk of the fluid only 1 cm above the field of view.

3.2.1 Temperature Measurement

Two separate temperature measurements are implemented in the experiments presented here. The first is a temperature probe that is mounted flush with the inside wall of the test section of the cryostat. The temperature is determined using an Oxford ITC temperature controller that can be interfaced with a computer using GPIB for data acquisition purposes. The details of this temperature method are proprietary and therefore will not be presented here.

The second temperature probe is a calibrated thermistor that is immersed in the fluid only ~ 1 cm above the field of view. The resistance of the probe changes with temperature, particularly strongly in the temperature range of interest as shown in Fig. 3.8. The values of the calibration curve are given in section B.2. The temperature of the fluid, then, is determined by measuring the resistance of thermistor.

The technique used to measure the resistance of the thermistor is diagrammed in Fig. 3.9. The essential component to the measurement is the Stanford Research Systems SR830 DSP Lock-In Amplifier. The important settings for the lock-in amplifier are given in Table 3.1. The amplitude of 0.150 V is chosen in combination with the 450 k Ω resistor that is in series with the thermistor in order to limit the current through the thermistor to 0.33 μ A. The manufacturers of the thermistor suggest that such a low current be used in order to limit the Ohmic heating of the thermistor itself. If excessive current is used then the probe will heat up and the calibration will cease to be valid. Furthermore, limiting the heat input into the

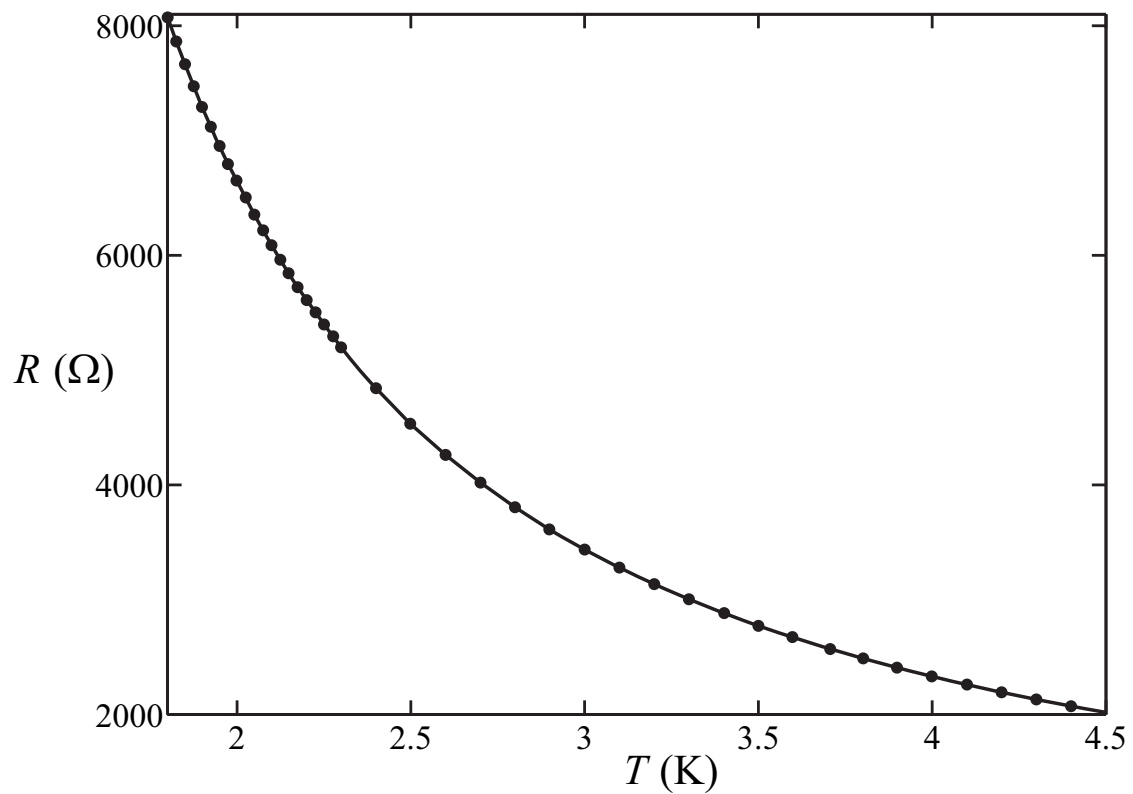


Figure 3.8: Calibration curve for the thermistor used for the temperature measurements. The data points are given in Table B.4.

Table 3.1: Parameters of the SR830 lock-in amplifier used to measure the resistance of the temperature probe.

Parameter	Value
Amplitude	0.150 V
Frequency	997 Hz
Phase	0 degrees
Harmonic	1
Source	Internal
Time Constant	1 second
Sensitivity	1–5 mV
Signal Input	A
Channel 1 Display	<i>X</i>
Channel 1 Output	<i>X</i>

He II itself is desirable so as to minimize spurious counterflows. The frequency of the AC driving signal for the circuit is chosen to be near 1 kHz in order to ensure sufficient signal averaging over the duration of the time constant chosen (1 s), but we avoid much higher frequencies where parasitic capacitances become significant. The sensitivity is chosen to be the lowest value possible without producing an overload, which occurs when the signal voltage at Input A is larger than the chosen sensitivity. The display and output of Channel 1 is chosen to be *X*, which is the in-phase component of the signal. We do not use $R = (X^2 + Y^2)^{1/2}$ because *Y* is the signal orthogonal to *X*, which is produced by capacitance rather than resistance. The appropriate GPIB settings must also be chosen to be in accord with those of the computer to ensure proper communication.

The circuit shown in Fig. 3.9 is a simple voltage divider. We are interested in determining the resistance of the thermistor *R*, which may then be used in conjunction with the calibration to yield the temperature. Assuming that the resistance of

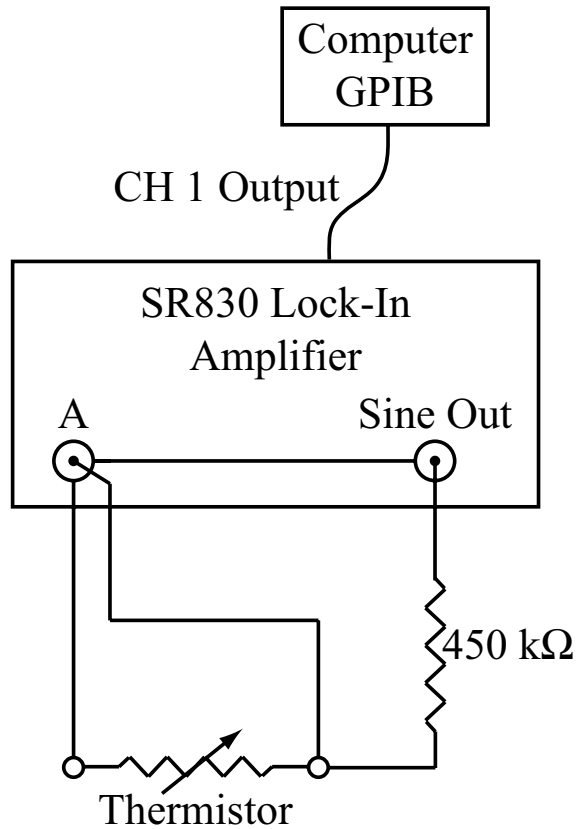


Figure 3.9: Schematic diagram of the resistance measurement of the temperature probe. The “Sine out” of the SR830 lock-in amplifier drives an alternating current through a pair of resistors — a 450 kΩ resistor outside of the cryostat used to restrict the current and the temperature-dependent thermistor immersed in the liquid helium used as the temperature probe. The voltage drop across the thermistor is measured by “Input A” on the lock-in amplifier and recorded by a computer through a GPIB interface.

the 450 k Ω resistor remains unchanged (appropriate wire-wound resistors with small temperature coefficients should be chosen), then the current through the circuit is given by

$$I = \frac{\Delta V}{450000 + R} = \frac{0.150}{450000 + R}. \quad (3.2)$$

The measurement of X by the lock-in amplifier provides the voltage drop across the thermistor given by

$$X = IR = \frac{0.150R}{450000 + R}. \quad (3.3)$$

Solving this equation for R we arrive at

$$R = \frac{450000X}{0.150 - X}. \quad (3.4)$$

In general, if a resistance R_1 and driving voltage V are used instead of the suggested values of 450 k Ω and 0.150 V then R is given by

$$R = \frac{R_1 X}{V - X}. \quad (3.5)$$

Upon measuring R it is straightforward to determine the temperature T of the thermistor by interpolation using the calibration. The MatLab codes that are used to perform this interpolation are given in Section A.1.

3.2.2 Temperature Control

Temperature control requires knowledge of the temperature and the ability to input and remove heat from the system. The means by which the temperature is measured are outlined in the previous subsection. Since the fluid is held at temperatures ~ 2 K and is thermal contact with a ~ 300 K environment, albeit

with very small thermal conductivities by design, there is always a source of heat. We therefore control the temperature by controlling the amount of cooling applied to the system. Temperature control could be improved by also having a tunable heat source present in the liquid.

The temperature of the working fluid is decreased by evaporative cooling. The saturated vapor pressure of He II is approximately 5000 Pa at T_λ and 750 Pa at 1.6 K, which is the minimum temperature achievable by the cryostat. The gaseous spaces above the free surfaces of the liquid in both the test section and the reservoir are connected to a roughing pump through a series of valves shown in Fig. 3.1. The roughing pump can achieve pressures as low as 0.5 Pa. By opening the valves between the gaseous spaces above the liquid and the roughing pump the ambient pressure is reduced to a level below the vapor pressure of the liquid, thereby producing evaporative cooling.

Since the vapor pressure of liquid ^4He decreases from atmospheric pressure ($\sim 10^5$ Pa) at 4.2 K to 750 Pa at 1.6 K, the maximum rate of cooling also decreases dramatically with temperature. This presents more of a problem at higher temperatures because the efficiency of the cooling depends upon the flow rate of gaseous helium through the pumping lines. As the flow rate increases the interaction between the gaseous helium and the 300 K walls of the pumping lines increases, which removes heat from the room and transfers it to the helium, reducing the cooling efficiency. This phenomenon is clearly evidenced by the condensation or freezing of water out of the air onto the exterior of the pumping lines. It is therefore suggested that cooling rates of ~ 3 mK/s should not be exceeded.

The cooling rate is toggled by the pressure drop across the pneumatic valve (Metra Inc. AAV-KF40) shown in Fig. 3.1. This valve is controlled by an applied pressure. For pressures below ~ 20 psi the valve will completely close while it will fully open for pressures in excess of ~ 60 psi. Therefore, applying a pressure P between 20 and 60 psi allows for modulation of the flow rate through the valve. The pressure applied to the pneumatic valve is controlled by a commercial current-to-pressure transducer. The transducer applies zero pressure for current values below 4 mA and maximum pressure for 20 mA. The zero and maximum values of pressure of the transducer have been tuned such that 4 mA corresponds to 20 psi, which closes the valve, and 20 mA yields 60 psi, which will completely open the valve. Using these settings provides the maximum dynamic range of the pneumatic valve.

Current is applied to the transducer using a computer-controlled analog output from a National Instruments data acquisition control board (DAQ). The DAQ is capable of producing voltages between 0 and 5 V, which then passes through a $250\ \Omega$ resistor. Voltages below 1 V produce currents less than 4 mA, thereby completely closing the valve. The maximum voltage of 5 V gives the maximum current accepted by the transducer of 20 mA. A standard proportional-integral-derivative (PID) control algorithm is used to control the temperature. The temperature typically oscillates about a given set temperature with an amplitude of ~ 10 mK as evidenced in the example temperature trace shown in Fig. 3.10.

The roughing pump is connected to both the helium reservoir and the test section as shown in Fig. 3.1. The reservoir and test section have independent needle valves that can be opened and closed manually to set which space is cooled while

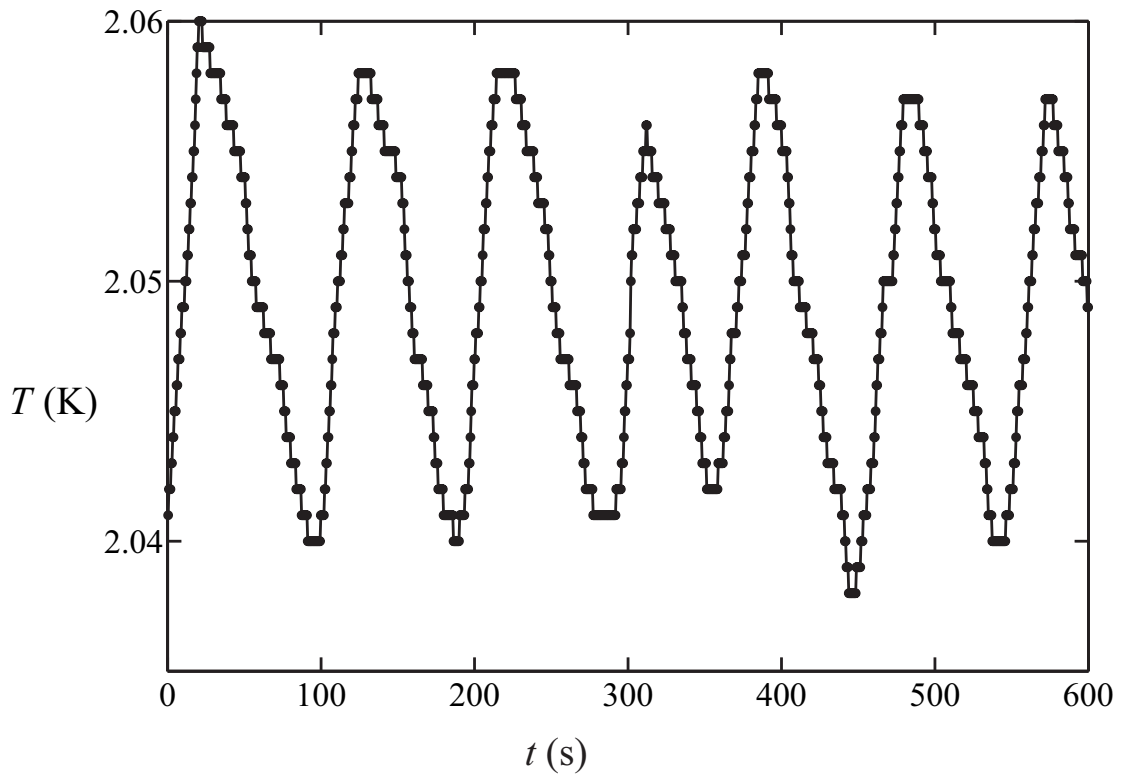


Figure 3.10: Plot of an example temperature trace showing typical oscillations about the set point ($T = 2.05$ K in this case). The temperature oscillates ± 10 mK because of the thermal inertia of the system and the particular control mechanism. Improved temperature control could be obtained by maintaining a constant pumping rate and modulating an internal heater, rather than only modulating the pumping rate.

also providing additional means of controlling the cooling rate. During the course of typical experiments, the reservoir and test section are held at the same temperature for a few important reasons. First, if only the test section is pumped then it is very difficult to control the temperature slew rate owing to the smaller volume of liquid compared to the reservoir. Furthermore, the helium in the test section becomes depleted over time and must be replenished by allowing liquid to be transferred from the reservoir to the test section. The test section is filled to the maximum attainable level, monitored by a level probe inside the test section, before each experimental run for purposes of repeatability. If the helium in the reservoir used to refill the test section is at a very different temperature than the test section, large temperature gradients form in the He I state, driving strong, disruptive convection. Therefore, we have found by experience that keeping the temperature in the reservoir, measured using the same technique as the test section and explained above, as close to the test section as possible yields optimal experimental conditions.

3.3 Visualization

The distinguishing characteristic of the experiments presented here is the ability to visualize both the motions of the normal fluid and the dynamics of the quantized vortices in He II [2–6]. The essential components of these experiments are the tracer particles discussed in Subsection 3.1.3 and the visualization technique composed of optics, cameras and a particle-tracking algorithm. The basic configuration of the optics and camera are shown in Fig. 3.1 and we give the details of the

visualization technique in the following subsections.

3.3.1 Optics

A commonly used means of visualizing fluid flows is to focus a camera on a thin laser sheet that passes through a region of interest within the flow. The optics used to form the laser sheet are shown schematically in Fig. 3.11. Two different lasers are used in these experiments; the results presented in Chapter 5 are obtained with a 3 mW green laser pointer and the results in Chapters 6 and 7 use an argon ion laser that is capable of 6 W of total power. In both cases the initial laser beam that is approximately 2 mm in diameter is expanded in the z -direction using a cylindrical, diverging lens. Once the beam has been sufficiently expanded to the desired height (~ 10 mm) it passes through a converging, convex lens that serves two purposes: (i) to collimate the beam in the z -direction and thereby prevent further expansion and (ii) focus the beam in the y -direction such that the desired sheet thickness is attained in the field of view. If the sheet is thicker than the depth of field of the camera optics, then some particles will be blurry and out of focus. A thinner sheet provides a higher intensity, thus making each illuminated particle brighter and more distinguishable from the background but results in a smaller illuminated volume of fluid. Therefore, a balance must be struck between obtaining the necessary intensity to visualize the particles as dictated by the camera sensitivity while also illuminating a large enough fluid volume to perform the experiments of interest.

Taking the assumptions associated with Gaussian optics, the waist of the laser

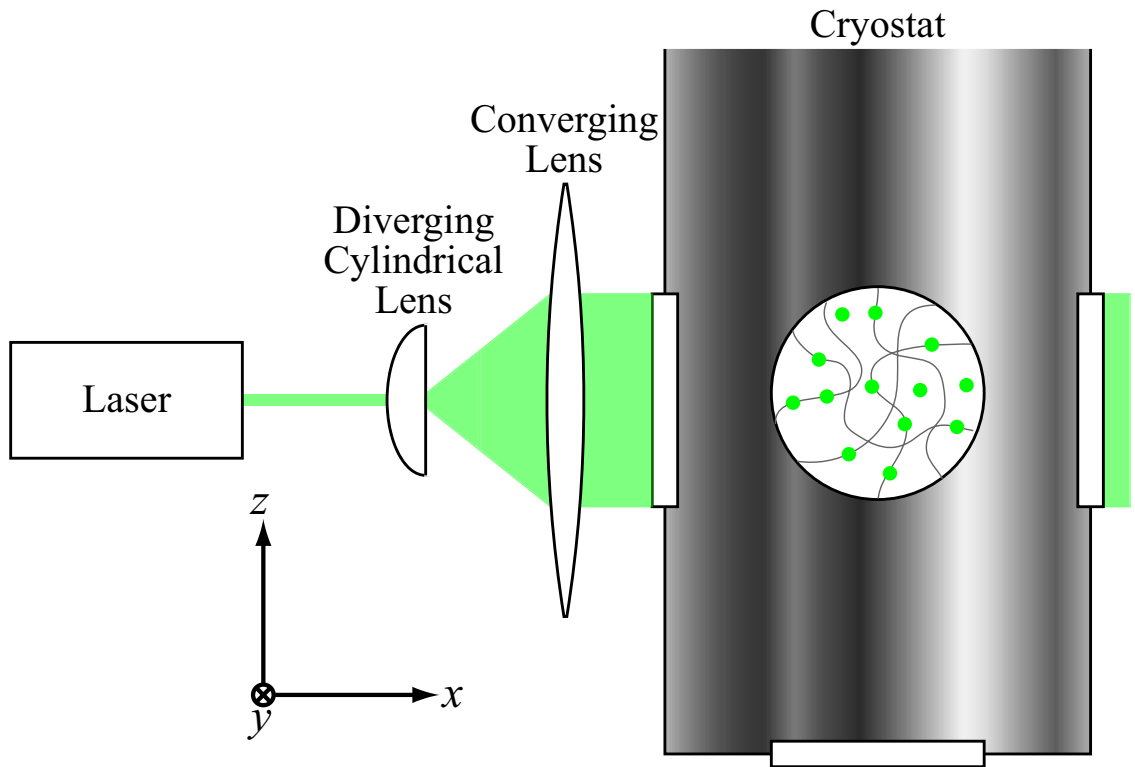


Figure 3.11: Schematic diagram of the visualization technique. A laser beam that propagates in the x -direction is first expanded in the z -direction by a diverging, cylindrical lens and then collimated in the z -direction and contracted in the y -direction by a convex, converging lens. The laser sheet passes through the center of two of the cryostat windows and 90° scattered light is observed by a camera aligned with a third window. The remaining two windows (one diametrically opposed to the camera-viewing window and the bottom window) are optically blocked to prevent stray light.

sheet is given by

$$d_0 = \frac{2\lambda l_f}{\pi r}, \quad (3.6)$$

where λ is the wavelength of light, l_f is the focal length of the converging lens and r is the initial laser beam radius. The minimum beam waist for all of the experiments presented here is between 100 – 400 μm . The resulting laser sheet propagates in the x -direction, is nearly uniform over its ~ 10 mm height in the z -direction and is thinnest in the y -direction at the center of the field of view. A camera is then used to detect 90° scattered light through one of the windows shown in Fig. 3.11.

3.3.2 Cameras

Two separate cameras are used in the experiments presented here. A Princeton Instruments PI-MAX is used for the counterflow studies presented in Chapter 5 while a Vision Research Phantom camera is used for the reconnection and turbulence studies discussed in Chapters 6 and 7. In all cases, a 105 mm Nikon macro lens is used with unity magnification. The cameras differ greatly in their sensitivity and intended use. For the intents and purposes of the experiments presented here, the Princeton Instruments camera is better suited in most respects, however it has only recently become available to us. The details of the two cameras are compared in Table 3.2.

The Princeton Instruments PI-Max camera has a 512×512 pixel cooled, amplified CCD sensor used for imaging. The intensified CCD (iCCD) provides excellent sensitivity and a very large dynamic range (16-bit). This increase in sensitivity al-

Table 3.2: Comparison between the specifications of the two cameras used in the experiments.

	PI-Max	Phantom
Sensor Type	iCCD	CMOS
Dynamic Range	16-bit	12-bit
Exposure Time	~ 1 ms	10–16 ms
Laser Power Used	3 mW	2–6 W
Pixel Size	$24 \mu\text{m}$	$16 \mu\text{m}$
Image Size	512×128	512×512
Field of View	12.3×3.1 mm	8.2×8.2 mm
Frame Rate	50 fps	60–100 fps

lows us to use the 3 mW laser pointer for illumination. In doing so, we greatly reduce the amount of heat absorbed by the windows, which drive spurious counterflows in the system, as compared with the 2–6 W necessary with the Phantom camera. The typical exposure time is chosen to be ~ 1 ms. The effective pixel size is $24 \mu\text{m} \times 24 \mu\text{m}$, which, along with the unity magnification of the lens, results in image pixels also corresponding to a spatial extent of $24 \mu\text{m} \times 24 \mu\text{m}$. In order to achieve the desired frame rate of 50 fps for the counterflow studies discussed in Chapter 5, only a subregion of 512×128 pixels are imaged. This results in a field of view that is 12.29 mm wide (x -direction) and 3.07 mm tall (z -direction).

The Phantom camera has a 1024×1024 pixel CMOS sensor. The camera also has 4 GB of onboard memory that allow it to store 4,000 megapixel images, or over 16,000 512×512 pixel subimages. The CMOS sensor is far less sensitive (12-bit) than the iCCD of the PI-Max camera, however it is much faster and able to acquire full images at 1,000 fps. The movies used for the data presented in Chapters 6 and 7 are acquired at either 60, 80 or 100 fps with corresponding exposure times

of 16, 12.5 and 10 ms. The decrease in sensitivity requires the use of 2–6 W of laser light in order to distinguish the micron-sized particles from the background. Movies at higher frames rates are desirable, however to do so the exposure time of the camera must be decreased to levels that would make it difficult to identify tracer particles. The pixels are $16 \mu\text{m} \times 16 \mu\text{m}$, which produce the same spatial extent in the acquired images. Only 512×512 subimages are acquired resulting in a field of view that is 8.19 mm wide and tall in the x - and z -directions, respectively.

3.4 Particle-Image Velocimetry vs. Particle-Tracking

Particle-image velocimetry and particle-tracking are two commonly used methods of determining fluid velocities from images of tracer particles. Depending upon the parameters and goals of the experiments, one technique is likely more advantageous than the other. In the following subsections we compare and contrast these two methods and give arguments for our choice to use particle-tracking in our experiments.

3.4.1 Particle Image Velocimetry

Particle image velocimetry (PIV) [94, 95] is a technique used in many turbulence experiments to determine the velocity field from images of tracer particles. Typically, two successive images are taken closely spaced in time Δt and the displacement of the particles $\Delta \mathbf{x}$ is computed to determine the velocity $\mathbf{v} = \Delta \mathbf{x} / \Delta t$. It is assumed that the flow is characterized by a single smoothly-varying velocity field

and that the velocities are approximately constant over the time between images.

To obtain more robust results, the displacements of groups of neighboring particles are used to determine the velocity. Specifically, pairs of images I_1 and I_2 are each divided into subimages and a single velocity vector is computed for each subimage. For example, an initial image I_1 containing 512×512 pixels may be divided into subimages I_1^{ij} of 16×16 pixels, where i, j are integers denoting the particular subimage. The mean displacement of the particles within each subimage is determined by computing the cross-correlation $C_{ij}(\Delta x, \Delta z)$ between two subimages I_1^{ij} and I_2^{ij} separated in time by Δt as follows

$$C_{ij}(\Delta x, \Delta z) = \int \int I_1^{ij}(x + \Delta x, z + \Delta z) I_2^{ij}(x, z) dx dz. \quad (3.7)$$

The peak of the cross-correlation, $C_{ij}(\Delta x_{\text{peak}}, \Delta z_{\text{peak}})$, is determined and the two-dimensional velocity for that subimage is

$$\mathbf{v}_{ij} = \frac{\Delta x_{\text{peak}}}{\Delta t} \hat{x} + \frac{\Delta z_{\text{peak}}}{\Delta t} \hat{z}. \quad (3.8)$$

The velocity is determined for all values of i and j , resulting in a two-dimensional velocity field for the entire field of view.

There are, however, several limitations of the PIV technique. The greatest limitation for the purposes of our study is the assumption that there is a single smoothly-varying velocity field. This assumption breaks down in quantum fluids owing to their two fluid nature. As discussed in detail in Chapter 4, tracer particles in He II can interact with both the normal fluid and superfluid components. Two attempts at using PIV for the purposes of studying counterflowing motions in He II are shown in Fig. 3.12. In the first example, Fig. 3.12(a), two distinguishable peaks

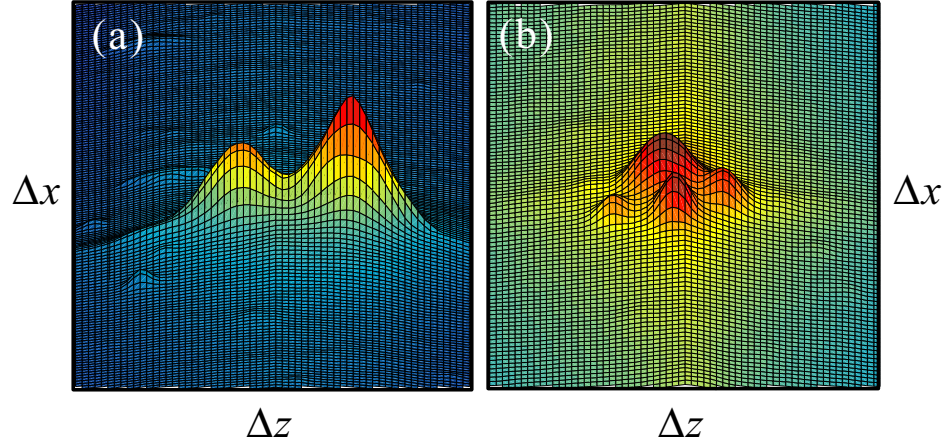


Figure 3.12: Two examples of the cross-correlation plane used in PIV measurements of our counterflow data. The value of the cross-correlation is given by color as well as the height of the surface. Two peaks are evident in (a), which may be interpreted as corresponding to the normal fluid and superfluid component motions. However, this interpretation breaks down in (b) where four peaks are clearly evident.

are evident. One could determine each peak separately and attribute one velocity to the normal fluid component and the other to the superfluid component. However, this method fails in Fig. 3.12(b) where more than two peaks are evident.

3.4.2 Particle Tracking

Particle tracking algorithms are commonly used to study Lagrangian statistics in fluid flows. Rather than computing the velocity in a particular region of the flow from a group of particles, the full trajectory of (ideally) every particle is determined. Therefore, one need not assume that there is a single smoothly-varying velocity field driving the motions of the particles. Since the particles can respond to both the normal fluid and superfluid components in He II, as discussed in detail in Chapter 4,

particle tracking is more suitable for our investigations.

In order to track the motion of individual particles several factors are quite important. Firstly, images of the tracer particles must be distinguishable from the background. The contrast between particles and the background can be improved by lengthening the exposure time, increasing the illumination intensity and selecting appropriate cameras and optics. The particles should also appear circular in the images — that is, the image intensity is highest for a pixel closest to the particle center and the neighboring particles appear successively dimmer as the distance from the center increases. If the particles move on the order of a pixel or more over the duration of the exposure time then they will appear to be rod-like rather than circular. Determining the position of a rod-like particle image is much less precise than a properly resolved circular image. Lastly, particle displacements between successive images should be less than the typical particle spacing. Obviously if only a single particle is to be tracked then this constraint does not apply. However, on the order of 10^4 particles per frame are typically tracked and therefore it is imperative to have a sufficiently high frame rate that the particles typically move less than 1 pixel per frame. Thus, a balance between the exposure time, frame rate, typical fluid velocities, and particle volume fraction must be struck in order to use this technique.

Particle tracking, to the author's knowledge, has never been used in flows of He II before. As such, a particle tracking algorithm developed by Eric Weeks and John Crocker was adapted to suit the present purposes. A detailed tutorial of the IDL algorithms that we use can be found in Ref. [96]. An example of the

```

epretrack, 'p6_1090_1720.tif', bplo=0.5, bphi=6, dia=8, mass=20, /multi
pt=read_gdf('pt.p6_1090_1720.tif')
plot_hist, pt(0,*) mod 1
t=track(pt, 5, goodenough=10, memory=0)
out=[t(6,*), t(5,*), t(0,*), t(1,*), t(3,*)]
write_gdf, out, 'p6_m20_r5_f1090.gdf'

```

Figure 3.13: An example batch of commands used to particle track a movie using the IDL particle-tracking algorithm.

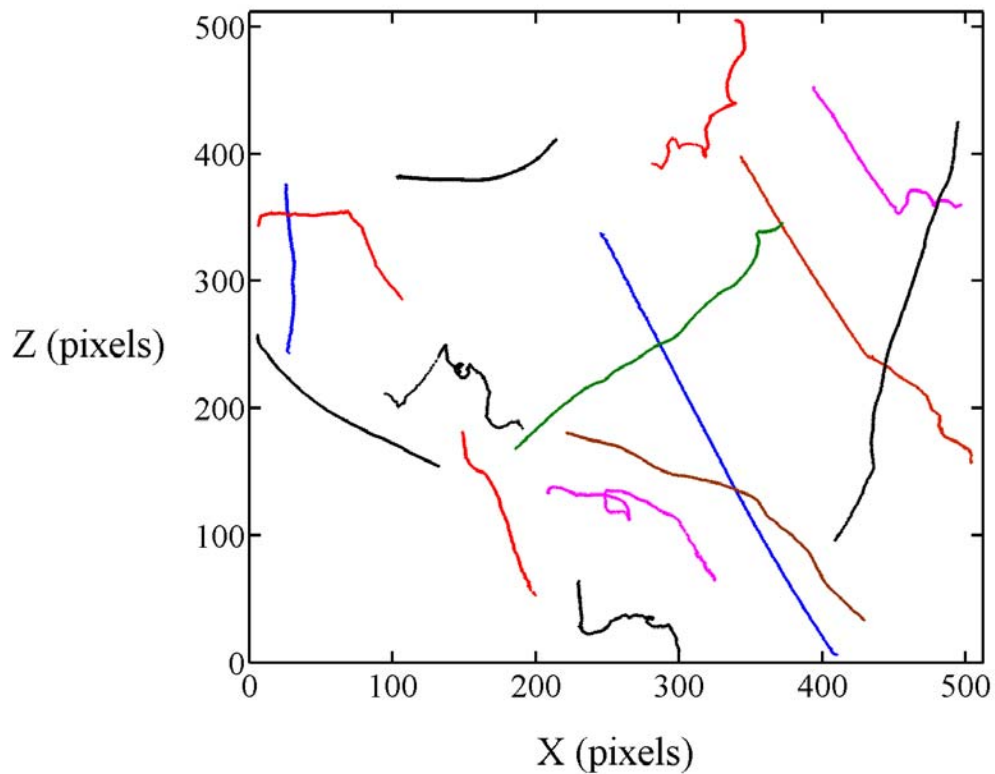


Figure 3.14: Example trajectories obtained by the particle-tracking algorithm. Each curve corresponds to a single particle trajectory.

series of commands in IDL used to track a particular movie is shown in Fig. 3.13. The output of this series of commands is a file with the first column denoting the particle identification number, the second is the frame number, the third is the x -position in pixels, the fourth is the z -position in pixels and the last is the radius of gyration, which may be used to distinguish tracer particle size for statistical purposes. Examples of typical particle trajectories are shown in Fig. 3.14. All of the algorithms implemented to then analyze the trajectories have been developed by the author and some are given in Appendix A.

Chapter 4

Tracer Particles in Superfluid ^4He

The greatest distinction of our experiments is the ability to directly observe the motions of both the normal fluid component and the quantized vortices in He II. Previous experiments by Yarmchuk, Gordon and Packard [33] have observed where the vortices end on a boundary as shown in Fig. 1.3(a). More recent experiments led by van Sciver [97–101] have examined particles interacting with the normal fluid component using PIV. The former studies could not observe the dynamics and structure of the quantized vortices in the bulk of the fluid and the latter cannot observe the motions of quantized vortices since they use PIV.

The dynamics of tracers in superfluid flows are more complicated than in viscous fluids since the particles can interact with the quantized vortices [43] in addition to the normal fluid. The details of these interactions depend upon the temperature, particle characteristics, line-length density of quantized vortices, and flow properties. Progress has been made in trying to understand precisely what tracer particles “track” in superfluid turbulence by Barenghi and coworkers [44–48], though many issues remain unanswered. In this chapter[†] we will introduce the mechanism by which particles can be trapped by quantized vortices, discuss the dependencies of this mechanism and examine the effects tracer particles can have

[†]The details of this chapter follow closely the discussion presented by Paoletti *et al.* in [5].

on the dynamics of quantum fluids.

4.1 Particle-trapping Mechanism

The trapping of ions and particles by quantized vortices in superfluid ^4He is generally agreed to occur by a mechanism proposed by Parks and Donnelly in 1966 [43]. The superfluid motion around a locally straight vortex can be expressed in cylindrical coordinates $\{s, \phi, z\}$ as $v_\phi = \kappa/2\pi s$ where $\kappa = h/m = 9.97 \times 10^{-4} \text{ cm}^2/\text{s}$ is the quantum of circulation with h as Planck's constant and m the mass of a ^4He atom. Trapping a particle or bubble on the vortex core causes a reduction in the kinetic energy owing to the displaced circulating superfluid helium. The reduction in energy is maximized when the particle is centered on the vortex core (where the kinetic energy density is largest). As a particle approaches a vortex, a gradient in energy causes an attractive force — although some dissipative mechanism is required to prevent the particle from oscillating radially. Drag between the particle and the normal fluid likely serves to dissipate the energy as the particle approaches the vortex.

The attractive force between a tracer particle and a quantized vortex can equivalently be described by pressure gradients. The Bernoulli pressure around the vortex resulting from the superfluid motion is

$$P = -\frac{\rho_s \kappa^2}{8\pi^2 s^2}, \quad (4.1)$$

where ρ_s is the superfluid density and κ the quantum of circulation [70]. The normal force on the particle is obtained by integrating the pressure gradient on the surface

of the particle. If the particle is many particle diameters away from the vortex core the total force may be approximated as

$$\mathbf{F}_{\text{trap}} = \frac{4}{3}\pi a^3 \nabla P \sim -s^{-3} \hat{s}. \quad (4.2)$$

Thus a local pressure gradient attracts particles on to the vortex, dissipatively mediated by Stokes drag.

This trapping mechanism is different than for a viscous vortex. Since superfluid flow has zero viscosity, the particle is not dragged into orbit around the vortex. In a viscous fluid, particles orbit azimuthally producing a centrifugal force in addition to the radial pressure gradient. If a small particle is neutrally buoyant then the centrifugal force is balanced by the pressure gradient and the particle circulates the vortex at constant cylindrical radius. Particles that are less dense than the fluid would be radially drawn to the vortex core whereas denser particles would be expelled to the boundaries. In a superfluid, all particles, independent of density are drawn to the quantized vortices. We have observed that solid hydrogen (less dense than liquid helium) and solid neon (denser than liquid helium) may be trapped by the quantized vortices.

4.2 Particle-trapping Dependencies

The forces that act on a tracer particle in a fluid may be broken into two categories — those acting on the volume of the particle and normal surface forces. The only force acting on the volume of a particle in our experiments is gravity. The density of the solid hydrogen particles ($\rho_{H_2} = 0.088 \text{ g/cm}^3$) is slightly less than that

of the liquid helium ($\sim 0.145 \text{ g/cm}^3$) and the particles are therefore positively buoyant. The buoyancy force scales with the particle volume, whereas normal surface stresses scale with the surface area. Therefore, keeping all else constant, the ratio of the surface forces to buoyancy increases with decreasing particle size. Since we use constant density for all of our solid hydrogen tracer particles, smaller particles are more desirable since the effects of buoyancy are reduced relative to dynamic pressure and viscous forces.

The surface stresses acting on the particle are very important to the dynamics. Specifically, the two most important forces in our experiments are Stokes drag induced by the normal fluid flow and trapping forces produced by the quantized vortices. The interplay of these two determines whether the particles simply follow the normal fluid or get trapped or scattered by the quantized vortices.

As mentioned above, when the particle is far from the vortex the trapping force may be approximated by $\mathbf{F}_{\text{trap}} = \frac{4}{3}\pi a^3 \nabla P \sim -s^{-3} \hat{s}$, where a is the particle radius, $P = -\rho_s \kappa^2 / 8\pi^2 s^2$ the pressure, and s the cylindrical radius from the vortex core. The pressure P is a linear function of the superfluid density ρ_s , which depends nonlinearly on temperature. The superfluid density is a small fraction of the total near the λ -transition (see Fig. 2.5), thereby making the trapping force weak.

Viscous drag is essential to the particle trapping mechanism, since it provides a means of dissipation as the particle falls into the vortex core. However, Stokes drag may also serve a different role. Vortex motions that oppose the flow of the normal fluid may dislodge particles from the vortices since Stokes drag is still relevant. Therefore, at any temperature, two regimes always exist: (*i*) for sufficiently low rela-

tive velocities between the normal fluid and the quantized vortex the trapping force dominates and the particles remain trapped and (ii) for sufficiently high relative velocities, Stokes drag is able to dislodge the particles from the vortex cores. The resulting picture is that understanding the population of trapped and untrapped particles must necessarily depend on both temperature and relative flows between the normal fluid and the quantized vortices.

The competition between weak trapping forces near the λ -transition and normal fluid drag is evidenced in our experiments by the lack of trapped particles within ~ 50 mK of transition. In classical fluids, the difference in velocity between two neighboring fluid elements typically follows an exponential distribution centered on zero. The difference in the velocity of the quantized vortices \mathbf{v}_L and \mathbf{v}_n need not be exponentially distributed about zero. In fact, we typically observe large velocity differences between these two flow fields, particularly in thermal counterflows. Particles attempting to trap on such counterflowing vortices will experience a Stokes drag proportional to $|\mathbf{v}_n - \mathbf{v}_L|$. If this force exceeds the maximum value of \mathbf{F}_{trap} , which is weakest near T_λ then particles may only be scattered, rather than trapped, by the vortices.

To explore this temperature dependence we observe the particle dynamics as the system continues cooling below the λ -transition at a rate of $-152 \mu\text{K/s}$ with a 4 mW/cm^2 heat flux applied to gently drive the quantized vortices in opposition to the normal fluid motion. The relative velocity \mathbf{v}_δ between all possible pairs of particles initially separated by less than $150 \mu\text{m}$ is determined by fitting the pairwise separation $\delta_{ij}(t) \equiv |\mathbf{r}_i(t) - \mathbf{r}_j(t)|$ to the form $\delta_{ij}(t) = v_\delta t + \delta_{ij}(0)$, where $\mathbf{r}_i(t)$ is the

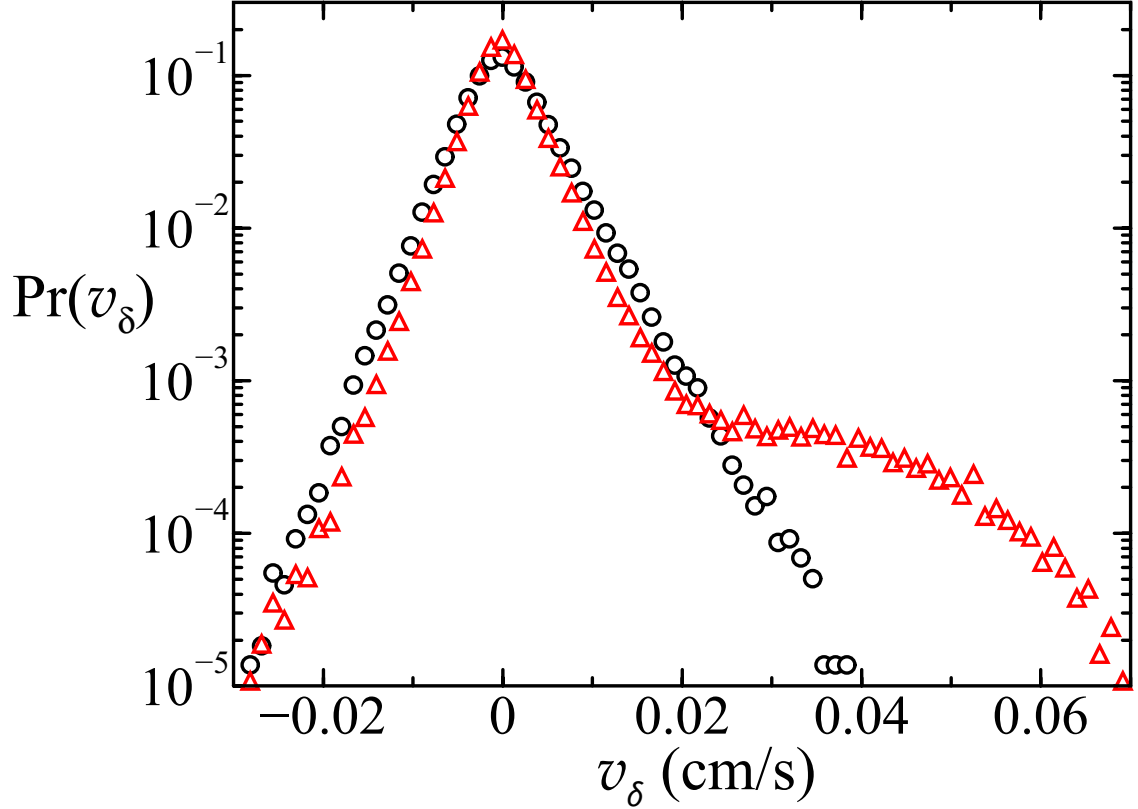


Figure 4.1: Statistics of pairwise particle separation velocities v_δ . The distributions are computed from particle trajectories while the system is cooled at a rate of $-152 \mu\text{K/s}$. A 4 mW/cm^2 heat flux is applied to drive a gentle counterflow between the normal fluid and superfluid. Each data set spans 20 seconds with temperature values $51 < T_\lambda - T < 53 \text{ mK}$ for the black circles and $55 < T_\lambda - T < 57 \text{ mK}$ for the red triangles. Only the lower temperature data (red triangles) show clear signs of counterflowing particles, evidenced by the tail for large v_δ , which signifies strong drag forces.

two-dimensional position vector of particle i at time t . The distributions of the values of v_δ are shown in Fig. 4.1. Each data set spans 20 seconds with temperature values $51 < T_\lambda - T < 53$ mK for the black circles and $55 < T_\lambda - T < 57$ mK for the red triangles. Only the lower temperature data (red triangles) show clear signs of counterflowing particles, evidenced by the tail for large v_δ , which signifies strong drag forces. We attribute this stark distinction to a crossover between Stokes-drag-dominated behavior at higher temperatures to a regime where particles are able to remain trapped on the quantized vortices.

In addition to temperature and flow properties, the competition between Stokes drag and particle trapping also depends upon particle size. Stokes drag scales linearly with the radius of the particle. The particle trapping force arises from excluded kinetic energy of circulating superfluid and therefore may be thought of as depending on the average kinetic energy density of the excluded superfluid. Since the kinetic energy density is greatest near the vortex core, the average kinetic energy density excluded by a trapped particle increases with decreasing particle size. Therefore, smaller particles, as we have observed, are more likely to become trapped by the quantized vortices. The technique of generating very small hydrogen particles is partly responsible for our ability to make the present observations. Ions and electron bubbles would be even more greatly trapped as evidenced by the historical and current work using these systems [30, 33, 43].

4.3 Effects of Particle Concentration

The hydrogen particles used in our experiments are not completely passive tracers. By trapping a particle on the core of a vortex, the vortex also becomes trapped on the particle. Thus, a particle trapped on a quantized vortex increases the coupling between the vortex and the normal fluid through the action of Stokes drag acting on the particle. Quantized vortex trapping on the hydrogen particles is analogous to the pinning of dislocations and domain walls on impurities in a solid. Realizing that the hydrogen particles may modify the stability and dynamics of the vortices we have endeavored to reduce the particle size and concentration. In the limit of very few, small particles, one might expect to obtain a minor modification to the superfluid state.

The effects of the hydrogen tracers on the helium dynamics may be studied by observing the system as one modifies the volume fraction of hydrogen. While a systematic variation of the volume fraction remains a useful future project, this section conveys our general observations on volume fraction effects over the last several years. While we give approximate volume fraction values below, the phenomenology likely depends upon the particle size distribution, the quantized vortex population (line-length density), and temperature.

The smallest volume fractions ($\phi_{\text{H}_2}/\phi_{\text{He}} < 10^{-8}$) are realized as only tens of micron-sized solid hydrogen particles in our field of view ($8 \text{ mm} \times 8 \text{ mm} \times 100 \mu\text{m}$) as shown in Fig. 4.2(a). The motions of the particles in superfluid helium, depending upon the various effects discussed above, split into two classes. Many of the

hydrogen particles smoothly drift via Stokes drag with the normal fluid. A subset of the observed particles, though, have velocities that clearly differ from this smooth, background velocity field. At times, the motions of closely spaced particles can even be antiparallel. We interpret the second observation as suggesting the trapping of particles by the quantized vortices.

At moderate volume fractions ($10^{-8} < \phi_{\text{H}_2}/\phi_{\text{He}} < 10^{-6}$) we observe multiple particles on each evident quantized vortex, e.g. Fig. 4.2(b). Unexpectedly, the particles are often uniformly spaced along the vortex core. These dotted lines appear with spacings that are both uniform on one vortex and do not substantially vary between vortices [1].

The observations of the uniform spacing imply particle-particle interactions present when they are trapped on the quantized vortices. We might hypothesize that the interaction originates from an inter-particle potential with both short-range repulsion (at least hard-core), and a long-range attraction such that the balance sets an equilibrium spacing (see Fig. 4.2(b)). The particle spacing is typically $\sim 100 \mu\text{m}$, which is much larger than the particle size. These observations imply that the effective interaction between trapped particles differs from the bare interaction present in the bulk of the fluid.

At yet higher volume fractions of hydrogen ($\phi_{\text{H}_2}/\phi_{\text{He}} > 10^{-5}$), the non-passivity of the hydrogen particles is clearly evident as seen in Fig. 4.2(c). Often, the particles come to fully cover the cores of the vortices. In cases where a continuous cylinder of solid hydrogen is present on the vortex core, branches and networks of vortices are stabilized, which should not be the case in the absence of particle loading.

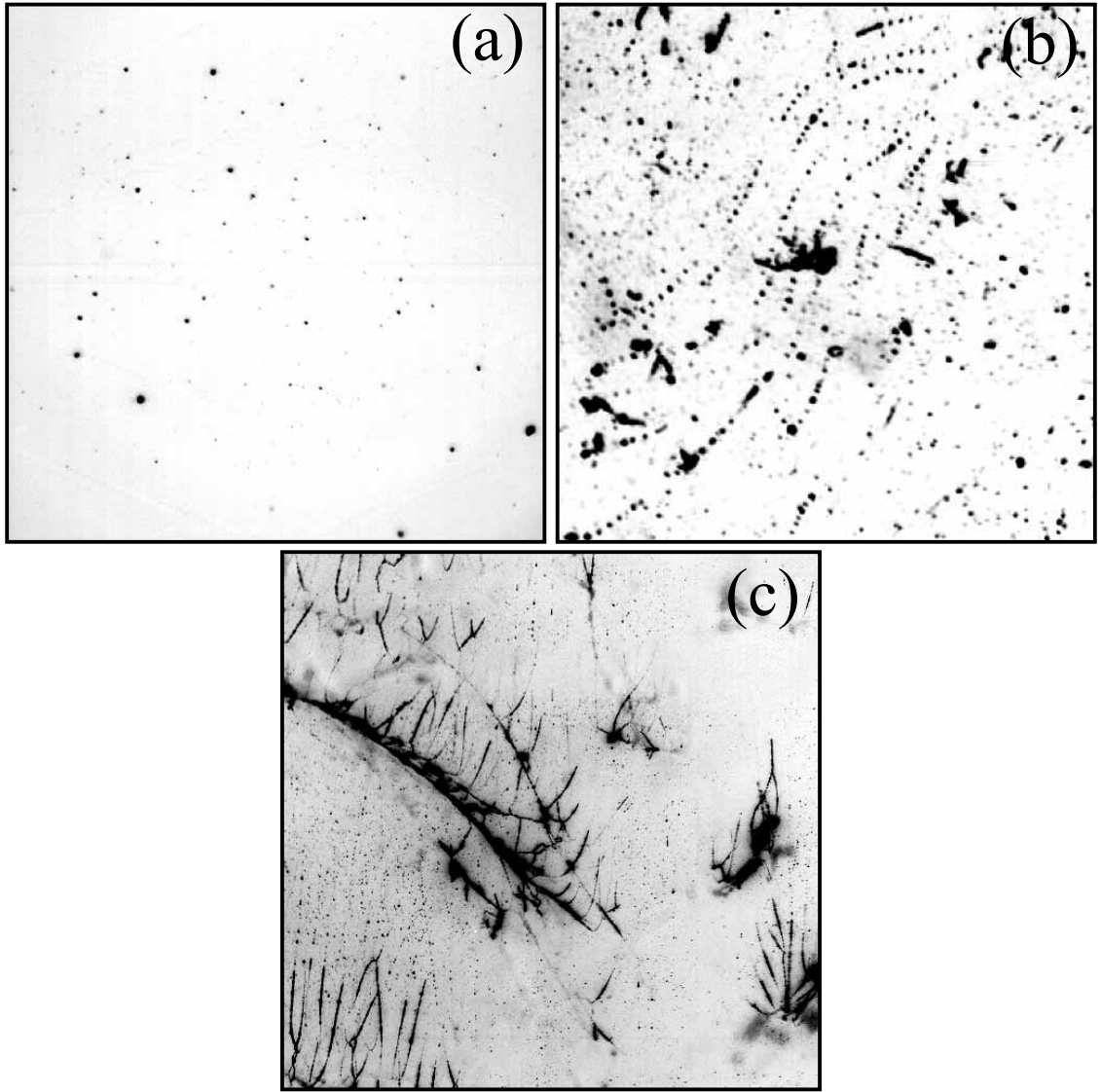


Figure 4.2: Intensity-inverted images showing varying hydrogen volume fractions. The images in (a) and (c) show the full field of view ($8 \text{ mm} \times 8 \text{ mm}$) and the image in (b) is $6.78 \text{ mm} \times 6.78 \text{ mm}$. (a) The lowest volume fraction ($\phi_{\text{H}_2}/\phi_{\text{He}} < 10^{-8}$) used in our experiments. (b) A moderate volume fraction ($10^{-8} < \phi_{\text{H}_2}/\phi_{\text{He}} < 10^{-6}$), which often results in multiple particles trapped on each visible vortex. In such cases, the trapped particles tend to be uniformly spaced along the vortex core. (c) The more extreme effects of very large hydrogen volume fractions ($\phi_{\text{H}_2}/\phi_{\text{He}} > 10^{-5}$) here in a rotating container. By completely decorating the core of a quantized vortex, the hydrogen may serve to stabilize branches and networks of vortices that should be unstable in their absence.

Chapter 5

Thermal Counterflows

The mechanism of heat transport described by the two-fluid model of Tisza [37] and Landau [38] has been a cornerstone of He II theory for more than half a century. The model predicts that a heat flux \mathbf{q} will drive flows in the normal fluid and superfluid components described by

$$\mathbf{v}_n = \frac{\mathbf{q}}{\rho S T}, \quad (5.1)$$

$$\mathbf{v}_s = -\frac{\rho_n}{\rho_s} \mathbf{v}_n. \quad (5.2)$$

Despite the long-standing acceptance of this prediction, there has yet to be a direct experimental confirmation of Eqs. (5.1, 5.2). In this chapter, we describe the results of our thermal counterflow studies that provide the first direct observation of the two-fluid nature of He II.[†]

5.1 Previous Work

Zhang and Van Sciver used solid polymer micro-spheres as tracers in counterflow turbulence [98]. The experiments were performed over the temperature range $1.62 \text{ K} < T < 2.0 \text{ K}$ for heat fluxes from 110 to 1370 mW/cm². The velocities of the particles were measured using the particle image velocimetry (PIV) technique. The most striking result from these experiments was that the velocities of the particles

[†]The details of this chapter follow closely the discussion presented by Paoletti *et al.* in [5].

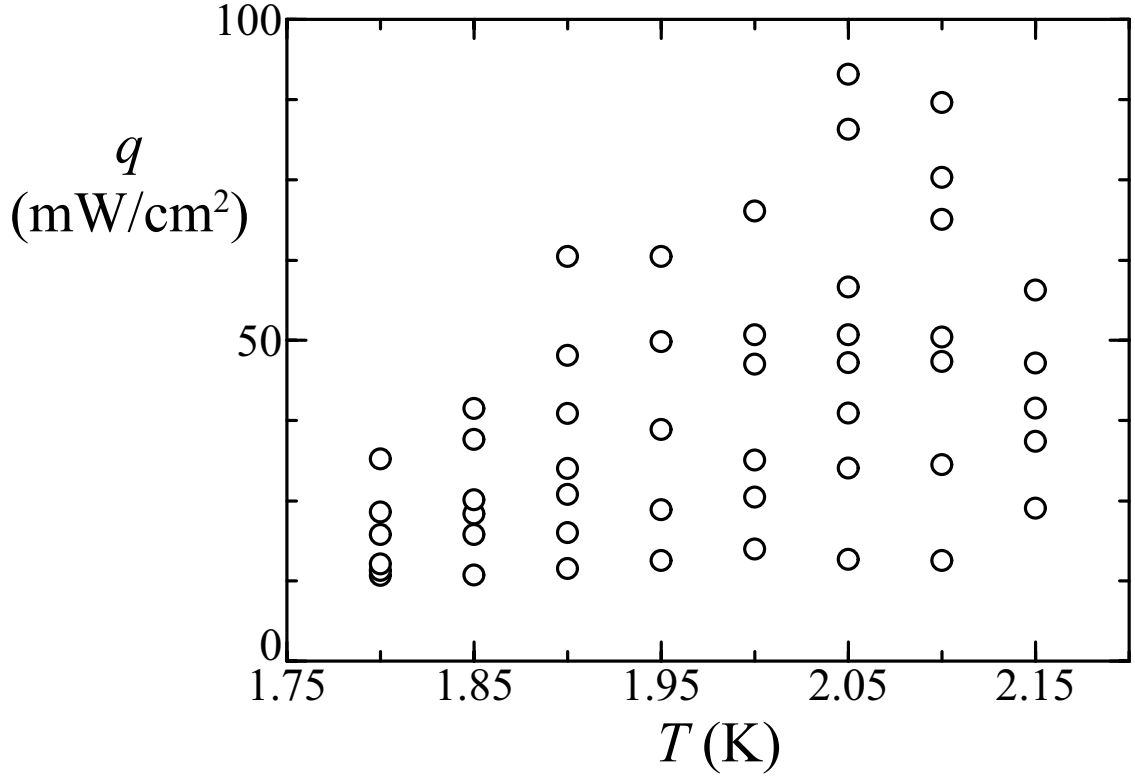


Figure 5.1: Parameter space diagram summarizing the thermal counter-flow experiments.

were approximately one half the average velocity of the normal fluid, independent of temperature. This disparity was attributed to momentum transfer between the tracer particles and the quantized vortices. Specifically, Zhang and Van Sciver proposed a form for a body force that would act on the tracer particles, which was shown to produce a temperature-independent velocity difference between \mathbf{v}_n and the observed particle velocity in agreement with their observations. The results of these experiments were discussed theoretically by Sergeev *et al* [45]. By applying theoretical arguments, they were able to obtain quantitative agreement with the experiments but at odds with Eq. (5.1).

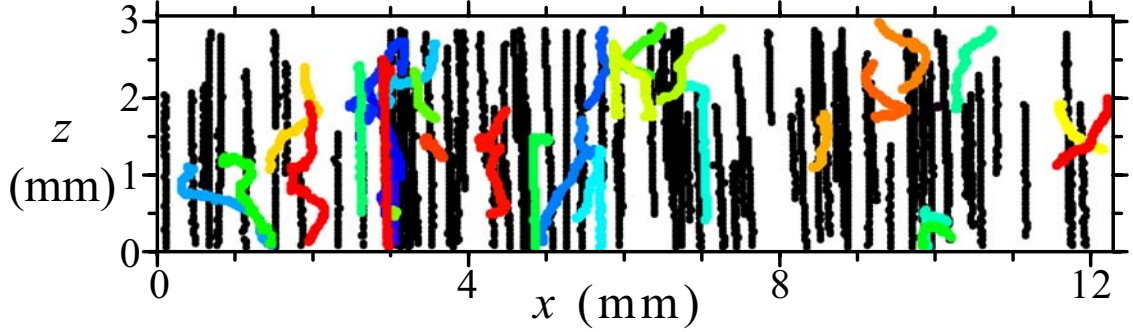


Figure 5.2: Example particle trajectories from a counterflow with $T = 1.95$ K and $q = 36$ mW/cm². Trajectories that move upward with the normal fluid ($v_z > 0$) are shown in black while tracers trapped in the vortex tangle ($v_z < 0$) move downward and are shown in color.

5.2 Particle Trajectories

The experimental parameters used in our studies are summarized in Fig. 5.1. We characterize the resulting dynamics by analyzing the particle trajectories. Several example trajectories from a typical counterflow experiment are shown in Fig. 5.2. Two distinct types of behavior are observed: *(i)* trajectories that move upward in the direction of the heat flux (\hat{z}) are denoted by black and *(ii)* trajectories that oppose this motion and move downward ($-\hat{z}$) are shown in color. The upward trajectories appear smooth and remarkably uniform, whereas the downward trajectories can be quite erratic. In the context of the two-fluid model, we interpret upward-moving particles as being dragged by the normal fluid while downward-moving particles as trapped in the vortex tangle.

5.3 Effects of Temperature and Vortex-line Density

To test these interpretations we compute distributions of the vertical and horizontal velocity components, v_z and v_x , which are shown in Figs. 5.3 and 5.4. The velocities are computed by performing a least-squares fit of the form $\mathbf{x}(t) = \mathbf{v}t + \mathbf{x}(0)$ for $0 < t < 0.1$ s. In most cases the vertical velocity distributions are bimodal, as expected. The fraction of downward-moving trajectories increases with: (i) decreasing temperature for constant heat flux and (ii) increasing heat flux at constant temperature. These trends may be attributed to: (i) the increase in vortex line-length density that occurs by increasing either $|\mathbf{v}_n - \mathbf{v}_s|$ or q and (ii) the increase in the particle trapping force with decreasing temperature. It is important to note, however, that for each temperature (heat flux) particles will cease to trap in the vortex tangle above a given heat flux (temperature) as discussed in Subsection 4.2 (e.g. black circles in Fig. 5.3(a)).

The distributions of v_x also exhibit a general trend; $\Pr(v_x)$ broadens with increasing fraction of downward-moving trajectories, as shown in Fig. 5.4(a). Such behavior is exhibited by the trajectories shown in Fig. 5.2 consisting of upward-moving trajectories that are vertical with v_x near zero for all times, whereas particles trapped in the vortex tangle move erratically in the x -direction, producing a broad distribution of horizontal velocities. This distinction is further illuminated by the distributions of the trajectory angle $\theta \equiv \arctan(v_z/v_x)$ shown in Fig. 5.4(b). In every experiment $\Pr(\theta/\pi)$ has a sharp peak near $\theta/\pi = 0.5$, which corresponds to trajectories aligned with the direction of the heat flux, and thereby aligned with

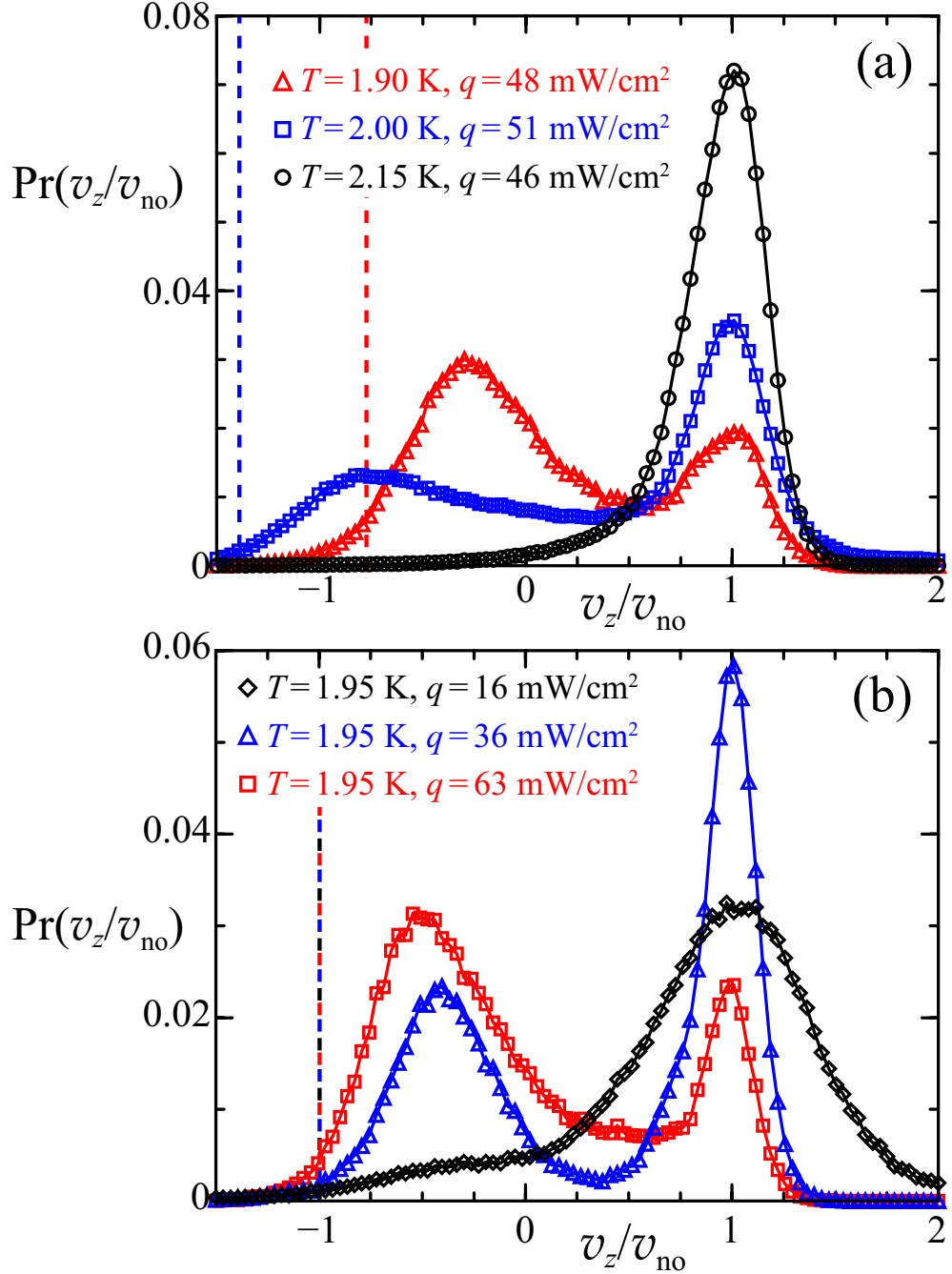


Figure 5.3: Vertical velocity statistics of example thermal counterflow experiments. All of the vertical velocity v_z distributions are scaled by the observed normal fluid velocity v_{no} as given in Fig. 5.5(a). The predicted values of the superfluid velocity v_s given by eq. (5.2) and scaled by v_{no} are shown by vertical dashed lines. (a) Variation of vertical velocity distributions with varying temperature for (approximately) constant heat flux with the experimental parameters given by the legend. (b) Variation of vertical velocity distributions with varying heat flux at constant temperature with the experimental parameters given by the legend.

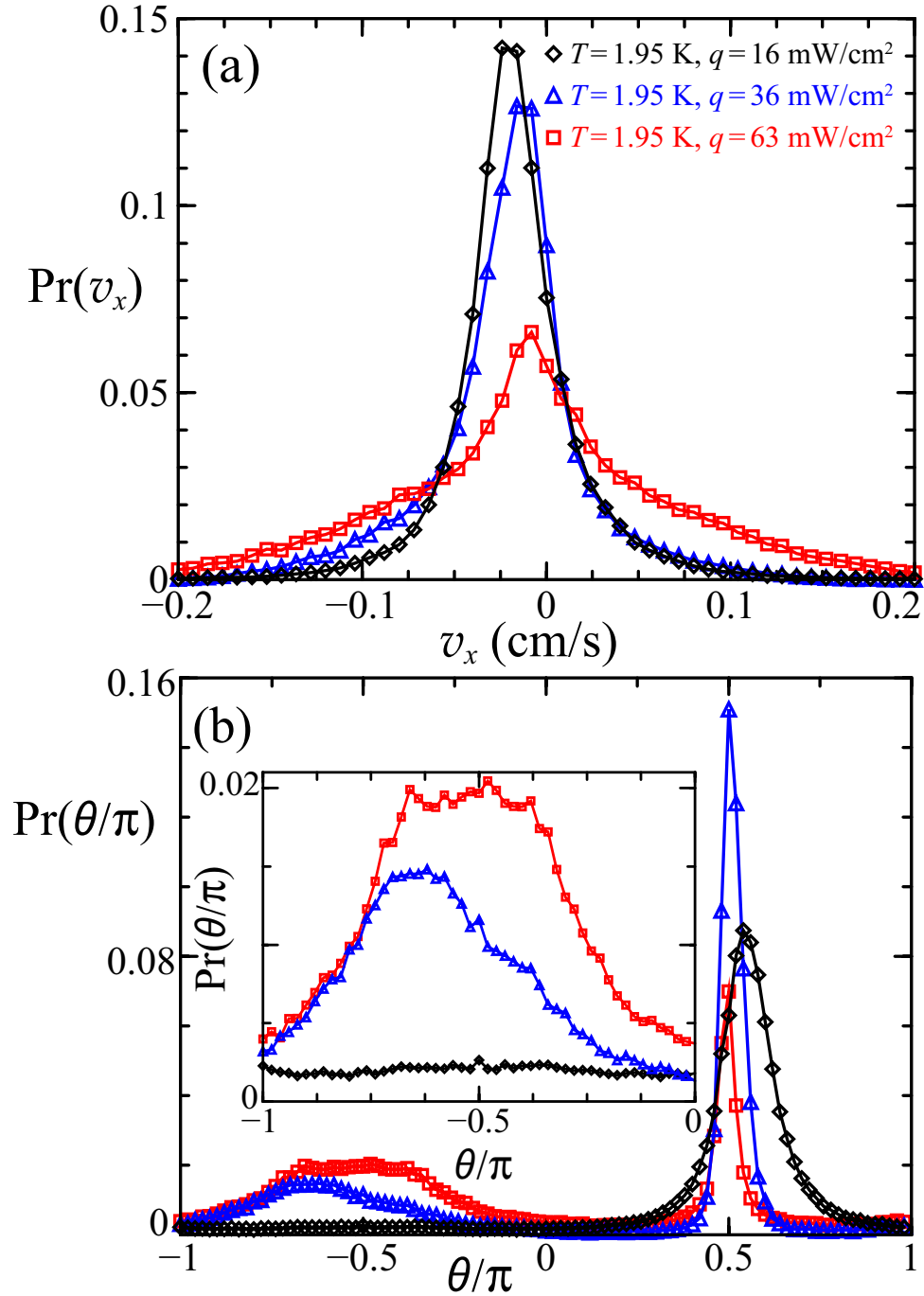


Figure 5.4: Horizontal velocity and trajectory angle statistics for example counterflow experiments with the parameters given by the legend in (a). (a) Horizontal velocity v_x distributions. (b) Distributions of the trajectory angle $\theta \equiv \arctan(v_z/v_x)$, with $\theta/\pi = 0.5$ corresponding to trajectories aligned with the direction of the heat flux (\hat{z}). The inset shows only trajectories that move downward ($v_z < 0$).

\mathbf{v}_n . In cases with a significant fraction of downward-moving trajectories, a peak also develops at $\theta/\pi = -0.5$, as shown in the inset of Fig. 5.4(b). These secondary peaks are often flat and centered at $\theta/\pi = -0.5$. We believe that these observations can be explained by mutual friction [19–21], which is one source of the horizontal velocity component for the vortex tangle. However, to do so, the geometry of the vortices needs to be specified and the subject may, therefore, be more appropriate for numerical simulations.

5.4 Measured Normal Fluid and Vortex Tangle Velocities

To compare with eq. (5.1), the observed normal fluid velocity v_{no} is computed for each experiment by fitting a Gaussian to the vertical velocity distribution function $\text{Pr}(v_z)$ for $v_z > 0$. Similarly, the \hat{z} -component of the vortex tangle velocity v_L is computed by fitting a Gaussian to $\text{Pr}(v_z)$ for $v_z < 0$. If there is no peak for $v_z < 0$, as is the case for the black circles in Fig. 5.3(a), we do not compute v_L . The observed normal fluid velocities are shown in Fig. 5.5(a). For all experimental parameters v_{no} agrees with v_n , giving a quantitative confirmation of eq. (5.1). The values of v_L , though, are systematically less negative than v_s , particularly for higher heat fluxes and temperatures, as shown in Fig. 5.5(b). This may be due to mutual friction, but we cannot comment further on the observed values of v_L .

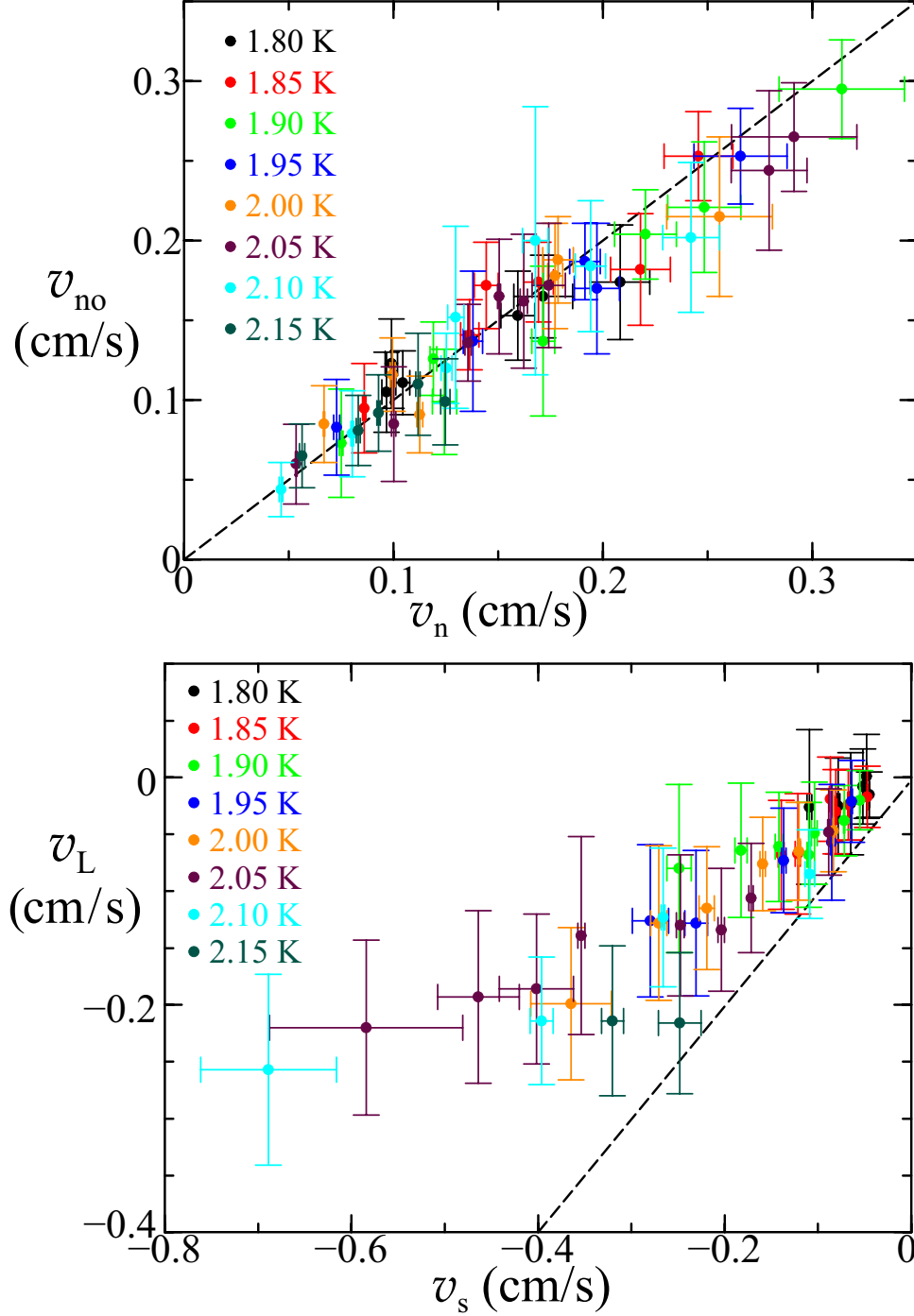


Figure 5.5: (a) Observed normal fluid velocity v_{no} as a function of the calculated normal fluid velocity v_n given by eq. (5.1). The dashed line corresponds to the prediction $v_{no} = v_n$. The horizontal error bars in both plots are due to temperature variations over the course of the run while the vertical error bars are given by the standard deviations computed by the Gaussian fits to each peak. (b) Vertical velocity of the vortex tangle v_L as a function of the calculated superfluid velocity v_s given by eq. (5.2). The dashed line corresponds to $v_L = v_s$.

5.5 Discussion

The results of these studies do not agree with the previous experiments of Zhang and van Sciver as discussed in [98]. Mostly notably, we find that tracer particles that are not trapped by quantized vortices follow closely the calculated normal fluid velocity given by eq. (5.1). Zhang and van Sciver [98], on the other hand, found that the measured particle velocity $v_{p,a}$ was approximately $0.5v_n$ for the entire range of temperatures they explored (see Fig. 1 in Ref. [98]). Several important features must be considered when comparing these studies. The velocities in Ref. [98] were determined using PIV, which computes the velocity using cross-correlation of sub-images containing many tracer particles and is designed for smoothly varying velocity fields. However, as evidenced in Fig. 5.2, the velocity field as computed from the particle trajectories is not smoothly varying owing to the interaction with quantized vortices. By co-mingling tracers that are moving primarily under the influence of Stokes drag with those trapped in the vortex tangle when measuring the velocity, it is very difficult to disentangle the effects of the quantized vortices on the tracer particles. The heat fluxes used in the two sets of experiments (110 to 1370 mW/cm² in Ref. [98] and 13 to 91 mW/cm² here) are disjoint but adjacent. Even so, there is a discrepancy between our data and those of Zhang and van Sciver. This discrepancy may be due to the difference in analysis technique. In particular, Zhang and Van Sciver's analysis did not allow for the influence of quantized vortices on the trajectories of *individual* tracer particles, as we have done.

The theoretical explanation given in Ref. [45] by Sergeev *et al.* for the results

of Zhang and Van Sciver also appears to be different from ours. According to their calculations, we should have also seen significant deviations from eq. (5.1). The underlying assumption in their calculation that seems to break down is that every particle is affected by the quantized vortices. As we have shown in Fig. 5.2, a fraction of the particles move on vertical trajectories unaffected by quantized vortices, whereas other trajectories are dominated by their motion. Lastly, the temperature dependence in both our experiments and previous work must be better understood. In our experiments, there is a very clear temperature dependence of the effects of the quantized vortices on the particle motions as evidenced by the varying fraction of downward-moving trajectories. However, in both the experiments of Zhang and Van Sciver and the theoretical explanation given by Sergeev *et al.*, the claim is made that the disparity between the particle velocities and v_n is independent of temperature. Clearly the motion of tracer particles in thermal counterflow requires further attention.

Chapter 6

Reconnection

Reconnection has long been considered to play an important dissipative role in quantum turbulence. Vinen [19–21] described how the balance of reconnection and mutual friction leads to saturated vortex line lengths in counterflow turbulence, which is analogous to the saturation of dynamo action [8] or the magnetorotational instability [9] produced by magnetic reconnection in astrophysical plasmas. In this chapter we provide a detailed characterization of approximately 20,000 individual reconnection events in He II.[†] We compare the dynamics before and after individual events to those predicted by dimensional arguments in Eq. (2.30). The possible temperature dependence of the dynamics, anisotropy and time-reversibility are also explored.

6.1 Pulsed-Counterflow Experiments

A quantum vortex tangle and its accompanying cascade of reconnection events is induced by reproducibly driving the system away from equilibrium by a thermal counterflow, which increases the total vortex line length present in the system [19–21, 54]. Upon cessation of the counterflow, we acquire data while the system relaxes toward equilibrium [29]. A fixed heat flux in the range $0.058 \text{ W/cm}^2 < q <$

[†]The details of this chapter follow closely the discussion presented by Paoletti *et al.* in [6].

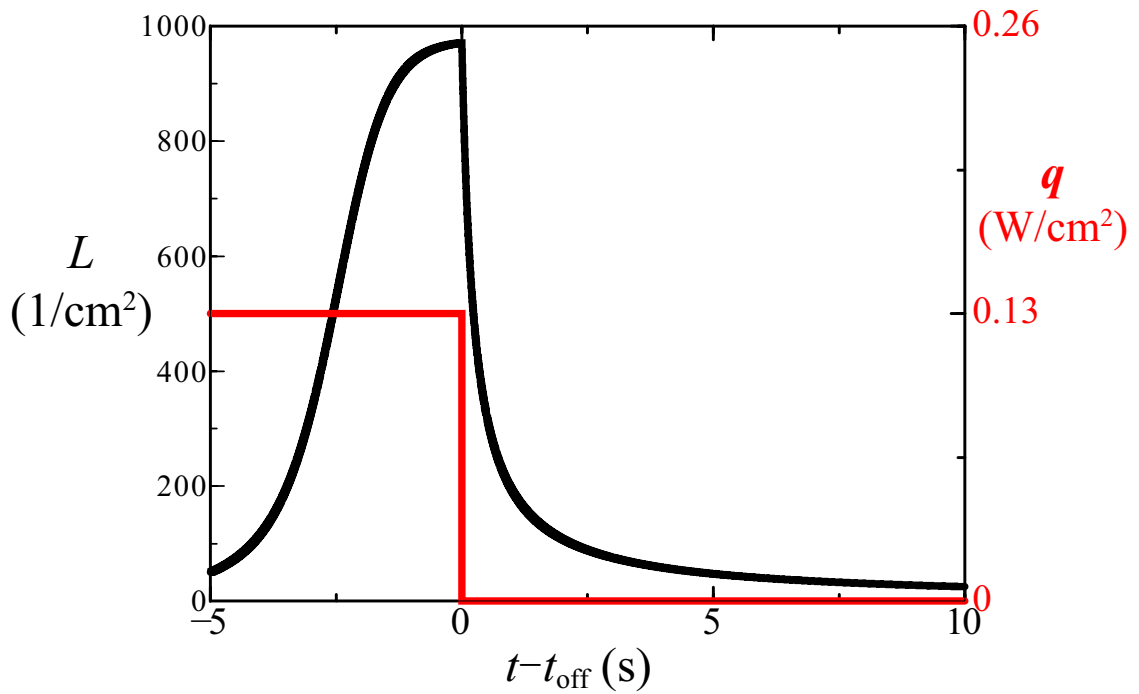


Figure 6.1: Plot of the vortex line length density L and heat flux q as a function of time measured from when the heater is turned off at t_{off} . The vortex line length density is determined by numerically integrating the Vinen equation given in Eq. (2.27). This technique provides a reproducible means of driving the system away from equilibrium since L reaches a statistically steady-state determined by the temperature and heat flux.

0.17 W/cm² drives the system for approximately 5 s, after which it is allowed to relax for approximately 10 s before repeating the process (see Figs. 6.1 and 6.2). Figure 6.1 shows the evolution of the vortex line length density L as a function of time measured from the moment the heater is turned off at t_{off} . This technique allows us to reproducibly drive the system away from equilibrium, since L reaches a statistically steady state. All of the data presented in this chapter is for times when the heater is off.

6.2 Visualizing and Identifying Reconnection Events

Near the reconnection moment t_0 , reconnecting vortices move with high, atypical velocities and accelerations. An example of a reconnection event is shown in Fig. 6.3 (also see Fig. 2 in [3] and note that reconnection is clearly evidenced in the online movies in [4]). In this example, the particle density is high so that both vortices are marked by multiple trapped hydrogen particles. The two vortices merge, exchange tails, then separate as indicated by the velocity vectors in the middle row of images in Fig. 6.3.

Since the hydrogen particles are not completely passive [5], the hydrogen volume fraction in the pulsed counterflow experiments presented here has typically been kept one to two orders of magnitude lower than that shown in Fig. 6.3. For such low volume fractions, each identified vortex has only one to a few hydrogen particles trapped, thereby minimizing the effects of the hydrogen on the reconnection dynamics [5]. A reconnection event is characterized, then, by a pair of particles

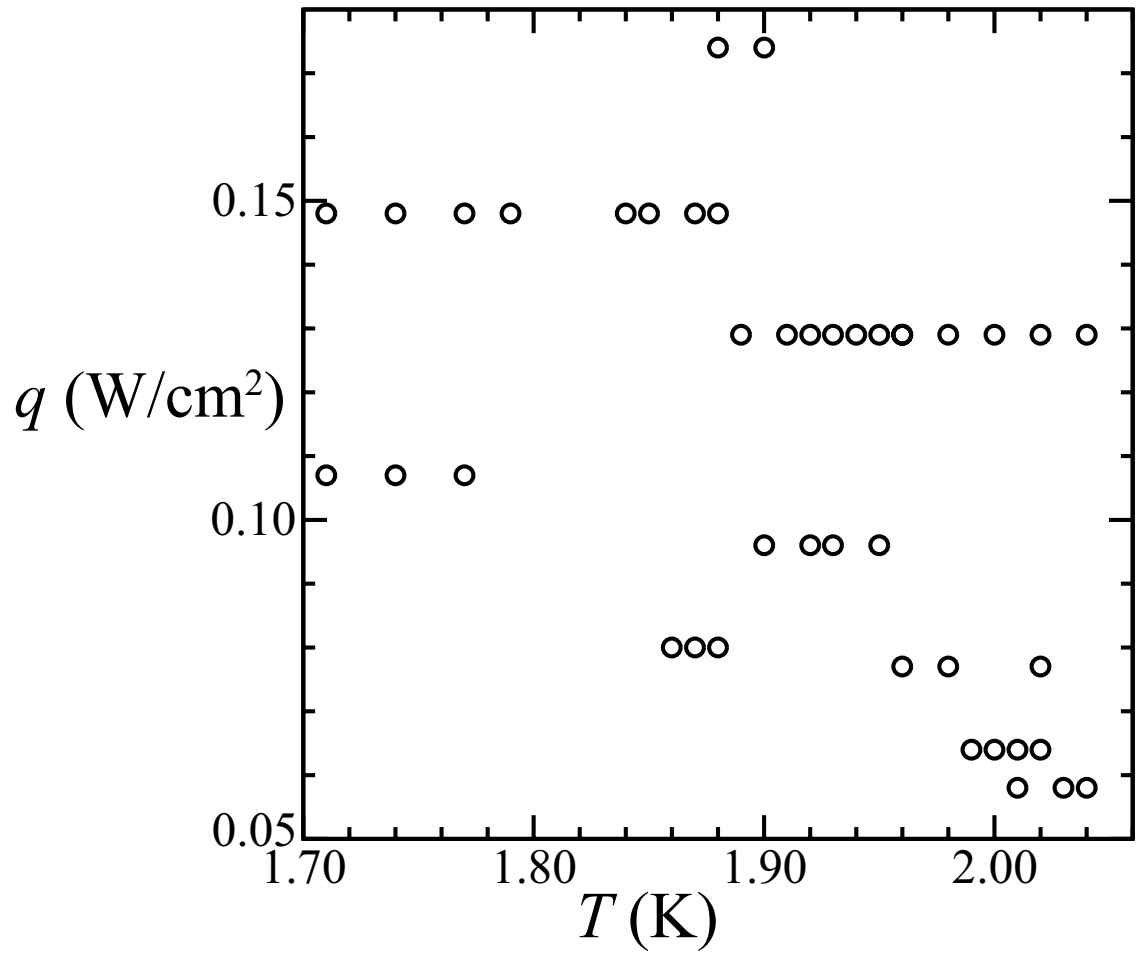


Figure 6.2: Parameter space diagram summarizing the ranges of heat fluxes q and temperatures T for the pulsed counterflows used to generate quantum turbulence.

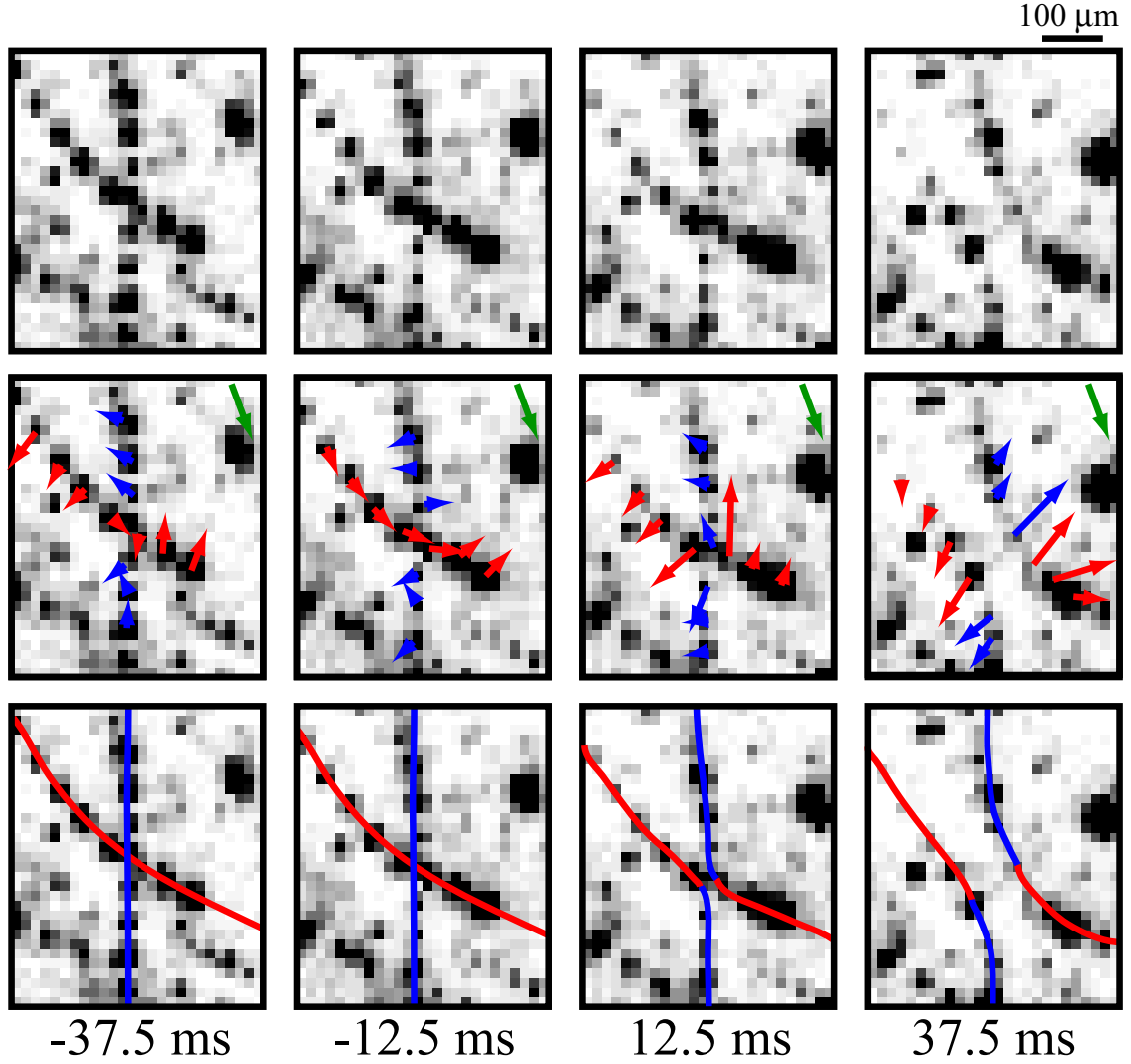


Figure 6.3: Contrast-enhanced negative images of particles trapped on reconnecting vortices (top) along with velocity vectors (middle) and our interpretation of the pre- and post-reconnection configurations of the vortices denoted by the red and blue lines (bottom) with time measured from t_0 at $T = 1.90$ K. The green vectors show the background drift that is subtracted from all velocity vectors. The red and blue velocity vectors (middle) correspond to the red and blue marked vortices in the bottom images. The volume fraction of hydrogen in these images (10^{-5}) is higher than for all the pulsed counterflow experiments discussed below. Reconnection is particularly unambiguous in the online movies in [4].

rapidly approaching or separating. The number of possible particle pairs analyzed is $\sim 10^{10}$, which requires an *ad hoc* criterion to determine likely reconnection events. We define particles i and j as marking a reconnection event at time t if the pairwise separation $\delta_{ij}(t) = |\mathbf{r}_i(t) - \mathbf{r}_j(t)|$ satisfies

$$\xi_{ij} \equiv \frac{\delta_{ij}(t \pm 0.25 \text{ s})}{\delta_{ij}(t)} > 4, \quad (6.1)$$

where $\mathbf{r}_i(t)$ is the two-dimensional projection of the position of particle i at time t and the plus (minus) sign indicates particles that separated after (approached before) an event, which we label as forward (reverse) events. We choose the temporal duration of 0.25 s to allow a sufficient range to perform the power-law fits to the data while curtailing greater times, which are dominated by boundary effects and the presence of neighboring vortices. The criterion (6.1) excludes all but a fraction of possible pairs, namely $\sim 5 \times 10^4$ forward and a similar number of reverse events.

It is important to note that we are assuming $\delta(t) \simeq \delta_{ij}(t)$; however, the particles (i, j) may not be located as close as desirable to the point of reconnection. We do not observe any correlations between the measured quantities discussed below and the initial particle separations or the values of ξ_{ij} as defined in (6.1); nevertheless, more detailed theoretical analyses of vortex reconnection are needed to reveal and quantify systematic effects that may be caused by interpreting our measurements of $\delta_{ij}(t)$ as good approximations to $\delta(t)$.

6.3 Arbitrary Power-Law Model

We characterize the dynamics of reconnection by measuring the separation $\delta(t) \simeq \delta_{ij}(t)$ of pairs of particles (i, j) that meet the criterion (6.1). As mentioned in Section 2.5, previous dimensional and theoretical arguments predict that $\delta(t)$ behaves asymptotically as a power-law with a scaling exponent $\alpha = 0.5$. To test this hypothesis we fit our data to an arbitrary power-law of the form

$$\delta(t) = B|t - t_0|^\alpha. \quad (6.2)$$

The values of B and t_0 are determined by a linear least-squares fit of $[\delta(t)]^{1/\alpha}$ for 500 values of α evenly-spaced in the interval $0 < \alpha < 2$. For each set of $\{\alpha, B, t_0\}$ we compute the error in the fit

$$\chi^2(\alpha) \equiv \frac{1}{n} \sum_{m=1}^n \left[\frac{\delta_m^{\text{fit}} - \delta_m}{\sigma} \right]^2, \quad (6.3)$$

where m denotes the movie frame, $\sigma = 4 \mu\text{m}$ (0.25 pixels) is an estimate of the uncertainty of the particle positions, and $n = 15, 20, 25$ for data collected at 60, 80, or 100 frames per second, respectively. We then choose the set of $\{\alpha, B, t_0\}$ that minimizes χ^2 (see Fig. 6.4).

The measured separations $\delta(t)$ for four forward events are shown in Fig. 6.5, along with the predicted asymptotic form $\delta(t) = (\kappa|t - t_0|)^{1/2}$ for comparison. Fits to (6.2) are shown as solid lines with the scaling exponent α given in the legend. The most frequent fitted exponents cluster around the predicted value of $\alpha = 0.5$ and their corresponding amplitudes B are of order $\kappa^{1/2}$; however, there is a broad spread in both quantities.

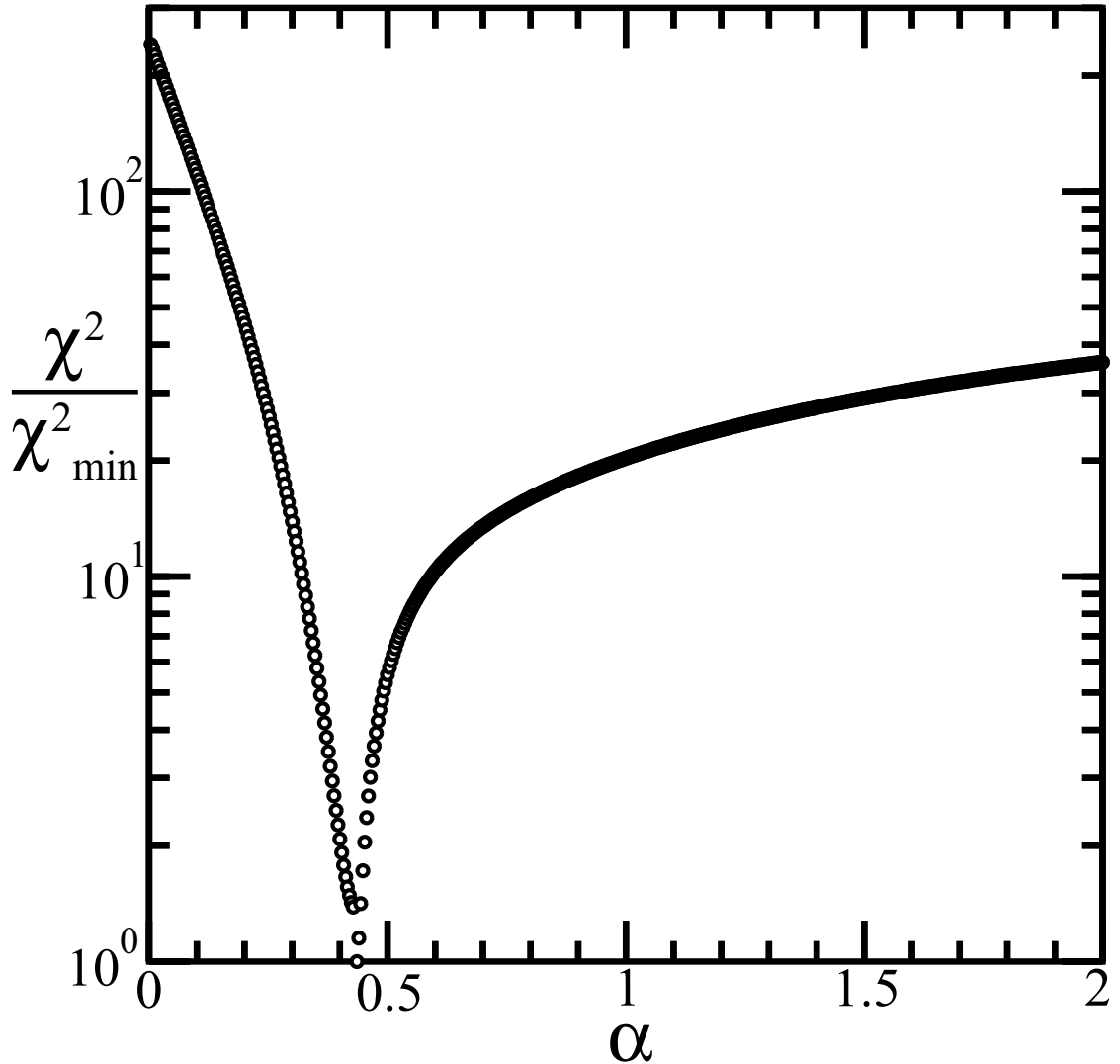


Figure 6.4: Variation of $\chi^2(\alpha)$ normalized by its minimum value $\chi_{\min}^2 = 0.73$ as a function of the scaling exponent α for the event shown by the red squares in Fig. 6.9 below. This event was observed at a temperature $T = 1.90$ K, but it should be stressed (as also for Figs. 6.5, 6.8, and 6.9) that fully comparable plots can be found at all temperatures in the range explored ($1.70 \text{ K} < T < 2.05 \text{ K}$). We choose the parameters of the arbitrary power-law fit $\{\alpha, B, t_0\}$ that minimize χ^2 as a function of α defined by (6.3).

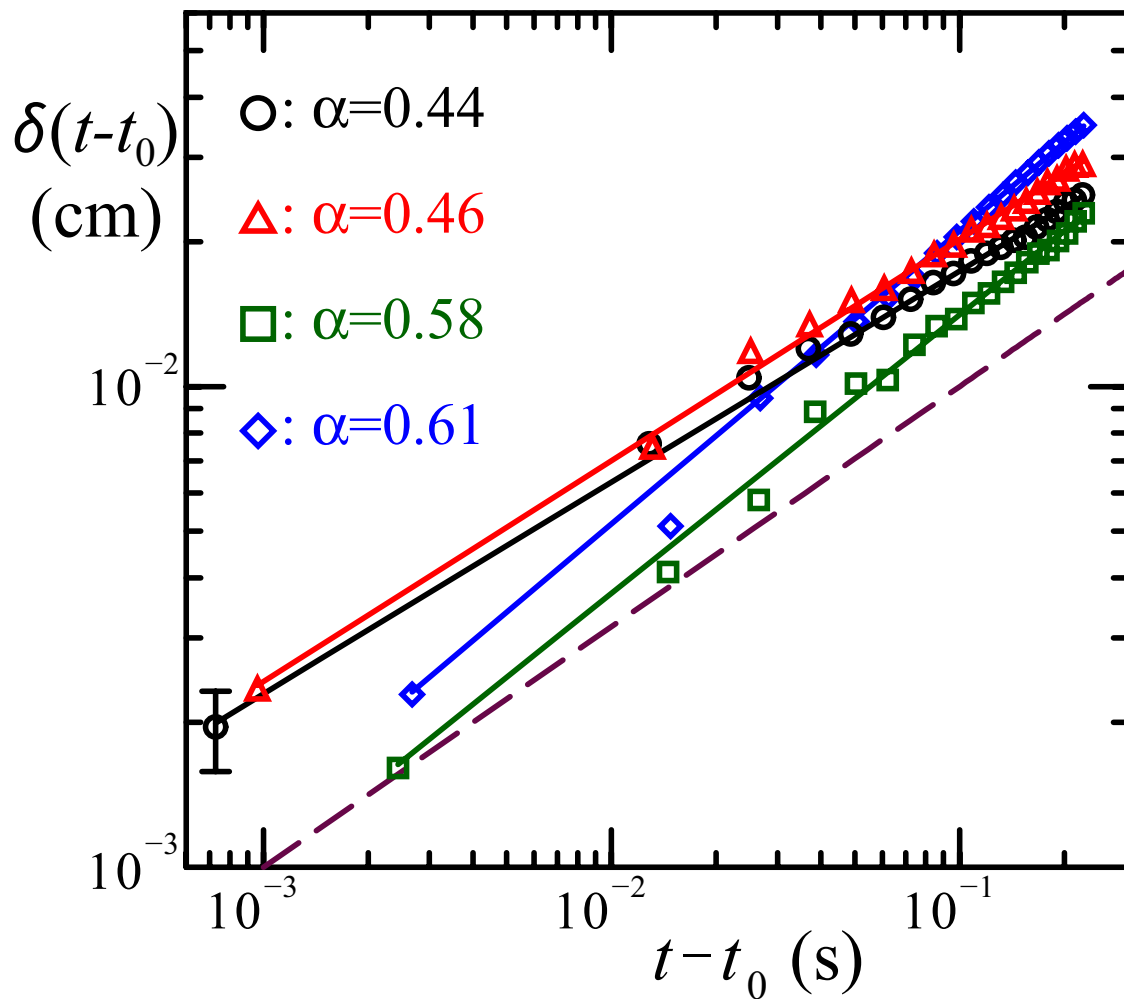


Figure 6.5: Four forward events at $T = 1.90$ K well fit by the arbitrary power-law expression (6.2). Symbols denote the measured separation $\delta(t)$ of pairs of particles on reconnecting vortices with an example error bar $\sigma = 4 \mu\text{m}$ while solid lines show fits to $\delta(t) = B|t - t_0|^\alpha$ with α given in the legend. The predicted asymptotic scaling $\delta(t) = (\kappa|t - t_0|)^{1/2}$ is shown by the purple dashed line.

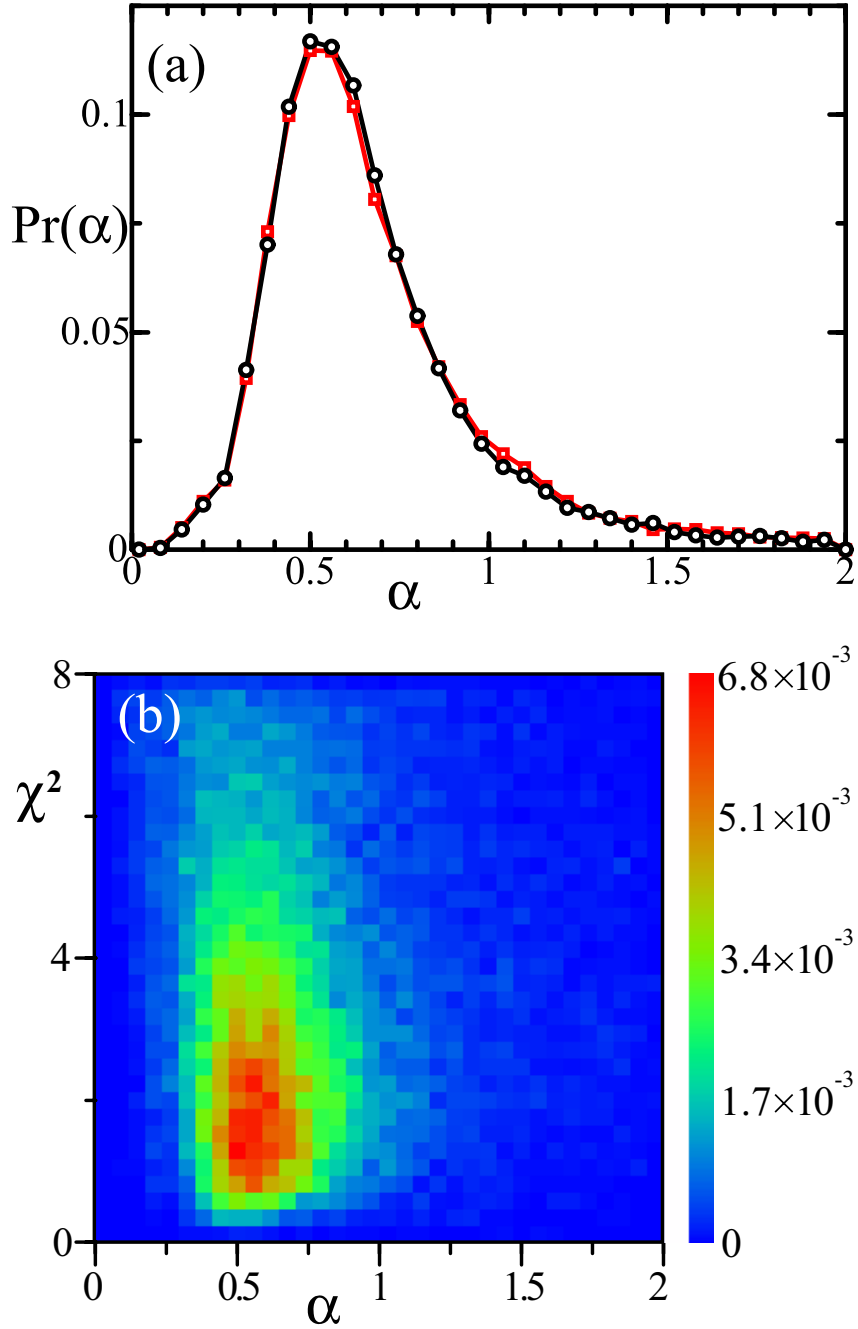


Figure 6.6: (a) Normalized frequency distributions of α computed for 19,150 forward events (black circles) and 18,900 reverse events (red squares). Note that the data displayed here (as also in Figs. 6.7, 6.10, 6.11, 6.13, 6.16, and 6.17 below) have been collected from the range of heat fluxes and temperatures described in Fig. 6.2. The mean values of α for forward and reverse events are 0.68 and 0.69, respectively. (b) Two-dimensional contour diagram of χ^2 versus α for forward events. The peak near $\alpha = 0.5$ with low values of χ^2 indicates that (6.2) best describes events with dynamics near those predicted in (2.30).

Distributions of α for both the forward and reverse events, determined from fifty distinct experimental heat pulses, are shown in Fig. 6.6(a). The distributions are formed from events with $\chi^2 < 4$. Approximately 40% of the 50,000 pairs that meet the criterion in (6.1) meet this χ^2 criterion. Both distributions are asymmetric but peaked within 10% of the predicted value $\alpha = 0.5$. Furthermore, as shown in Fig. 6.6(b), events with fitted values near 0.5 typically have lower values of χ^2 .

The amplitudes B for the same events are strongly correlated with the scaling exponent α as shown in Fig. 6.7. We find that events with $\alpha \simeq 0.5$ have amplitudes $B \simeq \sqrt{\kappa}$, as expected from dimensional analysis. However, de Waele and Aarts [57] measured $B \simeq \sqrt{\kappa/2\pi}$ in numerical simulations of quantized vortex reconnection in superfluid ^4He using line-vortex methods; this is approximately 30% of our experimentally determined value. The time-scales in our experiments differ greatly from these numerical simulations; de Waele and Aarts determined their value of B for $0 < t_0 - t < 3 \mu\text{s}$, whereas our time-scales span $1 \text{ ms} < |t - t_0| < 100 \text{ ms}$. In addition de Waele and Aarts quote an amplitude only for two initially antiparallel vortices; other initial orientations might yield different values for B . On the other hand, we observe only a two-dimensional projection of each reconnection event, which would lead us to underestimate B , potentially furthering the discrepancy. Clearly, resolving the source of this discrepancy warrants additional investigation.

The predicted scaling of $\alpha = 0.5$ is derived from the assumption that the quantum of circulation κ is the only relevant parameter over the length- and time-scales of interest. This assumption is valid in the context of line-vortex methods, and holds approximately for the Gross-Pitaevskii equation at length scales large

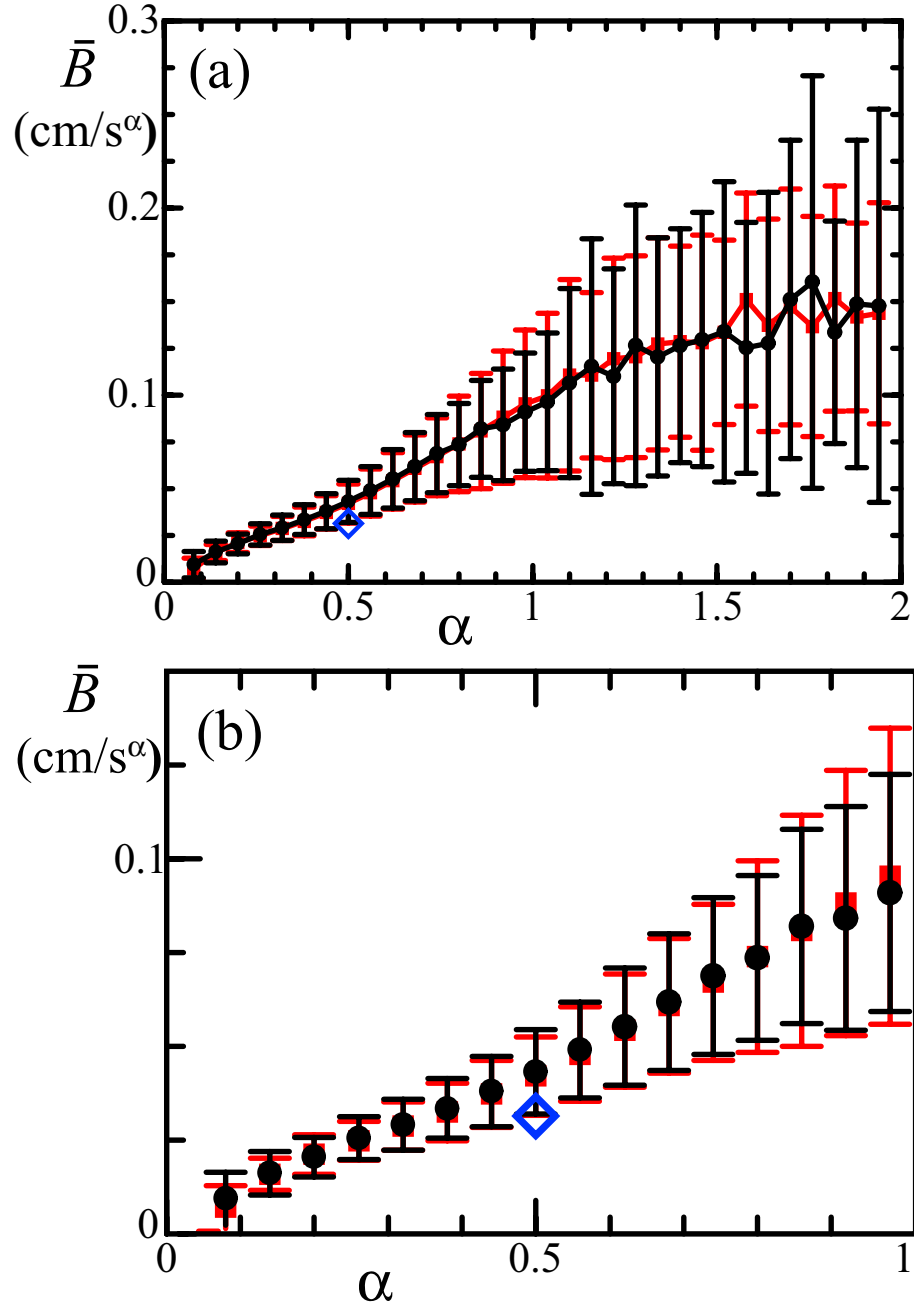


Figure 6.7: Plots of the average fitted amplitude \bar{B} as correlated with the scaling exponent α for 19,150 forward events (black circles) and 18,900 reverse events (red squares). The error bars indicate the standard deviation of the data within the given range of α . The blue diamonds at $\alpha = 0.5$ show $\bar{B} = \kappa^{1/2}$ to compare to the predicted scaling. (a) The entire range of α ; (b) range restricted to $0 < \alpha < 1$.

compared with the core diameter. However, deviations from $\alpha = 0.5$ might be obtained, at least conceptually, in two ways. First, adapting arguments that were proposed for multiscaling solutions of the Euler equation related to intermittency in classical fluid turbulence [102], one might suppose the precise value of κ is irrelevant to the dynamics of reconnection on the length scales we observe; then it should be possible to form a continuous family of solutions with differing values of α . However, it is difficult to imagine conditions under which κ would be irrelevant in our experiments given that the observed velocity magnitudes seem closely related to κ and to the distances involved, as expected.

Second, if another parameter with units different from κ were relevant then it is possible to rationalize reconnection dynamics with $\alpha \neq 0.5$. If any parameter such as a vortex-core length-scale, core surface tension, typical intervortex spacing, local velocity gradients, or system size, were relevant to the reconnection dynamics, then we may construct putative solutions with variable values of α . For example, if a core surface tension γ were relevant, we could contemplate an expression of the form

$$\delta(t) = B|t - t_0|^\alpha \kappa^{2-3\alpha} (\gamma/\rho)^{2\alpha-1}, \quad (6.4)$$

where we use the density ρ to construct a kinematic surface tension γ/ρ . Note that for $\alpha = 0.5$ we recapture the predicted behavior (2.30). The value of α for a particular reconnection event, in this interpretation, is either determined by the allowed values of α from the nonlinear equations of motion, or should that not be unique, additionally by the initial and boundary data for each particular event.

Further deeper theoretical investigations are required to determine if such solutions could be realized under experimental conditions.

6.4 Correction-factor Expression

The dynamics of reconnection may alternatively be described by supplementing the predicted asymptotic scaling of (2.30) with a correction factor. The simplest and natural expectation is the three-parameter form

$$\delta(t) \approx A (\kappa|t - t_0|)^{1/2} (1 + c|t - t_0|). \quad (6.5)$$

To test this expression we have performed a linear least-squares fit to determine A and c for 500 values of t_0 evenly spaced $125 \mu\text{s}$ apart (see Fig. 6.8); we then select the set of $\{A, c, t_0\}$ that minimizes χ^2 as defined in (6.3).

The measured separations $\delta(t)$ for four forward events are shown in Fig. 6.9, along with the predicted scaling of (2.30) for comparison. Solid line fits to the correction-factor expression in (6.5) describe the data well. Distributions of the amplitude A , computed from the same fifty distinct experimental heat pulses used to form Figs. 6.6 and 6.7, are shown in Fig. 6.10(a). As before, we require $\chi^2 < 4$. For both the forward and reverse events, the distributions of A are peaked near unity, in accord with the dimensional arguments; however as in Fig. 6.7, the values typically exceed unity (so being about three times greater than found in the special case studied numerically by de Waele and Aarts [57]). Events with A near unity typically have lower values of χ^2 , as shown in Fig. 6.10(b), again supporting the inferences based on dimensional analysis.

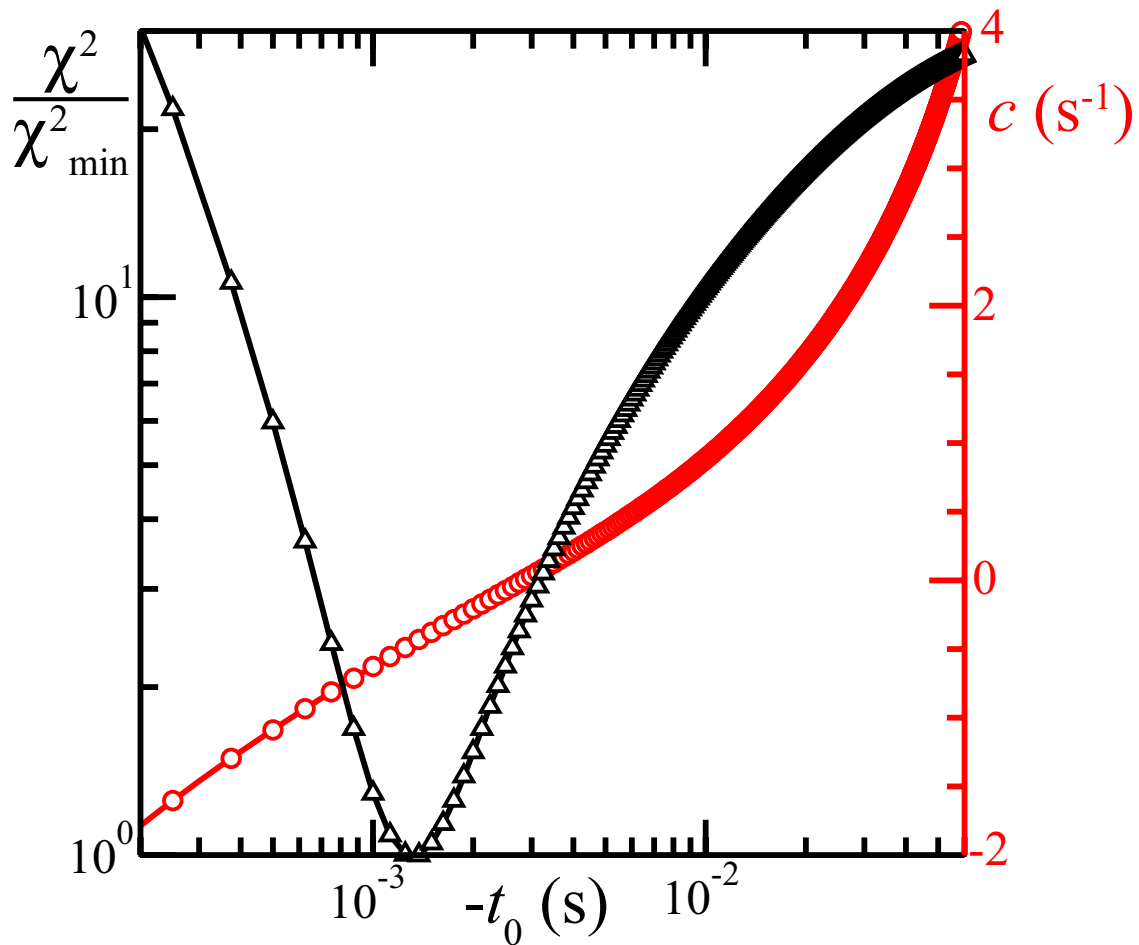


Figure 6.8: Variation of $\chi^2(t_0)$ normalized by its minimum value $\chi^2_{\min} = 0.73$ (black triangles) and the corresponding correction factor c (red circles) as a function of the time origin t_0 for the event shown by the red squares in Fig. 6.9 at $T = 1.90$ K. We choose the parameters of the correction-factor expression $\{A, c, t_0\}$ that minimize χ^2 as defined by (6.3).

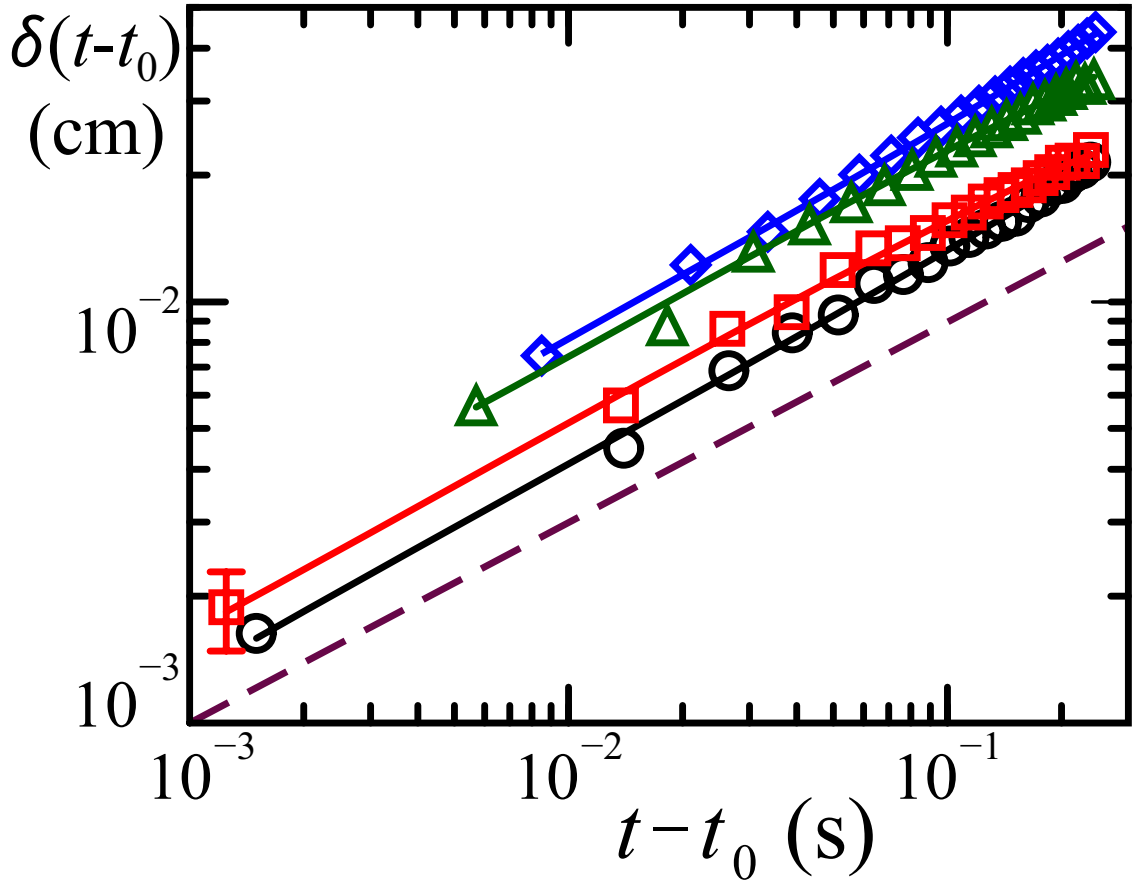


Figure 6.9: Four forward events at $T = 1.90$ K well fit by the correction-factor expression. Symbols denote the separation $\delta(t)$ of pairs of particles on reconnecting vortices with an example error bar $\sigma = 4 \mu\text{m}$ while solid lines show fits to the correction-factor expression (6.5). The predicted asymptotic form $\delta(t) = (\kappa|t-t_0|)^{1/2}$ is shown by the purple dashed line.

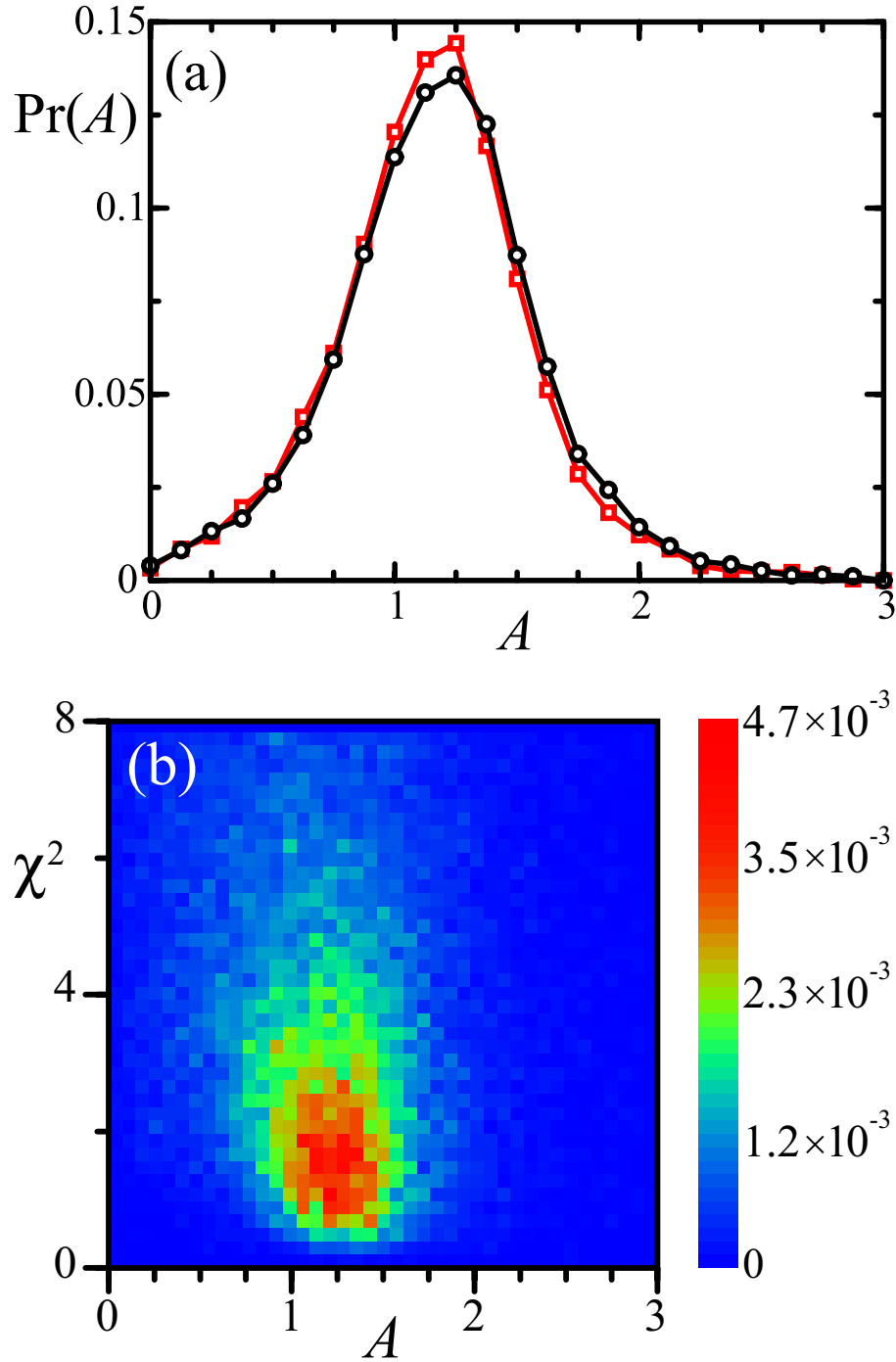


Figure 6.10: (a) Normalized frequency distributions of the amplitude A for 19,600 forward events (black circles) and 19,300 reverse events (red squares). Both distributions are broad with a peak at $A = 1.25$, the means of the forward and reverse distributions of A being 1.25 and 1.23, respectively. (b) Two-dimensional contour diagram of χ^2 versus A for the forward events. The peak near $A = 1$ at low values of χ^2 indicates that (6.5) describes optimally events with dynamics close to those predicted in (2.30).

The distributions of the correction amplitude c for the forward and reverse events are shown in Fig. 6.11(a). The distributions are peaked at $c = 0$, indicating that many events follow rather closely the simple scaling of (2.30). However, for both the forward and reverse events, the distributions are broad compared to their mean values of 0.63 and 0.71 s^{-1} , respectively, signifying strong event to event variation. The correction factor also varies systematically with the fitted value of the time origin t_0 , as illustrated in Fig. 6.8 and easily understood algebraically. Thus, uncertainties in the estimation of t_0 will induce corresponding changes in estimates for c .

It is useful to consider the magnitude of the correction term, since larger magnitudes imply a greater departure from the asymptotic form (2.30). This departure can be quantified by $|\overline{c(t - t_0)}|$, where the overbar implies a time-average over the duration that we use to fit the data, namely $0 < |t - t_0| < 0.25$ s. The ensemble mean value of $|\overline{c(t - t_0)}|$ for both the forward and reverse events is $\langle |\overline{c(t - t_0)}| \rangle = 0.15$, but it ranges from 10^{-6} to values greater than unity. This implies that while the deviations vary from event to event, they typically amount to less than ± 20 % as evidenced in Fig. 6.11(b).

The need to supplement the simple form (2.30), derived by dimensional analysis, with a correction factor stems from several potential sources. Independent of a specific origin, one must always expect a subdominant term in asymptotic power-law scaling forms like (2.30) which describe behavior from a micro- or mesoscopic domain up to some appropriate infrared cutoff at long times or large length-scales. A functional form including a correction factor along with the dominant power-law

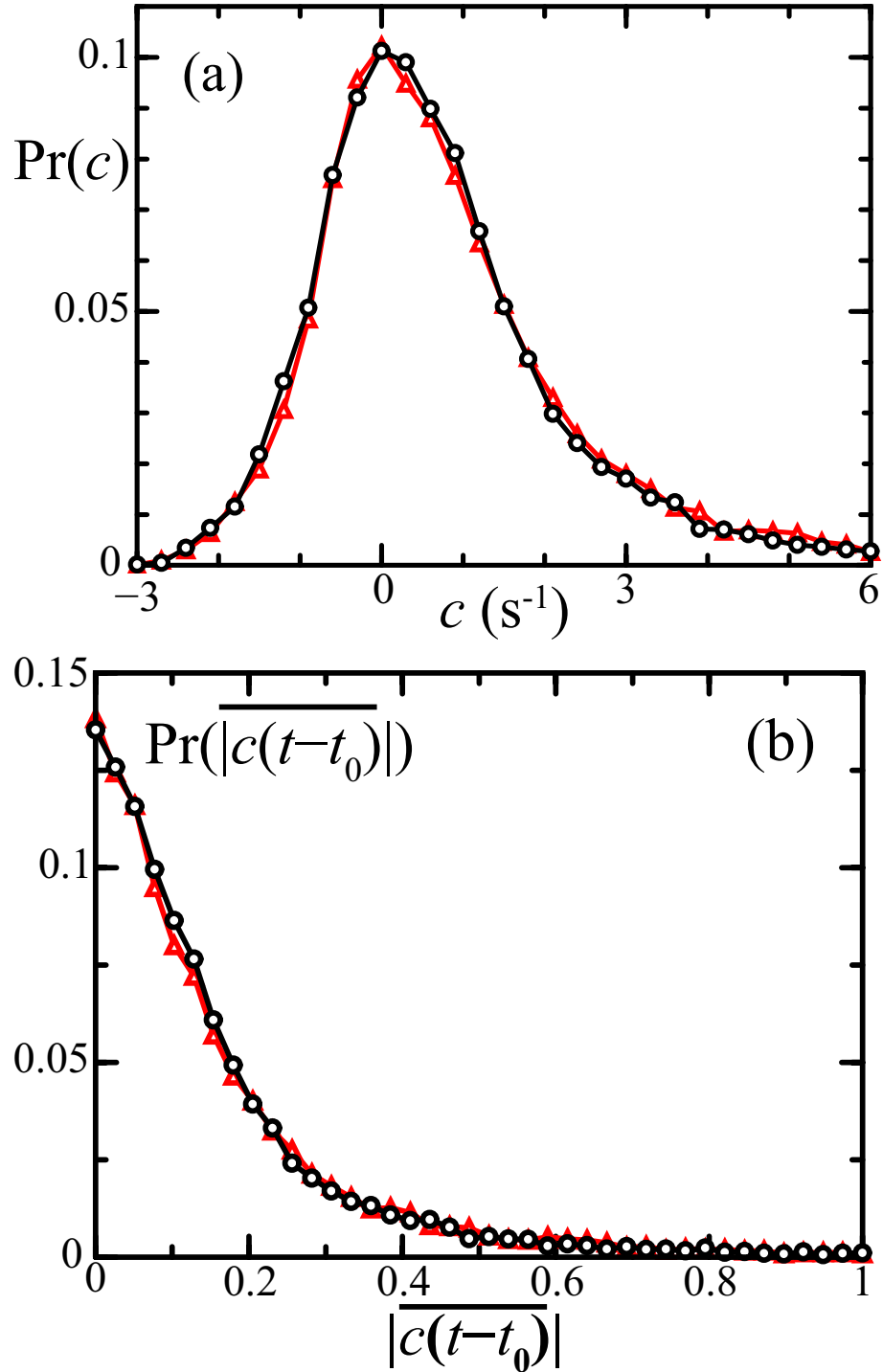


Figure 6.11: (a) Normalized frequency distributions of the correction amplitude c for 19,600 forward events (black circles) and 19,300 reverse events (red triangles). (b) Normalized distributions of the magnitude of the correction factor $|c(t-t_0)|$ time-averaged over 0.25 s for each trajectory for the forward (black circles) and reverse (red triangles) events.

allows for a crossover between scales. In our case, one certainly should expect deviations from (2.30) on length scales comparable to the typical intervortex spacing of 0.1 to 1.0 mm. Indeed, if one introduces a correction length scale, say l , by rewriting the correction term as

$$c|t - t_0| \equiv \pm\kappa|t - t_0|/l^2, \quad (6.6)$$

for forward and reverse trajectories, one finds that the corresponding forward and reverse mean values of c correspond to $l = 0.40$ mm and 0.38 mm, respectively. Thus the dominant correction may well represent the influence of neighboring vortices and their ability to distort the observed trajectories.

In addition, however, other spatial and temporal aspects of the local environment may also significantly affect the dynamics of reconnection, beyond the leading behavior accounted for by dimensional analysis. Local velocity gradients or other initial and boundary conditions could all produce deviations from pure square-root scaling, thereby necessitating a nonzero correction factor. More intriguing theoretically, however, and challenging experimentally, is the possibility of nonanalytic correction terms such as $c_\theta|t - t_0|^\theta$ with θ nonintegral. The presence of such terms with nontrivial values of $\theta \simeq 0.5$ is well established in the study of critical phenomena in ferromagnets, superfluids, at gas-liquid transitions, etc.: see, e.g., [103–105].

6.5 Effects of Temperature

The experiments are conducted between $1.70 \text{ K} < T < 2.05 \text{ K}$, which may also broaden the above distributions since many of the physical parameters describing

Table 6.1: Summary of the temperature ranges, number of events, peak values of the amplitude A and correction amplitude c , as well as the full-width at half-maximum (FWHM) values of A and c for the normalized frequency distributions shown in Fig. 6.12.

	Lowest	Middle	Highest
Range of T (K)	1.70 – 1.88	1.88 – 1.96	1.96 – 2.05
Forward Events	8,000	6,000	5,600
Peak A	1.24	1.14	1.14
FWHM A	0.85 – 1.60	0.88 – 1.57	0.74 – 1.52
Peak c (s^{-1})	0.41	0.10	0.10
FWHM c (s^{-1})	-0.80 – 1.70	-0.98 – 1.65	-1.0 – 1.18

superfluid ^4He vary with temperature. To examine this possibility, we divided the data into three distinct temperature ranges each composed of an equal number of pulses (see Table B.6) then recomputed the distributions of A and c , as shown in Fig. 6.12 and summarized in Table 6.1. The distributions show at most a very weak temperature dependence and the pronounced event to event variation seen in Figs. 6.10 and 6.11 persists.

6.6 Model Comparison

The two expressions (6.2) and (6.5) are both modified versions of the asymptotic dynamics which suggest somewhat distinct theoretical interpretations. In both cases, the majority of the fitted events exhibit behavior very similar to the dimensional predictions (i.e., $\alpha = 0.5$ or $c \simeq 0$); although, both also show strong variations from event to event. One might hope to distinguish the quality of the two fits by comparing the observed distributions of χ^2 , the overall deviation in the fits. In fact and unsurprisingly, the two distributions shown in Fig. 6.13 are rather similar and

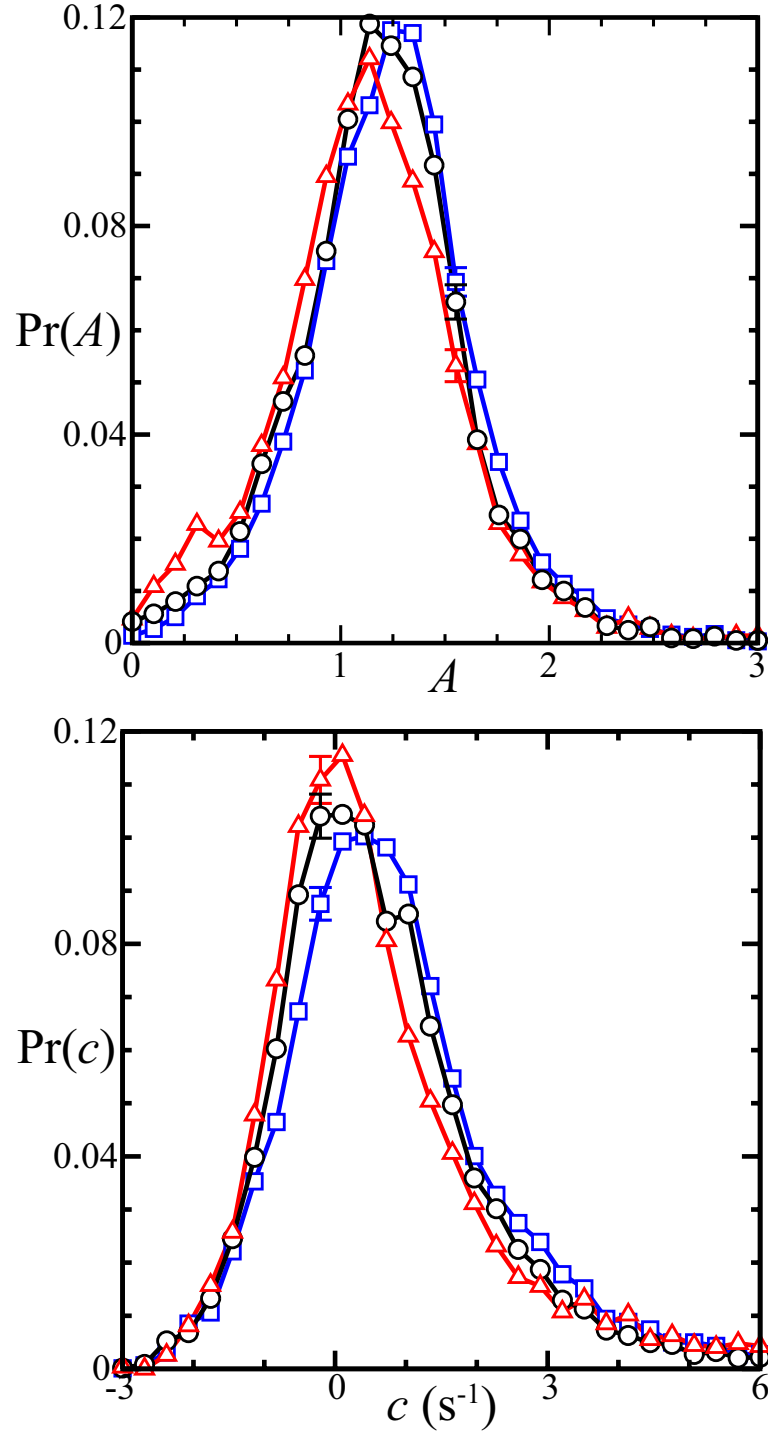


Figure 6.12: Normalized frequency distributions of (a) the amplitude A and (b) the correction amplitude c with example error bars for three distinct ranges of temperature. The lowest temperature range ($1.70 \text{ K} < T < 1.88 \text{ K}$) is shown by blue squares, the middle range ($1.88 \text{ K} < T < 1.96 \text{ K}$) is denoted by black circles, while the highest range ($1.96 \text{ K} < T < 2.05 \text{ K}$) is marked by red triangles. The details of these distributions are summarized in Table 6.1.

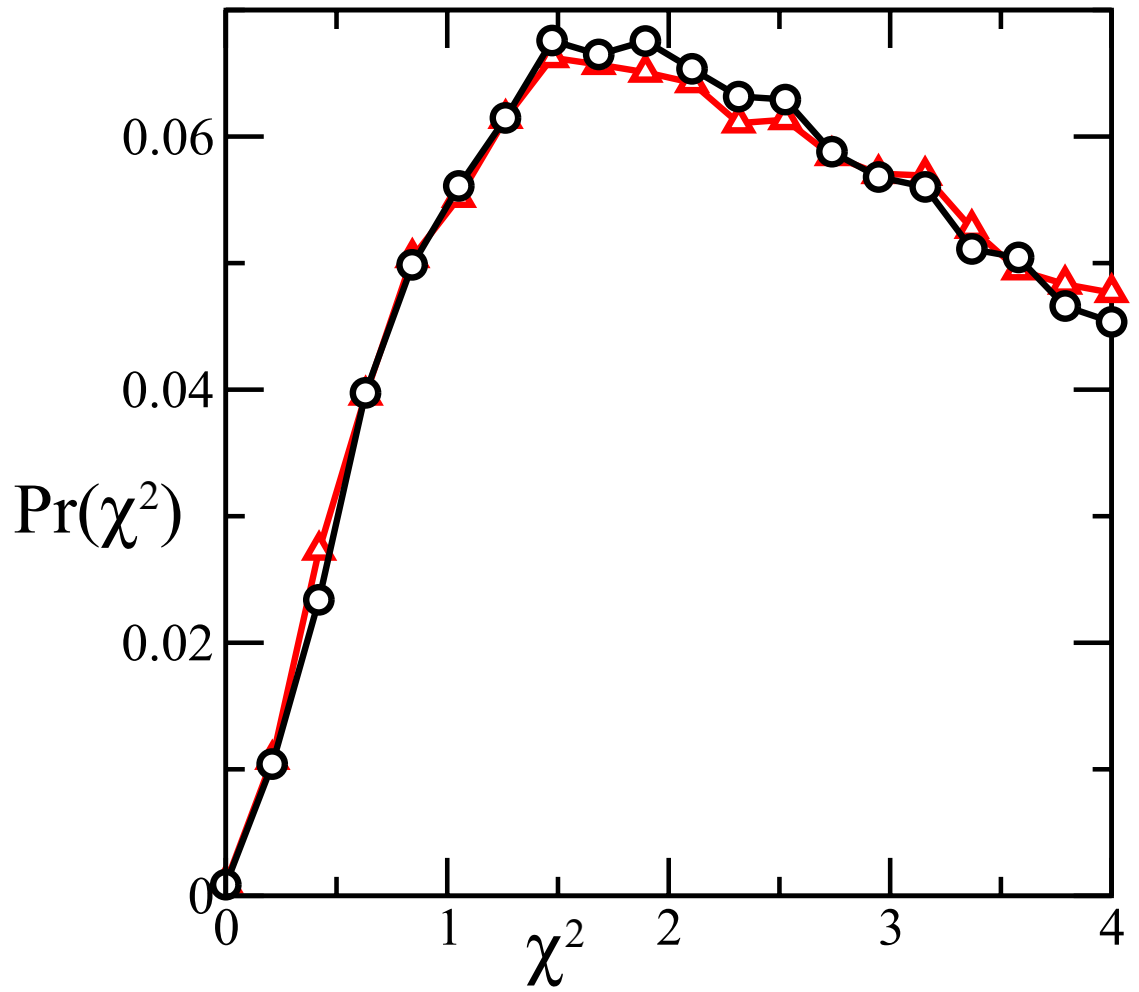


Figure 6.13: Normalized frequency distributions of χ^2 from both the forward and reverse events fit to the arbitrary power-law expression (black circles) and the correction-factor expression (red triangles).

no firm basis for making any distinctions emerges.

On balance at this point we favor the correction-factor expression as best embodying our experimental data for quantized vortex reconnection. Our typical observations of the dynamics show only relatively slight deviations from those predicted by dimensional analysis. It therefore appears that the dominant parameter is indeed the quantum of circulation κ , which sets the leading scaling exponent of $\alpha = 0.5$. We expect the deviations from the corresponding asymptotic form in our experimental range to be caused by the local environment and the initial and boundary conditions of the event, as opposed to other parameters such as a surface tension of the vortex cores. Indeed, such parameters would likely vary with temperature and we have not observed any correlations between our fit parameters and the temperature of the system over the range $1.70 \text{ K} < T < 2.05 \text{ K}$. Experiments and numerical simulations that control the local environment (velocity gradients, neighboring vortices, strains, etc.) as well as the initial and boundary conditions (configuration of the vortices, initial velocities and curvatures, etc.) could directly test this hypothesis and are clearly desirable.

6.7 Time-Reversibility

The Gross-Pitaevskii equation as used for quantized vortex reconnection [58, 93] is fully symmetric under time reversal; thus solutions of the equation may also be time-reversible symmetric. However, many previous theoretical works have concluded that reconnection dissipates energy by emitting acoustic and Kelvin waves

[17, 32, 106, 107] that may be absorbed by the boundaries, and so would break locally the time-reversibility. We have compared the pre- and post-reconnection dynamics by separately fitting forward and reverse events. All of the distributions of the fit parameters (see Figs. 6.6, 6.7, 6.10 and 6.11) for the forward and reverse events show striking similarity, as would be expected if the dynamics were statistically time-reversible. While it is clear, however, that some energy is dissipated overall in our experiments, as evidenced by the decay of the turbulent state, it is not evidenced in the statistics of individual events.

Overall the close statistical similarity of the forward and reverse events suggests an effective equilibrium has been established in quantum turbulence on the time scales (≤ 0.25 s) we have investigated. However, this does not imply that individual reconnection events are time-reversal symmetric. Three example trajectories of pairs of particles on reconnecting vortices both before and after the event are shown in Fig. 6.14. The square of the separation $\delta(t - t_0)^2$ is plotted to illuminate portions of the trajectories show exhibit nearly square-root behavior. The black and blue curves in Fig. 6.14 exhibit similar behavior before and after t_0 , whereas the red curve shows markedly different dynamics.

We independently fit the pre- and post-reconnection separations to the correction-factor expression as follows:

$$\delta(t) = \begin{cases} A_- (\kappa|t - t_0|)^{1/2} (1 + c_-|t - t_0|) & \text{if } t < t_0, \\ A_+ (\kappa|t - t_0|)^{1/2} (1 + c_+|t - t_0|) & \text{if } t > t_0. \end{cases} \quad (6.7)$$

The limited statistics of all the events observed are shown in Fig. 6.15 as scatter

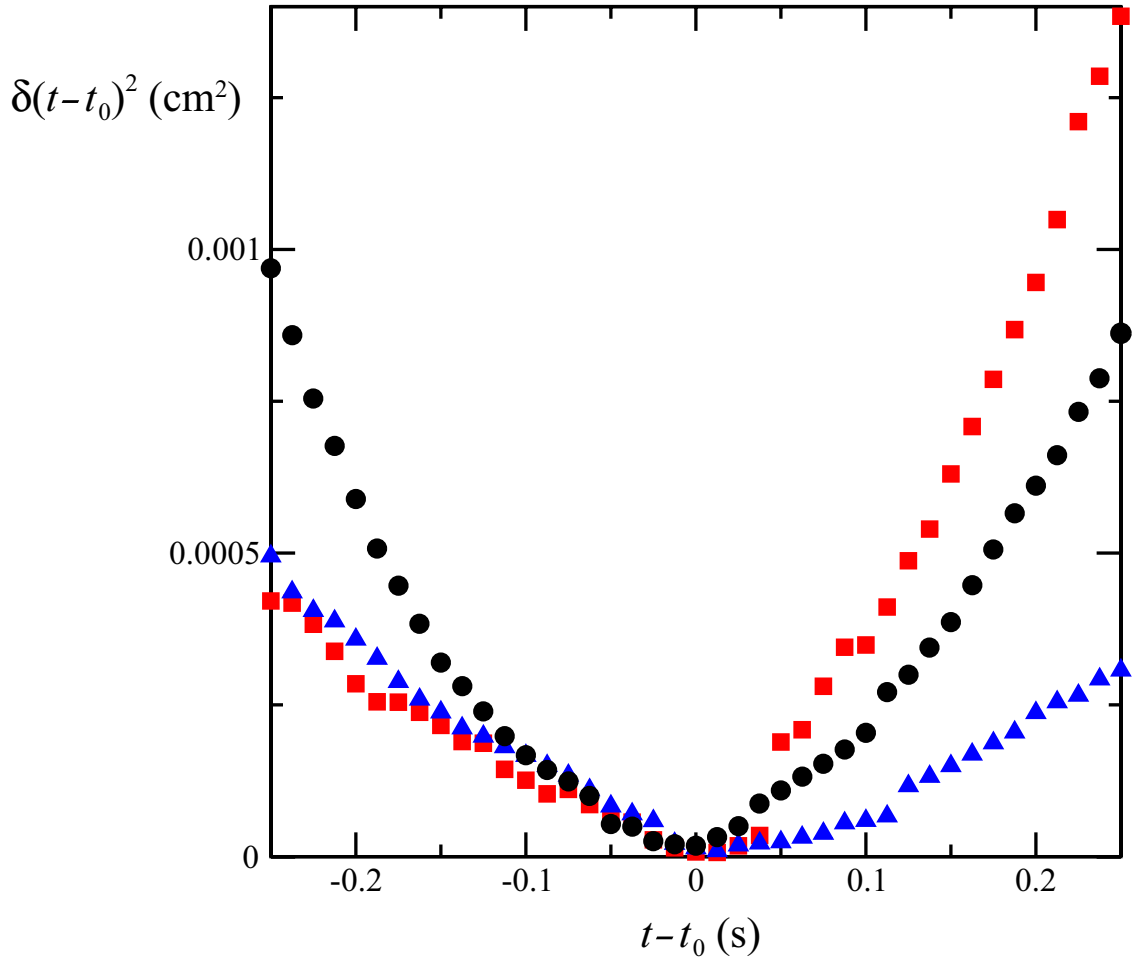


Figure 6.14: Three pairs of particles showing both reverse and forward events. The square of the separation $\delta(t - t_0)^2$ is plotted as a function of time measured from the fitted value of the reconnection moment t_0 to illuminate the square-root behavior predicted by dimensional arguments. The two events shown in black and blue exhibit similar behavior before and after the event, whereas the data shown in red is clearly not symmetric under time-reversal.

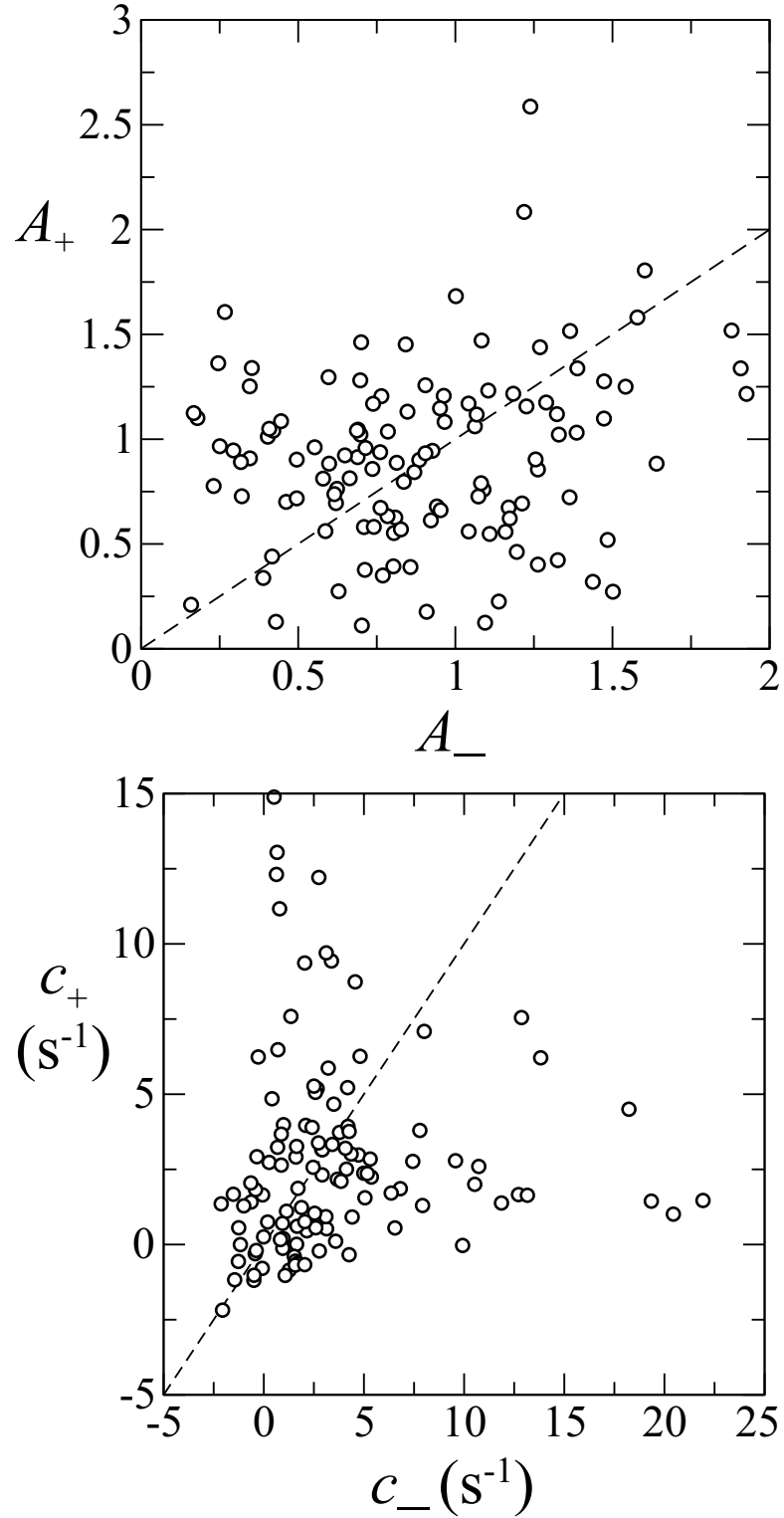


Figure 6.15: Scatter plots of the correction-factor expression fit parameters separately determined pre- and post-reconnection as defined in Eq. (6.7). Dashed lines correspond to $A_+ = A_-$ and $c_+ = c_-$ in panels (a) and (b), respectively.

plots of the pre- and post-reconnection fit parameters. The time-reversal symmetric values of $A_- = A_+$ and $c_- = c_+$ are shown by dashed lines. Evidently, individual reconnection events are not necessarily time-reversal invariant.

6.8 Anisotropy

In addition to the fit parameters, we may also investigate the total displacement of the vortices before and after events. We define the displacement vector of particle i as

$$\Delta \mathbf{r}_i = \mathbf{r}_i(t_0 + 0.25 \text{ s}) - \mathbf{r}_i(t_0) = \hat{x} \Delta x_i + \hat{z} \Delta z_i. \quad (6.8)$$

Figs. 6.16(a) and (b) show the \hat{x} - and \hat{z} -components of the displacement vectors for all of the particles identified with forward (black) and reverse (red) reconnection events. Indeed, the forward and reverse displacement vectors also show striking similarities. The displacement vectors appear weakly correlated in the x -direction and anti-correlated in the z -direction. This anisotropy is clearly exhibited in Fig. 6.17, which shows the difference in the displacement vectors of the pairs of particles on reconnecting vortices. The forward and reverse events are found to be equally affected by these anisotropic effects.

We believe the anisotropy arises from the polarizing effect of the z -directed, initiating thermal counterflow. A possible interpretation of the anti-correlation in the z -direction is that the vortices are typically aligned or anti-aligned with the direction of the counterflow. Previous studies have also observed [108] or argued for [109–111] the presence of anisotropy in counterflow turbulence; although, subject to

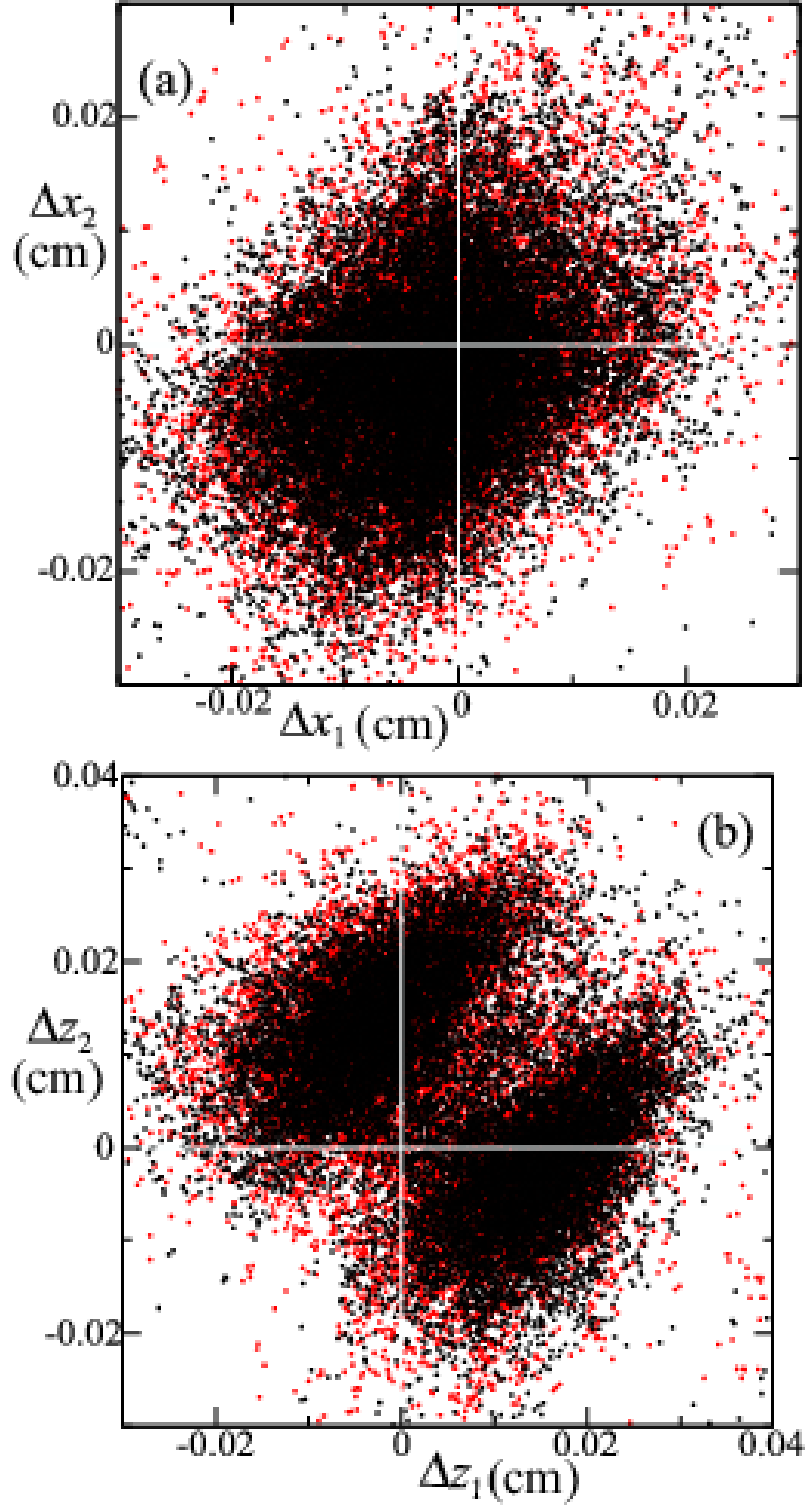


Figure 6.16: Scatter plots of (a) the \hat{x} -component and (b) the \hat{z} -component of the displacement vector $\Delta \mathbf{r}_i = \mathbf{r}_i(t_0 + 0.25 \text{ s}) - \mathbf{r}_i(t_0)$ for all forward (black) and reverse (red) event pairs (labeled as $i = 1$ and $j = 2$ for all pairs).

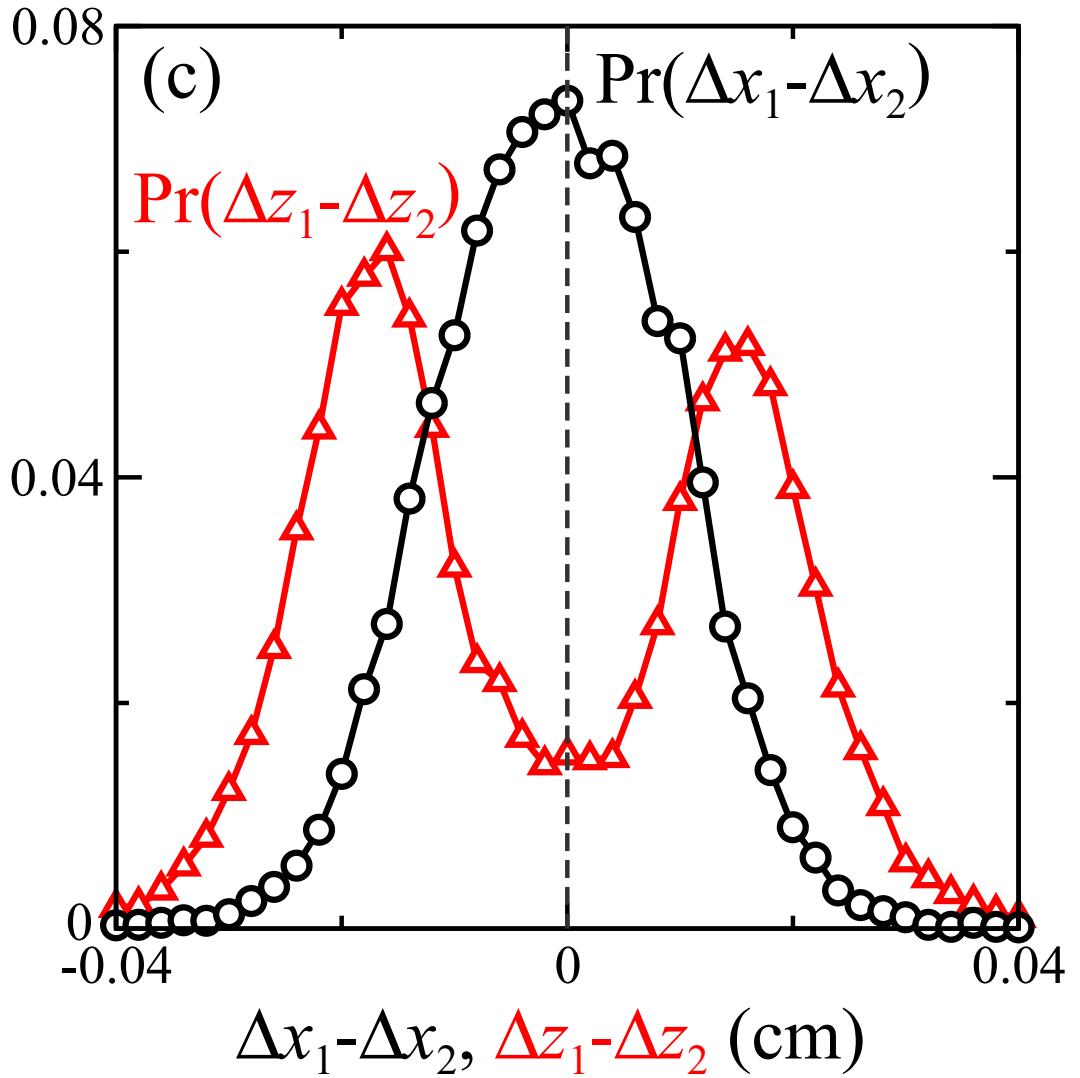


Figure 6.17: Normalized frequency distributions of the differences in \hat{x} -components (black circles) and the \hat{z} -components (red triangles) of the displacement vectors for each pair of particles on reconnecting vortices. The central peak at $\Delta x_1 - \Delta x_2 = 0$ signifies a strong correlation of the particle trajectories in the x -direction while the minimum at $\Delta z_1 - \Delta z_2 = 0$ implies a strong anti-correlation in the z -direction associated with the z -directed thermal counterflow.

interpretation, it is not clear that we agree on the polarization of the anisotropy.

6.9 Implications for Classical Turbulence

The scaling properties of velocity correlations in classical turbulence have received a great deal of attention. In particular, much debate has addressed the values of the exponents ζ_n of the longitudinal structure functions $\langle \Delta u_r^n \rangle \sim r^{\zeta_n}$, where $\Delta u_r \equiv u(\mathbf{x} + \mathbf{r}) - u(\mathbf{x})$ for a single velocity component u parallel to \mathbf{r} [12, 16, 112–129]. In analogy to the predictions of $\alpha = 0.5$ for quantized vortex reconnection, Kolmogorov used dimensional arguments to predict $\zeta_n = n/3$ [12]. His theory pivots on the assumption that the dissipation per unit mass ϵ is the only relevant parameter in the observed correlations and spectra. However, experimental observations report values of ζ_n that deviate slightly from Kolmogorov scaling [114, 121, 122, 125, 128]. Typically, arbitrary values of the exponents ζ_n are fit to the data [16, 112–123, 126–129], in analogy to our arbitrary power-law expression in (6.2). It should be noted, however, that models with variable ζ_n presuppose that arbitrary exponents are allowed, based either on the irrelevance of ϵ , or on dimensional grounds, by the admission of other relevant quantities that yield new power law forms [as illustrated in (6.4)].

We argue, though, that another option is available – that of correction-factors representing subdominant scalings. Similar connections between critical phenomena and turbulence have been explored previously [124, 130]. Here we specifically suggest that individual events in classical turbulence might be modeled both by a dominant

Kolmogorov term and a correction factor arising from various causes including at least the local neighborhood conditions and finite-size effects. The basic Kolmogorov scaling derives from the fact that with vanishing viscosity one obtains $\langle \Delta u_r^3 \rangle = -\frac{4}{5}\epsilon r$. If one interprets these statistics as stemming from many individual “Kolmogorov events” with $\Delta u_r \sim \delta/(t - t_0)$, then substituting $r \rightarrow \delta$ above yields, at least on a dimensional basis, $\delta \sim \epsilon^{1/2}(t - t_0)^{3/2}$, which is also known as Richardson scaling [31]. This can be obtained directly from a dimensional argument if δ depends only on ϵ and time. Note the units of ϵ are m^2/s^3 . If one then extends this model to a correction-factor expression, similar to (6.5), with an appropriately chosen correction, one might obtain behavior that would be difficult to distinguish from fluctuating power laws, though with a rather different interpretation.

6.10 Conclusion

In conclusion, we have observed and characterized the dynamics of individual reconnection events in superfluid ^4He . Although we observe significant deviations that vary from event to event from the mean behavior, the typical dynamics are close to those predicted by dimensional arguments. We regard this as our major finding. The deviations may be accounted for in two separate ways: (a) by supposing the scaling exponent of the dynamics can fluctuate as in (6.2), or (b) by recognizing that the predicted power laws must be supplemented by a correction factor such as in (6.5). The two three-parameter expressions describe the data almost equally well from a χ^2 perspective, but suggest distinct physical interpretations. Thus, we ob-

serve that a variable scaling exponent should result from either a lack of importance of the precise value of the quantum of circulation κ or from the competing relevance of another physical quantity of distinct dimensions (such as a length-scale, surface tension, etc.).

On the other hand and more naturally, we interpret the correction factor as arising from initial conditions and boundary effects, such as the vorticity distribution and intervortex spacing, and from properties of the local environment at reconnection, such as velocity gradients, pressure gradients, and thermal fluctuations. Since the dynamics appear to be well characterized by the predictions that assume that the only relevant physical parameter is the quantum of circulation κ , we believe our data indicate that the environment, as opposed to other parameters, is most likely the origin of the observed deviations. Further investigations experimentally and theoretically could focus on: (i) considering alternate forms of the correction term, such as $c_\theta |t - t_0|^\theta$ with $\theta \neq 1$, and (ii) systematically changing the initial and boundary conditions as well as the local environment near reconnection and investigating the resulting deviations from the dimensionally predicted asymptotic form.

Chapter 7

Quantum Turbulence

A great deal of information regarding turbulent states in He II has been gleaned from experimental studies despite the inability to directly probe the local velocity field. Many recent investigations have been concerned with similarities between quantum turbulence and classical turbulence, which we briefly review below. These experiments all study the characteristics of the flow on length scales greater than the typical intervortex spacing. In this chapter, we characterize the dynamics of turbulent He II on length scales smaller than the typical intervortex spacing by directly measuring the local velocity field.[†] We predict and measure the distributions of velocities in turbulent He II and compare them to those typical of classical fluid turbulence.

7.1 Similarities with Classical Turbulence

Many recent studies have focussed on the behavior of quantum turbulence on length scales sufficiently large that the interactions of individual quantized vortices may be neglected. These previous works concluded that on such length scales quantum turbulence shares many characteristics with classical turbulence [18, 23–29, 40, 49, 131–138]. Even though the quality of the supporting evidence has been

[†]The details of this chapter follow closely the discussion presented by Paoletti *et al.* in [4].

questioned [139], it will be summarized here.

Experiments on turbulence generated in ^4He by two counter-rotating disks observed Kolmogorov energy spectra that were indistinguishable above and below the superfluid transition [26]. The spectra were determined by measuring pressure fluctuations using a probe ~ 1 mm in size, which is larger than the typical intervortex spacing l . A similar Kolmogorov energy spectrum was also seen in numerical simulations of the Gross-Pitaevskii equation with small-scale dissipation added to the otherwise energy-conserving dynamics [18]. However, it is unclear if such an equation is applicable to turbulence in He II — the chosen form for the dissipation was designed to resemble a classical fluid.

The classical decay of vorticity [23] has been observed in towed grid [23, 27], thermal counterflow [29], and impulsive spin down [30] experiments. In all of these studies the decay of the vortex line length density L was measured and used to make an analogy with the energy dissipation rate in a classical fluid. The quantity L is globally averaged and cannot be used to probe the local dynamics. As we pointed out in Subsection 1.4.1, it is possible to have $L > 0$ without dissipation, for example in a rotating container. Therefore, several caveats must be added in order to compare the decay rate of L to the energy dissipation rate.

In this chapter, we study the velocity statistics of quantum turbulence generated by a thermal counterflow on length scales between our experimental resolution ($\sim 1 \mu\text{m}$) and the typical intervortex spacing ($\sim 0.1 - 1$ mm). On such length scales the interactions of individual quantized vortices are important. Specifically, quantized vortex reconnection [3, 4, 6, 53, 57, 58, 93], where two vortices merge at

a point, change topology by exchanging parts, and separate (Fig. 2.11), produces high, atypical velocities. By analyzing the trajectories of micron-sized solid hydrogen tracers, we may compute both the velocity statistics of quantum turbulence, and identify and assess the effects of individual reconnection events.

7.2 Pulsed Counterflow Experiments

We study the velocity statistics in decaying quantum turbulence initiated by a reproducible thermal counterflow, as discussed in Subsection 6.1. A fixed heat flux in the range $0.058 \text{ W/cm}^2 < q < 0.17 \text{ W/cm}^2$ drives the system for approximately 5 s, after which it is allowed to relax for approximately 10 s before repeating the process (see Fig. 6.1). The experimental parameters are the same as those presented in Fig. 6.2. We use this technique since it is reproducible and it has also been used in Refs. [29, 110, 111], which observed similarities to classical fluid turbulence by measuring L . Except for Fig. 7.1, all of the data presented in this chapter is acquired while the heater is off.

7.3 Time-Varying Velocity Distributions

Time-varying distributions of the horizontal and vertical velocity components, v_x and v_z , computed by forward differences, are shown in Fig. 7.1 for a typical thermal pulse. The v_x distributions are always peaked near zero. However, as predicted by the two-fluid model, the v_z distributions exhibit different behavior for $t < t_{\text{off}}$ as compared to $t > t_{\text{off}}$. The bimodal v_z distributions when the heater is

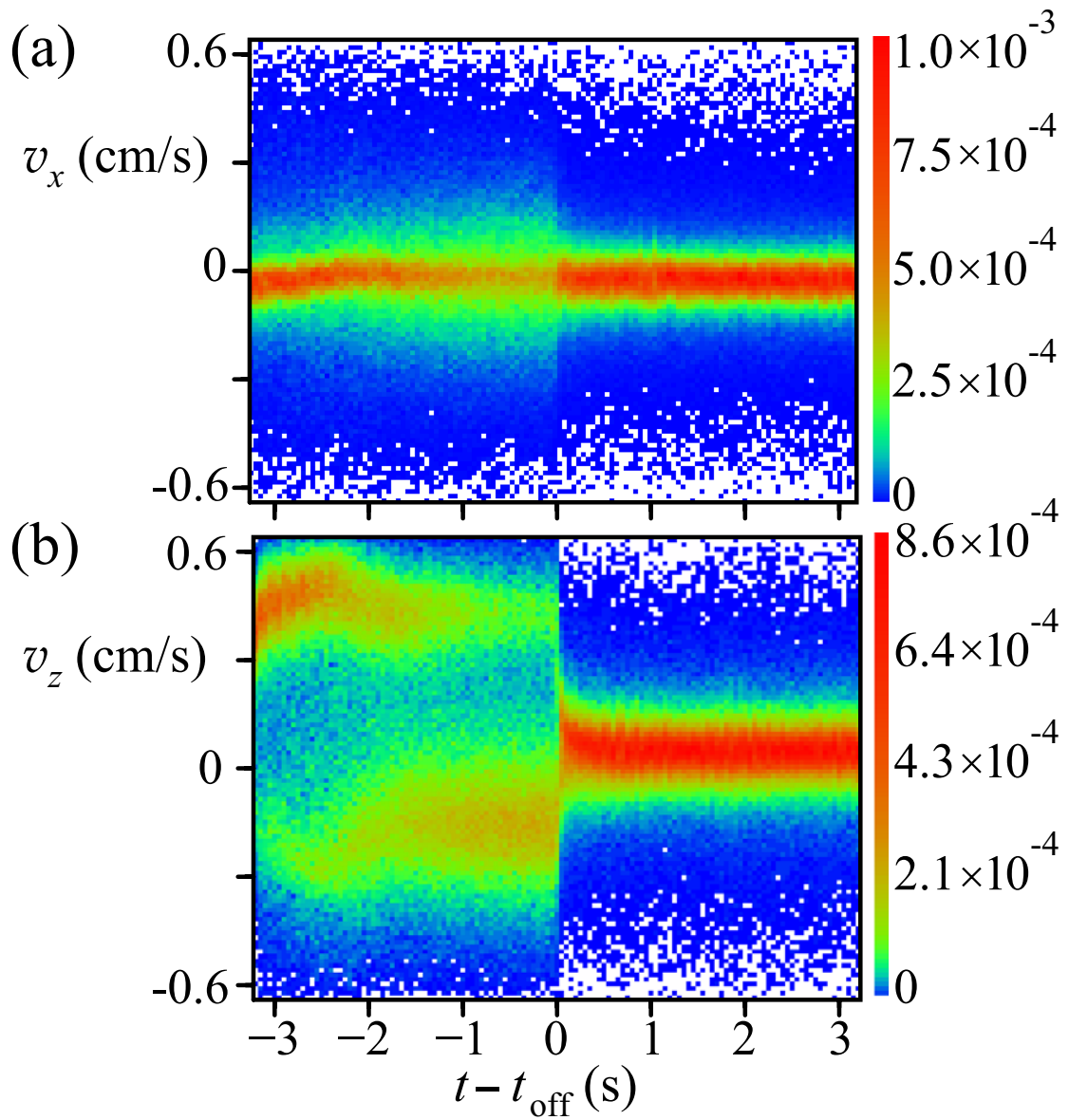


Figure 7.1: Time-varying pulsed counterflow velocity distributions at $T = 1.90$ K showing (a) v_x and (b) v_z for a portion of a heat pulse of 0.17 W/cm² with the heater turned off at $t = t_{\text{off}}$. White denotes amplitudes with zero probability.

on represent particles with $v_z > 0$ moving upward with the normal fluid owing to Stokes drag while particles with $v_z < 0$ are trapped in the vortex tangle that moves downward. Once the heat pulse ends, the vertical velocities collapse to distributions peaked near zero. Although the distributions for both v_x and v_z are peaked near zero when the heater is off, many high velocity events remain; these we attribute to the quantized vortices as explained below.

7.4 Predictable Power-Law Tails

The assumptions used to argue for the classical nature of quantum turbulence break down on length scales smaller than the typical intervortex spacing, which is what we have probed with our measurements. It is clear from the online movies (see [4]) that our turbulent states in superfluid ^4He differ drastically from those observed in classical fluids as a result of the topological interactions of the quantized vortices. Specifically, reconnection produces anomalously large velocities in highly-localized areas, which are not diffusively smoothed by viscosity. If length-scales are evolving asymptotically as $R(t) = \tilde{A}|\kappa(t - t_0)|^{1/2}$, as discussed in Chapter 6, then we expect the velocities to scale as

$$v(t) = \frac{\tilde{A}}{2} \sqrt{\frac{\kappa}{|t - t_0|}}, \quad (7.1)$$

which far exceed typical fluid velocities when $t \rightarrow t_0$. Note, however, that we expect such velocities to be cut-off by the speed of first sound (and may anticipate related differences in the spectrum of pressure fluctuations [140]).

To model the probability distribution function (pdf) of the velocity derived

from particle trajectories, we may use the transformation

$$\Pr_v(v)dv = \Pr_t[t(v)]dt, \quad (7.2)$$

$$\Pr_v(v) = \Pr_t[t(v)]|dt/dv|, \quad (7.3)$$

where $\Pr_v(v)dv$ is the probability of observing a velocity between v and $v + dv$ at any time while $\Pr_t(t)dt$ is the uniform probability of taking a measurement at a time between t and $t + dt$. Hence, accepting the scaling relation (7.1), we predict for large v (small t) the behavior

$$\Pr_v(v) \propto |dt/dv| \propto |v|^{-3}. \quad (7.4)$$

In fact, as pointed out by Min *et al.* [141], the velocity distribution around a straight, singular vortex has the same power-law tails. The velocity field around such a vortex located along the z -axis is given by

$$\mathbf{v} = \frac{\Gamma}{2\pi s} \hat{\phi}, \quad (7.5)$$

where Γ is the circulation. To model the pdf of this velocity field we may use the following

$$\Pr_v(v)dv = \Pr_s[s(v)]ds, \quad (7.6)$$

$$\Pr_v(v) = \Pr_s[s(v)]|ds/dv|, \quad (7.7)$$

where $\Pr_v(v)dv$ is again the probability of observing a velocity between v and $v + dv$ at any radius while $\Pr_s(s)ds$ is the probability of taking a measurement at a radius between s and $s + ds$. The probability of taking a measurement at a radius between

s and $s + ds$ is proportional to s , or equivalently v^{-1} . Assuming the velocity field given by Eq. (7.5), the ratio $|ds/dv|$ is proportional to v^{-2} . Thus we again arrive at

$$\text{Pr}_v(v) \propto |dt/dv| \propto |v|^{-3}. \quad (7.8)$$

7.5 Velocity Statistics

The v_x and v_z pdfs derived from *all* particle trajectories for $t > t_{\text{off}}$ for the same pulse in Fig. 7.1 are shown in Fig. 7.2. The solid lines are fits to Eq. (7.4) allowing for a mean flow. Indeed, the simple arguments used to derive Eq. (7.4) are able to predict the tails of the velocity distributions in reconnection-dominated quantum turbulence. It is quite remarkable that we are able to observe velocities that are an order of magnitude larger than the standard deviation. Furthermore, the tails of these distributions are truncated by particle tracking constraints; data obtained at higher frame rates than those used here (60, 80, 100 fps) could observe further extended tails.

To emphasize the distinction with classical turbulence, a velocity pdf from an oscillating-grid experiment in water [142] is shown in blue in Fig. 7.2. Evidently the velocity pdfs in superfluid helium differ drastically from the near-Gaussian velocity pdfs observed experimentally [143], and in direct numerical simulations of homogeneous and isotropic classical turbulence [119, 144]. We attribute this distinction to the topological interactions of the quantized vortices, which do not exist in classical turbulence where the velocity field is diffusively smoothed by viscosity. One must note, however, that tracer particles in superfluid helium respond separately to the

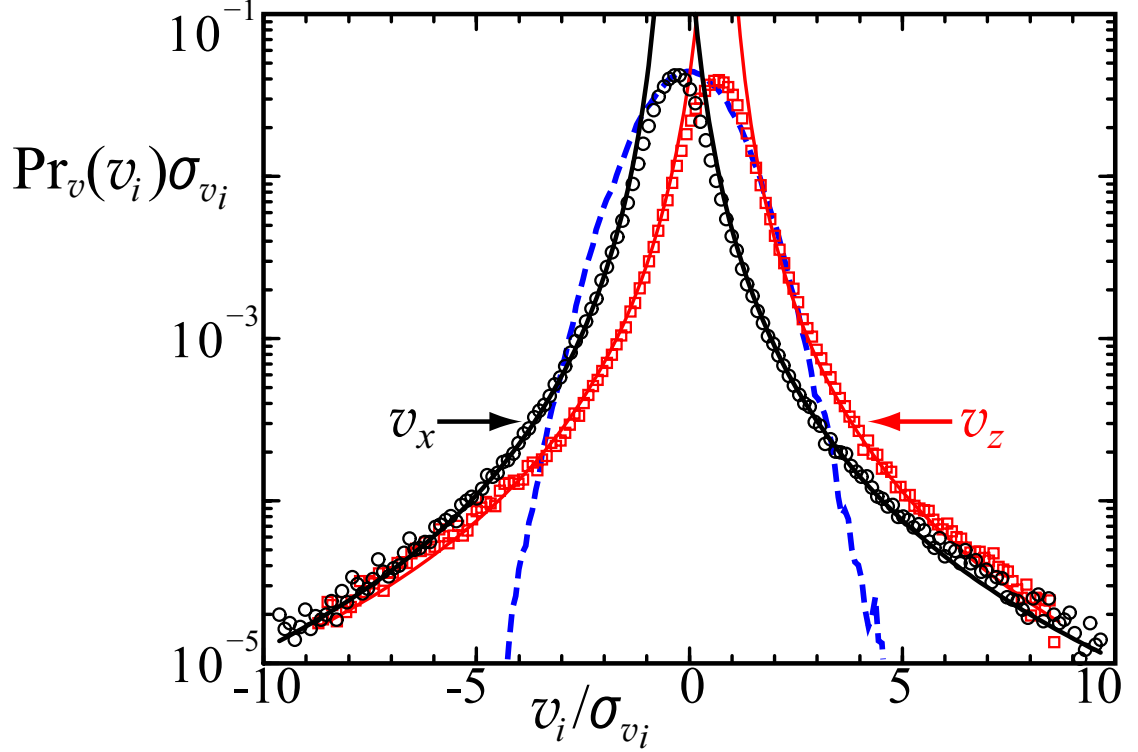


Figure 7.2: Local velocity statistics derived from the data in Fig. 7.1 for all particle trajectories with $t > t_{\text{off}}$ (computed from over 1.1×10^6 values of velocity). All distributions are scaled to give unit variance using $\sigma_{v_x} = 0.066$ or $\sigma_{v_z} = 0.074$ cm/s. The probability distribution functions of v_x and v_z are shown by black circles and red squares, respectively. The solid lines are fits to $\text{Pr}_v(v_i) = a|v_i - \bar{v}_i|^{-3}$, where i is either x (black) or z (red) and \bar{v}_i is the mean value of v_i . For comparison the dashed (blue) line shows the distribution for classical turbulence in water [142] computed from over 10^7 velocity values. The distribution is scaled using $\sigma_v = 0.25$ cm/s, and with a peak value matched to the v_x data. The velocity statistics in water are close-to-Gaussian over five decades in probability.

normal fluid and the quantized vortices (which are influenced by the normal fluid and superfluid); this is fundamentally different from that in water.

7.6 Analogies with MHD

Previous studies have argued that the interactions of magnetic field lines can cause the velocity statistics of magnetohydrodynamic (MHD) turbulence also to differ from classical turbulence, particularly in astrophysical plasmas with extremely small resistivities. In such environments magnetic field lines become “frozen” into the underlying velocity field. If two field lines are driven sufficiently close together they may also reconnect by diffusive processes. The power-law tails in the distributions of electron energies observed in astrophysical settings (Fig. 3 in [79] and Fig. 2 in [10]) have been attributed to magnetic reconnection [81, 82]. Furthermore, theories for MHD turbulence propose that fractional diffusion may be the dominant transport mechanism [145]. Such diffusion is associated with power-law tails in velocity distribution functions.

By the same arguments made in Section 7.4, the tails of the pdf for the kinetic energy per unit mass $E = (v_x^2 + v_z^2)/2$ will be dominated by reconnections. Accepting the relation (7.1), we have $E(t) \propto |t - t_0|^{-1}$ and so for large E we expect

$$\Pr_E(E) \propto |dt/dE| \propto E^{-2}. \quad (7.9)$$

The pdf of E computed from the data in Fig. 7.2 (which includes all particle trajectories) is shown in Fig. 7.3(a). A single-parameter fit of the form $\Pr_E(E) = aE^{-2}$ is shown as a solid, red line for comparison. The departure from the predicted

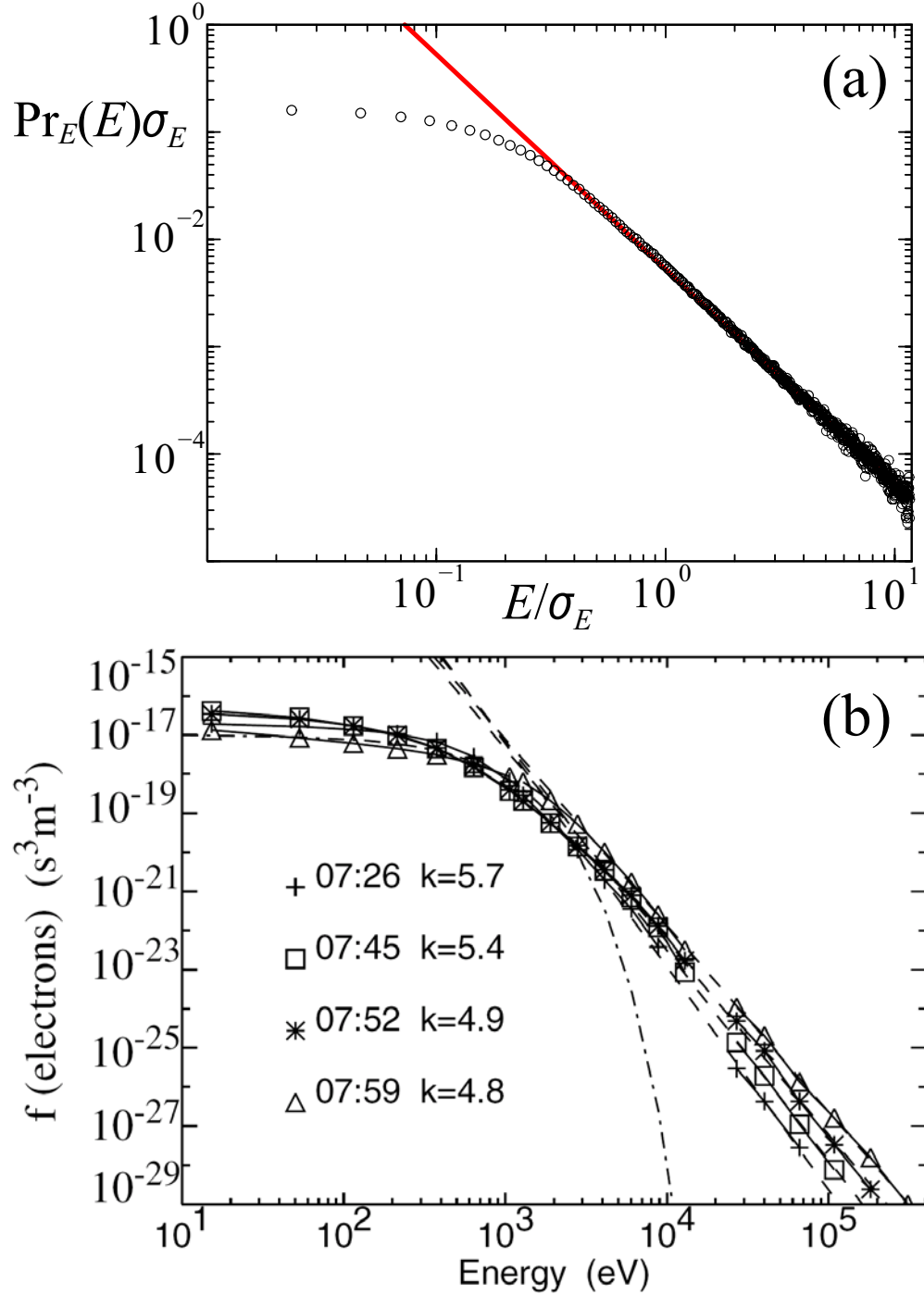


Figure 7.3: Local energy statistics derived from the data in Fig. 7.1 for all particle trajectories with $t > t_{\text{off}}$ (computed from over 1.1×10^6 values of velocity) compared to those of electrons (presumably) accelerated by magnetic reconnection in the diffusion region of the earth's magnetotail. (a) The distribution of the kinetic energy per unit mass $E = (v_x^2 + v_z^2)/2$ in He II with a fit of the form $\text{Pr}_E(E) = aE^{-2}$ shown in red. The distribution is scaled to give unit variance using $\sigma_E = 0.017 \text{ (cm/s)}^2$. (b) Electron energy distribution observed by Øieroset *et al.* [79].

power-law behavior for low energies may reasonably be attributed to effects from the boundaries and nearby vortices as well as to the background drift of the normal fluid. We compare this distribution to the electron energy distribution observed by Øieroset *et al.* [79] shown in Fig. 7.3(b).

It is clear that the two distributions in Fig. 7.3 bear resemblance, however several important distinctions must be made. The distribution computed from our data is the kinetic energy per unit mass of the He II, with the tails dominated by the motions *of the quantized vortices themselves*. In the MHD case taken from Ref. [79], the distributions are computed from electrons that are *accelerated by the magnetic field lines*, rather than of the magnetic field lines themselves. The mechanism by which electrons are accelerated in regions near magnetic reconnection is a process unto itself and is still actively studied [81, 82]. Furthermore, reconnection in astrophysical plasmas is a much more complicated process. In He II reconnection occurs between identical, topologically-constrained quantized vortices whereas magnetic field lines do not share the same constraints. Nevertheless, taking the reductionist approach, studying reconnection-dominated quantum turbulence could aid in the study of MHD turbulence in low resistivity environments.

7.7 Conclusions

In conclusion we have shown that the velocity statistics of quantum turbulence in superfluid ^4He differ drastically from those for classical turbulence owing to the topological interactions of vortices that are different from those in classical fluids.

Instead, it appears that turbulence in He II may bear stronger analogy to other systems characterized by interacting topological defects. Since reconnection is a principal dissipative mechanism in superfluids near absolute zero, superfluid experiments might provide another “laboratory” for studying strong MHD turbulence, as well as other systems exhibiting one-dimensional topological defects [71] such as liquid crystals, superconductors, Bose-Einstein condensates, and cosmic strings. Furthermore, the normal fluid present in these experiments is relatively quiescent and additional future directions could include examining the velocity statistics for the case where both the normal fluid and superfluid are turbulent, since the two fluids couple through friction acting on the quantized vortices [19–21].

Chapter 8

Conclusions and Future Work

In this chapter we summarize the conclusions that may be drawn from our work and provide potential future directions of inquiry. The suggestions for future work include additional experiments that can readily be conducted with the existing apparatus, potential improvements to the injection technique and related computational studies.

8.1 Summary

In this thesis, we have presented experimental characterizations of turbulent processes in He II by implementing a newly developed visualization technique [1]. This technique uses micron-sized solid hydrogen particles as tracers, which are capable of revealing motions of the normal fluid component and of the quantized vortices. To our knowledge, the ability to observe the dynamics of quantized vortices in the bulk of He II remains unique. By implementing this technique we have been able to supplement the vast body of work concerning He II by providing the first observations of the two-fluid motions in thermal counterflows [5], quantized vortex reconnection [3, 6], and quantum turbulence [4].

We began by characterizing properties of the motion of tracer particles in He II [5], which are complicated by interactions with the quantized vortices. We

have observed a clear transition between regimes where the particles are only scattered by the vortices as opposed to being trapped near T_λ . We attribute this transition to a crossover in the magnitude of the trapping force relative to Stokes drag that acts to dislodge particles from counterflowing vortices. We argue that for all temperatures there is a counterflowing velocity above which particles will become dislodged from the vortices. There have been several notable studies of the motion of tracer particles in turbulent He II [44–48]. Since we know the density of our tracer particles, their typical size and the characteristics of the flow it should be possible to make quantitative comparisons between our observations and these models.

Hydrogen tracer particles were used to characterize the two-fluid motions in a thermal counterflow [5]. These studies provided the first direct observation of the two-fluid motions in He II and a quantitative verification of the normal fluid velocity \mathbf{v}_n dependence on the driving heat flux q given by

$$\mathbf{v}_n = \frac{\mathbf{q}}{\rho ST}. \quad (8.1)$$

The response of the tracer particles is shown to depend upon both the temperature and the heat flux. For constant heat flux, the fraction of particles that become trapped on quantized vortices increases with decreasing temperature owing we presume to the increase in the trapping potential. At constant temperature, the fraction of trapped particles increases with increasing heat flux as the vortex line length density also increases. Above a threshold heat flux for a given temperature, though, Stokes drag will dominate and prevent particles from becoming trapped on vortices.

The dynamics of the quantized vortices in counterflow turbulence are more

complicated than those of the normal fluid. We observed that the quantized vortices typically have velocities less than the superfluid velocity \mathbf{v}_s . This is to be expected, since the quantized vortices exchange momentum with the normal fluid [19–21]. However, the specific values of the vertical component of the vortex line velocity \mathbf{v}_L cannot yet be explained. In order to do so, the geometry of the vortices must be known; preliminary results from computational studies have recently been reported showing initial agreement with our measurements [55, 56].

We also report detailed characterization of approximately 20,000 individual reconnection events [6], which had never before been visualized in He II. To the author’s knowledge, this is by far the largest collection of observed reconnection events in any physical system. The dynamics strongly fluctuate from event to event, although mean quantities correspond to those predicted by simple dimensional arguments. The observed deviations from the predicted scaling are accounted for in two different ways: (a) by allowing the scaling exponent of the dynamics to fluctuate or (b) by supplementing the predicted scaling with a correction-factor to account for variations in the local environment and to allow for a crossover in scales. These two expressions fit the data equally well, but result in quite distinct physical interpretations. We claim that a variable scaling exponent implies that the precise value of the quantum of circulation κ is negligible or that other physical parameters of distinct dimensions are also relevant (such as a length-scale, surface tension, etc.). The correction-factor is interpreted as arising from variations in the boundary and initial conditions as well as the local environment. We find the correction-factor expression is a more natural explanation of the dynamics. The statistics of the fit

parameters that describe the reconnection dynamics immediately before and after the event are found to be essentially indistinguishable, even though individual events are not necessarily symmetric under time-reversal.

Lastly, we have characterized the local velocity field of turbulent states in He II for the first time [4]. Turbulence was only manifested in the superfluid component; the normal fluid component was quiescent. We argued that the interactions between quantized vortices, such as quantized vortex reconnection, would dominate the tails of the velocity distribution. Assuming such, we predicted that the tails of the pdf of velocity should decay as v^{-3} . These predictions were confirmed by our measurements of the velocity statistics, which is in stark contrast to the near-Gaussian velocity statistics always observed in classical homogeneous, isotropic turbulence. We argue that a stronger analogy may exist between turbulence in He II and MHD turbulence in astrophysical plasmas where the reconnection of magnetic field lines is an important process.

8.2 Ring Collapse - Dynamics and Effects on Velocity Statistics

The dynamics of quantized vortex rings plays an important role in quantum turbulence. As initially envisioned by Feynman in 1955, and depicted in Fig. 2.12, reconnection can lead to the formation of vortex rings. These rings will propagate because of their self-induced velocity and at temperatures above 1 K are seen to decay. For lower temperatures, these rings may dissipate vortex line length by interacting with the boundaries or by forming successively smaller rings.

We have made preliminary observations of the dynamics and collapse of vortex rings that agree quite well with theoretical predictions [146]. It is clear that many such ring collapse events occur in our decaying counterflow turbulence experiments. Each of these events removes quantized vortex line length from the system, thereby aiding the relaxation toward equilibrium. A systematic characterization of many of these events could shed light on this relaxation process and the role of ring collapse in quantum turbulence.

The self-induced velocity of quantized vortex rings increases with decreasing radius. Since the circulation of the vortex ring is topologically constrained, ring collapse produces very large velocities in a manner very similar to reconnection. The quantum of circulation governs the dynamics in both cases, and therefore we expect that arguments made in Section 7.4 may also apply to ring collapse. Thus, fully understanding the tails of the velocity distributions also requires knowledge of the dynamics and the role of ring collapse events in addition to reconnection.

8.3 Narrow Channel Counterflows

The counterflow channel used in the experiments presented in this thesis is a 4.45 cm diameter cylinder. The entire fluid in the test section is heated in this case, which makes temperature control difficult. This particular setup was used to aid the visualization technique, although we think that improvements could be made by using a narrower channel as detailed in the following subsections.

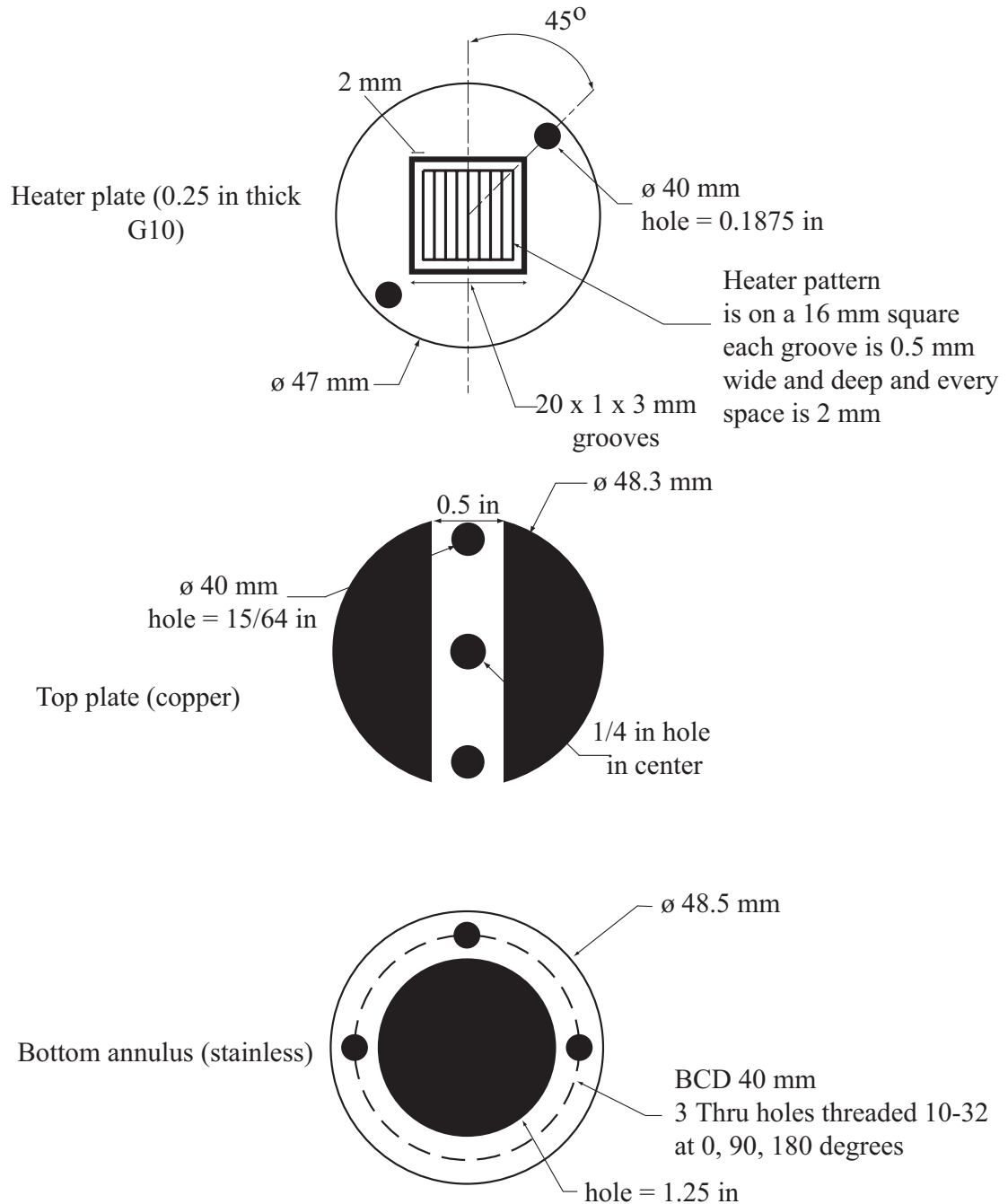


Figure 8.1: Drawings of the square heater designed and built for use in narrower counterflow channel experiments. Nichrome wire (22 AWG) is laid in a serpentine pattern in the grooves of the heater plate and held in place using stycast. The positions of the heater plate and the top plate (copper) are shown in Fig. 8.2. The bottom annulus, made of stainless steel, rests in the bottom of the test section and threaded rods are used to set the height of the heater relative to the viewing windows.

8.3.1 Extended Range of Heat Fluxes

In other experimental systems, much narrower channels (10^{-2} cm) are typically used for studying thermal counterflows. In fact, prior to our experiments 0.1 cm tubes, which are $50\times$ narrower than ours, were considered “wide channels.” Such channels were chosen for multiple reasons. First, the heat flux is inversely proportional to the channel area. Thus, for the same electrical power higher heat fluxes are achievable in channels with smaller areas. Secondly, temperature control is vastly improved in these small channels by immersing them in a He II bath. Between driving the system with less electrical power and only heating a fraction of the He II volume, better control over the experimental conditions is achieved.

For our visualization experiments, though, we must also consider the optical constraints. The present optics available to us place a lower bound on the size of the counterflow channel. We have designed and constructed a smaller counterflow channel, which is shown in Figs. 8.1 and 8.2. This channel has an area of 4 cm^2 , as opposed to 15.52 cm^2 for the one shown in Fig. 3.4(a). Furthermore, the counterflow channel is only 7.3 cm tall yielding a total volume of 29.2 cm^3 , which is only $\sim 10\%$ of the fluid volume surrounding the channel.

Given the smaller area and the surrounding He II, this channel should be able to span a larger range of heat fluxes as well as obtain better temperature control. The lowest heat flux for the experiments in Chapter 5 is set by competition with spurious counterflows from the windows of the test section. This channel, though, is surrounded by isothermal He II, which should yield a much calmer environment.

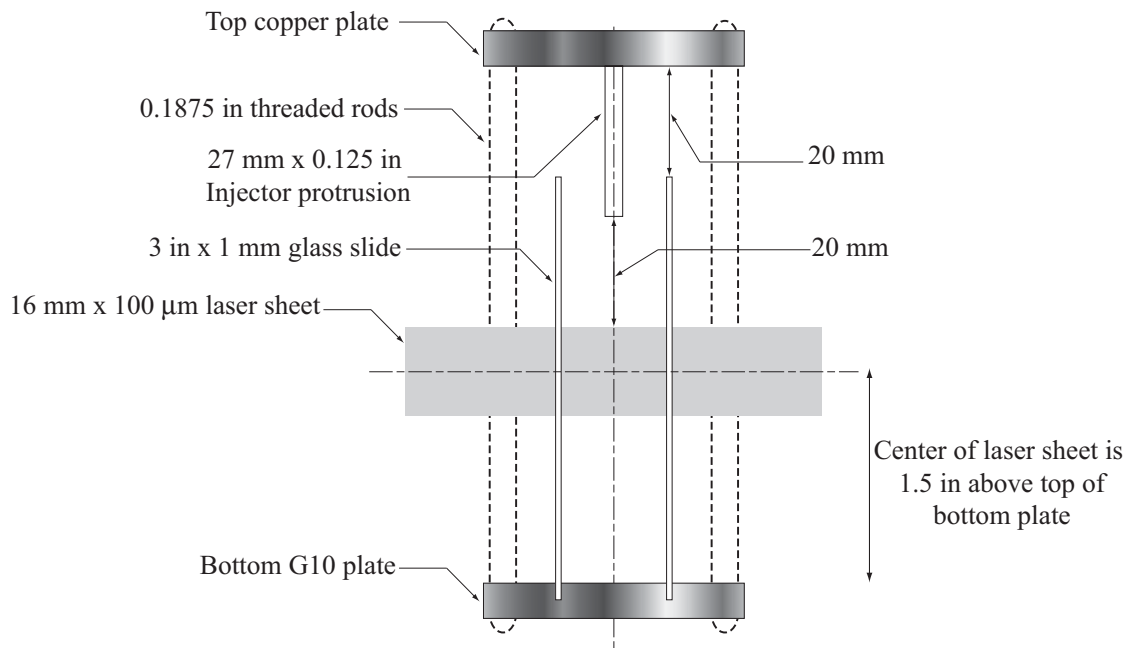


Figure 8.2: Glass cell designed and built to serve as a narrower counterflow channel. The microscope slides form the boundaries of the counterflow channel, which is open to the surrounding He II at the top. They are placed into grooves in the heater plate (see Fig. 8.1) and held in place with either stycast or vacuum grease. Threaded rods are used in conjunction with the bottom annulus shown in Fig. 8.1 to place the mid-height of the counterflow channel at the center of the viewing windows of the cryostat.

The highest heat flux for the work presented here is set by the maximum cooling rate of the pumping system. By reducing the heated fluid volume and the area of the channel, much higher heat fluxes should be attainable. In fact, preliminary experiments have shown improvements in reducing spurious counterflows as well as temperature control.

With this new experimental apparatus, several important areas of investigation are now possible. The discrepancy between the data shown in Fig. 5.5 and the results presented by Zhang and van Sciver [98] remains unresolved. The range of heat fluxes between the two experiments is adjacent but not overlapping, with all of our heat fluxes lower than those in Ref. [98]. The maximum heat flux achievable with the new counterflow channel should be well within the range of those examined by Zhang *et al.* [98], which will allow for direct comparison for the first time.

8.3.2 Poiseuille Flow

Additional experiments using thinner counterflow channels could investigate the boundary conditions for the normal fluid. It is always assumed that the normal fluid has no-slip boundary conditions, even though it has not been directly verified. By observing an entire cross-section of the flow inside a narrow channel, one could verify or refute this assumption.

As a result of the assumed boundary conditions, it is also often supposed that the normal fluid has a Poiseuille flow profile in thermal counterflows. Poiseuille flow

characterizes the parabolic velocity profile of laminar pipe flow and is given by [147]

$$\mathbf{v} = -\frac{1}{\mu} \frac{dP}{dz} (R^2 - r^2) \hat{z}, \quad (8.2)$$

where μ is the dynamic fluid viscosity, dP/dz is the uniform pressure gradient that drives the flow, R is the radius of the pipe, r is the distance from the center of the pipe, and \hat{z} is the direction of flow along the pipe's axis. We have not been able to verify or refute this assumption for a few reasons. Firstly, we only observe the center $\sim 25\%$ of the flow, which makes it difficult to precisely determine the flow profile. Secondly, the Poiseuille flow profile does not fully develop until the fluid has traversed ~ 40 pipe diameters beyond the entrance of the pipe [147]. In our experiments, we observe the flow within only two pipe diameters from the heater, which serves as the pipe entrance. Thus, a much narrower and longer counterflow channel will be necessary in order to test if the Poiseuille flow profile is established many pipe diameters away from the heater.

8.3.3 Turbulent Normal Fluid

The steady-state vortex line length density L_0 in thermal counterflows is typically given by

$$L_0 = \gamma(T) |\mathbf{v}_{\text{ns}}|^2, \quad (8.3)$$

where $\gamma(T)$ depends upon temperature and the geometry of the counterflow channel and $\mathbf{v}_{\text{ns}} = \mathbf{v}_{\text{n}} - \mathbf{v}_{\text{s}}$. It is known that for $v_{\text{ns}} > v_{\text{c}2}$, the system undergoes a transition to a state with much higher values of L [148]. This transition has been referred to as the TI – TII transition. Recent theoretical work associates this transition with

an instability in the flow of the normal fluid component [149]. The flow of a classical fluid in a pipe is always linearly stable. The instability in He II is associated with the interactions between the normal fluid and the superfluid vortices, rather than a hydrodynamic instability of a single fluid.

We do not directly measure L in the thermal counterflow studies presented in Chapter 5. However, comparing the geometry and velocities of our experiments to theoretical predictions and experimental characterizations of the TI – TII transition, we can conclude that all of our data has been obtained in the TII state. From the trajectories of particles tracing the normal fluid (black curves in Fig. 5.2), the normal fluid does not resemble the “swirling motions” we so often associate with turbulence. Specifically, the upward-moving trajectories do not deviate in the x -direction as evidenced by the sharp peak in the distributions of the trajectory angle θ at $\pi/2$ as shown in Fig. 5.4(b). Lastly, as described in Subsection 1.3.1, inertial effects are extremely important in turbulent classical fluids. However, once the heater is turned off the motions in the normal fluid cease, as shown in the time-varying distributions of the velocity components in Fig. 7.1. The only evidence that we presently have for potential turbulence in the normal fluid is that the observed normal fluid velocities v_{no} vary in time and from particle to particle, as exemplified by the standard deviations plotted in Fig. 5.5(a). To directly test these predictions, TI flow states must also be directly visualized and compared to TII states. Observing TI flow states requires using a smaller channel as well as lower heat fluxes, both of which should be possible with the channel shown in Fig. 8.2.

8.4 Rotating Superfluids

Strong initial evidence that hydrogen tracer particles may be used to visualize quantized vortices was provided by studying He II under uniform rotation. As discussed in Subsection 1.3.2, Feynman made a specific prediction for the number density of quantized vortices for a superfluid rotating at a uniform rate of Ω . This prediction stems from the following arguments. A fluid uniformly rotating at Ω has vorticity $2\Omega \text{ s}^{-1}$. A cross-section of a superfluid with n vortex lines per cm^2 produces a vorticity $\boldsymbol{\omega} = n\kappa \text{ s}^{-1}$, where $\kappa = 9.97 \times 10^{-4} \text{ cm}^2/\text{s}$ is the quantum of circulation. Thus, equating these two, Feynman predicted that one should observe $n = 2\Omega/\kappa$ quantized vortex lines per cm^2 .

Qualitative agreement with this prediction using hydrogen tracers was provided in Ref. [1]. The agreement was only qualitative because the array of vortices was viewed from an xz -plane. This introduces systematic effects and greatly limits the resolution of the measurement. The desired vantage point is a xy -plane, as shown from other experimental systems in Fig. 1.3. The previous cryostat used in Ref. [1] was incapable of providing such a view. However, the Oxford cryostat used for the studies presented here is capable of viewing a xy -plane of the system. As such, the author constructed all of the necessary apparatus to rotate the cryostat without losing the abilities to measure and control the temperature, inject the hydrogen-helium mixture, and acquire images of the dynamics. Preliminary experiments have already taken place and are discussed briefly in the subsections below.

8.4.1 Lattice Formation

The details of the formation and destruction of regular lattices of quantized vortices, to our knowledge, has not been explored. In particular, if we begin with a state describing stationary He I, that is $(\Omega = 0, T > T_\lambda)$, then we may arrive at the final state of a rotating superfluid $(\Omega > 0, T < T_\lambda)$ by two different paths shown in the following commutation diagram:

$$\begin{array}{ccc}
 (\Omega = 0, T > T_\lambda) & \xrightarrow{\text{rotate}} & (\Omega > 0, T > T_\lambda) \\
 \downarrow \text{cool} & & \downarrow \text{cool} \\
 (\Omega = 0, T < T_\lambda) & \xrightarrow{\text{rotate}} & (\Omega > 0, T < T_\lambda)
 \end{array}$$

That is, we can either transition to the superfluid state then rotate the system or we can bring the system to solid-body rotation then pass through the λ -transition. If equilibrium is attained the final state is insensitive to the path taken; however the dynamics of the formation of the lattice could be quite different between these scenarios.

We have performed preliminary studies of the lattice formation in He II. A typical image from one of our movies is shown in Fig. 8.3 along with a blown up patch showing the locations of neighboring vortices. Clearly the lattice structure is not as evident as the cases displayed in Fig. 1.3. There are at least two reasons for this. Firstly, spurious counterflows from the windows drive flows that will disturb any lattice structure. These can be minimized by isolating a portion of the fluid in a cell immersed in a He II bath, as suggested for the counterflow studies as well

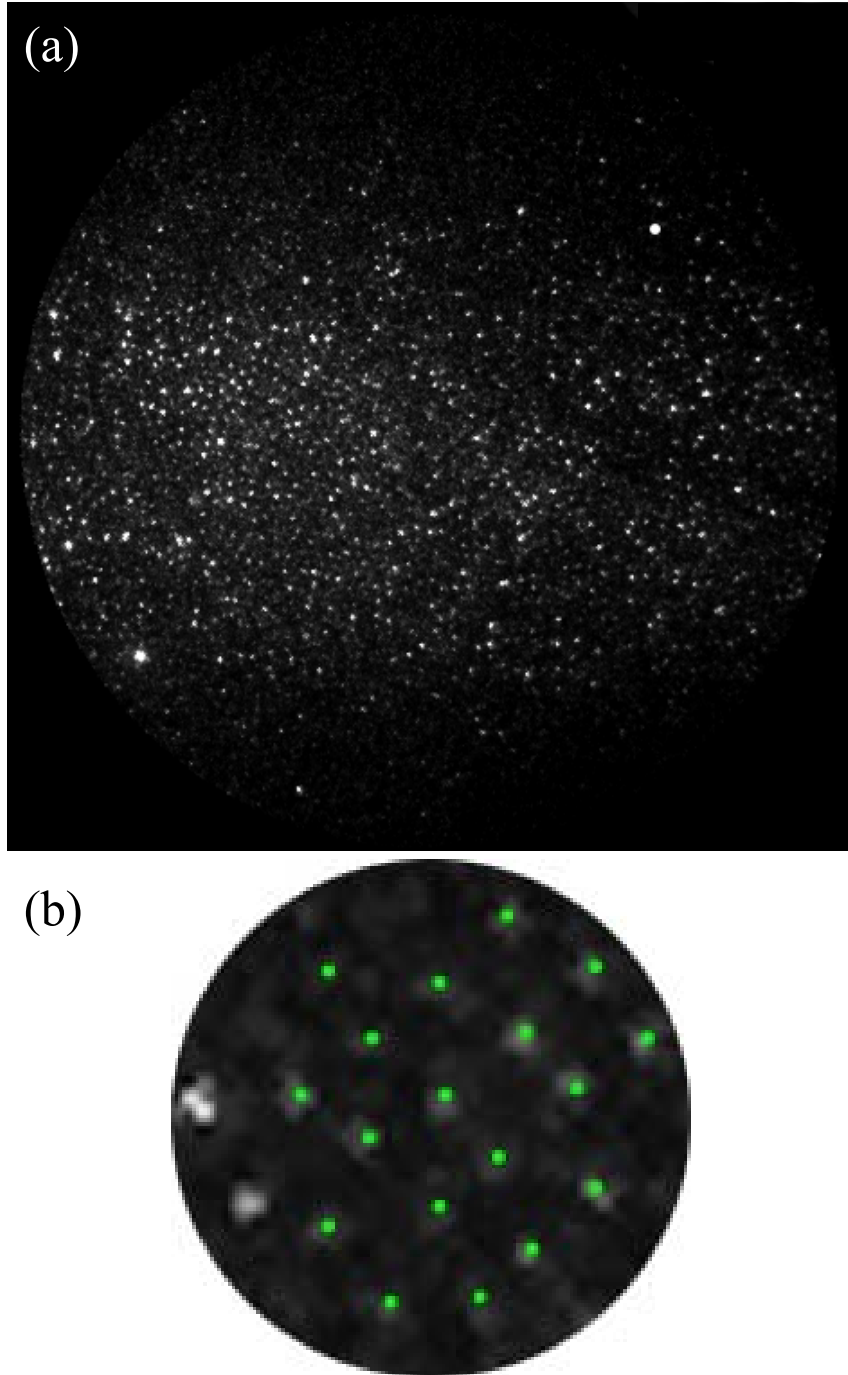


Figure 8.3: Images from preliminary experiments of uniformly rotating He II with $\boldsymbol{\Omega} = \Omega \hat{z}$. (a) The full field of view ($8 \text{ mm} \times 8 \text{ mm}$) showing an xy cross-section of the fluid. (b) A magnified view of a portion of the fluid with green dots denoting particle centers that we interpret as marking the positions of quantized vortices. The lattice structure is not as clearly evidenced as the previous experimental images shown in Fig. 1.3. The lattice structure is distorted by wave motions and inadequate control of the experimental conditions.

in Subsection 8.3.1. Secondly, the lattice is able to support wave modes, which are clearly evident in the movies. These waves offer an independent future direction of inquiry as detailed in the next subsection.

8.4.2 Tkachenko Waves and Rotating Counterflows

Lattices of quantized vortices are capable of sustaining wave modes, often referred to as Tkachenko waves [150]. These waves are transverse oscillations of the quantized vortices and are restored by the vortex line tension and elasticity of the lattice itself. Our experiments and particle-tracking algorithm provide an excellent means of testing calculations pertaining to Tkachenko oscillations.

In addition to lattice oscillations, applying a counterflow along the axis of rotation is also an active area of study in He II. Rotation tends to align quantized vortices with the axis of rotation whereas mutual friction and counterflowing motions tend to stretch them in orthogonal directions. This competition can be systematically studied by varying the relative ratio of the rotational forcing and the counterflow forcing. We expect that this type of flow will yield very interesting dynamics and steady-states. Furthermore, results from this type of system may be relevant to others that are characterized by a competition between organizing and disorganizing effects — the first example to come to mind would be magnetic field lines in a star that are organized by rotational effects and disorganized from convection and other forms of turbulence.

8.4.3 Taylor-Couette Flow

The flow between independently rotating cylinders is referred to as Taylor-Couette flow. This system has been studied extensively in classical turbulence because many rich phenomena may be studied within a single apparatus. The rotating cryostat could be modified to contain an independently rotating inner cylinder, allowing for Taylor-Couette flow studies in both He I and He II within the same apparatus. Since the similarities and distinctions between classical turbulence and quantum turbulence is such an active area of study, performing identical experiments and measurements within the same apparatus using both classical and quantum fluids could provide valuable information to this field of study.

8.5 Injection Improvements

The injection technique discussed in Gregory Bewley's thesis [1] has served the studies contained in his thesis as well as this one quite well. In fact, the number of new discoveries that have been made using this technique in only a few years is quite remarkable. However, there are a few aspects of the technique that we feel might be able to be improved.

8.5.1 Pre-cooled Mixtures

Presently a room temperature mixture of hydrogen and helium is injected directly into the bulk of the liquid helium immediately above T_λ . This room temperature gas introduces a significant amount of heat input into the system. Indeed,

for sufficiently long injections one is able to directly observe the increase in temperature of the entire fluid in the test section.

We have observed that using the very same technique immediately below T_λ does not yield satisfactory results. Rather than obtaining a “mist” of sub-micron particles, the hydrogen tends to be orders of magnitude larger and clumped into localized areas of the fluid. One potential explanation for this is that the heat that is injected with the mixture causes a vigorous, localized counterflow. This counterflow produces many quantized vortices inside and very near the injector tube that cause the particles to clump as they form.

Independent of whether or not the heat input precludes injection directly into the He II state, reducing the amount of heat into the system is desirable. This may be achieved by a few different means. Firstly, the injection lines can be passed through a vessel filled with liquid nitrogen (77 K), which could remove a significant fraction of the heat. Or, the mixture could be allowed to pass into a temperature-controlled vessel within the cryostat itself. This vessel would be positioned above the free surface of the liquid helium and would be cooled by the evaporated helium gas as it passes into the pumping lines. The mixture would be held at a temperature above the boiling point of hydrogen (20 K at atmospheric pressure) with an internal heater. Then a solenoid valve between the containment vessel and the injection tube (all inside of the test section) could be opened to allow the pre-cooled mixture to be injected into the liquid helium. A similar technique has already been implemented by the group of van Sciver.

8.5.2 Injection Below Transition

The greatest restriction on the efficiency of conducting the experiments is the necessity to inject the hydrogen mixture above T_λ . The typical procedure is to inject, slowly cool the system for approximately 20–50 minutes, take measurements for a few minutes, then allow the system to heat back up above T_λ over a span of tens of minutes again. This process greatly consumes time as well as liquid helium, which eventually evaporates by the end of the work day.

If one were able to directly inject into the He II state then the efficiency of the experiments would be drastically improved. As we discussed in the previous subsection, pre-cooling the hydrogen mixture could provide a means of injecting directly into the He II state. Other groups have also removed the injector tube from the bulk of the liquid such that the injected gas impinges on the free surface of the liquid. Another possibility would be to allow the hydrogen to very slowly “leak” into the cryostat by greatly restricting the flow rate through the injection line. We have unintentionally observed that residual hydrogen gas from the day before is capable of producing excellent tracer particles below T_λ . Lastly, we have also had some success injecting into the helium reservoir then transferring the He I in the reservoir into a much cooler test section partially filled with He II.

One other distinction between the He I and He II states may explain the difference in the quality of the tracer particles. The He I state is characterized by very strong, vigorous mixing produced by convection from (unavoidable) heat leaks into the test section through the vacuum insulation. Once the system transitions into

the He II state, the effective thermal conductivity grows by a factor of 10^7 , resulting in a much calmer state in He II. When we inject in He I, therefore, the hydrogen particles are very rapidly mixed throughout the entire fluid volume. In the He II state, on the other hand, we observe that the hydrogen is always concentrated in localized patches of the fluid. Therefore, we propose that intentionally driving flows in the He II state as one injects such that the hydrogen properly mixes throughout the system may yield more desirable results.

8.6 Computational Studies

In addition to the experimental studies suggested above, we believe there are several potentially interesting computational studies related to this work. Many numerical simulations of counterflow turbulence [50–56] and decaying counterflow turbulence [110, 111] have been performed. However, almost all of these studies focus on the vortex line length density L because it is the most common experimental measurement. We are not aware of any computational studies that have looked at the velocity field in great detail, even though it is readily available in such simulations. Now that we have an experimental means of determining the velocity field one could make direct comparisons with the velocity statistics, for example, in numerical simulations of counterflow turbulence and decaying counterflow turbulence. Preliminary results have already been obtained by Tsubota and coworkers [55] comparing our measured values of the vortex line velocities \mathbf{v}_L to those in numerical simulations.

We have also observed an anisotropy in reconnection events in our decaying counterflow turbulence experiments (see Section 6.8). Even though the implementation is *ad hoc*, numerical simulations of decaying counterflow turbulence involve many reconnection events. The statistics of the displacements vectors in these computations could be directly compared to the data shown in Figs. 6.16 and 6.17. This is a potentially useful benchmark for numerical simulations that assume the localized induction approximation (LIA). Adachi *et al.* [56] recently pointed out a clear discrepancy in the reconnection process and the resulting anisotropy between simulations that assume the LIA as compared to those that compute the full Biot-Savart integral.

Lastly, we argue that the observed fluctuations in the reconnection dynamics are caused by the local environment and initial and boundary conditions. Numerical computations using either line-vortex models or the Gross-Pitaevskii equation could systematically change these conditions to see if our hypothesis is true. The previous work of de Waele and Aarts [57] only computes the dynamics within $3 \mu\text{s}$ before the reconnection event whereas we investigate the dynamics up to 0.25 s away from the event both before and after. We conjecture that the observed effects become more pronounced away from the moment of reconnection.

Appendix A

Codes

In this appendix, we provide a few of the analysis codes that have been greatly used throughout the work presented here. We begin with MatLab codes that are part of the temperature control algorithm that convert the measured voltage drop across the thermistor into the temperature. In the final section, examples of the codes used to find and analyze individual reconnection events are presented.

A.1 Matlab Codes

In this section, we provide the two MatLab codes that are used to convert the voltage measurements described in Subsection 3.2 and shown in Fig. 3.9 into temperature. Assuming the recommended resistors and voltages described in Table 3.1 are used, the voltage drop across the thermistor may be directly converted into the temperature using `givetemplo.m` for $T < 4.5$ K. For $T > 4.5$ K, `givetemphi.m` must be used in conjunction with 0.450 V amplitude on the SR830 lock-in amplifier as opposed to 0.150 V appropriate for lower temperatures.

```

% givetemplo.m

% give temperature from voltage reading from calibration curve
% for low temp thermistor number "three."
% LOW TEMP RANGE assumes 0.33 microamp excitation, which is
% achieved by driving a 0.150 V AC signal with SR830
% through the thermistor and a 450kOhm resistor in series.
%
% temp = givetemp(voltage);

function temp = givetemplo(voltage)

% Enter calibration curve data in the
% form [Temperature, Resistance, irrelevant column]
data = [
1.800300002 8072.55998 0.246999994;
1.825049996 7862.677129 0.246999994;
1.850149989 7664.535781 0.246999994;
1.87529999 7473.027109 0.259000003;
1.899199963 7291.78334 0.259000003;
1.924499989 7119.815859 0.270999998;
1.949799955 6952.30832 0.270999998;
1.97359997 6794.911855 0.286000013;
1.998400033 6650.839531 0.286000013;
2.024950027 6503.725 0.286000013;
2.049649954 6354.258691 0.300000012;
2.075049996 6217.476191 0.300000012;
2.09920001 6087.396309 0.314999998;
2.124599934 5960.873809 0.314999998;
2.148300052 5843.206738 0.330000013;
2.174200058 5722.037949 0.330000013;
2.20025003 5609.416719 0.347000003;
2.225999951 5503.337129 0.347000003;
2.250150084 5396.935195 0.347000003;
2.276499987 5294.59502 0.363999993;
2.299299955 5197.700918 0.363999993;
2.399649978 4842.040098 0.400999993;
2.498350024 4532.586836 0.419999987;
2.600000024 4260.749922 0.442000002;
2.700399995 4019.612676 0.463999987;
2.79974997 3804.92917 0.488999993;
2.898350000 3611.965762 0.537000000;
3.000050068 3436.598633 0.56400001;
3.100150108 3279.08293 0.593999982;
3.20025003 3135.242705 0.593999982;

```

Figure A.1: Givetemplo.c code used to convert the voltage measurements of the thermistor into temperature for $T < 4.5$ K.

```

3.300049901 3002.996465 0.623000026;
3.401650071 2882.870586 0.654999971;
3.500050068 2771.296182 0.685999999;
3.597750068 2673.941113 0.721000016;
3.706599951 2569.893887 0.757000029;
3.801400065 2488.492051 0.757000029;
3.898849964 2407.517256 0.794000003;
3.998700023 2331.509541 0.833000004;
4.10014987 2259.982393 0.833000004;
4.199800014 2192.751523 0.874000013;
4.299749851 2130.458213 0.874000013;
4.399649858 2071.630635 0.917999983;
4.500849962 2016.927378 0.964999974];

Tdata = data(:,1); % get a vector of temperatures
Rdata = data(:,2); % get corresponding vector of resistances

voltage = abs(voltage); % make sure the voltage is positive
R = (450000*voltage)./(0.150-voltage); % compute resistance of
                                     % thermistor using simple
                                     % voltage divider equations

%perform interpolation to determine the temperature of the probe
temp = interp1(Tdata,Rdata,R, 'spline', 'extrap');

end

```

Givetemplo.m (continued)

```

% givetemphi.m

% give temperature from voltage reading from calibration curve
% for low temp thermistor number "three."
% HIGH TEMP RANGE assumes 1.0 microamp excitation, which is
% achieved by driving a 0.450 V AC signal with SR830
% through the thermistor and a 450kOhm resistor in series.
%
% temp = givetemp(voltage);

function temp = givetemphi(voltage)

% Enter calibration curve data in the
% form [Temperature, Resistance, irrelevant column]
data = [3.998700023 2331.509541 0.833000004;
4.10014987 2259.982393 0.833000004;
4.199800014 2192.751523 0.874000013;
4.299749851 2130.458213 0.874000013;
4.399649858 2071.630635 0.917999983;
4.500849962 2016.927378 0.964999974;
4.999499798 1785.242959 1.065000057;
5.497499943 1605.918066 1.174999952;
6.000200033 1462.983594 1.294999957;
6.501349926 1346.336016 1.425999999;
7.006900072 1247.984604 1.496999979;
7.501100063 1167.28792 1.651000023;
7.999600172 1097.337813 1.733999968;
8.498399734 1036.367891 1.820000052;
8.999300003 983.2316699 1.909999967;
9.499549866 935.9788281 2.005000114;
9.999300003 894.0801343 2.105999947;
15.00329971 632.0136621 2.963000059;
20.00139999 500.5533069 3.78399992;
25 418.798894 4.59499979;
29.99835014 362.06172 5.300000191;
34.99995041 320.109989 5.813000202;
40.00014877 287.6628088 6.69299984;
45.00105095 261.7299915 7.352000237;
49.99979973 240.5499414 7.718999863;
55.00174904 222.8740015 8.475999832;
60.00094986 207.8785101 9.331000328;
65.0014534 194.9755261 9.795000076;
70.00124741 183.7570465 10.28299999;
75.00090027 173.8747992 10.79599953;
80.00219727 165.1155725 11.33399963;

```

Figure A.2: Givetemphi.c code used to convert the voltage measurements of the thermistor into temperature for $T > 4.5$ K. For these higher temperatures, $1 \mu\text{A}$ of current excitation should be used rather than $0.33 \mu\text{A}$ appropriate for lower temperatures.

```

85.0027504 157.2766211 11.89500046;
90.00284958 150.2006915 12.48200035;
95.00250244 143.7938147 13.09200001;
100.0016975 137.9665094 13.72700024;
150.0240021 99.19679352 19.22299957;
200.0272446 78.20579163 24.47500038;
250.0323486 65.09776489 29.70199966;
300.0477905 56.1993222 34.31900024];

Tdata = data(:,1); % get a vector of temperatures
Rdata = data(:,2); % get corresponding vector of resistances

voltage = abs(voltage); % make sure the voltage is positive
R = (450000*voltage)./(0.450-voltage); % compute resistance of
% thermistor using simple
% voltage divider equations

%perform interpolation to determine the temperature of the probe
temp = interp1(Tdata,Rdata,R, 'spline', 'extrap');

end

```

Givetemphi.m (continued)

A.2 C codes for data analysis

In this section we present the essential C codes that have been used to analyze the reconnection events presented in Chapter 6. All of the codes take a trajectory file formatted as rows of [track number, frame number, x -position, z -position, radius of gyration] as the first input. The codes then determine all possible pairs of particles that meet the criterion (6.1). For each pair that meet this criterion, the pairwise-separation $\delta(t)$ is fit to either the arbitrary power-law expression given by Eq. (6.2) or the correction-factor expression given by Eq (6.5) depending upon the particular C code.

The program used to fit forward events to the correction-factor expression, `pairsubcritexp.c`, is shown in Fig. A.3. For each pair of particles that meet the criterion (6.1), 500 evenly-spaced values of t_0 are fit and the set of $\{A, c, t_0\}$ that minimizes χ^2 is output. The values of A and c for each t_0 are determined by a linear-least squares fit to the following equation

$$\frac{\delta(t)}{(t - t_0)^{1/2}} = m(t - t_0) + b. \quad (\text{A.1})$$

Once the values of m and b are determined, they may be converted into A and c by

$$A = \frac{b}{\sqrt{k}} \quad (\text{A.2})$$

$$c = \frac{m}{b}. \quad (\text{A.3})$$

The corresponding code used to fit reverse events to the correction-factor expression is `pairsubcritexp_rev.c`. The two programs are identical except that `pairsubcritexp_rev.c` negates all of the times and reverses the order of the trajectory file, which

allows us to then preserve the rest of the algorithm used for the forward events.

The code used to fit forward events to the arbitrary power-law expression, `pairedtavecscreal.c`, is shown in Fig. A.4. For each pair of particles that meet the criterion (6.1), 500 evenly-spaced values of α in the interval $0 < \alpha < 2$ are fit and the set of $\{\alpha, B, t_0\}$ that minimizes χ^2 is output. The values of B and t_0 for each α are determined by a linear least-squares fit of $[\delta(t)]^{1/\alpha}$. Other than the particular fitting function, the details of `pairedtavecscreal.c` are identical to those in `pairsubcritexp.c`. We therefore only thoroughly comment `pairsubcritexp.c`. The corresponding algorithm for reversed events is `pairedtavecscreal_rev.c`, which again negates the times and reverses the order of the trajectory file as in `pairsubcritexp_rev.c`.

```

/* pairsubcritexp.c */
#include <stdio.h>
#include <math.h>
#include <stdlib.h>
struct fitpar { double slope; double inter; double r2; };
struct fitpar fitit(double *dx, double *dy, int n);
main(argc, argv)
int argc;
char *argv[];
{
    /* Define variables */
    int i,j,k,n,index=0, numt0;
    double alpha,delx, dely, sumn, sum,f,g,v1,v2;
    static float datax[10000000][4];
    float epsilon, delta, fps;
    double dx[2048],dy[2048],dxshift[2048];
    double dyshift[2048], dxsqrt[2048];
    double tmp2,tmp3,numdecs, delta2, A, c;
    double minA, minc, mint0;
    double minalpha,minchi, minsl, mininter, finalsep;
    int mint[150000],maxt[150000], tminloc[150000];
    double tmp,a,b,sumx,sumy,sumxy,sumx2,sumy2,r2;
    double chi2, del2, del3, t0, initsep;
    double displacement, spacing, inv,amp;
    double foveri, meanrad1, meanrad2, sumrad1=0;
    double sumrad2=0, v1max=-1, v2max=-1;
    double delx1, dely1, delx2, dely2, mag1, mag2;
    double unitx1, unity1, unitx2, unity2;
    double diffx, diffy, magdiff, magsum, angle;
    struct fitpar thisfit;
    int track,tracks,d,m, count, numalphas;
    int increm=1,shift, print=0, geom=0;
    FILE *fpi,*fpi2,*fpo;
    d=atoi(argv[2]); /* d is the number of
                        movie frames used in the fits */
    numt0=250; /* numt0 is the number of values
                of t0 used in the fit */
    delta=atof(argv[3]);/* define the delta
                        ratio criterion */
    delta2=delta*delta;
    fps=atof(argv[4]); /* read in the frame rate
                        of the movie in frames per second */
    spacing=5.0/(numt0*fps);/* define the spacing
                        between values of t0 */
    /* determine if it is possible
       to read in the movie file */

```

Figure A.3: Pairsubcritexp.c code used to fit the correction-factor expression to the reconnection events. An example execution is pairsubcritexp p42_m20_r5.gdf.f.f 20 4 80 > out.dat.

```

if ((fpi=fopen(argv[1],"r"))==NULL) {
    fprintf(stderr,"File 2 opened is stdin for input\n");
    fpi=stdin;
}
/* initialization */
for (i=0; i<150000; i++) {
    mint[i]=1000000;
    maxt[i]=-100000;
    tminloc[i]=-1;
}
n=0;
/* read in the movie file */
while (fread(&datax[n][0],4,1,fpi)==1) {
    fread(&datax[n][1],4,1,fpi);
    fread(&datax[n][2],4,1,fpi);
    fread(&datax[n][3],4,1,fpi);
    fread(&tmp,4,1,fpi);
    /* determine the first frame of each particle track */
    if (mint[(int)datax[n][0]]>(int)datax[n][1]) {
        mint[(int)datax[n][0]]=(int)datax[n][1];
        tminloc[(int)datax[n][0]]=n;
    }
    /* determine the last frame of each particle track */
    if (maxt[(int)datax[n][0]]<(int)datax[n][1])
        maxt[(int)datax[n][0]]=(int)datax[n][1];
    n++;
}
tracks=(int)datax[n-2][0]; /* determine the number of
                           particle tracks */
/* this code assumes:
   column 0 is track number
   column 1 is time
   column 2 is x position
   column 3 is z position */
/* begin the massive loop over all rows of the trajectory file */
for (i=0; i<n-d; i+=increment) {
    /* check if the particle track in row i and
       row i+d-1 are the same particle */
    if ((datax[i][0]==datax[i+d-1][0])) {
        increment=1;
        /* loop over all other particles
           with a greater track number */
        for (track=(int)datax[i][0]+1; track<tracks; track++) {
            /* check if second particle track under consideration
               is the same in row i and row i+d-1 */

```

Pairsubcritexp.c (continued)

```

if (((int)datax[i][1]>=mint[track]) &&
((int)datax[i+d-1][1]<=maxt[track])) {
    k=tminloc[track]+datax[i][1]-mint[track];
    /* determine separation in x-direction */
    tmp2=datax[i][2]-datax[k][2];
    /* determine separation in z-direction */
    tmp3=datax[i][3]-datax[k][3];
    /* determine initial particle separation */
    initsep=(tmp2*tmp2+tmp3*tmp3);
    /* measure x-component of delta vector */
    del2=datax[i+d-1][2]-datax[k+d-1][2];
    /* measure z-component of delta vector */
    del3=datax[i+d-1][3]-datax[k+d-1][3];
    /* measure final separation */
    finalsep=(del2*del2+del3*del3);
    /* determine if pair of particles meets
    the delta criterion */
    foveri=finalsep/initsep;
    /* if it meets the delta criterion make
    vectors of time and delta to fit */
    if (foveri>=delta2) {
        for (j=0; j<d; j++) {
            tmp2 =datax[i+j][2]-datax[k+j][2];
            tmp3 =datax[i+j][3]-datax[k+j][3];
            dx[j]=datax[i+j][1]/fps;
            /* multiply by 16E-4
            to convert pixels to cm */
            dy[j]=sqrt(tmp2*tmp2+tmp3*tmp3)*16E-4;
        }
        /* perform loop over all possible values of
        t0 and determine the value that minimizes chi2 */
        for (minchi=1000000,m=0; m<numt0; m++) {
            t0=(dx[0]-(m*spacing));
            if ((dx[0]-t0)>=0) {
                for (j=0; j<d; j++) {
                    dxshift[j]=dx[j]-t0;
                    dxsqrt[j]=sqrt(dxshift[j]);
                    dyshift[j]=dy[j]/dxsqrt[j];
                }
                /* perform fit to correction-factor expression */
                thisfit=fitit(dxshift,dyshift,d);
                A=thisfit.inter;
                if (A!=0) c=thisfit.slope/A; else c=-100;
                sumx2=0;
                for (j=0; j<d; j++) {

```

Pairsubcritexp.c (continued)

```

        /* compute chi2 normalized by 4E-4 cm
        which is estimate in error */
        dely=(dy[j]-(A*dxsqrt[j]*(1+c*dxshift[j])))/4E-4;
        sumx2+=dely*dely;
    }
    chi2=sumx2/d;
    if (chi2<minchi) {
        mint0=t0;
        minchi=chi2;
        minA=A;
        minc=c;
        print=1;
    }
}
}

if ((print) && (c!=-100)) {
    /* print values of the fit parameters that
    minimize chi2 and the particle track numbers,
    and time of the event in seconds */
    printf("%g %g %g %g ",minA, minc, mint0, minchi);
    printf("%g %g %g\n",datax[i][0],datax[k][0],datax[i][1]/fps);
    print=0;
}
}
}
}
} else {
    shift=tminloc[(int)datax[i][0]+1]-i;
    if ((shift>1)) increm=shift;
    else increm=1;
}
}

return(0);
}

/* perform a linear fit and output the slope and intercept */
struct fitpar fitit(dx, dy, n)
double dx[2048],dy[2048];
int n;
{
    double sumn, sumx, sumy, sumx2, sumy2, sumxy;
    double tmp, delx, dely, ra, rb;
    struct fitpar tmp2;
    int i;
    sumn=0; sumx=0; sumy=0; sumx2=0; sumy2=0; sumxy=0;
    for (i=0; i<n; i++) {

```

Pairsubcritexp.c (continued)

```
        sumn++;
        sumx += dx[i];
        sumy += dy[i];
        sumx2 += dx[i]*dx[i];
        sumy2 += dy[i]*dy[i];
        sumxy += dx[i]*dy[i];
    }
    tmp2.slope=(sumn*sumxy-sumx*sumy)/(sumn*sumx2-sumx*sumx);
    tmp2.inter=(sumy-tmp2.slope*sumx)/sumn;
    return(tmp2);
}
```

Pairsubcritexp.c (continued)

```

/* pairedtavecsreal.c */
#include <stdio.h>
#include <math.h>
#include <stdlib.h>
struct fitpar { double slope; double inter; double r2; };
struct fitpar fitit(double *dx, double *dy, int n);
main(argc, argv)
int argc;
char *argv[];
{
    int i,j,k,n,index=0;
    double alpha,dex, dey, sumn, sum,f,g,v1,v2,fps;
    static float datax[10000000][4];
    float epsilon, delta;
    double dx[2048],dy[2048],dya[2048];
    double tmp2,tmp3,numdecs, delta2;
    double minalpha,minchi, minsl, mininter, mint0,finalsep;
    int mint[150000],maxt[150000], tminloc[150000];
    double tmp,a,b,sumx,sumy,sumxy,sumx2,sumy2,r2;
    double chi2, del2, del3, t0, initsep, displacement;
    double spacing, inv,amp;
    double foveri, meanrad1, meanrad2, sumrad1=0;
    double sumrad2=0, v1max=-1, v2max=-1;
    double delx1, dey1, dex2, dey2, mag1, mag2;
    double unitx1, unity1, unitx2, unity2;
    double diffx, diffy, magdiff, magsum, angle;
    struct fitpar thisfit;
    int track,tracks,d,m, count, numalphas;
    int increm=1,shift, print=0, geom=0;
    FILE *fpi,*fpi2,*fpo;
    d=atoi(argv[2]);
    numalphas=500;
    delta=atof(argv[3]);
    fps=atof(argv[4]);
    delta2=delta*delta;
    spacing=2.0/numalphas;
    if ((fpi=fopen(argv[1],"r"))==NULL) {
        fprintf(stderr,"File 2 opened is stdin for input\n");
        fpi=stdin;
    }
    for (i=0; i<150000; i++) {
        mint[i]=1000000;
        maxt[i]=-100000;
        tminloc[i]=-1;
    }
}

```

Figure A.4: Pairedtavecsreal.c code used to perform the arbitrary power-law fits to the reconnection events. An example execution is pairedtavecsreal p42_m20_r5.gdf.f.f 20 4 80 > out.dat.

```

n=0;
while (fread(&datax[n][0],4,1,fpi)==1) {
    fread(&datax[n][1],4,1,fpi);
    fread(&datax[n][2],4,1,fpi);
    fread(&datax[n][3],4,1,fpi);
    fread(&tmp,4,1,fpi);
    if (mint[(int)datax[n][0]]>(int)datax[n][1]) {
        mint[(int)datax[n][0]]=(int)datax[n][1];
        tminloc[(int)datax[n][0]]=n;
    }
    if (maxt[(int)datax[n][0]]<(int)datax[n][1])
        maxt[(int)datax[n][0]]=(int)datax[n][1];
    n++;
}
tracks=(int)datax[n-2][0];
/* this code assumes:
   column 0 is track number
   column 1 is time
   column 2 is x position
   column 3 is y position */
for (i=0; i<n-d; i+=incred) {
    if ((datax[i][0]==datax[i+d-1][0])) {
        increm=1;
        for (track=(int)datax[i][0]+1; track<tracks; track++) {
            if (((int)datax[i][1]>=mint[track]) && ((int)datax[i+d-1][1]<=maxt[
[track]])) {
                k=tminloc[track]+datax[i][1]-mint[track];
                tmp2=datax[i][2]-datax[k][2];
                tmp3=datax[i][3]-datax[k][3];
                initsep=(tmp2*tmp2+tmp3*tmp3);
                del2=datax[i+d-1][2]-datax[k+d-1][2];
                del3=datax[i+d-1][3]-datax[k+d-1][3];
                finalsep=(del2*del2+del3*del3);
                foveri=finalsep/initsep;
                if (foveri>=delta2) {
                    for (j=0; j<d; j++) {
                        tmp2 =datax[i+j][2]-datax[k+j][2];
                        tmp3 =datax[i+j][3]-datax[k+j][3];
                        dx[j]=datax[i+j][1];
                        dy[j]=sqrt(tmp2*tmp2+tmp3*tmp3);
                    }
                    delx1=datax[i+d-1][2]-datax[i][2];
                    dely1=datax[i+d-1][3]-datax[i][3];
                    delx2=datax[k+d-1][2]-datax[k][2];
                    dely2=datax[k+d-1][3]-datax[k][3];

```

Pairedtavecsreal.c (continued)

```

        /* mag1=sqrt (delx1*delx1+dely1*dely1);
        mag2=sqrt (delx2*delx2+dely2*dely2);
        unitx1=delx1/mag1;
        unity1=dely1/mag1;
        unitx2=delx2/mag2;
        unity2=dely2/mag2;
        diffx=unitx1-unitx2;
        diffy=unity1-unity2;
        magdiff=sqrt (diffx*diffx+diffy*diffy);
        sumx=unitx1+unitx2;
        sumy=unity1+unity2;
        magsum=sqrt (sumx*sumx+sumy*sumy);
        angle=atan (magdiff/magsum) /3.14159265;
        */
for (minchi=1000000,m=0; m<numalphas; m++) {
    alpha=spacing*(m+1)+0.1;
    inv=1.0/alpha;
    for (j=0; j<d; j++) {
        dya[j]=pow (dy[j],inv);
    }
    thisfit=fitit (dx,dya,d);
    t0=-1.0*thisfit.inter/thisfit.slope;
    if ((t0>=dx[0])) {
        sumx=0; sumxy=0; t0=dx[0]-0.01;
        for (j=0; j<d; j++) {
            sumx+=pow (dx[j]-t0,2*alpha);
            sumxy+=pow (dx[j]-t0,alpha)*dy[j];
        }
        amp=sumxy/sumx;
    }
    else amp=pow (thisfit.slope,alpha);
    sumx2=0;
    for (j=0; j<d; j++) {
        dely=dy[j]-(amp*pow (dx[j]-t0,alpha));
        sumx2+=dely*dely;
    }
    chi2=sumx2/d;
    if ((chi2<minchi) && (fabs (datax[i][1]-t0)<100)){
        minalpha=alpha;
        minchi=chi2;
        minsl=amp;
        mint0=t0;
        print=1;
    }
}
}

```

Pairedtavecsreal.c (continued)

```

        if ((print) && (minalpha<2.0) && (minalpha>0.1)) {
/* this line converts the fitamplitude A into units
of cm/s^{alpha} */
        minsl=minsl*16E-4*pow(fps, minalpha);
/* this is to convert it to nondimensional units
assuming our estimate of our error is 4 microns */
        minchi=minchi*16.0;
        printf("%g %g %g %g %g ",minalpha,sqrt(foveri),minsl,
mint0, minchi);
        printf("%g %g %g %g ",delx1,dely1,delx2, dely2);
        printf("%g %g %g\n",datax[i][0],datax[k][0],datax[i][1]);
        print=0;
        }
    }
}
} else {
    shift=tminloc[(int)datax[i][0]+1]-i;
    if ((shift>1)) increm=shift;
    else increm=1;
}
}
return(0);
}
struct fitpar fitit(dx, dy, n)
double dx[2048],dy[2048];
int n;
{
    double sumn, sumx, sumy, sumx2, sumy2, sumxy;
    double tmp, delx, dely, ra, rb;
    struct fitpar tmp2;
    int i;
    sumn=0; sumx=0; sumy=0; sumx2=0; sumy2=0; sumxy=0;
    for (i=0; i<n; i++) {
        sumn++;
        sumx += dx[i];
        sumy += dy[i];
        sumx2 += dx[i]*dx[i];
        sumy2 += dy[i]*dy[i];
        sumxy += dx[i]*dy[i];
    }
    tmp2.slope=(sumn*sumxy-sumx*sumy)/(sumn*sumx2-sumx*sumx);
    tmp2.inter=(sumy-tmp2.slope*sumx)/sumn;
    return(tmp2);
}

```

Pairedtavecscreal.c (continued)

Appendix B

Raw Data and Parameters

In this appendix we include tables of raw data plotted throughout the thesis as well as parameters important to dynamics in He II.

B.1 Counterflow Experiments

Table B.1: Experimental parameters for the counterflow experiments presented in Chapter 5 and plotted in Fig. 5.1. The Date and Run denote the source of the data, T is the temperature shown in the legend of Fig. 5.5, T_{\min} is the minimum temperature during the run, T_{\max} is the maximum temperature during the run, Q is the heater power and q is the applied heat flux.

Date	Run	T (K)	T_{\min} (K)	T_{\max} (K)	Q (W)	q (mW/cm ²)
041608	8	1.80	1.788	1.799	0.207	13.3
042508	2	1.80	1.794	1.811	0.219	14.1
041708	10	1.80	1.798	1.817	0.235	15.1
042408	4	1.80	1.749	1.778	0.306	19.7
041808	1	1.80	1.767	1.813	0.361	23.3
041508	10	1.80	1.800	1.840	0.489	31.5
041608	7	1.85	1.826	1.831	0.208	13.4
042408	3	1.85	1.797	1.816	0.306	19.7
041708	5	1.85	1.823	1.845	0.356	22.9
042408	5	1.85	1.802	1.827	0.39	25.1
042308	7	1.85	1.815	1.852	0.536	34.5
041708	6	1.85	1.818	1.856	0.611	39.4
041708	2	1.90	1.887	1.893	0.224	14.4
042408	2	1.90	1.846	1.854	0.311	20.0
041508	2	1.90	1.900	1.930	0.403	26.0
042408	6	1.90	1.852	1.872	0.466	30.0
041808	2	1.90	1.843	1.883	0.599	38.6
042408	8	1.90	1.869	1.911	0.739	47.6
041708	8	1.90	1.876	1.934	0.979	63.1

continued on next page

continued from previous page

Date	Run	T (K)	T_{\min} (K)	T_{\max} (K)	Q (W)	q (mW/cm ²)
042308	10	1.95	1.918	1.930	0.243	15.7
040408	3	1.95	1.845	1.865	0.366	23.6
042408	1	1.95	1.873	1.895	0.56	36.1
042508	6	1.95	1.957	1.990	0.773	49.8
041708	7	1.95	1.930	1.981	0.979	63.1
041708	1	2.00	1.982	1.985	0.271	17.5
042308	6	2.00	1.975	1.982	0.397	25.6
041508	9	2.00	1.998	2.006	0.486	31.3
042308	4	2.00	1.969	1.993	0.718	46.3
042508	3	2.00	2.005	2.018	0.789	50.8
040908	6	2.00	1.970	2.030	1.089	70.2
042308	1	2.05	2.019	2.024	0.246	15.9
041708	4	2.05	2.023	2.029	0.467	30.1
042408	7	2.05	2.006	2.013	0.6	38.7
042308	2	2.05	2.008	2.015	0.722	46.5
042508	4	2.05	2.061	2.064	0.789	50.8
040408	4	2.05	2.045	2.075	0.905	58.3
041608	5	2.05	2.002	2.042	1.286	82.9
041708	3	2.05	2.009	2.074	1.419	91.4
042308	9	2.10	2.056	2.069	0.243	15.7
041508	6	2.10	2.099	2.103	0.475	30.6
041508	7	2.10	2.088	2.101	0.725	46.7
042508	5	2.10	2.099	2.115	0.784	50.5
042508	7	2.10	2.111	2.131	1.068	68.8
041508	8	2.10	2.096	2.116	1.17	75.4
041608	6	2.10	2.065	2.101	1.351	87.1
041608	3	2.15	2.123	2.136	0.37	23.8
042308	8	2.15	2.119	2.125	0.532	34.3
041608	4	2.15	2.128	2.133	0.612	39.4
042308	5	2.15	2.122	2.127	0.721	46.5
041008	4	2.15	2.150	2.160	0.897	57.8

Table B.2: Measured normal fluid velocities compared to the theoretically computed velocities as plotted in Fig. 5.5(a). The temperature given in the legend of Fig. 5.5(a) is given in the first column, Q is the heater power, q the heat flux, v_n is the mean normal fluid velocity given by Eq. (2.25), σ_n is the variation in v_n caused by the fluctuation in T over the duration of the run, v_{no} is the measured value of the normal fluid velocity and σ_{no} is the standard deviation of v_{no} .

T (K)	Q (W)	q (mW/cm ²)	v_n (mm/s)	σ_n (mm/s)	v_{no} (mm/s)	σ_{no} (mm/s)
1.80	0.21	13.34	0.97	0.02	1.05	0.25
1.80	0.22	14.11	0.99	0.03	1.23	0.28
1.80	0.24	15.14	1.04	0.03	1.11	0.20
1.80	0.31	19.72	1.59	0.08	1.53	0.28
1.80	0.36	23.26	1.72	0.14	1.65	0.26
1.80	0.49	31.51	2.08	0.14	1.74	0.36
1.85	0.21	13.40	0.86	0.01	0.95	0.28
1.85	0.31	19.72	1.36	0.04	1.41	0.22
1.85	0.36	22.94	1.44	0.06	1.72	0.27
1.85	0.39	25.13	1.69	0.07	1.74	0.25
1.85	0.54	34.54	2.18	0.14	1.82	0.35
1.85	0.61	39.37	2.46	0.16	2.53	0.28
1.90	0.22	14.43	0.75	0.01	0.73	0.34
1.90	0.31	20.04	1.19	0.02	1.26	0.23
1.90	0.40	25.97	1.24	0.06	0.99	0.33
1.90	0.47	30.03	1.71	0.06	1.37	0.47
1.90	0.60	38.60	2.20	0.15	2.04	0.28
1.90	0.74	47.62	2.48	0.17	2.21	0.41
1.90	0.98	63.09	3.14	0.30	2.95	0.31
1.95	0.24	15.66	0.73	0.01	0.83	0.30
1.95	0.37	23.59	1.38	0.05	1.37	0.44
1.95	0.56	36.09	1.91	0.07	1.87	0.24
1.95	0.77	49.81	1.97	0.11	1.70	0.41
1.95	0.98	63.09	2.66	0.22	2.53	0.30
2.00	0.27	17.46	0.67	0.00	0.85	0.24
2.00	0.40	25.58	1.00	0.01	1.16	0.23
2.00	0.49	31.32	1.12	0.01	0.91	0.24
2.00	0.72	46.27	1.79	0.07	1.88	0.27
2.00	0.79	50.84	1.77	0.04	1.78	0.33
2.00	1.09	70.18	2.56	0.25	2.15	0.50
2.05	0.25	15.85	0.54	0.00	0.60	0.25
2.05	0.47	30.09	1.00	0.01	0.85	0.36
2.05	0.60	38.66	1.36	0.01	1.36	0.24

continued on next page

continued from previous page

T (K)	Q (W)	q (mW/cm ²)	v_n (mm/s)	σ_n (mm/s)	v_{no} (mm/s)	σ_{no} (mm/s)
2.05	0.72	46.53	1.62	0.02	1.62	0.42
2.05	0.79	50.84	1.50	0.01	1.65	0.36
2.05	0.91	58.32	1.74	0.08	1.72	0.39
2.05	1.29	82.87	2.79	0.18	2.44	0.50
2.05	1.42	91.44	2.91	0.30	2.65	0.34
2.10	0.24	15.66	0.46	0.01	0.44	0.17
2.10	0.48	30.61	0.80	0.01	0.79	0.27
2.10	0.73	46.72	1.25	0.03	1.20	0.22
2.10	0.78	50.52	1.30	0.04	1.52	0.57
2.10	1.07	68.82	1.68	0.06	2.00	0.84
2.10	1.17	75.40	1.94	0.07	1.84	0.41
2.10	1.35	87.06	2.42	0.14	2.02	0.47
2.15	0.37	23.84	0.56	0.01	0.65	0.20
2.15	0.53	34.28	0.83	0.01	0.81	0.22
2.15	0.61	39.44	0.93	0.01	0.92	0.24
2.15	0.72	46.46	1.12	0.01	1.10	0.32
2.15	0.90	57.80	1.25	0.02	0.99	0.27

Table B.3: Measured vortex line velocities compared to the theoretically computed superfluid velocities as plotted in Fig. 5.5(b). The temperature given in the legend of Fig. 5.5(b) is given in the first column, Q is the heater power, q the heat flux, v_s is the mean superfluid velocity given computed by Eq. (2.26), σ_s is the variation in v_s caused by the fluctuation in T over the duration of the run, v_L is the measured value of the vortex line velocity and σ_L is the standard deviation of v_L .

T (K)	Q (W)	q (mW/cm ²)	V_s (mm/s)	σ_s (mm/s)	V_L (mm/s)	σ_L (mm/s)
1.80	0.21	13.34	-0.45	0.002	-0.15	0.20
1.80	0.22	14.11	-0.48	0.004	0.01	0.37
1.80	0.24	15.14	-0.52	0.006	-0.08	0.33
1.80	0.31	19.72	-0.65	0.008	-0.23	0.45
1.80	0.36	23.26	-0.78	0.017	-0.25	0.42
1.80	0.49	31.51	-1.09	0.025	-0.26	0.68
1.85	0.21	13.40	-0.47	0.001	-0.17	0.27
1.85	0.31	19.72	-0.67	0.007	-0.24	0.31
1.85	0.36	22.94	-0.81	0.010	-0.30	0.37
1.85	0.39	25.13	-0.87	0.013	-0.19	0.37
1.85	0.54	34.54	-1.22	0.026	-0.67	0.53
1.85	0.61	39.37	-1.39	0.032	-0.68	0.48
1.90	0.22	14.43	-0.55	0.002	-0.20	0.26
1.90	0.31	20.04	-0.72	0.004	-0.38	0.31
1.90	0.40	25.97	-1.04	0.032	-0.49	0.45
1.90	0.47	30.03	-1.10	0.017	-0.68	0.46
1.90	0.60	38.60	-1.42	0.042	-0.61	0.48
1.90	0.74	47.62	-1.83	0.064	-0.64	0.59
1.90	0.98	63.09	-2.49	0.131	-0.80	0.74
1.95	0.24	15.66	-0.64	0.008	-0.21	0.36
1.95	0.37	23.59	-0.85	0.013	-0.57	0.51
1.95	0.56	36.09	-1.37	0.023	-0.73	0.46
1.95	0.77	49.81	-2.31	0.121	-1.28	0.64
1.95	0.98	63.09	-2.80	0.195	-1.26	0.67
2.00	0.27	17.46	-0.83	0.004	-0.47	0.36
2.00	0.40	25.58	-1.20	0.013	-0.65	0.43
2.00	0.49	31.32	-1.59	0.029	-0.76	0.41
2.00	0.72	46.27	-2.19	0.081	-1.15	0.54
2.00	0.79	50.84	-2.71	0.087	-1.28	0.68
2.00	1.09	70.18	-3.65	0.432	-1.99	0.67
2.05	0.25	15.85	-0.89	0.010	-0.48	0.38
2.05	0.47	30.09	-1.72	0.024	-1.06	0.48
2.05	0.60	38.66	-2.04	0.036	-1.34	0.54

continued on next page

continued from previous page

T (K)	Q (W)	q (mW/cm ²)	v_s (mm/s)	σ_s (mm/s)	v_L (mm/s)	σ_L (mm/s)
2.05	0.72	46.53	-2.48	0.043	-1.30	0.62
2.05	0.79	50.84	-3.54	0.038	-1.39	0.87
2.05	0.91	58.32	-4.02	0.398	-1.86	0.66
2.05	1.29	82.87	-4.64	0.437	-1.93	0.76
2.05	1.42	91.44	-5.84	1.036	-2.20	0.77
2.10	0.24	15.66	-1.09	0.050	-0.85	0.39
2.10	0.48	30.61	-2.66	0.020	-1.23	0.61
2.10	0.73	46.72	-3.96	0.124	-2.14	0.56
2.10	0.78	50.52	-4.40	0.028		
2.10	1.07	68.82	-6.46	0.749		
2.10	1.17	75.40	-6.54	0.047		
2.10	1.35	87.06	-6.89	0.726	-2.57	0.84
2.15	0.37	23.84	-2.48	0.229	-2.16	0.62
2.15	0.53	34.28	-3.20	0.118	-2.14	0.66
2.15	0.61	39.44	-4.12	0.154		
2.15	0.72	46.46	-4.47	0.140		
2.15	0.90	57.80	-9.54	0.850		

B.2 Thermistor Calibration

Table B.4: Thermistor calibration values for the temperature probe.

T (K)	R (Ω)	T (K)	R (Ω)	T (K)	R (Ω)
1.800	8072.56	2.898	3611.97	8.999	983.23
1.825	7862.68	3.000	3436.60	9.500	935.98
1.850	7664.54	3.100	3279.08	9.999	894.08
1.875	7473.03	3.200	3135.24	15.003	632.01
1.899	7291.78	3.300	3003.00	20.001	500.55
1.924	7119.82	3.402	2882.87	25.000	418.80
1.950	6952.31	3.500	2771.30	29.998	362.06
1.974	6794.91	3.598	2673.94	35.000	320.11
1.998	6650.84	3.707	2569.89	40.000	287.66
2.025	6503.73	3.801	2488.49	45.001	261.73
2.050	6354.26	3.899	2407.52	50.000	240.55
2.075	6217.48	3.999	2331.51	55.002	222.87
2.099	6087.40	4.100	2259.98	60.001	207.88
2.125	5960.87	4.200	2192.75	65.001	194.98
2.148	5843.21	4.300	2130.46	70.001	183.76
2.174	5722.04	4.400	2071.63	75.001	173.87
2.200	5609.42	4.501	2016.93	80.002	165.12
2.226	5503.34	4.999	1785.24	85.003	157.28
2.250	5396.94	5.497	1605.92	90.003	150.20
2.276	5294.60	6.000	1462.98	95.003	143.79
2.299	5197.70	6.501	1346.34	100.002	137.97
2.400	4842.04	7.007	1247.98	150.024	99.20
2.498	4532.59	7.501	1167.29	200.027	78.21
2.600	4260.75	8.000	1097.34	250.032	65.10
2.700	4019.61	8.498	1036.37	300.048	56.20

B.3 Mutual Friction Coefficients

Table B.5: Values of the mutual friction parameters defined in Eq. (2.23).

T (K)	α	α'	T (K)	α	α'
1.30	0.034	0.0138	2.12	0.581	-0.0563
1.35	0.042	0.0154	2.14	0.753	-0.1249
1.40	0.051	0.0167	2.16	1.097	-0.3096
1.45	0.061	0.0175	2.162	1.15	-0.3453
1.50	0.072	0.0177	2.164	1.21	-0.3883
1.55	0.084	0.0172	2.166	1.279	-0.4416
1.60	0.097	0.0161	2.168	1.362	-0.5103
1.65	0.111	0.0144	2.170	1.577	-0.6358
1.70	0.126	0.0123	2.172	1.769	-0.7747
1.75	0.142	0.0100	2.174	2.113	-1.0240
1.80	0.16	0.0082	2.176	3.195	-1.8070
1.85	0.181	0.0074	2.1761	3.339	-1.9110
1.90	0.206	0.0083	2.1762	3.514	-2.0370
2.00	0.279	0.0120	2.1763	3.732	-2.1940
2.02	0.302	0.0110	2.1764	4.017	-2.4010
2.04	0.33	0.0083	2.1765	4.417	-2.6900
2.06	0.366	0.0030	2.1766	5.049	-3.1470
2.08	0.414	-0.0067	2.1767	6.347	-4.0860
2.10	0.481	-0.0241			

B.4 Pulsed Counterflow Parameters

Table B.6: Experimental parameters for the pulsed counterflow experiments presented in Chapters 6 and 7 and plotted in Fig. 6.2. The color of the text corresponds to the lowest (blue), middle (black) and highest (red) temperature ranges used to form the temperature-conditioned distributions in Fig. 6.12 and summarized in Table 6.1. The Date, Movie File and Pulse denote the source of the data, q is the heat flux and T is the temperature.

Date	Movie File	Pulse	q mW/cm ²	T (K)
101707	pulsed7_80fps_2300mW	1	148	1.71
101707	pulsed7_80fps_2300mW	2	148	1.74
101707	pulsed7_80fps_2300mW	3	148	1.77
101707	pulsed7_80fps_2300mW	4	148	1.79
101707	pulsed5_60fps_1250mW	1	80	1.86
101707	pulsed5_60fps_1250mW	2	80	1.87
101707	pulsed5_60fps_1250mW	3	80	1.88
102307	pulsed4_80fps_2700mW	1	174	1.88
102507	pulsed6_80fps_1660mW	1	107	1.71
102507	pulsed6_80fps_1660mW	2	107	1.74
102507	pulsed6_80fps_1660mW	3	107	1.77
102507	pulsed5_100fps_2300mW	1	148	1.84
102507	pulsed5_100fps_2300mW	2	148	1.85
102507	pulsed5_100fps_2300mW	3	148	1.87
102307	pulsed1_80fps_1500mW	1	96	1.90
102307	pulsed1_80fps_1500mW	2	96	1.92
102307	pulsed1_80fps_1500mW	3	96	1.93
102307	pulsed1_80fps_1500mW	4	96	1.95
102307	pulsed2_60fps_2000mW	1	129	1.91
102307	pulsed2_60fps_2000mW	2	129	1.93
102307	pulsed2_60fps_2000mW	3	129	1.96
102307	pulsed3_60fps_2000mW	1	129	1.89
102307	pulsed3_60fps_2000mW	2	129	1.92
102307	pulsed3_60fps_2000mW	3	129	1.94
102307	pulsed4_80fps_2700mW	2	174	1.90
102307	pulsed6_100fps_2000mW	1	129	1.95
102307	pulsed6_100fps_2000mW	2	129	1.96
102507	pulsed5_100fps_2300mW	4	148	1.88
101707	pulsed1_80fps_1000mW	1	64	1.99
101707	pulsed1_80fps_1000mW	2	64	2.00
101707	pulsed1_80fps_1000mW	3	64	2.01

continued on next page

continued from previous page

Date	Movie File	Pulse	q mW/cm ²	T (K)
101707	pulsed1_80fps_1000mW	4	64	2.02
102307	pulsed6_100fps_2000mW	3	129	1.98
102507	pulsed4_100fps_1200mW	1	77	1.96
102507	pulsed4_100fps_1200mW	2	77	1.98
102507	pulsed4_100fps_1200mW	3	77	2.02
102507	pulsed2_80fps_2000mW	1	129	2.00
102507	pulsed2_80fps_2000mW	2	129	2.02
102507	pulsed2_80fps_2000mW	3	129	2.04
102507	pulsed3_80fps_900mW	1	58	2.01
102507	pulsed3_80fps_900mW	2	58	2.03
102507	pulsed3_80fps_900mW	3	58	2.04

Bibliography

- [1] G. P. Bewley. *Using frozen hydrogen particles to observe rotating and quantized flows in liquid helium*. PhD thesis, Department of Mechanical Engineering, Yale University, New Haven, CT USA, 2006.
- [2] G. P. Bewley, D. P. Lathrop, and K. R. Sreenivasan. Superfluid Helium: Visualization of quantized vortices. *Nature*, 441:588, 2006.
- [3] G. P. Bewley, M. S. Paoletti, K. R. Sreenivasan, and D. P. Lathrop. Characterization of Reconnecting Vortices in Superfluid Helium. *Proc. Natl. Acad. Sci. U.S.A.*, 105:13707, 2008.
- [4] M. S. Paoletti, M. E. Fisher, K. R. Sreenivasan, and D. P. Lathrop. Velocity Statistics Distinguish Quantum Turbulence from Classical Turbulence. *Phys. Rev. Lett.*, 101:154501, 2008.
- [5] M. S. Paoletti, R. B. Fiorito, K. R. Sreenivasan, and D. P. Lathrop. Visualization of Superfluid Helium Flow. *J. Phys. Soc. Japan*, 77(11):111007, 2008.
- [6] M. S. Paoletti, M. E. Fisher, and D. P. Lathrop. Reconnection Dynamics for Quantized Vortices. *Physica D*, 2010.
- [7] A. T. Winfree. Electrical Turbulence in Three-Dimensional Heart Muscle. *Science*, 266:1003–1006, 1994.
- [8] S.I. Vainshtein and F. Cattaneo. Nonlinear restrictions on dynamo action. *Astrophys. J.*, 393:165–171, 1992.
- [9] S. A. Balbus and J. F. Hawley. Instability, turbulence, and enhanced transport in accretion disks. *Rev. Mod. Phys.*, 70(1):1–53, 1998.
- [10] G. D. Holman, L. Sui, R. A. Schwartz, and A. G. Emslie. Electron Bremsstrahlung Hard X-Ray Spectra, Electron Distributions, and Energetics in the 2002 July 23 Solar Flare. *Astrophys. J.*, 595:L97–L101, 2003.
- [11] M. V. Goldman. Strong turbulence of plasma waves. *Rev. Mod. Phys.*, 56:709–735, 1984.
- [12] A. Kolmogorov. The Local Structure of Turbulence in Incompressible Viscous Fluid for Very Large Reynolds' Numbers. *Dokl. Akad. Nauk SSSR*, 30:301–305, 1941. [Proc. R. Soc. Lond. A **434**, 9 (1991)].
- [13] A. Kolmogorov. Dissipation of energy in the locally isotropic turbulence. *Dokl. Akad. Nauk SSSR*, 31:538–540, 1941. [Proc. R. Soc. Lond. A **434**, 15 (1991)].
- [14] R. P. Feynman. Applications of quantum mechanics to liquid helium. In C. J. Gorter, editor, *Progress in Low Temperature Physics*, volume 1, pages 17–53, Amsterdam, 1955. North-Holland.

- [15] W. F. Vinen, M. Tsubota, and A. Mitani. Kelvin-Wave Cascade on a Vortex in Superfluid ^4He at a Very Low Temperature. *Phys. Rev. Lett.*, 91(13):135301, 2003.
- [16] U. Frisch. *Turbulence: The Legacy of A. N. Kolmogorov*. Cambridge Univ. Press, Cambridge, UK, 1995.
- [17] S.-i. Ogawa, M. Tsubota, and Y. Hattori. Study of Reconnection and Acoustic Emission of Quantized Vortices in Superfluid by the Numerical Analysis of the Gross-Pitaevskii Equation. *J. Phys. Soc. Japan*, 71:813, 2002.
- [18] M. Kobayashi and M. Tsubota. Kolmogorov Spectrum of Superfluid Turbulence: Numerical Analysis of the Gross-Pitaevskii Equation with a Small-Scale Dissipation. *Phys. Rev. Lett.*, 94(6):065302, 2005.
- [19] W. F. Vinen. Mutual Friction in a Heat Current in Liquid Helium-II .I. Experiments on Steady Heat Currents. *Proc. Roy. Soc. A*, 240:114–127, 1957.
- [20] W. F. Vinen. Mutual Friction in a Heat Current in Liquid Helium-II .II. Experiments on Transient Effects. *Proc. Roy. Soc. A*, 240:128, 1957.
- [21] W. F. Vinen. Mutual Friction in a Heat Current in Liquid Helium II. III. Theory of the Mutual Friction. *Proc. Roy. Soc. A*, 242:493–515, 1957.
- [22] D. C. Samuels. Velocity matching and Poiseuille pipe flow of superfluid helium. *Phys. Rev. B*, 46:11714–11724, 1992.
- [23] M. R. Smith, R. J. Donnelly, N. Goldenfeld, and W. F. Vinen. Decay of vorticity in homogeneous turbulence. *Phys. Rev. Lett.*, 71:2583–2586, 1993.
- [24] C. F. Barenghi, D. C. Samuels, G. H. Bauer, and R. J. Donnelly. Superfluid vortex lines in a model of turbulent flow. *Phys. Fluids*, 9:2631–2643, 1997.
- [25] C. Nore, M. Abid, and M. E. Brachet. Kolmogorov Turbulence in Low-Temperature Superflows. *Phys. Rev. Lett.*, 78:3896–3899, 1997.
- [26] J. Maurer and P. Tabeling. Local investigation of superfluid turbulence. *Europhys. Lett.*, 43:29–34, 1998.
- [27] S. R. Stalp, L. Skrbek, and R. J. Donnelly. Decay of Grid Turbulence in a Finite Channel. *Phys. Rev. Lett.*, 82:4831–4834, 1999.
- [28] W. F. Vinen. Classical character of turbulence in a quantum liquid. *Phys. Rev. B*, 61:1410–1420, 2000.
- [29] L. Skrbek, A. V. Gordeev, and F. Soukup. Decay of counterflow He II turbulence in a finite channel: Possibility of missing links between classical and quantum turbulence. *Phys. Rev. E*, 67(4):047302, 2003.

- [30] P. M. Walmsley, A. I. Golov, H. E. Hall, A. A. Levchenko, and W. F. Vinen. Dissipation of quantum turbulence in the zero temperature limit. *Phys. Rev. Lett.*, 99(26):265302, 2007.
- [31] L. F. Richardson. Atmospheric Diffusion Shown on a Distance-Neighbour Graph. *Proc. R. Soc. London. A*, 110:709–737, 1926.
- [32] W. F. Vinen. Decay of superfluid turbulence at a very low temperature: The radiation of sound from a kelvin wave on a quantized vortex. *Phys. Rev. B*, 64(13):134520, 2001.
- [33] E. J. Yarmchuk, M. J. V. Gordon, and R. E. Packard. Observation of Stationary Vortex Arrays in Rotating Superfluid Helium. *Phys. Rev. Lett.*, 43:214–217, 1979.
- [34] H. F. Hess, R. B. Robinson, R. C. Dynes, J. M. Valles, Jr., and J. V. Waszczak. Scanning-tunneling-microscope observation of the Abrikosov flux lattice and the density of states near and inside a fluxoid. *Phys. Rev. Lett.*, 62:214–216, 1989.
- [35] J. R. Abo-Shaeer, C. Raman, J. M. Vogels, and W. Ketterle. Observation of Vortex Lattices in Bose-Einstein Condensates. *Science*, 292:476–479, 2001.
- [36] Y. Gasteuil, W. L. Shew, M. Gibert, F. Chillá, B. Castaing, and J.-F. Pinton. Lagrangian Temperature, Velocity, and Local Heat Flux Measurement in Rayleigh-Bénard Convection. *Phys. Rev. Lett.*, 99(23):234302, 2007.
- [37] L. Tisza. Transport Phenomena in Helium II. *Nature*, 141:913, 1938.
- [38] L. Landau. Theory of the Superfluidity of Helium II. *Phys. Rev.*, 60:356–358, 1941.
- [39] W. H. Keesom, A. P. Keesom, and B. F. Saris. A few measurements on the heat conductivity of liquid helium II. *Physica*, 5:281–285, 1938.
- [40] W. F. Vinen and J. J. Niemela. Quantum turbulence. *J. Low Temp. Phys.*, 128(5-6):167–231, 2002.
- [41] G. P. Bewley, D. P. Lathrop, L. R. M. Maas, and K. R. Sreenivasan. Inertial waves in rotating grid turbulence. *Phys. of Fluids*, 19(7):071701, 2007.
- [42] G. P. Bewley, K. R. Sreenivasan, and D. P. Lathrop. Particles for tracing turbulent liquid helium. *Experiments in Fluids*, 44:887–896, 2008.
- [43] P. E. Parks and R. J. Donnelly. Radii of Positive and Negative Ions in Helium II. *Phys. Rev. Lett.*, 16:45–48, 1966.
- [44] D. R. Poole, C. F. Barenghi, Y. A. Sergeev, and W. F. Vinen. Motion of tracer particles in He II. *Phys. Rev. B*, 71(6):064514, 2005.

- [45] Y. A. Sergeev, C. F. Barenghi, and D. Kivotides. Motion of micron-size particles in turbulent helium II. *Phys. Rev. B*, 74(18):184506, 2006.
- [46] C. F. Barenghi, D. Kivotides, and Y. A. Sergeev. Close Approach of a Spherical Particle and a Quantised Vortex in Helium II. *J. Low Temp. Phys.*, 148:293–297, 2007.
- [47] D. Kivotides, C. F. Barenghi, and Y. A. Sergeev. Collision of a tracer particle and a quantized vortex in superfluid helium: Self-consistent calculations. *Phys. Rev. B*, 75(21):212502, 2007.
- [48] D. Kivotides, C. F. Barenghi, and Y. A. Sergeev. Interactions between particles and quantized vortices in superfluid helium. *Phys. Rev. B*, 77(1):014527, 2008.
- [49] L. Skrbek, J. J. Niemela, and R. J. Donnelly. Four Regimes of Decaying Grid Turbulence in a Finite Channel. *Phys. Rev. Lett.*, 85:2973–2976, 2000.
- [50] K. W. Schwarz. Turbulence in superfluid helium: Steady homogeneous counterflow. *Phys. Rev. B*, 18:245–262, 1978.
- [51] M. Tsubota, T. Araki, and S. K. Nemirovskii. Dynamics of vortex tangle without mutual friction in superfluid ^4He . *Phys. Rev. B*, 62:11751–11762, 2000.
- [52] L. P. Kondaurova, V. A. Andryuschenko, and S. K. Nemirovskii. Numerical Simulations of Superfluid Turbulence under Periodic Conditions. *J. Low Temp. Phys.*, 150:415–419, 2008.
- [53] K. W. Schwarz. Three-dimensional vortex dynamics in superfluid ^4He : Line-line and line-boundary interactions. *Phys. Rev. B*, 31:5782–5804, 1985.
- [54] K. W. Schwarz. Three-dimensional vortex dynamics in superfluid ^4He : Homogeneous superfluid turbulence. *Phys. Rev. B*, 38:2398–2417, 1988.
- [55] H. Adachi, S. Fujiyama, and M. Tsubota. Steady State of Counterflow Quantum Turbulence: Vortex filament Simulation with the Full Biot-Savart Law. *ArXiv e-prints*, 2009.
- [56] H. Adachi and M. Tsubota. Numerical Studies of Counterflow Turbulence. Velocity Distribution of Vortices. *J. Low Temp. Phys.*, 158:422–427, 2010.
- [57] A. T. A. M. de Waele and R. G. K. M. Aarts. Route to vortex reconnection. *Phys. Rev. Lett.*, 72:482–485, 1994.
- [58] J. Koplik and H. Levine. Vortex reconnection in superfluid helium. *Phys. Rev. Lett.*, 71:1375–1378, 1993.
- [59] R. J. Donnelly and C. F. Barenghi. The Observed Properties of Liquid Helium at the Saturated Vapor Pressure. *J. Phys. Chem. Ref. Data*, 27:1217–1274, 1998.

- [60] For a review see W. H. Keesom. *Helium*. Elsevier, Amsterdam, 1942.
- [61] W. H. Keesom and J. N. van der Ende. *Proc. Roy. Ac. Amsterdam*, 33:24, 1930.
- [62] W. H. Keesom and A. P. Keesom. On the heat conductivity of liquid helium. *Physica*, 3:359–360, 1936.
- [63] J. F. Allen, R. Peierls, and M. Z. Uddin. Heat Conduction in Liquid Helium. *Nature*, 140:62–63, 1937.
- [64] R. J. Donnelly. *Experimental Superfluidity*. The University of Chicago Press, Chicago, 1967.
- [65] J. O. Wilhelm, A. D. Misener, and A. R. Clark. The Viscosity of Liquid Helium. *Proc. Roy. Soc. London A*, 151:342–347, 1935.
- [66] P. Kapitza. Viscosity of Liquid Helium below the λ -Point. *Nature*, 141:74, 1938.
- [67] J. F. Allen and A. D. Misener. Flow of Liquid Helium II. *Nature*, 141:75, 1938.
- [68] J. F. Allen and H. Jones. New Phenomena Connected with Heat Flow in Helium II. *Nature*, 141:243–244, 1938.
- [69] F. London. The λ -Phenomenon of Liquid Helium and the Bose-Einstein Degeneracy. *Nature*, 141:643–644, 1938.
- [70] L. D. Landau and E. M. Lifshitz. *Fluid mechanics 2nd edition*. Pergamon Press, Oxford, UK, 1987.
- [71] I. Chuang, B. Yurke, R. Durrer, and N. Turok. Cosmology in the laboratory — Defect dynamics in liquid crystals. *Science*, 251:1336–1342, 1991.
- [72] G. Blatter, M. V. Feigel’Man, V. B. Geshkenbein, A. I. Larkin, and V. M. Vinokur. Vortices in high-temperature superconductors. *Rev. Mod. Phys.*, 66:1125–1388, 1994.
- [73] E. Priest and T. Forbes. *Magnetic Reconnection: MHD Theory and Applications*. Cambridge Univ. Press, Cambridge, UK, 2000.
- [74] R. P. Lin and H. S. Hudson. 10–100 keV electron acceleration and emission from solar flares. *Sol. Phys.*, 17:412–435, 1971.
- [75] R. P. Lin, S. Krucker, G. J. Hurford, D. M. Smith, H. S. Hudson, G. D. Holman, R. A. Schwartz, B. R. Dennis, G. H. Share, R. J. Murphy, A. G. Emslie, C. Johns-Krull, and N. Vilmer. RHESSI Observations of Particle Acceleration and Energy Release in an Intense Solar Gamma-Ray Line Flare. *Astrophys. J.*, 595:L69–L76, 2003.

- [76] T. Terasawa and A. Nishida. Simultaneous observations of relativistic electron bursts and neutral-line signatures in the magnetotail. *Planet. Space Sci.*, 24:855–866, 1976.
- [77] D. N. Baker and E. C. Stone. Energetic electron anisotropies in the magnetotail — Identification of open and closed field lines. *Geophys. Res. Lett.*, 3:557–560, 1976.
- [78] P. V. Savrukhin. Generation of suprathermal electrons during magnetic reconnection at the sawtooth crash and disruption instability in the t-10 tokamak. *Phys. Rev. Lett.*, 86(14):3036–3039, 2001.
- [79] M. Øieroset, R. P. Lin, T. D. Phan, D. E. Larson, and S. D. Bale. Evidence for electron acceleration up to ~ 300 keV in the magnetic reconnection diffusion region of earth’s magnetotail. *Phys. Rev. Lett.*, 89(19):195001, 2002.
- [80] P. Dmitruk, W. H. Matthaeus, N. Seenu, and M. R. Brown. Test Particle Acceleration in Three-dimensional Magnetohydrodynamic Turbulence. *Astrophys. J.*, 597:L81–L84, 2003.
- [81] J. F. Drake, M. A. Shay, W. Thongthai, and M. Swisdak. Production of Energetic Electrons during Magnetic Reconnection. *Phys. Rev. Lett.*, 94(9):095001, 2005.
- [82] J. F. Drake, M. Swisdak, H. Che, and M. A. Shay. Electron acceleration from contracting magnetic islands during reconnection. *Nature*, 443:553–556, 2006.
- [83] E. H. Brandt. Thermal Depinning and Melting of the Flux-Line Lattice in High- T_c Superconductors. *Int. J. of Mod. Phys. B*, 5:751–795, 1991.
- [84] M. Bou-Diab, M. J. Dodgson, and G. Blatter. Vortex Collisions: Crossing or Recombination? *Phys. Rev. Lett.*, 86:5132–5135, 2001.
- [85] M. B. Hindmarsh and T. W. B. Kibble. Cosmic strings. *Rep. Prog. Phys.*, 58:477–562, 1995.
- [86] T. Fohl and J. S. Turner. Colliding vortex rings. *Phys. Fluids*, 18(4):433–436, 1975.
- [87] W. T. Ashurst and D. I. Meiron. Numerical study of vortex reconnection. *Phys. Rev. Lett.*, 58:1632–1635, 1987.
- [88] R. M. Kerr and F. Hussain. Simulation of vortex reconnection. *Physica D*, 37:474–484, 1989.
- [89] E. D. Siggia. Collapse and amplification of a vortex filament. *Phys. Fluids*, 28:794–805, 1985.

- [90] B. M. Caradoc-Davies, R. J. Ballagh, and P. B. Blakie. Three-dimensional vortex dynamics in Bose-Einstein condensates. *Phys. Rev. A*, 62(1):011602, 2000.
- [91] T. Lipniacki. Evolution of quantum vortices following reconnection. *Eur. J. Mech. B-Fluids*, 19:361–378, 2000.
- [92] D. Kivotides, C. F. Barenghi, and D. C. Samuels. Superfluid vortex reconnections at finite temperature. *Europhys. Lett.*, 54:774–778, 2001.
- [93] S. Nazarenko and R. J. West. Analytical solution for nonlinear Schrodinger vortex reconnection. *J. Low Temp. Phys.*, 132:1, 2003.
- [94] R. J. Adrian and C. S. Yao. In G. Patterson and J. L. Zakin, editors, *Proceedings, Eighth Biennial Symposium on Turbulence*, pages 170–186, Rolla, 1984. U. Missouri.
- [95] R. J. Adrian. Particle-imaging techniques for experimental fluid-mechanics. *Ann. Rev. Fluid Mech.*, 23:261–304, 1991.
- [96] For an overview of the particle-tracking algorithm consult: <http://www.physics.emory.edu/weeks/idl/tracking.html>.
- [97] T. Zhang and S. W. van Sciver. Use of the particle image velocimetry technique to study the propagation of second sound shock in superfluid helium. *Phys. Fluids*, 16:L99–L102, 2004.
- [98] T. Zhang and S. W. Sciver. The motion of micron-sized particles in He II counterflow as observed by the PIV technique. *J. Low Temp. Phys.*, 138:865–870, 2005.
- [99] T. Zhang and S. W. van Sciver. Large-scale turbulent flow around a cylinder in counterflow superfluid ^4He (He (II)). *Nature Phys.*, 1:36–38, 2005.
- [100] T. Xu and S. W. van Sciver. Particle image velocimetry measurements of the velocity profile in He II forced flow. *Phys. Fluids*, 19(7):071703, 2007.
- [101] S. W. van Sciver, S. Fuzier, and T. Xu. Particle Image Velocimetry Studies of Counterflow Heat Transport in Superfluid Helium II. *J. Low Temp. Phys.*, 148:225–233, 2007.
- [102] K. R. Sreenivasan and C. Meneveau. Singularities of the equations of fluid motion. *Phys. Rev. A*, 38:6287–6295, 1988.
- [103] F. J. Wegner. Corrections to scaling laws. *Phys. Rev. B*, 5(11):4529–4536, 1972.
- [104] J.-H. Chen, M. E. Fisher, and B. G. Nickel. Unbiased estimation of corrections to scaling by partial differential approximants. *Phys. Rev. Lett.*, 48(9):630–634, 1982.

- [105] R. Guida and J. Zinn-Justin. 3D Ising model: the scaling equation of state. *Nucl. Phys. B*, 489:626–652, 1997.
- [106] M. Leadbeater, T. Winiecki, D. C. Samuels, C. F. Barenghi, and C. S. Adams. Sound Emission due to Superfluid Vortex Reconnections. *Phys. Rev. Lett.*, 86:1410–1413, 2001.
- [107] W. F. Vinen. How is turbulent energy dissipated in a superfluid? *J. Phys. Cond. Matter*, 17:3231, 2005.
- [108] R. T. Wang, C. E. Swanson, and R. J. Donnelly. Anisotropy and drift of a vortex tangle in helium II. *Phys. Rev. B*, 36(10):5240–5244, 1987.
- [109] A. V. Gordeev, T. V. Chagovets, F. Soukup, and L. Skrbek. Decaying Counterflow Turbulence in He II. *J. Low Temp. Phys.*, 138:549–554, 2005.
- [110] C. F. Barenghi, A. V. Gordeev, and L. Skrbek. Depolarization of decaying counterflow turbulence in He II. *Phys. Rev. E*, 74(2):026309, 2006.
- [111] C. F. Barenghi and L. Skrbek. On Decaying Counterflow Turbulence in He II. *J. Low Temp. Phys.*, 146:5–30, 2007.
- [112] A. N. Kolmogorov. A refinement of previous hypotheses concerning the local structure of turbulence in a viscous incompressible fluid at high Reynolds number. *J. Fluid Mech.*, 13:82–85, 1962.
- [113] R. Benzi, G. Paladin, A. Vulpiani, and G. Parisi. On the multifractal nature of fully developed turbulence and chaotic systems. *J. Phys. A*, 17:3521–3531, 1984.
- [114] F. Anselmet, Y. Gagne, E. J. Hopfinger, and R. A. Antonia. High-order velocity structure functions in turbulent shear flows. *J. Fluid Mech.*, 140:63–89, 1984.
- [115] C. Meneveau and K. R. Sreenivasan. Simple multifractal cascade model for fully developed turbulence. *Phys. Rev. Lett.*, 59:1424–1427, 1987.
- [116] L. C. Andrews, R. L. Phillips, B. K. Shivamoggi, J. K. Beck, and M. L. Joshi. A statistical theory for the distribution of energy dissipation in intermittent turbulence. *Phys. Fluids*, 1:999–1006, 1989.
- [117] S. Kida. Log-stable distribution and intermittency of turbulence. *J. Phys. Soc. Japan*, 60:5–8, 1991.
- [118] Z.-S. She and S. A. Orszag. Physical model of intermittency in turbulence: Inertial-range non-gaussian statistics. *Phys. Rev. Lett.*, 66(13):1701–1704, 1991.
- [119] A. Vincent and M. Meneguzzi. The spatial structure and statistical properties of homogeneous turbulence. *J. Fluid Mech.*, 225:1–20, 1991.

- [120] G. Stolovitzky and K. R. Sreenivasan. Scaling of structure functions. *Phys. Rev. E*, 48:33, 1993.
- [121] R. Benzi, S. Ciliberto, R. Tripicciono, C. Baudet, F. Massaioli, and S. Succi. Extended self-similarity in turbulent flows. *Phys. Rev. E*, 48(1):R29–R32, 1993.
- [122] R. Benzi, S. Ciliberto, C. Baudet, G. Ruiz Chavarria, and R. Tripicciono. Extended self-similarity in the dissipation range of fully developed turbulence. *Europhys. Lett.*, 24:275, 1993.
- [123] Z.-S. She and E. Leveque. Universal scaling laws in fully developed turbulence. *Phys. Rev. Lett.*, 72:336–339, 1994.
- [124] G. I. Barenblatt and N. Goldenfeld. Does fully developed turbulence exist? Reynolds number independence versus asymptotic covariance. *Phys. Fluids*, 7:3078–3082, 1995.
- [125] A. Arneodo, C. Baudet, F. Belin, R. Benzi, B. Castaing, B. Chabaud, R. Chavarria, S. Ciliberto, R. Camussi, F. Chillà, B. Dubrulle, Y. Gagne, B. Hebral, J. Herweijer, M. Marchand, J. Maurer, J. F. Muzy, A. Naert, A. Noullez, J. Peinke, F. Roux, P. Tabeling, W. van de Water, and H. Willaime. Structure functions in turbulence, in various flow configurations, at Reynolds number between 30 and 5000, using extended self-similarity. *Europhys. Lett.*, 34:411–416, 1996.
- [126] O. N. Boratav and R. B. Pelz. Structures and structure functions in the inertial range of turbulence. *Physics of Fluids*, 9:1400–1415, 1997.
- [127] K. R. Sreenivasan and R. A. Antonia. The Phenomenology of Small-Scale Turbulence. *Ann. Rev. Fluid Mech.*, 29:435–472, 1997.
- [128] G. S. Lewis and H. L. Swinney. Velocity structure functions, scaling, and transitions in high-reynolds-number couette-taylor flow. *Phys. Rev. E*, 59(5):5457–5467, 1999.
- [129] L. Chevillard, S. G. Roux, E. Lévêque, N. Mordant, J.-F. Pinton, and A. Arnéodo. Intermittency of Velocity Time Increments in Turbulence. *Phys. Rev. Lett.*, 95(6):064501, 2005.
- [130] J. Fineberg, D. P. Lathrop, and H. L. Swinney. Asymptotic scaling in turbulent couette-taylor flow. In R. Benzi, C. Basdevant, and S. Ciliberto, editors, *Turbulence in Spatially Extended Systems*. Nova Science Publishers, 1993.
- [131] C. F. Barenghi. Classical aspects of quantum turbulence. *J. Phys. Cond. Matter*, 11:7751–7759, 1999.
- [132] C. F. Barenghi, S. Hulton, and D. C. Samuels. Polarization of superfluid turbulence. *Phys. Rev. Lett.*, 89(27):275301, 2002.

- [133] C. F. Barenghi, D. C. Samuels, and D. Kivotides. Superfluid Vortex Reconnections. *J. Low Temp. Phys.*, 126:271–279, 2002.
- [134] M. Kobayashi and M. Tsubota. Decay of Quantized Vortices in Quantum Turbulence. *J. Low Temp. Phys.*, 145:209–218, 2006.
- [135] M. Kobayashi and M. Tsubota. Quantum turbulence in a trapped Bose-Einstein condensate. *Phys. Rev. A*, 76(4):045603, 2007.
- [136] V. S. L’Vov, S. V. Nazarenko, and O. Rudenko. Bottleneck crossover between classical and quantum superfluid turbulence. *Phys. Rev. B*, 76(2):024520, 2007.
- [137] T. V. Chagovets, A. V. Gordeev, and L. Skrbek. Effective kinematic viscosity of turbulent He II. *Phys. Rev. E*, 76(2):027301, 2007.
- [138] K. Morris, J. Koplik, and D. W. I. Rouson. Vortex locking in direct numerical simulations of quantum turbulence. *Phys. Rev. Lett.*, 101(1):015301, 2008.
- [139] I. Procaccia and K. R. Sreenivasan. The state of the art in hydrodynamic turbulence: Past successes and future challenges. *Physica D*, 237:2167–2183, 2008.
- [140] D. Kivotides, J. C. Vassilicos, C. F. Barenghi, M. A. I. Khan, and D. C. Samuels. Quantum signature of superfluid turbulence. *Phys. Rev. Lett.*, 87(27):275302, 2001.
- [141] I. A. Min, I. Mezic, and A. Leonard. Lévy stable distributions for velocity and velocity difference in systems of vortex elements. *Phys. Fluids*, 8:1169–1180, 1996.
- [142] B. W. Zeff, D. D. Lanterman, R. McAllister, R. Roy, E. J. Kostelich, and D. P. Lathrop. Measuring intense rotation and dissipation in turbulent flows. *Nature*, 421:146–149, 2003.
- [143] A. Noullez, G. Wallace, W. Lempert, R. B. Miles, and U. Frisch. Transverse velocity increments in turbulent flow using the RELIEF technique. *J. Fluid Mech.*, 339:287–307, 1997.
- [144] T. Gotoh, D. Fukayama, and T. Nakano. Velocity field statistics in homogeneous steady turbulence obtained using a high-resolution direct numerical simulation. *Phys. Fluids*, 14:1065–1081, 2002.
- [145] D. del-Castillo-Negrete, B. A. Carreras, and V. E. Lynch. Fractional diffusion in plasma turbulence. *Phys. Plasmas*, 11:3854–3864, 2004.
- [146] R. J. Donnelly. *Quantized Vortices in Helium II*. Cambridge Univ. Press, Cambridge, UK, 1991.

- [147] S. P. Suter and R. Skalak. The history of Poiseuille's law. *Ann. Rev. Fluid Mech.*, 25:1–19, 1993.
- [148] K. P. Martin and J. T. Tough. Evolution of superfluid turbulence in thermal counterflow. *Phys. Rev. B*, 27:2788–2799, 1983.
- [149] D. J. Melotte and C. F. Barenghi. Transition to Normal Fluid Turbulence in Helium II. *Phys. Rev. Lett.*, 80:4181–4184, 1998.
- [150] C. D. Andereck, J. Chalups, and W. I. Glaberson. Tkachenko Waves in Rotating Superfluid Helium. *Phys. Rev. Lett.*, 44:33–36, 1980.